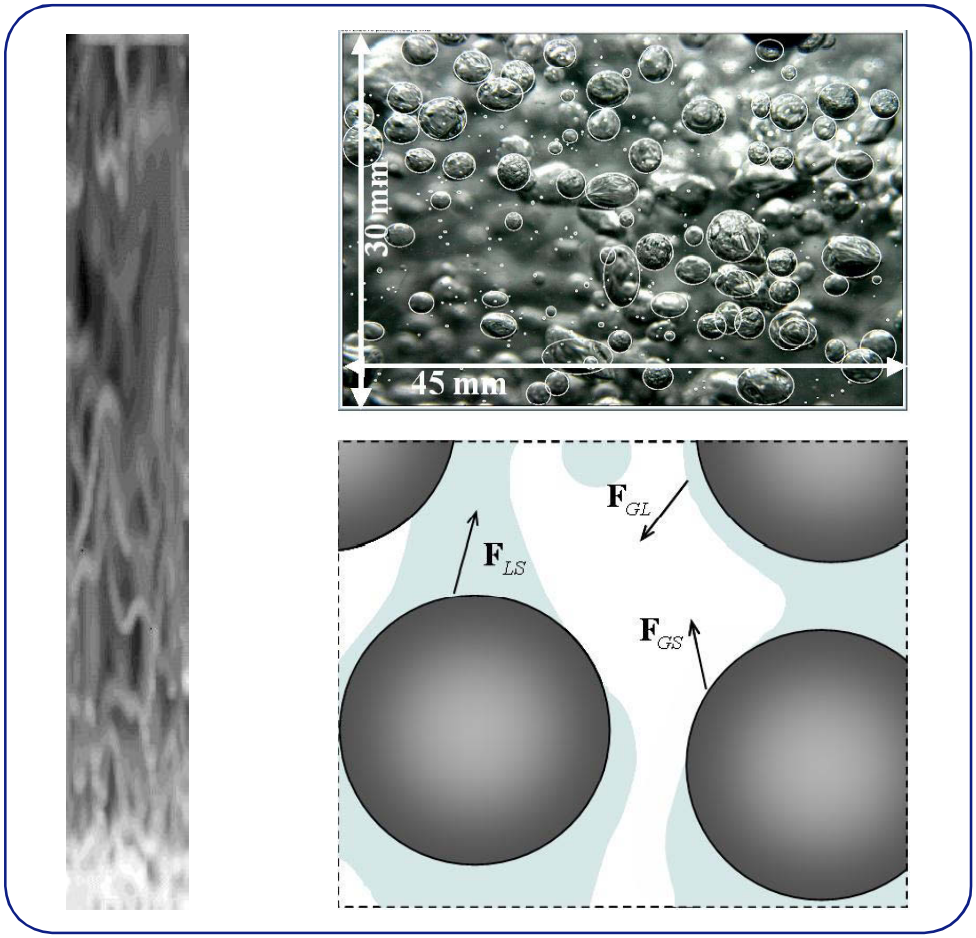

Modelling of multiphase chemical reactors (ModCheR)

Final report

VTT TIEDOTTEITA – RESEARCH NOTES 2340

Modelling of multiphase chemical reactors (ModCheR)

Final report

Mikko Manninen[1] (ed.)

Ulla Ojaniemi, Markus Olin, Timo Pättikangas, Maiju Seppälä, Veikko Taivassalo[1]

Juhani Aittamaa, Ville Alopaeus, Katja Hynynen, Suvi Jussila, Marko Laakkonen, Maret Liiri, Pasi Moilanen, Asta Nurmela, Iiro Pulkkinen[2]

Hannu Alatalo, Henry Hatakka, Juha Kallas, Arto Laari, Zuoliang Sha, Ilkka Turunen[3]

Alf Hermanson, Sirpa Kallio[4]

Hannu Eloranta, Markus Honkanen, Pentti Saarenrinne, Taija Saikkonen[5]

[1] VTT Technical Research Centre of Finland
[2] Helsinki University of Technology
[3] Lappeenranta University of Technology
[4] Åbo Akademi University
[5] Tampere University of Technology

ISBN 951–38–6793–5 (soft back ed.)
ISSN 1235–0605 (soft back ed.)

ISBN 951–38–6794–3 (URL: http://www.vtt.fi/publications/index.jsp)
ISSN 1455–0865 (URL: http://www.vtt.fi/publications/index.jsp)

JULKAISIJA – UTGIVARE – PUBLISHER

VTT, Vuorimiehentie 3, PL 1000, 02044 VTT
puh. vaihde 020 722 111, faksi 020 722 4374

VTT, Bergsmansvägen 3, PB 1000, 02044 VTT
tel. växel 020 722 111, fax 020 722 4374

VTT Technical Research Centre of Finland, Vuorimiehentie 3, P.O.Box 1000, FI-02044 VTT, Finland
phone internat. +358 20 722 111, fax +358 20 722 4374

VTT, Lämpömiehenkuja 3 A, PL 1000, 02044 VTT
puh. vaihde 020 722 111, faksi 020 722 5000

VTT, Värmemansgränden 3 A, PB 1000, 02044 VTT
tel. växel 020 722 111, fax 020 722 5000

VTT Technical Research Centre of Finland, Lämpömiehenkuja 3 A, P.O. Box 1000, FI-02044 VTT, Finland, phone internat. + 358 20 722 111, fax + 358 20 722 5000

Technical editing Anni Kääriäinen

Valopaino Oy, Helsinki 2006

Manninen, Mikko (ed.). Modelling of multiphase chemical reactors (ModCheR). Final report. Espoo 2006. VTT Tiedotteita – Research Notes 2340. 181 p.

Keywords chemical reactors, modelling, multiphase flow, crystallization, computational fluid dynamics, trickle bed reactors, fluidised beds, drag reduction, gas-liquid processes, mass transfer, population balance, flotation

Abstract

The project “Modelling of multiphase chemical reactors (ModCheR)” was carried out by research groups from Helsinki University of Technology, VTT, Lappeenranta University of Technology, Åbo Akademi University and Tampere University of Technology. The model development was concentrated on CFD, but population balance models, cell interaction models and simple algebraic reactor models were also included. Extensive experimental work was carried out in order to provide data for model validation. Five topics were studied in the project. In crystallization, the subjects covered single crystal growth, batch crystallization and continuous crystallization. Both experimental work and model development were carried out. As gas-liquid processes, stirred reactors, bubble columns and flotation were studied. The modelling approaches included CFD and multiblock models. Modelling of trickle bed reactors involved both CFD and simpler approaches and important part of the work consisted of developing models for the interaction and dispersion terms in the equations. Work on drag reducing agents included measurements of the DR-effect in stirred reactors and pipe flow and model development for describing the effect of DRA on turbulence. In modelling of fluidised beds, models of turbulent bed and circulating bed were developed and validated, in particular, mixing of gas and solid, drag models, and macroscopic models were investigated. This final report describes the main results of the project. More detailed information can be found in the reports and publications produced in the project and referred to in this report.

Preface

The ModCheR-project (Modelling of multiphase chemical reactors) was carried out 1.1.2004–31.3.2006 in collaboration between Helsinki University of Technology, VTT, Lappeenranta University of Technology, Åbo Akademi University and Tampere University of Technology. Five topics involving multiphase flows were included in the project: crystallization, gas-liquid processes, trickle reactors, drag reduction, and fluidised beds. Cooperation between the research teams was intensive within each topic throughout the project. Most of the industrial partners (Neste Oil, Outokumpu Research, Kemira, Foster Wheeler, OMG) conducted their own industrial research projects closely related to the ModCheR-project. In many cases, the research groups of the project also acted as subcontractors in the industrial projects. This was highly beneficial, because it ensured the coupling of the model development and experimental work of the ModCheR-project directly to the industrial needs.

This final report consists of an introduction and fairly detailed description of the results of the ModCheR-project. The report is organised so that one section is devoted to each of the five topics.

The project consortium gratefully acknowledges the Finnish Funding Agency for Technology and Innovation (Tekes), Neste Oil Oy, Outokumpu Research Oy, Kemira Oyj, Foster Wheeler Energia Oy, and OMG Harjavalta Nickel Oy for funding of the project.

Contents

Abstract....3

Preface....4

1. Introduction....9

2. CFD modelling for crystallization processes and crystallizer design....12
   - 2.1 Introduction....12
   - 2.2 Modelling of single crystal growth (binary and ternary)....12
     - 2.2.1 Theory....13
     - 2.2.2 Geometry of the system....15
     - 2.2.3 Physical properties....17
     - 2.2.4 Growth model....18
     - 2.2.5 Crystal growth rates....23
     - 2.2.6 Discussion and conclusions about single crystal study....25
   - 2.3 Batch experiments....26
     - 2.3.1 Crystallizer....26
     - 2.3.2 Water experiments....28
     - 2.3.3 Batch crystallization....30
     - 2.3.4 Slip velocity....33
   - 2.4 Continuous experiments....35
     - 2.4.1 Experimental setting....35
     - 2.4.2 Experiments....36
     - 2.4.3 Results....36
   - 2.5 Modelling of suspension crystallizer....40
     - 2.5.1 Flows and heat transfer....40
     - 2.5.2 Classification of the crystals and effect of the crystals on flow profile....42
     - 2.5.3 Slip velocities....44
     - 2.5.4 Crystal growth....45
     - 2.5.5 Population balance model....46
   - 2.6 Summary....47

3. CFD simulation of gas-liquid processes....50
   - 3.1 Introduction....50
   - 3.2 Modelling gas-liquid mass transfer in agitated reactors....51
     - 3.2.1 Experimental....51
     - 3.2.2 Multiblock stirred tank model....52
     - 3.2.3 The simulated vs. measured local bubble size distributions....53
     - 3.2.4 Simulated vs. measured gas-liquid mass transfer....55

3.2.5 Gas-liquid mass transfer simulations with CFD 57
3.2.6 Dynamic modelling of batch xanthan fermentation....59
3.2.7 Conclusions....61
3.3 Development of CFD models for bubble columns....62
3.3.1 Model development....62
3.3.2 CFD models....64
3.3.3 Verification of the CFD calculations by PIV measurements....66
3.3.4 Computational study of bubble dynamics....66
3.3.5 Conclusions....67
3.4 Application of algebraic slip mixture model for bubbly flows....68
3.4.1 Population models for bubbly flow in a stirred tank....68
3.4.2 Results of the breakup model comparisons....69
3.4.3 Sensitivity analysis of the models....73
3.4.4 Conclusions....75
3.5 CFD modelling of flotation....75
3.5.1 The probability models for flotation subprosesses....76
3.5.2 Results of flotation simulation....78
3.5.3 Conclusions....82

4. CFD model development in trickling and pulsing flow in solid/liquid/gas systems....87
4.1 Introduction....87
4.2 Experimental setup....87
4.3 Experiments....90
4.3.1 One phase experiments....90
4.3.2 Two phase experiments....91
4.4 Modeling....95
4.4.1 CFD modelling....95
4.4.2 Model improvement....99
4.4.3 Simplified, analytically solvable models....106
4.4.4 Cell interaction models....108

5. Drag reduction effects....111
5.1 Introduction....111
5.2 Effects of DRA on power number, bubble size distribution and mass transfer in agitated vessels....112
5.2.1 Experimental setup....112
5.2.2 Results....112
5.2.3 Conclusions....116
5.3 Effects of DRA on flow and turbulence in stirred tank reactors....116
5.3.1 Background....116
5.3.2 Mixing tank with a Rushton turbine and water soluble high polymer....118

5.3.3 Mixing tank with pitched blade turbine and hydrocarbon soluble high polymer 128
5.3.4 Further studies with two high polymers 134
5.3.5 Conclusions 137
5.4 The effect of drag reducing polymers in pipe flow 138
5.4.1 Background 138
5.4.2 Equipment 138
5.4.3 Measurements 139
5.4.4 Results 140
5.5 Turbulence model for polymeric drag reduction 142
5.5.1 Background 142
5.5.2 Governing equations for viscoelastic flow 142
5.5.3 Viscoelastic energy balance 143
5.5.4 1- and 2-dimensional studies 143
5.5.5 Reynolds averaged models 145
5.5.6 Summary and conclusions 150

6. Modelling of fluidised beds 153
6.1 Background 153
6.2 Measurements of flow patterns and mixing in a turbulent fluidised bed 155
6.3 Simulations of turbulent fluidization 158
6.3.1 Validation of turbulent bed simulation results 160
6.3.2 Simulation of mixing in a turbulent fluidized bed 162
6.3.3 Turbulent bed simulation with modified drag 165
6.3.4 MFIX simulation 166
6.4 Simulations of riser flow 168
6.5 Macroscopic modelling 170
6.6 Summary 172

7. Summary and applications of the results 175
7.1 CFD modelling of crystallization and crystallization design 175
7.2 CFD simulation of gas-liquid processes 175
7.3 CFD model development for trickling and pulsing flow in solid/liquid/gas systems 176
7.4 Drag reduction effects 177
7.5 Modelling of fluidized bed risers 177

8. List of publications produced in the project 178

1. Introduction

Computational fluid dynamics (CFD) techniques have been developed to a level that allows complex flow situations to be modelled with a reasonable degree of detail and accuracy. The use of computational fluid dynamics to multiphase systems has been growing during the recent years. Despite the widespread use of CFD, there is still a lack of validated, predictive models of many relevant transport phenomena, especially in the field of multiphase flows. In particular, the validation together with sophisticated modelling should be emphasized when a trustworthy design basis for process equipment and operation for multiphase systems is considered.

The ModCheR-project has been an extensive effort to develop and validate models for complex multiphase systems. Five research topics were selected for the project: 1. CFD modelling for crystallization processes and crystallizer design; 2. CFD simulation of gas liquid processes; 3. CFD model development in trickling and pulsing flow in solid/liquid/gas systems; 4. Drag reduction effects; 5. Modelling of fluidised beds. All of these tropics involved both model development and measurements in order to provide experimental data for model validation.

Modelling of crystallization process is complicated because of the many phenomena as nucleation, agglomeration, crystal growth and breakage, involved simultaneously. Comprehensive modelling of crystallization processes requires population balance modelling or a representative form of it coupled to advanced CFD modelling of a multiphase system. The goal in the ModCheR-project was develop models applicable in improving the performance and controllability of crystallization processes. Extensive modelling and experimental research was carried out in the areas of single crystal growth, batch and continuous crystallization, and population balance model development.

Gas-liquid processes are common in industrial processes and CFD modelling of such systems has become popular. Compared to solid-liquid suspensions, modelling of bubbly flows is more problematic, because the hydrodynamics is complicated due to the bubble deformation, break up and coalescence. The most important process equipment involving bubbly flows are bubble columns and agitated reactors with gas dispersion. Models for both of these systems were developed in the project.

In bubble columns, the research work consisted of breakup and coalescence model development, CFD modelling based on Eulerian multiphase models and multi-size-group approach, PIV-measurements, and study of bubble dynamics. For stirred reactors, a dynamic multiblock model was developed, including gas-liquid mass transfer. In

addition, breakup and coalescence models were coupled to algebraic slip mixture model and validated against measured bubble size distributions.

Flotation is an extension of bubbly flows, as it involves the solid particles as the third phase. The process is obviously more complicated than pure gas-liquid flows, because the collision and attachment processes have to be modelled and stability of the particle-bubble aggregates has to be considered. In the ModCheR-project, models based on the mixture model were developed and tested for flotation.

Trickle bed reactors consist of a packed catalyst bed and usually co-current flow of gas and liquid through the bed. The process forms therefore a three phase system, where the solid phase is stationary. The flow of the two fluid phases is determined by several intricate phenomena, including the drag forces between the phases, the capillary pressure and the horizontal dispersion due to pore structure. In model development, these terms in the equations are decisive for the ability of the model to describe the reactor behaviour correctly. In the ModCheR-project, several types of models were developed for packed bed reactors, ranging from simple algebraic and cell interaction models to 3D CFD models. Significant part of the subproject consisted of building an experimental apparatus and gathering measured data of pressure drop and liquid distribution in varying flow conditions of the bed. These data were used in model validation.

Drag reduction as such is usually not considered a multiphase problem, although it is based on polymer additives mixed in a liquid. It has been found indications that the drag reducing agents (DRA) may have a profound effect also in multiphase systems, such as polymerization and possibly gas-liquid systems. The objective of using DRA in such systems would be to attempt to control the particle or bubble size in a reactor. One of the goals in the ModCheR-project was to investigate these phenomena. In addition, the DR-effect as such was studied both experimentally and theoretically. The understanding of the drag reduction on the basis of damping of turbulence is currently under active research, but the fundamental mechanisms are still under debate.

In gas-solid flows, a complicating factor is the formation of meso-scale structures in the flow field, e.g. bubbles in dense suspensions and particle clusters and strands in riser flows. The length scales that are simultaneously important in gas-solid flows range from the particle length scale to clusters of particles to the scale of the process itself. The physical size of gas-solid flow processes like fluidized beds is typically large, up to tens of meters in height and width, which renders numerical resolution of the fine structures of the flow field impossible due to computational restrictions. Special models and sub-grid closure relations have to be developed and applied to obtain acceptable simulation results. In the ModCheR-project, measurements of gas and solid mixing in a turbulent

fluidised bed were carried out. These data were then used in validating Eulerian fluidised bed models. New drag models were developed and tested also for circulating fluidised beds. In addition, macroscopic modelling suitable for simulating fluidised beds using much coarser computational meshes was developed.

2. CFD modelling for crystallization processes and crystallizer design

Henry Hatakka[1], *Hannu Alatalo*[1], *Juha Kallas*[1], *Maret Liiri*[2] *and Juhani Aittamaa*[2]

2.1 Introduction

Solution crystallization encompasses the formation of solid phases from a fluid phase. It is applied extensively in the chemical industry, both as a purification process and a separation process. The characteristic feature of crystallization is that it produces substances of high purity, at a low level of energy consumption, and often at relatively mild process conditions. Though crystallization in practice is a well-known operation, the design and operation of crystallization processes still establish many problems as far as product quality is concerned. This is due to complex integration of crystallization phenomena, inhomogeneous, transient fluid and heat flow behaviour. A better understanding of crystallization phenomena and flow characteristics is imperative for the control, design and scale-up of industrial crystallizers.

The ultimate goal of the crystallization project is two-fold:

- to create a basis for the design and scale-up of crystallizers
- to improve the performance and controllability of crystallization processes.

Both of the objectives require

- a sophisticated computational model of crystallization which comprises the fundamental equations for crystallization phenomena, a population balance or a representative form of it integrated to flow field model for arbitrary geometries
- measurement and monitoring environment to validate the computational model with all-round experiments.

2.2 Modelling of single crystal growth (binary and ternary)

Crystal growth rate depends on both diffusion and surface reaction. In industrial crystallizers, in different regions there exist conditions for diffusion-controlled growth and surface reaction controlled growth. It is therefore essential to include the effect of

[1] Lappeenranta University of Technology, Department of Chemical Technology, Separation Technology

[2] Helsinki University of Technology, Department of Chemical Technology, Chemical Engineering and Plant Design

both steps into the crystal growth model. Using mathematical modelling and experimental information obtained from growth studies of single crystals it is possible to separate these phenomena and study how they are affected by concentration, slip velocities of particles, and finally estimate the parameters for crystal growth models.

The purpose of our work was to develop a model for crystal growth that can predict growth rate in various conditions but that is not computationally too demanding. Measurements from single crystal growth experiments of KDP were available from Enqvist et al. [1, 2]. Power-law model with activity-based supersaturation was used. The model was first developed for binary KDP-water case (presented in Liiri et al. [3]) and later for ternary KDP-water-ethanol case (presented in Liiri et al. [4]) and KDP-water-propanol case using the same method for model development.

2.2.1 Theory

The fundamental driving force for crystallization from electrolyte solutions is (Kim et al. [5]):

$$\frac{\Delta\mu}{RT} = \frac{\mu - \mu^*}{RT} = \nu \ln\left(\frac{a_\pm}{a_\pm^*}\right) = \nu \ln\left(\frac{\gamma_\pm c}{\gamma_\pm^* c^*}\right) = \sigma_{act}\,. \tag{2.1}$$

The same concept is also referred as activity based supersaturation σ_{act}. The thermodynamically exact overall crystal growth rate determined both by the mass transfer of solute and by the surface integration to the crystal lattice is (Kim et al. [5])

$$R_g = k_d'\nu \ln\frac{a_\pm}{a_{\pm i}} = k_r'\left(\nu \ln\frac{a_{\pm i}}{a_\pm^*}\right)^{n'}\,. \tag{2.2}$$

Notations of the activities $a_\pm$, $a_{\pm i}$ and $a_\pm^*$ in relevant locations are shown in Figure 2.1. Eliminating the interface activity $a_{\pm i}$ from Equation (2.2) gives

$$R_g = k_r'\left(\nu \ln\frac{a_\pm}{a_\pm^*} - \frac{R_g}{k_d'}\right)^{n'} = k_r'\left(\sigma_{act} - \frac{R_g}{k_d'}\right)^{n'}\,. \tag{2.3}$$

This overall growth rate R_g expressed by Equations (2.2) and (2.3) presents the kinetics of the growth over a wider range of concentration than the growth rate models using concentration-based supersaturation.

Mass transfer coefficient k_d' can be presented as

$$\frac{k_d^{'}}{kg/m^2 s} = \left(A + \frac{k_1}{z/mm} \right) \tag{2.4}$$

where A and k_1 are constants, z (mm) is the thickness of the mass transfer film.

Activity coefficients for binary KDP-water solution are calculated from Pitzer equations [6]:

$$\ln \gamma_{\pm} = f^{\gamma} + M B_{\pm}^{\gamma} + \frac{3}{2} M^2 C_{\pm}^{\Phi} \tag{2.5}$$

where

$$f^{\gamma} = -A_{\Phi} \left[\frac{\sqrt{M}}{1+1.2\sqrt{M}} + \frac{2}{1.2} \ln\left(1+1.2\sqrt{M}\right) \right] \tag{2.6}$$

$$B_{\pm}^{\gamma} = 2\beta_0 + \frac{\beta_1}{2M} \left[1 - \left(1 + 2\sqrt{M} - 2M\right) \exp\left(-2\sqrt{M}\right) \right]. \tag{2.7}$$

Parameter A_{Φ}, the Debye-Hückel parameter, depends on temperature. Parameters β_0, β_1 and $C_{\pm}^{\Phi}$ are dependent on the electrolyte.

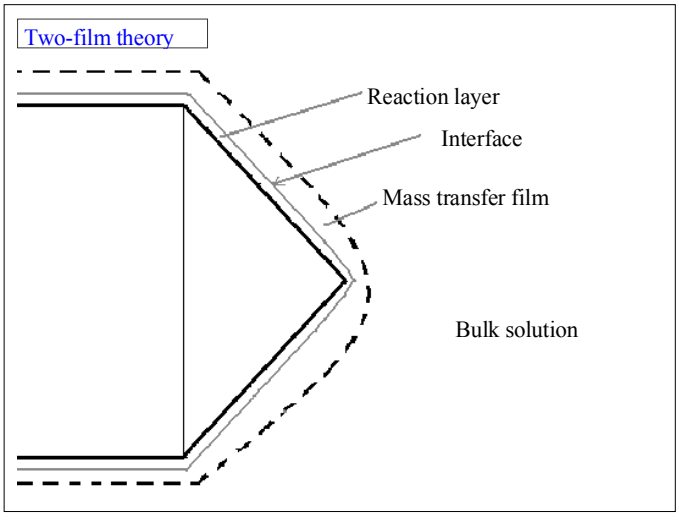

Figure 2.1. Concepts in the mass transfer model.

Activity coefficients for KDP in ternary KDP-water-organic solution are calculated with Pitzer equations (Partanen et al. [7], Enqvist et al. [1]), K = K^+, A = H_2PO_4-

$$\ln \gamma_{\pm} = \left[f^{\gamma} + B_{KA} \left(M_A + M_K \right) + f'(B) \right] + \lambda M_{org} \tag{2.8}$$

where

$$f^{\gamma} = -A_{\Phi}\left[\frac{\sqrt{M_{KDP}}}{1+1.2\sqrt{M_{KDP}}} + \frac{2}{1.2}\ln\left(1+1.2\sqrt{M_{KDP}}\right)\right] \tag{2.9}$$

$$B_{KA} = \beta_0 + \frac{\beta_1}{2I_m}\left[1-\left(1+2\sqrt{I_m}\right)\exp\left(-2\sqrt{I_m}\right)\right] \tag{2.10}$$

$$f'(B) = \frac{\beta_1 M_K M_A}{2I_m^2}\left[-1+\left(1+2\sqrt{I_m}+2I_m\right)\exp\left(-2\sqrt{I_m}\right)\right]. \tag{2.11}$$

A_{Φ} is the Debye-Hückel parameter; $I_m = \sqrt{M_K + M_A}$ is ionic strength; β_0, β_1, B_{KA} are parameters in Pitzer equation; f^{γ}, $f'(B)$ are functions in the Pitzer equation. M (mol/kgH_2O) is molarity, λ is ion-molecule interaction parameter, $\lambda = \lambda_{K,org} + \lambda_{A,org}$. Pitzer equations for calculating activity coefficients in binary KDP-water solution are available in Pitzer [6].

2.2.2 Geometry of the system

The growing crystal was located in the middle of a rectangular 1 cm x 1 cm tube. The dimensions of the modelled part of the system and the location of the crystal in the tube are presented in Figure 2.2. Structural grids were used for CFD simulations because those enable more accurate results within shorter computational time than unstructured grids.

The number of control volume elements especially in the mass transfer film should be large to get good accuracy but not too large to keep computational time reasonable. In our case three resolutions for computational grids were tested with two inlet velocities and two concentrations. Height of 0.007 mm for the first element on the crystal surface gave acceptable accuracy.

Geometry with length L (see Figure 2.2) including $1.3 \cdot 10^6$ control volume elements was used for studying the growth of the (1 0 1) face of the crystal and the physical conditions near that face. The grid was finest within 0.5 mm around the crystal to obtain enough accuracy in the mass transfer film. Part of the grid is presented in Figure 2.3.

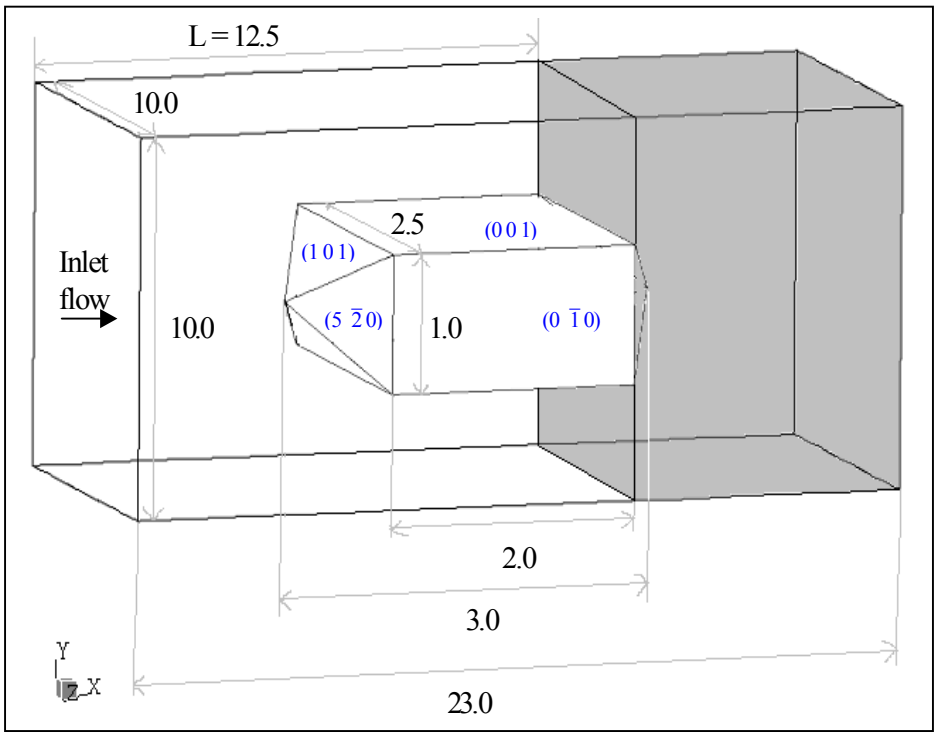

Figure 2.2. Geometry of the crystal and the modelled system, dimensions are in mm. Miller indices of crystal faces.

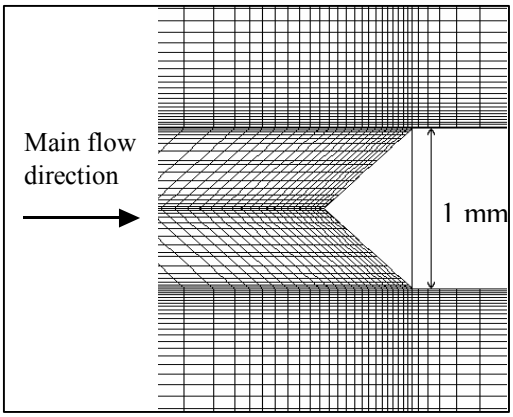

Figure 2.3. Details of the grid used in CFD simulations, area near the crystal.

2.2.3 Physical properties

Density and viscosity of KDP-water solution at 30 °C were calculated with equations available in Wang et al. [8]. Densities of the alcohols at 30 °C are 0.78 kg/dm^3 for ethanol and 0.80 kg/dm^3 for propanol. Binary KDP-water diffusivity in corresponding molarities of KDP was estimated from the data found from Bohenek et al. [9]. Binary diffusivities of the alcohols were estimated from the diffusivity data found from Easteal and Woolf [10] and Hawlicka and Grabowski [11]. Binary diffusivities of ethanol and propanol in water at 30 °C are higher than binary diffusivity of 1.3–1.7 molar KDP in water at the same temperature.

Wesseling and Krishna [12] suggested using a value close to the geometrical average of the '13' and '23' diffusivities in pure '3' for diffusivity of traces of '1' and '2' in '3'. In this study KDP and alcohol were handled like traces '1' and '2' in water and the equation for the geometric average was modified using weighting with molar fractions

$$D_{eff} = \left(\frac{M_{KDP}}{M_{KDP} + M_{AlcOH}} \right) D_{KDP,H2O} + \left(\frac{M_{AlcOH}}{M_{KDP} + M_{AlcOH}} \right) D_{AlcOH,H2O} \qquad (2.12)$$

where $D_{KDP,H2O}$ is binary diffusivity of KDP in water at bulk concentration M_{KDP}, and $D_{AlcOH,H2O}$ is binary diffusivity of alcohol in water at low concentrations (< 4mol-% used here). Binary diffusivity of KDP in water, effective diffusivities and densities for the solutions used here are presented in Table 2.1. Value of $1.5 \cdot 10^{-3}$ Pa s was used for viscosity in binary solutions and value of $1.4 \cdot 10^{-3}$ Pa s was used for viscosity in all the used ternary solutions.

Table 2.1. Diffusivities and densities used in CFD simulations.

$M_{Alcohol}$, $\frac{mol}{kgH_2O}$	$M_{KDP,ave}$, $\frac{mol}{kgH_2O}$	$D_{KDP,H2O}$, $\frac{cm^2}{s}$	D_{eff}, $\frac{cm^2}{s}$	ρ, $\frac{kg}{m^3}$
0	2.2	$5.7 \cdot 10^{-6}$	–	1170
1.1 ^{EtOH}	1.7	$6.0 \cdot 10^{-6}$	$8.7 \cdot 10^{-6}$	1120
2.2 ^{EtOH}	1.3	$7.3 \cdot 10^{-6}$	$1.1 \cdot 10^{-5}$	1080
0.83 ^{PrOH}	1.7	$6.0 \cdot 10^{-6}$	$7.5 \cdot 10^{-6}$	1120

2.2.4 Growth model

Parameters k_r', n', and k_d' in the growth rate equation (Eq. 2.3) need to be estimated and the model needs to be verified. Surface integration rate constant k_r' and growth order n' are specific constants for each crystallizing system. Mass transfer coefficient k_d' depends in addition on the thickness of the mass transfer film which is affected by the solution velocity over the crystal surface and by the solute concentration.

First step in model development was to use 3D CFD simulations for getting the information on the thickness of the mass transfer film next to the (1 0 1) face of the crystal as a function of slip velocity and KDP concentration. Local values for KDP weight fraction were estimated solving the mass transfer problem for KDP including convection and diffusion simultaneously with the Navier-Stokes equations for the conservation of mass and momentum. Second step was to fit parameters k_r', n' and k_1 in the growth rate equation using experimental data and the evaluated thickness of the mass transfer film. Third step was to import the developed growth model into CFX-5.7 and then to verify the model comparing CFD simulated crystal growth rates with experimental values.

Experimental

The experiments of single crystal growth described in Enqvist et al. [1] were conducted in a growth cell (cross-section of which was 1 cm x 1 cm) at a constant temperature of 30 °C. The crystal was glued from backsides on the platinum rod of the holder. The rod was located parallel to the walls of the growth cell.

Experimental growth rate of the (1 0 1) face of the crystal was defined by capturing images of the growing crystal at intervals of ten minutes and detecting from images the displacement of the face. Binary data included the dependency of the growth rate on solution velocity and on bulk concentration. Solution velocity was varied from 1.7 to 50.0 mm/s and the concentration of KDP from 2.06 to 2.28 molKDP/kgH_2O. During each run the velocity and the supersaturation were kept constant. Ternary data for KDP-water-ethanol case included crystal growth rates as a function of KDP bulk concentration with two ethanol concentrations and two slip velocities: 1) 1.1 M ethanol and U_{slip} = 8.4 mm/s, 2) 2.2 M ethanol and U_{slip} = 8.4 and 55 mm/s. Ternary data for KDP-water-propanol case included crystal growth rates as a function of KDP bulk concentration with two inlet velocities U_{slip} = 8.4 and 55 cm/s. Concentration of propanol was 0.83 M in all cases.

Driving force

The driving force for crystal growth i.e. activity based supersaturation in Equation (2.3) was calculated using Equations (2.5–2.7) for binary case and Equations (2.8–2.11) for ternary cases. Values for the parameters were taken from Partanen et al. [7] and Enqvist et al. [1]. The driving force against molar concentration of KDP in supersaturated solution at 30 °C was approximated with second order polynomial fit, within experimental concentration range

$$\sigma_{act,binary} = -0.11738M^2 + 1.01915M - 1.58730 \quad (2.13a)$$

$$\sigma_{act,M_{EtOH}=1.1} = -0.29341M^2 + 1.59991M - 1.71200 \quad (2.13b)$$

$$\sigma_{act,M_{EtOH}=2.2} = -0.54359M^2 + 2.29038M - 1.86901 \quad (2.13c)$$

$$\sigma_{act,M_{PrOH}=0.83} = -0.28811M^2 + 1.58195M - 1.70997\,. \quad (2.13d)$$

Local conditions from CFD

Slip velocity

Slip velocity is here defined as the highest velocity of the solution in the area between the crystal and the tube wall. This slip velocity is comparable with the slip velocity in suspension crystallization defined by velocity difference between the crystal and the solution. The effect of varying inlet velocity from 1.7 to 50.0 mm/s on slip and local velocities was studied by keeping the bulk concentration at experimental condition of M_{ref} = 2.2 molKDP/kgH_2O.

Slip velocity was a linear function of inlet velocity

$$U_{slip} = k_U U_{in,ave}\,. \quad (2.14)$$

Constant k_U is 1.65 when using original geometry and 1.77 when the crystal is rotated 90º in respect to the main flow direction.

Mass transfer film

CFD simulations for evaluating the thickness of the mass transfer film next to the (1 0 1) face of the crystal in varying conditions were done using experimentally determined growth rates for the KDP-flux at the crystal-solution interface. Transfer of KDP in the solution was modelled using transport equation

$$\frac{\partial c}{\partial t} + \nabla \cdot \left(\vec{U}c\right) = D\nabla^2 c \tag{2.15}$$

where c and D are concentration and diffusivity of KDP. The thickness of the mass transfer film was evaluated by evaluating the distance from the crystal face where the concentration of KDP reached the bulk concentration. Concentration of KDP and flows and streamlines around the crystal with two different configurations with varying slip velocities are presented in Figure *2.4*.

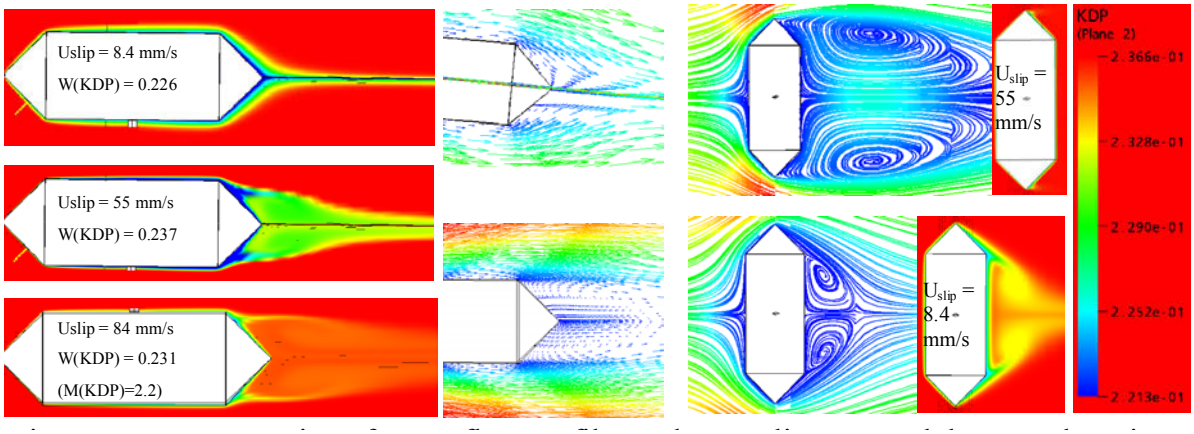

Figure 2.4. Concentration of KDP, flow profiles and streamlines around the crystal. Main flow direction is from left to right.

The thickness of the mass transfer film, z (mm), for both binary and ternary cases can be described with equation

$$z = B_1 * \left(\frac{U_{slip}}{mm}\right)^{B_2} + B_z \left(\frac{M_{KDP} - M_{KDP,ref}}{mol/kgH_2O}\right)\left(\frac{U_{slip}}{U_{slip,ref}}\right)^{B_3} \tag{2.16}$$

where the values of the constants B_1, B_2 and B_3 were found to be independent on the admixture concentration. The evaluated values of constants in Eq. (2.8) are B_1 = 0.22 mm, B_2 = –0.4 and B_3 = –0.25. Reference slip velocity, $U_{slip,ref}$, is 8.4 mm/s. Reference molarity $M_{KDP,ref}$ (mol/kgH_2O) of KDP and parameter B_z (mm) depend both on alcohol concentration (see Table 2.2). Solubility of KDP decreases with increasing ethanol concentration. Also propanol decreases solubility of KDP in water.

Decrease in slip velocity from 55 to 8.4 mm/s more than doubles the thickness of the mass transfer film. Increasing KDP concentration increases the thickness of the mass transfer film in supersaturated solution which is either binary or includes constant amount of alcohol. Increasing alcohol concentration increases slightly the thickness of the mass transfer film. The effect of slip velocity on the thickness of the mass transfer film next to the (1 0 1) face of the crystal is presented in Figure 2.5. The thickness of the

mass transfer film in various conditions is presented in Figure 2.6. Thickness of the mass transfer film estimated with Equation (2.16) fits well the data got from CFD simulations.

The thickness of the mass transfer film at solute concentration of M_{ref} = 2.2 molKDP/ kgH_2O is 0.08, 0.05 and 0.04 mm for slip velocities of 14, 40 and 70 mm/s, respectively. Our results are at the same range than experimental results by Onuma et al. [13] where film thickness of 0.05–0.08, 0.05 and 0.03 mm for flow rates of 30, 100 and 400 mm/s were presented for the (1 1 1) face of a growing K-alum crystal.

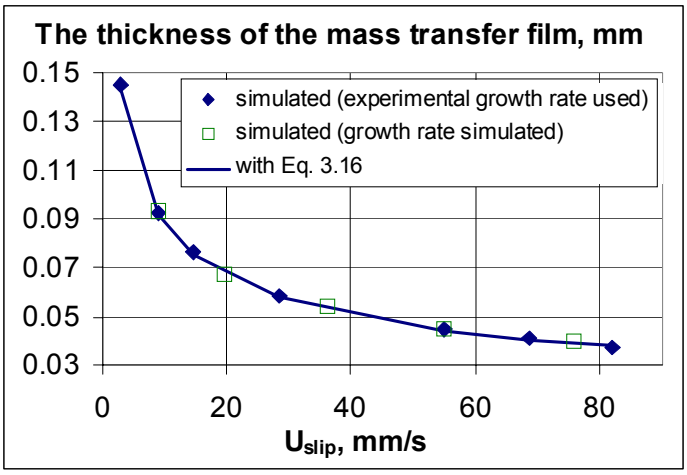

Figure 2.5. The thickness of the mass transfer film next to the (1 0 1) face of the crystal as a function of slip velocity, values calculated with Eq. 2.16 are compared with values evaluated from CFD simulations.

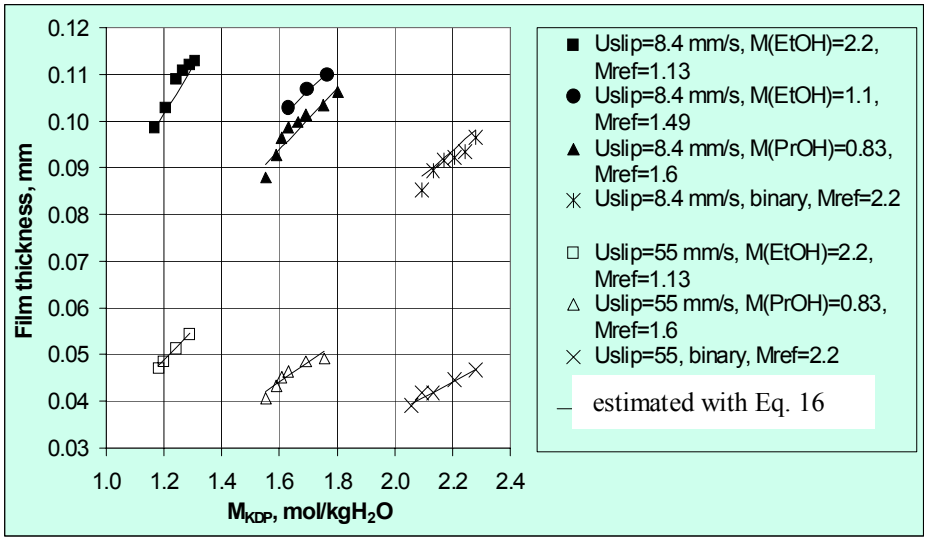

Figure 2.6. The thickness of the mass transfer film next to the (1 0 1) face of the crystal, as a function of KDP concentration, CFD simulated.

Parameters for the growth model

Estimated parameters for KDP in the growth rate Equation (2.3) are presented in Table 2.2. Solubility of KDP decreases when alcohol is added into the solution. Surface integration rate constant, k_r', and growth order, n', increase with increasing ethanol concentration in solutions including 0–2.2 M ethanol. In solutions including 0.83 M propanol the parameters k_r' and n' have higher values than in solutions including ≤ 2.2 M ethanol. Parameter k_1 is $3.8 \cdot 10^{-4}$ in all the cases. Mass transfer coefficient of KDP in 2.2 M binary solution with slip velocity of 8.4 mm/s is $4.2 \cdot 10^{-3}$ kg/(m^{2}s) when calculated from Equation (2.4). Enqvist et al. [1] got value of $5.6 \cdot 10^{-3}$ kg/(m^{2}s) for the same conditions.

Table 2.2. Parameters estimated for Equations (2.2) and (2.16).

$M_{Alcohol}, \frac{mol}{kgH_2O}$	$M_{KDP,ave}, \frac{mol}{kgH_2O}$	$M_{KDP,ref}, \frac{mol}{kgH_2O}$	$k_r', \frac{kg}{m^2 s}$	n'	B_z, *mm* ($U_{slip,ref}$=8.4mm/s)
0	2.2	2.2	$6.4 \cdot 10^{-3}$	1.40	0.053
1.1 ^{EtOH}	1.7	1.49	$1.9 \cdot 10^{-2}$	2.22	0.060
2.2 ^{EtOH}	1.3	1.13	$2.4 \cdot 10^{-2}$	2.56	0.106
0.83 ^{PrOH}	1.7	1.6	$6.0 \cdot 10^{-2}$	2.7	0.068

The growth model is most sensitive to changes in the value of n, 5% change results 10–30% change in the growth rate within conditional area used in this study. Sensitivity to changes in k_r' and k_1 is much smaller (5–6% change results 1–5% change in the growth rate).

Verification of the model

The crystal growth model was verified using CFD. Surface reaction equation $R_g = k_r' \left(\sigma_{act,i}\right)^{n'}$ with estimated parameters k_r' and n' was imported to CFX-5.7. The growth of the (1 0 1) face of the crystal was simulated. Figure 2.7 shows that growth rates for the binary case simulated with CFD, fitted with KINFIT and determined in experiments are in close agreement what prove the presented model valid.

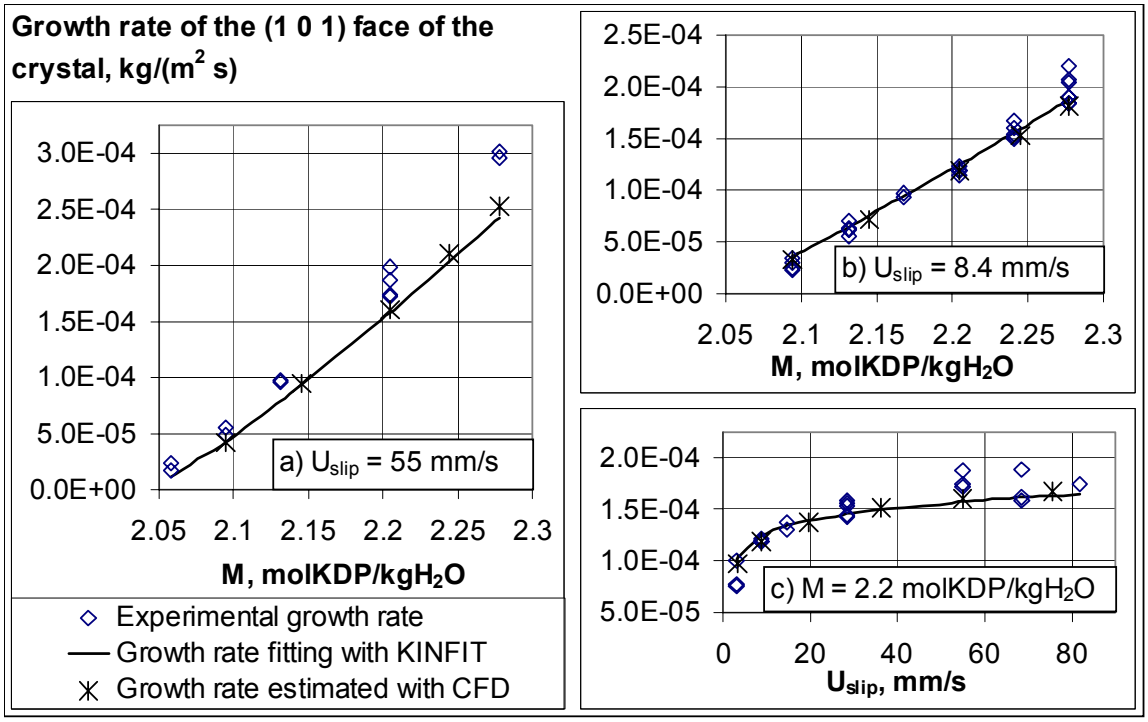

Figure 2.7. Comparison of simulated, fitted and experimental growth rate: with varying concentration and average inlet velocity of a) 33.3 mm/s and b) 5.1 mm/s and c) with constant concentration of 2.2 molKDP/kgH_2O and varying velocity.

2.2.5 Crystal growth rates

In industrial crystallizers the main flow direction to crystals changes continuously. Thus it is essential to know if the average growth rate of the whole crystal is affected by the main flow direction. Two configurations of the crystal in respect to the main flow direction were tested: the original one and the other 90° rotated (see Figures 2.2 and 2.4).

Growth rates of various faces of the crystal were studied first. Growth rate was fastest on the faces pointing towards the incoming flow (front faces). Average growth rate of the whole crystal was calculated from simulated facial growth rates. It was 65–80% of the growth rate of the front faces of the crystal in studied conditions with original configuration. The growth rates of all the faces of the crystal simulated with the two different configurations and the average growth rates of the whole crystal in various conditions are presented in Liiri et al. [3]. Average growth rates of the whole crystal with both geometries as a function of slip velocity are presented in Figure 2.8. Increasing slip velocity increases growth rate by decreasing mass transfer resistance from solution to the interface due thinning the mass transfer film. The difference in geometry does not have significant effect on the average growth rate.

CFD simulations of crystal growth of KDP from ternary KDP-water-ethanol solution were first made using binary diffusivity and later using effective diffusivity calculated with Equation (2.12). Better results were achieved using effective diffusivities.

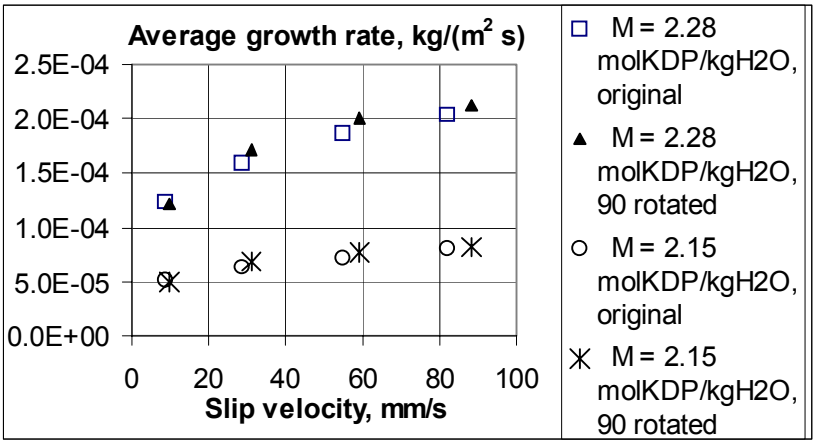

Figure 2.8. Average growth rate of the whole crystal as a function of slip velocity, comparison of CFD results using original and 90° rotated geometries.

Growth rate of KDP decreases with increasing alcohol concentration. Growth rates of KDP in ternary KDP-water-ethanol solution are compared to growth rates in binary solution at the same slip velocity of 8.4 mm/s in Figure 2.9. Growth rates in ternary solutions with two slip velocities, 8.4 and 55 mm/s, are presented in Figure 2.10: a) KDP-water-ethanol, b) KDP-water-propanol system.

Changes in KDP concentration over the mass transfer film and in surface reaction were examined with various bulk concentrations and slip velocities. Diffusion limits the growth rate quite a lot when slip velocity is small and KDP concentration is high. Surface reaction is the more limiting step with slip velocities of 55 mm/s and higher.

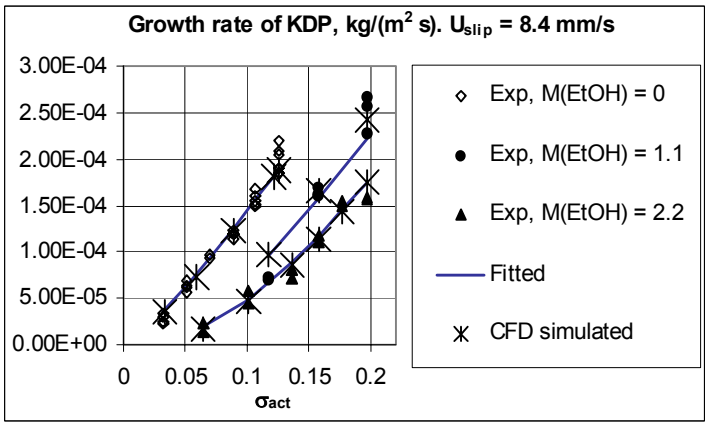

Figure 2.9. Growth rate of the (1 0 1) face of the KDP crystal in binary solution and in ternary KDP-water-ethanol solution.

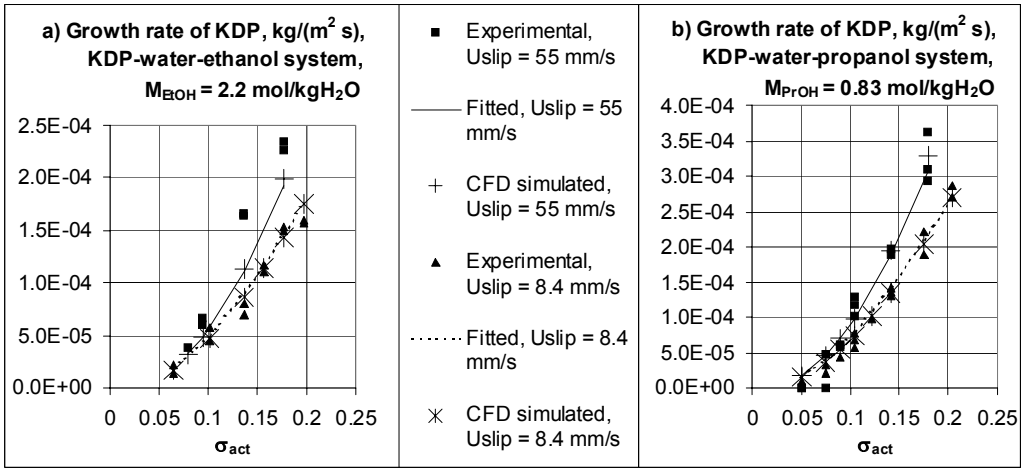

Figure 2.10. Growth rate of the (1 0 1) face of the KDP crystal in ternary solutions as a function of activity based supersaturation, with two slip velocities.

2.2.6 Discussion and conclusions about single crystal study

A new method to obtain crystal growth parameters from experimental data was developed. The method is useful for estimating growth model parameters when experimental data from single crystal growth is available. Local conditions in solution around the crystal can be analysed using CFD. The new method utilizes flow field calculation by CFD to separate mass transfer effects from surface reaction. Method seems to be suitable for both binary and ternary systems.

Simple power law model can well describe the growth rate of KDP single crystal with varying solution velocities and concentrations when activity based driving force is used. Parameters k_r' and n' were estimated for each system separately. Best fit was found for KDP-water-propanol system.

The thickness of the mass transfer film was evaluated with CFD. It decreases with increasing slip velocity and increases linearly with increasing concentration of the solute. Film thickness increases slightly with increasing alcohol concentration due increasing effective diffusivity. Binary diffusivity of KDP in water can be used as first estimate for effective diffusivity of KDP in ternary KDP-water-ethanol or KDP-water-propanol solution. However, using Eq. (2.12) for effective diffusivity gives better accuracy in prediction of growth rate of KDP. Deviation in simulated growth rates using binary diffusivity instead of effective diffusivity was less than 13% in the case of KDP-water-ethanol system. Growth rate of KDP decreases with increasing alcohol concentration mainly due to changes in surface reaction.

2.3 Batch experiments

2.3.1 Crystallizer

New crystallizer with two impeller mixing system, shaped bottom and baffles was developed in the project. The outlook of the crystallizer is shown in Figures 2.11 and 2.12. The diameter of the crystallizer was 400 mm and total volume 100 litres. Two different impeller pairs was used; 135 mm 6-flat-blade turbines and 135 mm 3-blade marine propellers. Four 40 mm baffles were used.

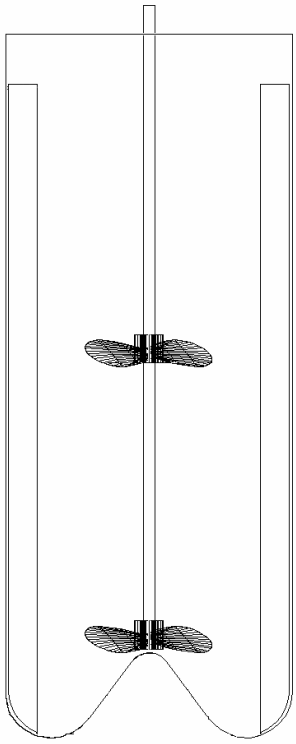

Figure 2.11. Crystallizer in the project.

Figure 2.12. Photo of the crystallizer.

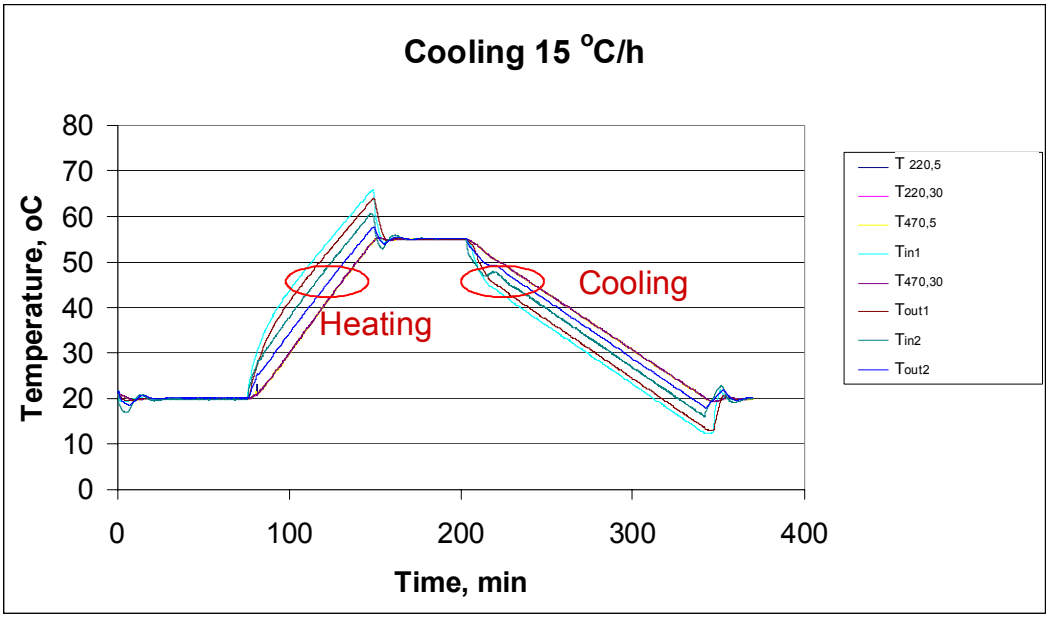

Figure 2.13. Measured temperature curves in water batch with 150 rpm mixing intensity of turbines.

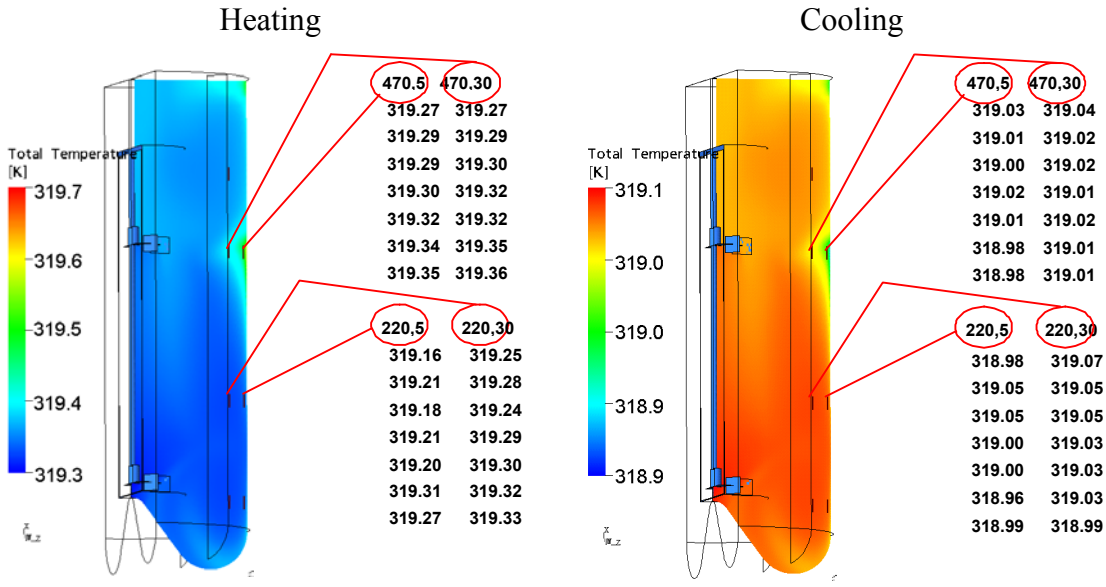

Figure 2.14. Comparison of measured and calculated temperatures.

Local temperatures were measured with four sensors inside of the crystallizer and with four sensors in cooling circuits. Local mother liquor concentration and suspension samples were taken from six positions. Flow patterns of the crystallizer were measured by PIV instrument using two windows built in the crystallizer.

2.3.2 Water experiments

Local temperatures and flow patterns were measured in water experiments to verify the CFD flow calculations. Discontinuation in cooling surface was found in calculations and that position was also partially measured. Measured temperature curves and comparison of measured and calculated values are shown in Figures 2.13 and 2.14.

Discontinuation in cooling surface was found in heating experiment but the temperature difference was lower. No discontinuation was found in cooling experiment.

Flow patterns of the water in the crystallizer were measured by PIV. Standard hollow glass spheres were used as a tracer. Two cameras setup was used to resolve the 3D flow patterns. One measurement area at the time was around 160 mm x 120 mm, six different locations were measured with every setup. Result of one measurement area was average vector field of 200 measurements recorded in 100 seconds. 250, 300 and 385 rpm rotation velocities were used for 2-propeller mixing system and 250 and 300 rpm rotation velocities for 2 turbine mixing system.

Examples of the results of PIV measurements are shown in Figure 2.15.

Figure 2.15. PIV measurements of water in crystallizer. Mixing velocity of propellers was 385 rpm. Color of the vectors describes the third dimension in right handed coordinates.

Conclusions of the flow pattern measurements are as follows:

- Two turbine system creates 2-circuit mixing profile in the crystallizer as expected.

- Two propeller system creates unexpected up flow in central part of crystallizer even the both propellers are downward pumping.

2.3.3 Batch crystallization

Initial temperature in batch crystallization was 55 ºC. The batch was cooled down to 20 ºC with two different cooling rates with and without seeding (50–100 µm). Potassium dihydrogen phosphate – water solution was used in all experiments. Batch experiments done in the project are listed in Figure 2.16.

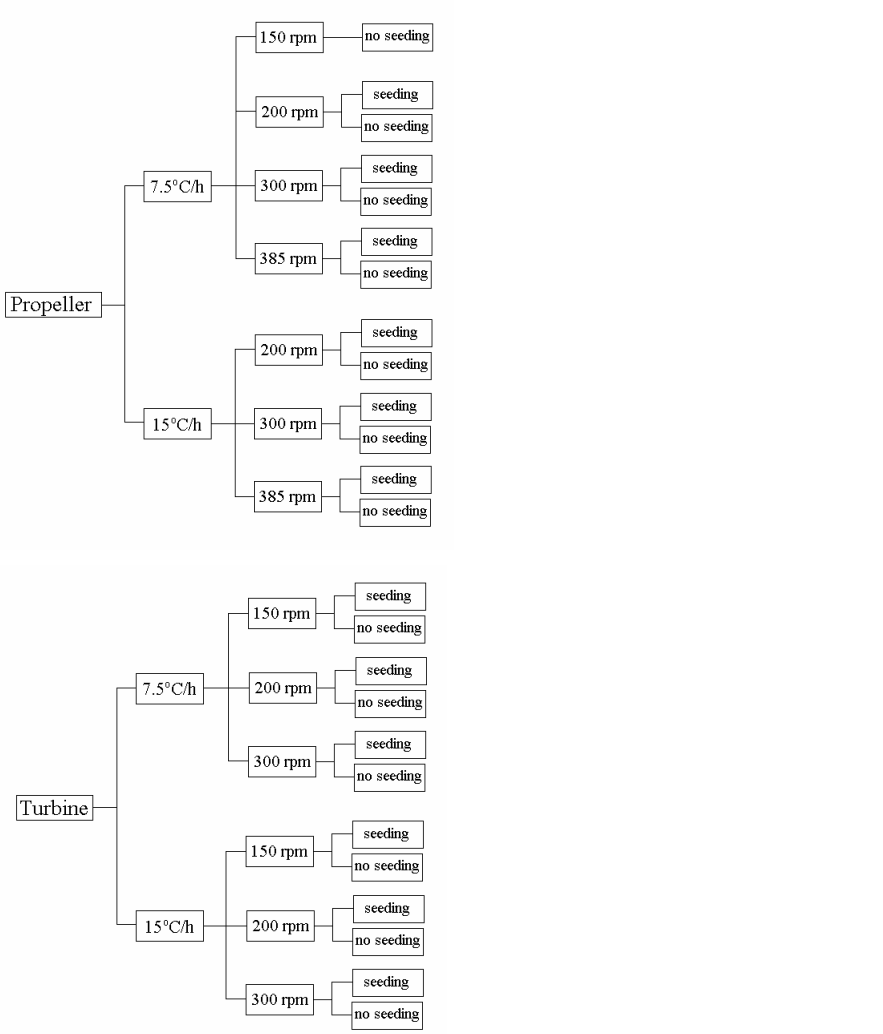

Figure 2.16. Batch experiments.

Temperatures were recorded simultaneously, suspension samples were taken at 40, 30 and 20 ºC, and mother liquor samples were taken at 45 and 25 ºC.

The solubility of used KDP in water was measured and result of that is shown in Figure 2.17.

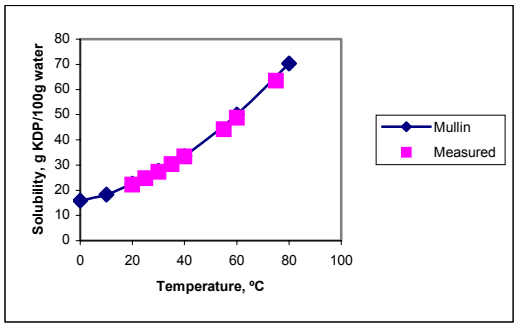

Figure 2.17. Solubility of KDP in water.

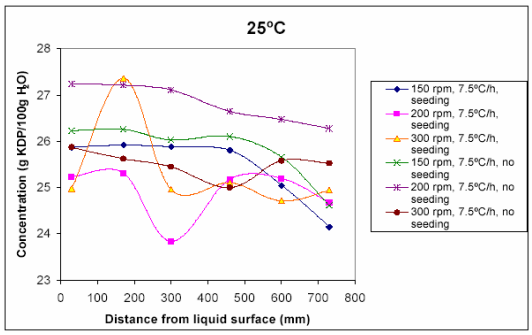

Figure 2.18. Mother liquor concentration against distance from liquid surface for 6-flat-blade turbine at 25 °C with different rotation velocities and cooling rate 7.5 °C/h.

As an example one set of concentration measurements is shown in Figure 2.18.

Following conclusions of mother liquor measurements can be made:

- Values with seeding are typically lower than without seeding. It is because there is more crystal surface to grow, and therefore the level of supersaturation is lower in batches with seeding than in batches without seeding.
- Increasing mixing power decreases the mother liquor concentration due to increasing nucleation rate.
- General tendency is that the concentration is lower at the bottom part of the crystallizer because non-ideal mixing. Larger crystals are settling down and therefore there is more crystal surface area on the bottom part than liquid surface part to decrease the supersaturation.

Suspension samples were used to find out local suspension densities and local crystal size distributions. Examples of suspension density and crystal size distribution results are shown in Figures 2.19 and 2.20.

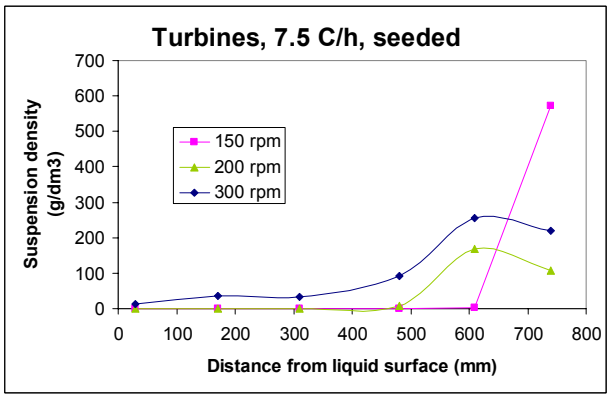

Figure 2.19. Suspension density against distance from liquid surface for 6-flat-blade turbine at 20 ºC with different rotation velocities and cooling rate 7.5 ºC/h.

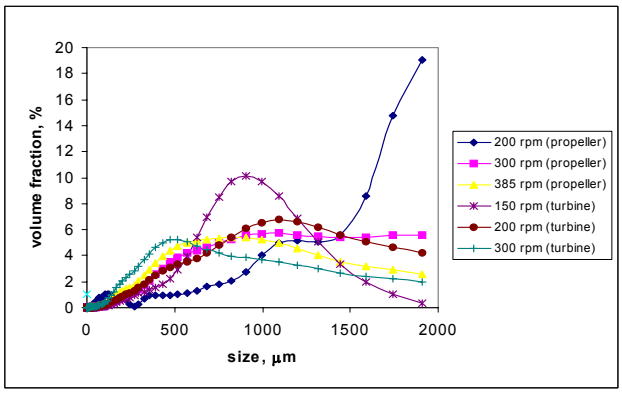

Figure 2.20. CSD for the 6-flat-blade turbine and for the 3-blade marine type propeller at the end of the experiment (20 °C) at 730 mm from the liquid surface with cooling rate 7.5 ºC/h and no seeding.

Main conclusions of suspension density results are as follows:

- The higher the mixing power the more uniform suspension density in the crystallizer. Classification of crystals is very affective in crystallizer.
- Suspension density is more uniform at the beginning of the batch due to smaller crystal size.

Conclusions of CSD results are as follows:

- Increasing mixing power decreases the average crystal size and wideness of distribution. Impeller type have a negligible effect on CSD if mixing power is constant (see the measured mixing power in Figure 2.21).

- Seeded batches are more controllable due to lower supersaturation levels in crystallizer. That means smaller average crystal size and narrower distribution in seeded batches than in unseeded batches.
- Faster cooling rate produces typically larger average crystal sizes, especially in seeded batches due to higher supersaturation and lower mixing time, ie lower secondary nucleation.

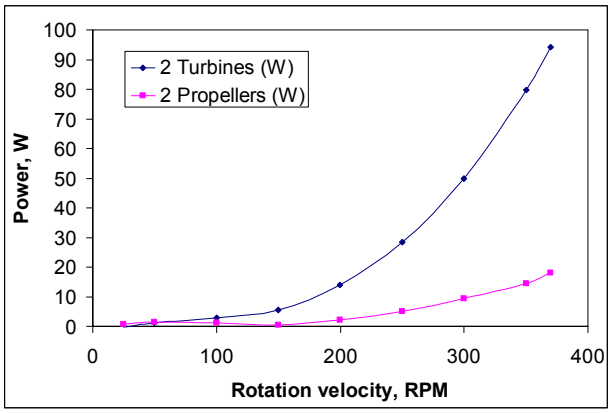

Figure 2.21. Measured mixing powers of two different impeller pairs.

2.3.4 Slip velocity

Slip velocities of crystals were measured by PIV in saturated KDP-water solution (at 19 ºC). Two cameras setup was used to resolve 2D slip velocities of crystals. Flow velocities of single size crystals (50–100 µm and 500–710 µm) were recorded by the first camera (filtered reflecting wave length 532 nm). Flow velocities of fluid were recorded by the second camera (high pass filtered 540 nm) using fluorescence tracers in fluid. One measurement area at the time was around 160 mm x 120 mm, six different locations were measured with every setup. Crystal and fluid velocities of one measurement area was calculated separately. Calculated fluid velocities subtracted from crystal velocities was resolving the momentary slip velocities. Average vector field of 200 measurements recorded in 100 seconds were calculated as average slip velocities. However, simple averaging is not a good method to resolve actual average slip velocities since the stochastic mixing system results different directions of velocities which are subtracting the average values. Root mean square value is more useful for resolving actual slip velocities without direction. 300 and 385 rpm rotation velocities were used for 2-propeller mixing system and 250 and 300 rpm rotation velocities for 2 turbine mixing system.

Examples of the results of slip velocities measurements are shown in Figure 2.22.

Conclusions of slip velocity measurements are as follows:

- Slip velocities are increasing in lower part of crystallizer when the crystal size is increasing since settling in the crystallizer.
- Slip velocities of small crystals are rather uniform in the crystallizer except near impeller area.

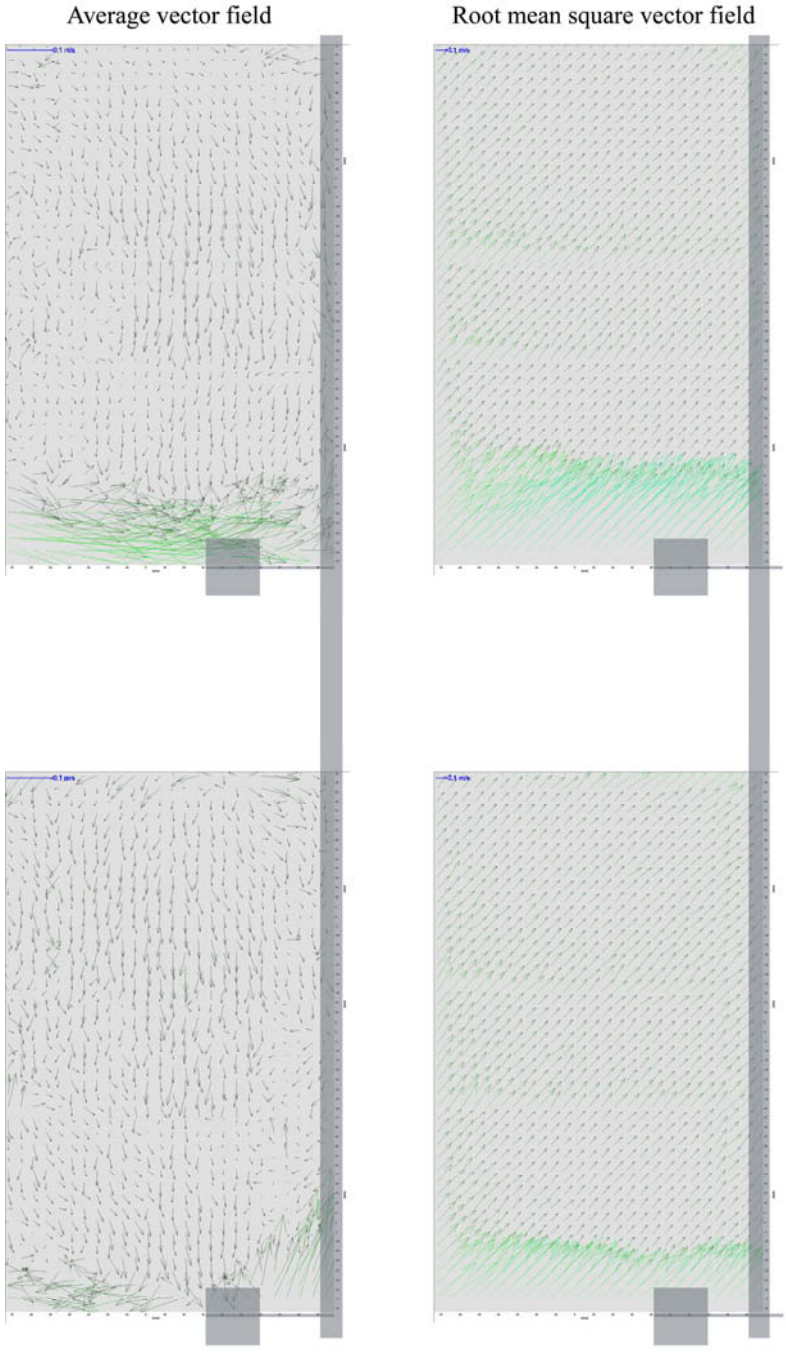

Figure 2.22. Slip velocities of 500–710 µm KDP crystals in saturated solution at 19 ºC. Mixing velocity of turbines was 250 rpm.

2.4 Continuous experiments

This part of work is done to find out local conditions in continuous crystallization. Local information is gathered up for concentration, suspension density, crystal size distribution and temperature. Process conditions varied are mixing and residence time.

2.4.1 Experimental setting

Continuous crystallization equipment includes a closed circulation system. Suspension from the crystallizer was pumped to dissolving tank wherefrom dissolved solution overflowed to feed tank. Saturated solution was pumped with constant flow velocity back to crystallizer. The flow velocity of the pump controls the residence time of crystallizer. Volume of the crystallizer was 100 litres, dissolving tank 700 litres and feed tank 300 litres. Temperature of the crystallizer was 20 ºC, dissolving tank 50–60 ºC and feed tank 30 ºC. The flow sheet of the system is shown in Figure 2.23.

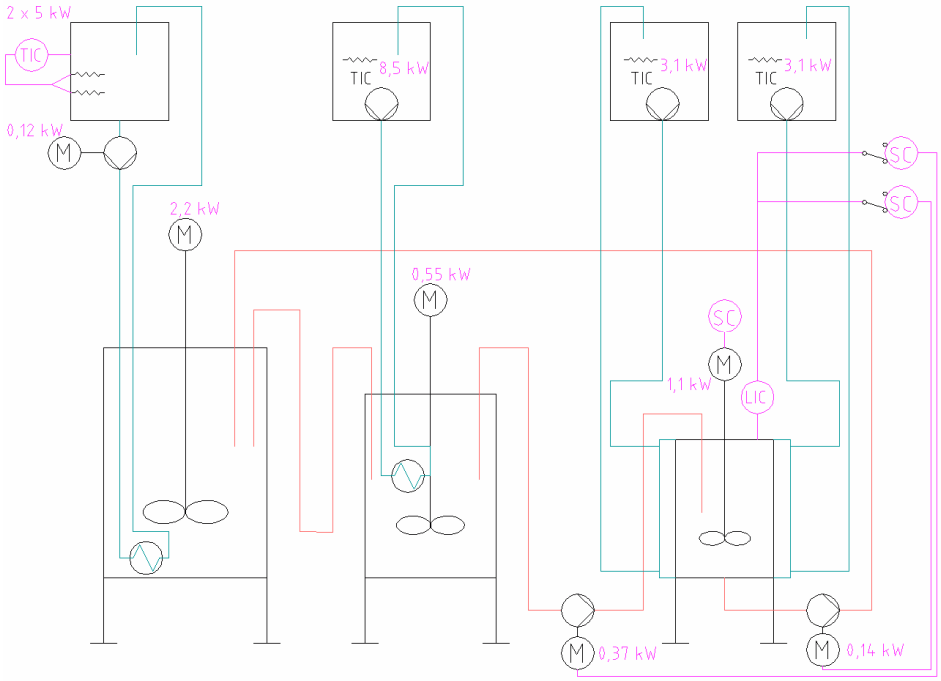

Figure 2.23. Flow sheet of the continuous crystallization equipment.

Table 2.3. Conditions used in experimental work. Crystallized material is KDP. Temperature in crystallizer was 20 °C.

	τ min	Impellers	Mix rpm	Product	c_0 g(KDP)/100 g(H_2O)
1.12.2005	30	Turbine	250	300	26.9
2.12.2005	30	Turbine	250	200	26.7
13.12.2005	30	Turbine	300	200	26.9
14.12.2005	60	Turbine	300	200	26.8
6.2.2006	30	Turbine	300	200	27.3
7.2.2006	30	Marine Turbine	300	200	27.1
8.2.2006	30	Marine Turbine	385	200	26.9
10.2.2006	30	Marine Turbine	385	200	27.0
13.2.2006	60	Marine Turbine	385	200	27.1

2.4.2 Experiments

Experimental conditions, i.e. residence time in crystallizer, impellers used in mixing and their rotation velocities, product removal pipe position from bottom and concentration of KDP in feed, used in the experiments are presented in Table 2.3.

2.4.3 Results

Size distribution

Examples of development of crystal size distribution in crystallizer during the experiment are presented in Figures 2.24 with turbine mixing and 2.26 with propeller mixing. Samples are taken from the same position, 220 mm from bottom, i.e. 20 mm up from product removal position. Figures 2.25 and 2.27 show crystal size distributions from all six sampling points at the steady-state, i.e. over 8 times residence time from the start-up.

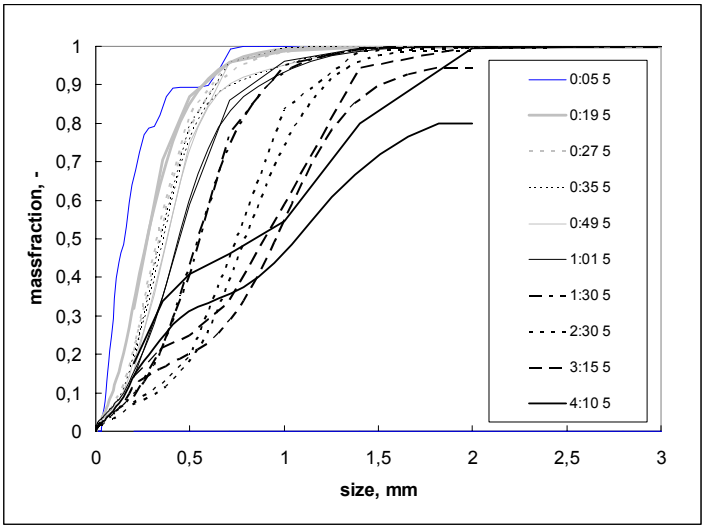

Figure 2.24. Kinetic experiment up to eight times residence time. Sieve analyze and coulter LS tornado results. Samples are taken from location 5. Resident time 30min, mixing 300 rpm with turbine, feed liquid concentration 27.3 g(KDP)/100 g(H_2O).

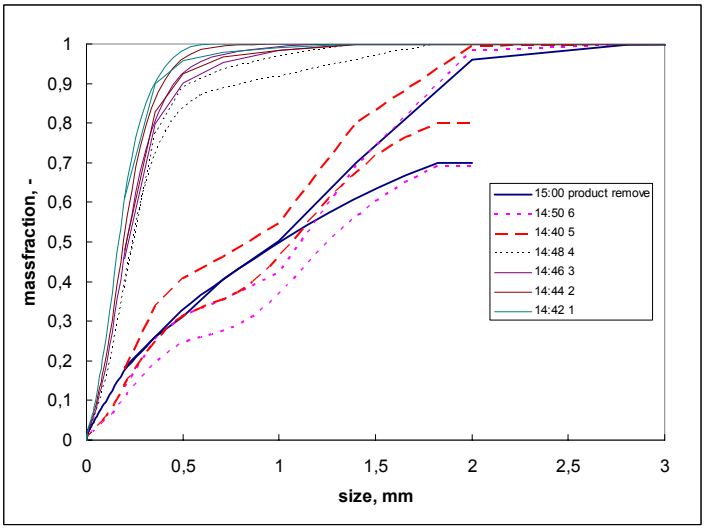

Figure 2.25. Crystal size distributions at different locations after 4 h 12 min. Sieve analyze and coulter LS tornado results. Residence time 30 min, mixing 300 rpm with turbine, feed liquid concentration 27.3 g(KDP)/100 g(H_2O).

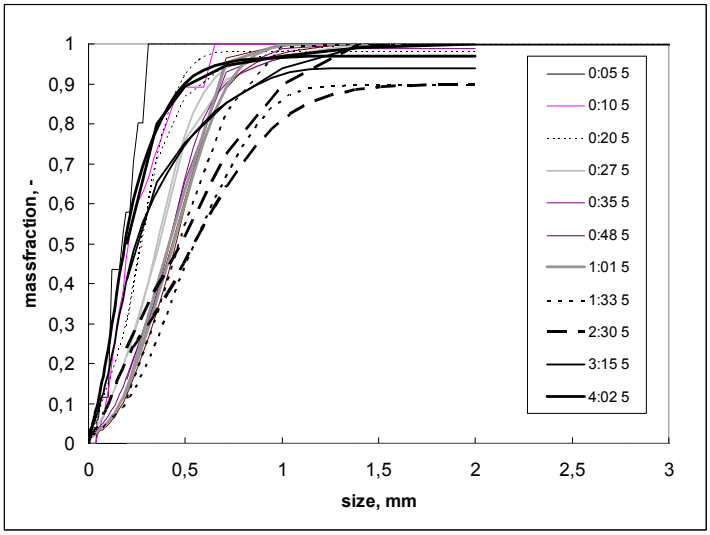

Figure 2.26. Kinetic experiment up to eight times residence time. Sieve analyze and coulter LS tornado results. Samples are taken from location 5. Resident time 30 min, mixing 385 rpm with marine turbine, feed liquid concentration 27.0 g(KDP)/100 g(H_2O).

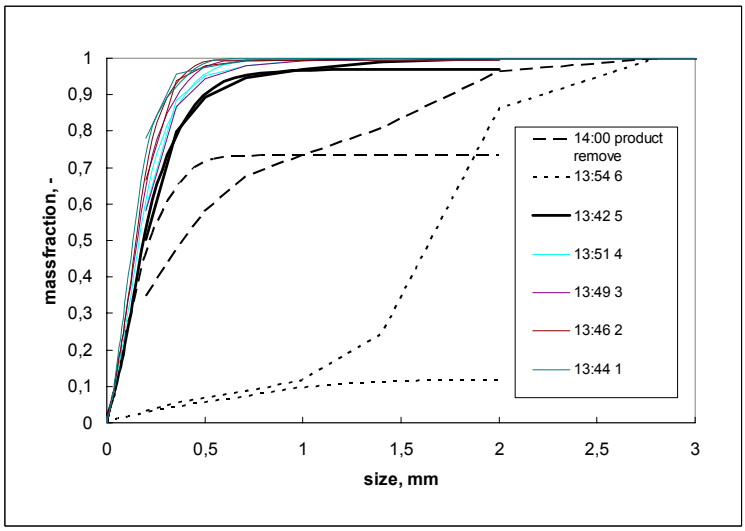

Figure 2.27. Crystal size distributions at different locations after 4 h. Sieve analyze and coulter LS tornado results. Residentce time 30 min, mixing 385 rpm with marine turbine, feed liquid concentration 27.0 g(KDP)/100 g(H_2O).

Concentrations and suspension densities

All the suspension samples are filtered and dried at 88 °C. Mother liquor samples are sucked through filter. Concentration is measured gravimetrically. Measured local mother liquor concentrations and suspension densities are shown in Figures 2.28 and

2.29. Examples of the development of these parameters during the experiment are shown in Figure 2.30.

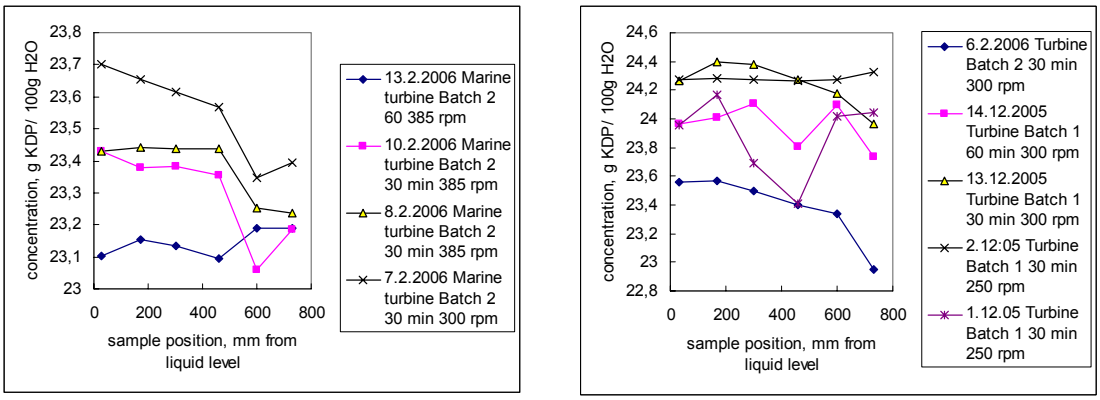

Figure 2.28. Local mother liquor concentrations with marine impeller and with turbine.

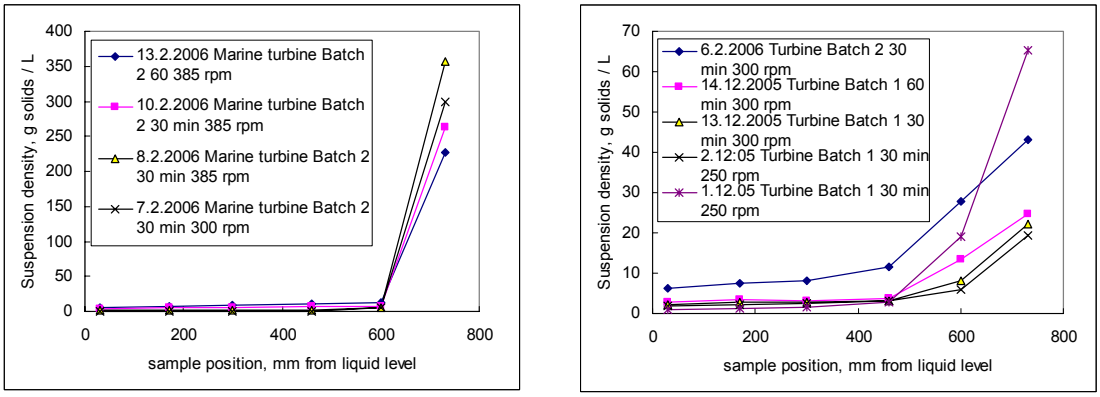

Figure 2.29. Local suspension densities with marine impeller and with turbine.

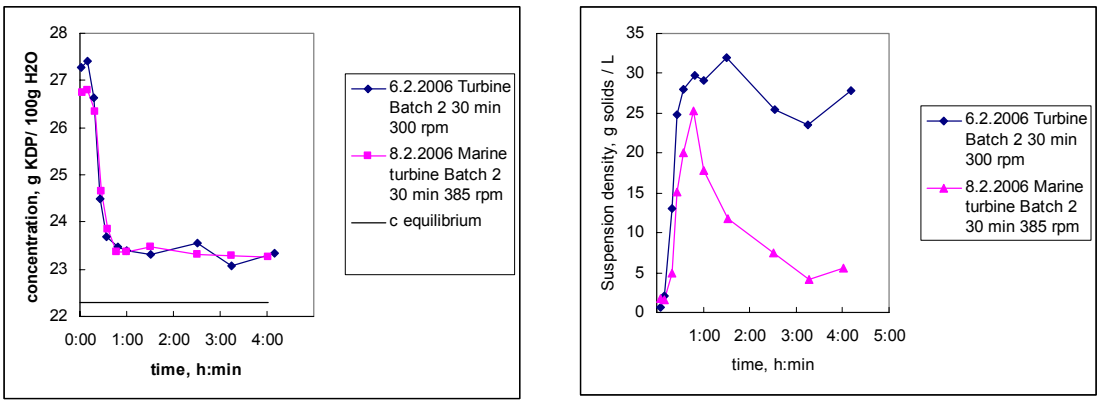

Figure 2.30. Kinetic changes in mother liquor concentration and suspension density. Samples are taken 600 mm from liquid level and 10 mm from cooling surface. Feed concentration was 6.2.06 27.3 g(KDP)/100 g(H_2O) and 8.2.06 26.9 g(KDP)/100 g(H_2O).

Notes and conclusions of continuous crystallization experiments are as follows:

- Local concentration and suspension density differences can be produced, ie. there was non-ideal mixing in crystallizer.
- Local crystal size distributions were measured.
- Crystallization with small mixing rate seems to produce unstable supersaturation level. A new primary nucleation can be seen during the experiment after first nuclei are grown and settled down because secondary nucleation is not present.
- Increasing mixing power decreases differences in local conditions.
- Product removal position is critical in non-ideal mixing crystallizer. If the position is on the bottom the suspension density in crystallizer is very low.
- Supersaturation during the experiment reaches constant level at the time inversed proportional to residence time. With residence time 30 min constant level is reached in 45min and with residence time 60 min in 35 min.
- Development of suspension density during the experiment is dominated by mixing power. With low mixing power suspension density increases until sudden decrease after crystal size grows to critical settling size.
- Reproducibility of experiment based on CSD is good.

2.5 Modelling of suspension crystallizer

Simulations of suspension crystallizer were made for the new crystallizer (volume of 100 dm^3) built in LUT, using two turbine impellers. Rotation speeds of 150 and 300 rpm were used when simulating flows of fluid and crystals, slip velocities, and classification of the crystals. Rotation speed of 150 rpm was used in heat transfer and crystal growth simulations.

2.5.1 Flows and heat transfer

Inlet of the cooling/heating fluid was at the lowest part of the jacket and outlet at the uppest part of the jacket giving higher temperature differences between the cooling/heating fluid and the fluid/suspension inside the crystallizer at the lower part of the crystallizer. Average heat flux was calculated from experimental heating/cooling rate. In simulations the heat flux was set to change linearly as a function of the height in the vessel, heat flux from the lowest part of the jacket was 4/3 of the average heat flux and from the uppest part 2/3 of the average heat flux. Figure 2.31 shows flow and temperature profiles in different locations in the crystallizer. Temperature differences in

the vessel are qualitatively similar in simulations and experiments but quantitatively there exist some differences. However, the temperature differences inside the crystallizer are very small, both in experiments and simulations.

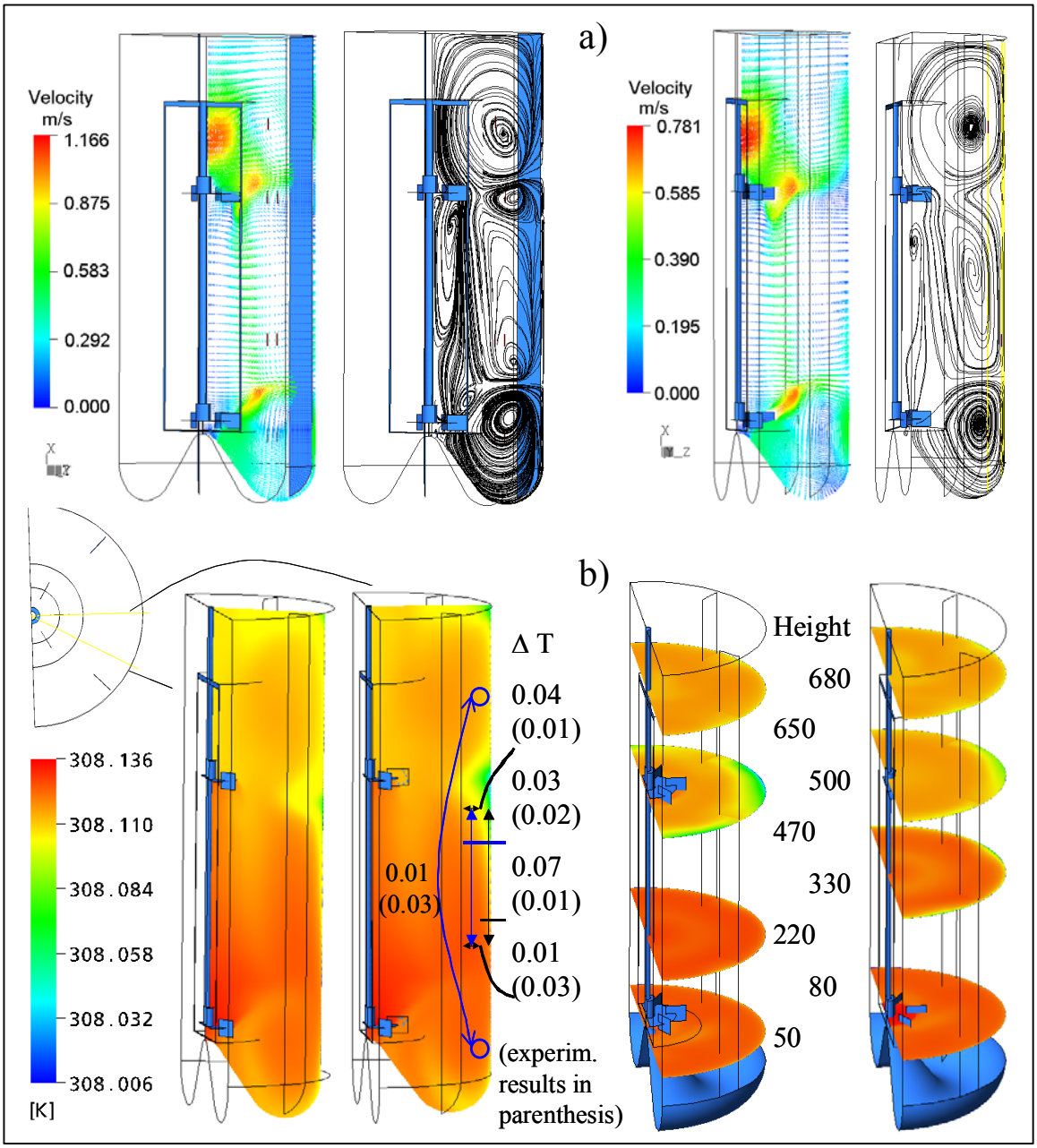

Figure 2.31. Velocity vectors and streamlines (a) and temperature profiles (b) in the suspension crystallizer. Impeller rotation speed is 150 rpm.

2.5.2 Classification of the crystals and effect of the crystals on flow profile

Average volume fraction of crystals of 0.05 was used in classification simulations. Cases with different crystal sizes were studied separately. Flows and classification of crystals with 150 rpm are presented in Figure 2.32. Experimental results of fractions of crystals of different sizes in various heights in the crystallizer with impeller speed of 150 rpm are presented in Figure 2.33. Crystals of size of 0.1 mm or smaller are suspended well, both in simulations and in experiments, and no changes in flow profile is observed. Crystals of size of 0.5 mm are mostly located at the bottom of the crystallizer and thus change the flows at the lower part of the crystallizer. Flows and classification of crystals with 300 rpm are presented in Figure 2.34. With this impeller speed crystals of size of 0.2 mm are suspended quite well but crystals of size of 0.5 mm are located mostly at the lower half of the crystallizer.

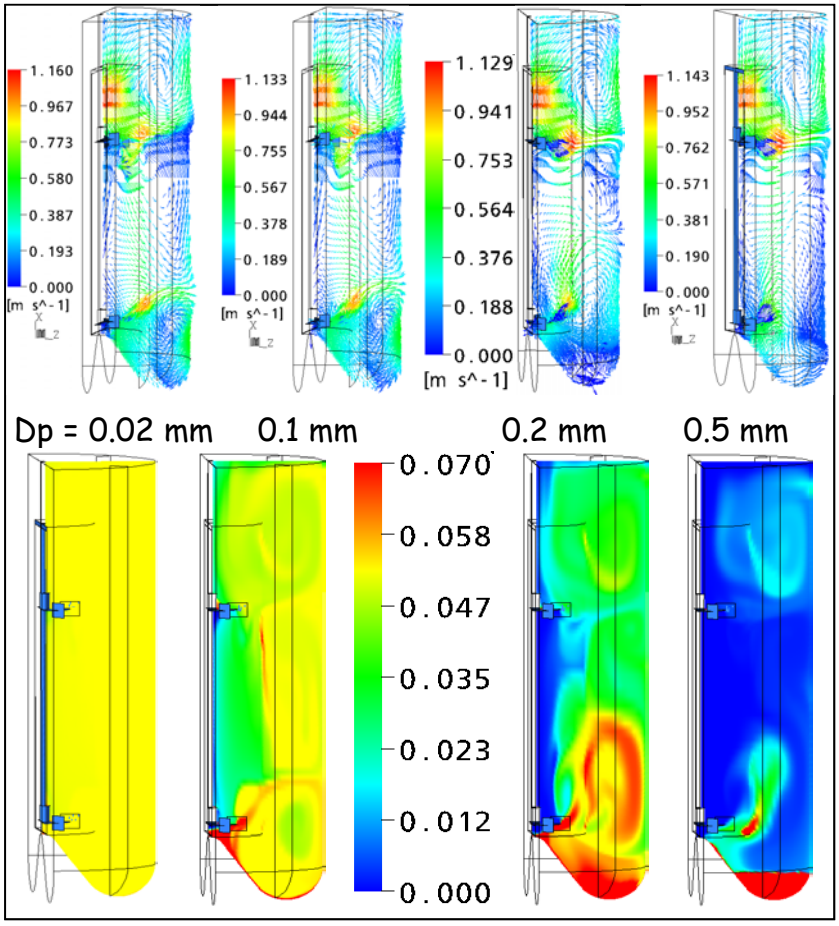

Figure 2.32. Velocity vectors (up) and local volume fractions of the crystals (down) with different particle sizes. Impeller rotation speed is 150 rpm.

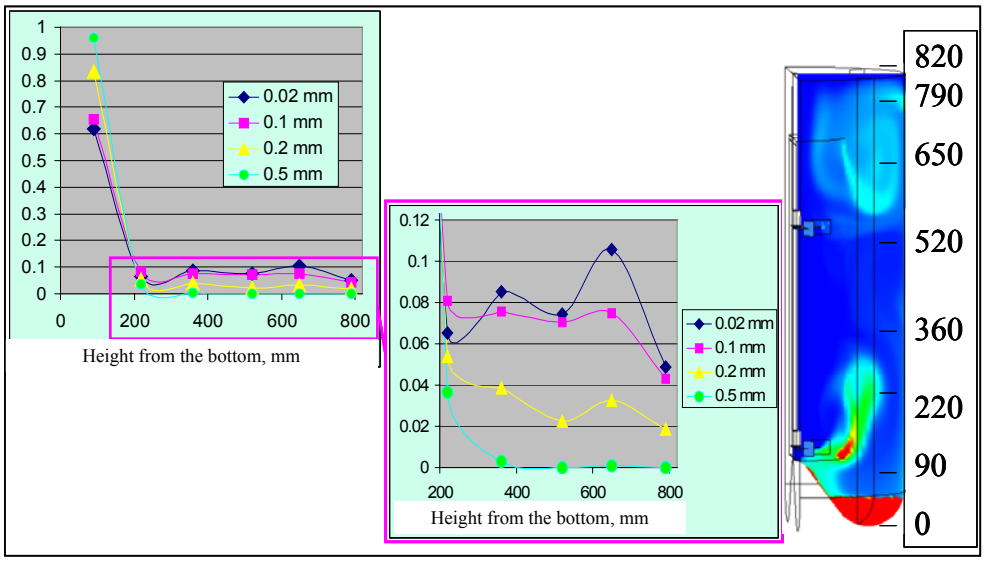

Figure 2.33. Experimental results of fractions of crystals of different sizes as a function of vessel height.

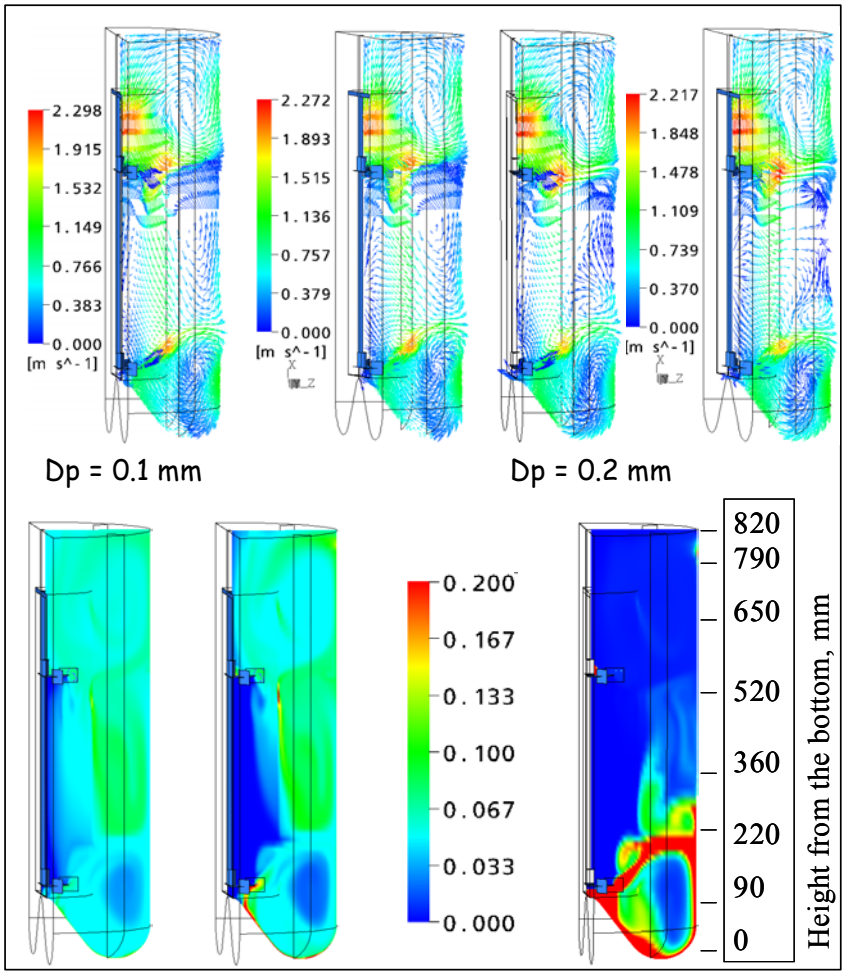

Figure 2.34. Velocity vectors (up) and local volume fractions of the crystals (down) with different particle sizes. Impeller rotation speed is 300 rpm.

2.5.3 Slip velocities

Slip velocities of crystals of sizes 0.1 and 0.3 mm with impeller speed of 150 rpm are compared in Figure 2.35. Magnitudes of the highest slip velocities with two impeller speeds and with several crystal sizes are presented in Table 2.4. Slip velocities are higher for larger crystals and with higher impeller speed.

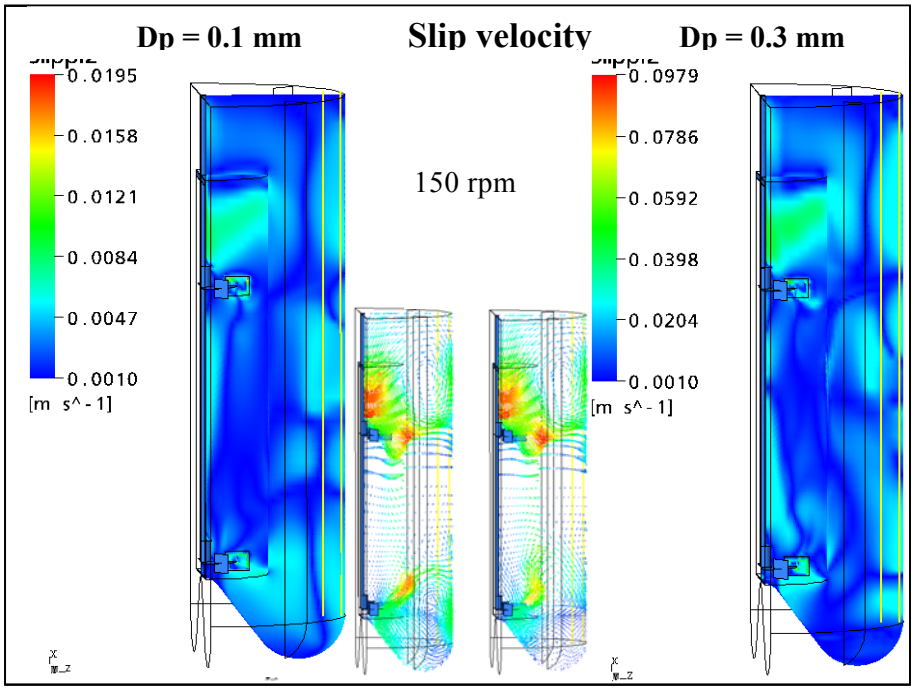

Figure 2.35. Local slip velocities in suspension crystallizer with impeller speed of 150 rpm.

Table 2.4. Magnitudes of simulated slip velocities, effect of crystal size and impeller speed. Density of the crystals is 2340 kg/dm^3.

	150 rpm	**300 rpm**
Dp = 0.5 mm	~0.03–0.12 m/s	~0.07–0.2 m/s
Dp = 0.3 mm	~0.01–0.04 m/s	
Dp = 0.2 mm		~0.01–0.06 m/s
Dp = 0.1 mm	~0.003–0.007 m/s	~0.005–0.02 m/s
Dp = 0.02 mm	~0.0002–0.0004 m/s	

2.5.4 Crystal growth

Growth rate of the crystals depends on supersaturation and on slip velocity. In our model the effect of crystal size on growth rate is expressed through differences in slip velocity. Local growth rates for crystals of sizes of 0.1 and 0.3 mm are presented in Figure 2.36. In this case solute concentration is assumed to be the same in the whole crystallizer. Classification of crystals of sizes 0.1 and 0.3 mm and consumption of KDP from the solution by the same crystals are presented in Figure 2.37. Consumption is highest at the lower parts of the crystallizer where the volume fraction of the crystals is highest causing higher decrease of supersaturation in the lower part of the crystallizer. This is in agreement with experimental results where lower supersaturations were detected in lower parts of the crystallizer.

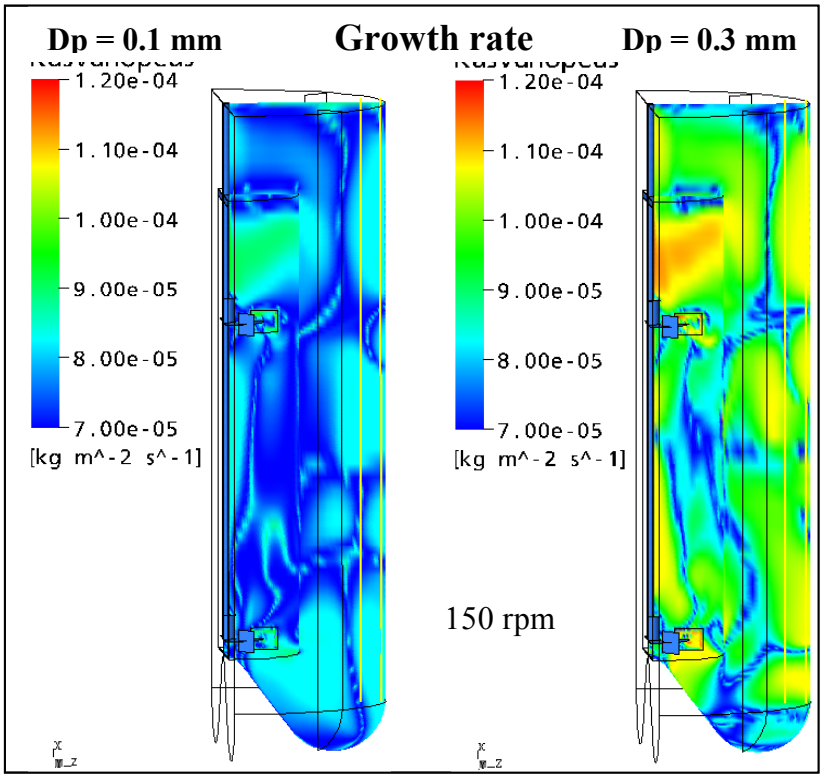

Figure 2.36. Local growth rates in the suspension crystallizer, impeller speed is 150 rpm.

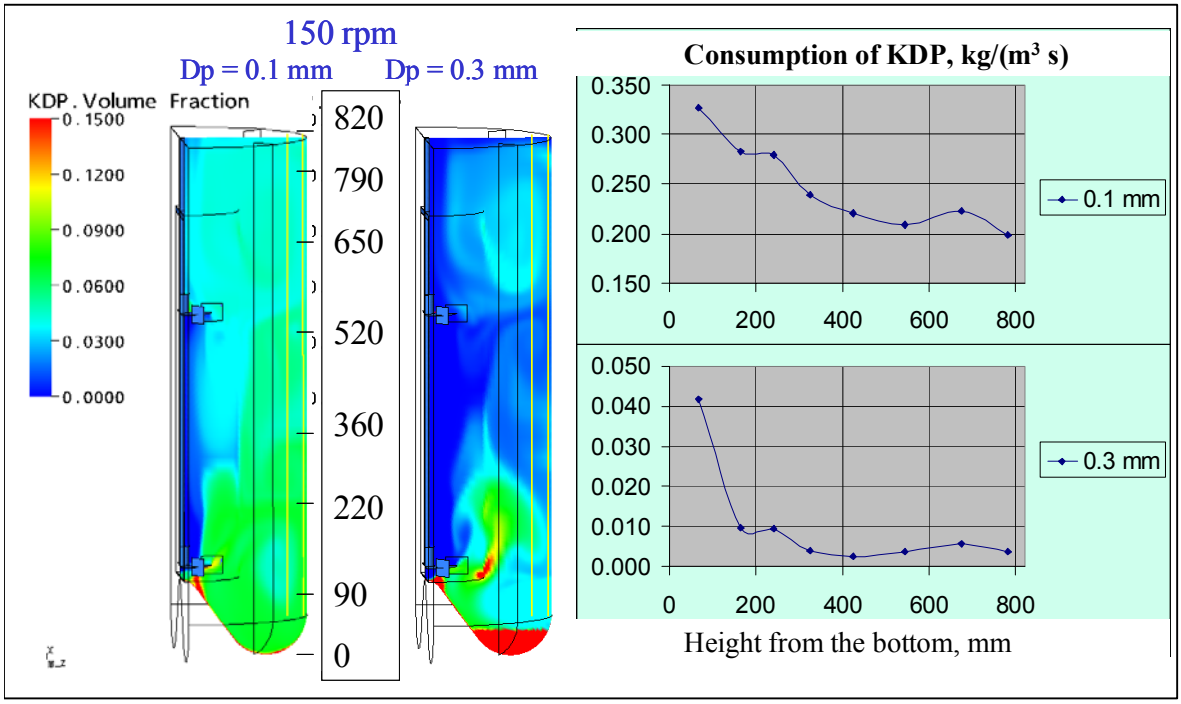

Figure 2.37. Local volume fractions of the crystals and consumption of KDP from solution as a function of height in the vessel. Impeller speed is 150 rpm.

2.5.5 Population balance model

A new method to solve population balances was developed in the project to avoid typical numerical oscillation in advective growth term. Our proposal is to use the Particle Transport Method PTM in population balance calculations. The PTM is a semi-Lagrangian explicit technique for solving convection-reaction problems. This approach belongs to the class of monotone numerical schemes. PTM captures sharp front, which is typical for the problem concerned, with high accuracy due to an adaptivity procedure. The scheme is based on the classical method of characteristics. As a moving mesh a system of numerical particles is used, which can be projected onto any fixed mesh with special monotone projection technique. The basic principle of the method is illustrated in Figure 2.38. For more details, see Hatakka et al. [14] and Smolianski et al. [15].

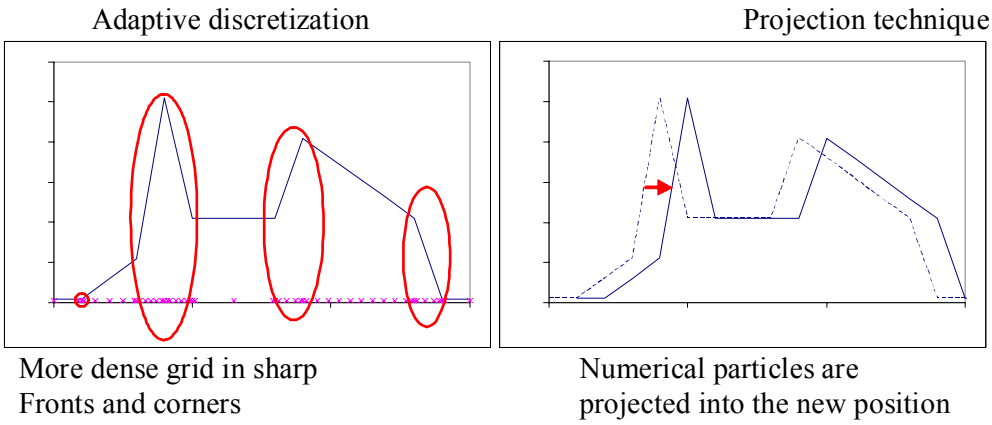

Figure 2.38. Procedure of the Particle Transport Method.

2.6 Summary

A new method to develop crystal growth models from single crystal measurements was developed. The effects of diffusion and surface reaction rates on crystal growth rate are examined. The new method utilizes flow field and mass transfer calculations with CFD and experimental data from single crystal growth. The method can be applied for both binary and ternary systems.

A good amount of experimental data was collected making experiments in the new suspension crystallizer developed in this project. Flow patterns of water and slip velocities of the crystals were measured using PIV. Simulated and measured flow patterns were very similar giving validation for simulated flow profiles. Variations of local temperatures inside the crystallizer were less than 0.1 ºC, which made difficult to get exact enough temperature data for quantitative analysis. Qualitatively, the simulated and measured variations in local temperatures were similar. Local suspension densities and crystal size distributions were measured at six vertically different locations. Simulated classifications of crystals were compared to the experimental data and quite good agreement was observed.

The new growth model of KDP developed in single crystal study in this project was imported into a CFD software. Local growth rates of the crystals in the suspension crystallizer were simulated. Variations in growth rate with crystal size and with location in the crystallizer were included to the model through local slip velocities. Consumption of KDP from mother liquor at different heights in the crystallizer was calculated from the simulated local growth rates and volume fractions of the crystals. The result was compared to experimental local concentrations of KDP in the mother liquor. Qualitative agreement between experimentals and simulations was found giving validation to our simulation model.

A new method to solve population balances by using the semi-Lagrangian explicite Particle Transport Method PTM was developed.

References

1. Enqvist, Y. 2004. Comprehensive study of crystal growth from solution. Doctoral Thesis. Acta Universitatis Lappeenrantaensis 182. Lappeenranta University of Technology, Finland.

2. Enqvist, Y., Partanen, J., Louhi-Kultanen, M. & Kallas, J. 2003. Thermodynamics and kinetics of KDP crystal growth from binary and ternary solutions. Trans. IChemE, 81A, 1354.

3. Liiri, M., Enquist, Y., Kallas, J. & Aittamaa, J. 2006. CFD modelling of single crystal growth of potassium dihydrogen phosphate (KDP) from binary water solution at 30°C. J. Cryst. Growth, 286, 413.

4. Liiri, M., Kallas, J. & Aittamaa, J. 2005. CFD modelling of single crystal growth of potassium dihydrogen phosphate (KDP) in water solution including one admixture. Proc. of ISIC16, Dresden, Germany, 187.5. Kim, S. & Myerson, A. S. 1996. Metastable Solution Thermodynamic Properties and Crystal Growth Kinetics. Ind. Eng. Chem. Res.**,** 35, 1078.

6. Pitzer, K. S. (ed.) 1991. Activity Coefficients in Electrolyte Solutions, 2nd ed. CRC Press, London.

7. Partanen, J. I., Mori, Y., Louhi-Kultanen, M. & Kallas, J. 2003. Activity Coefficients of Potassium Dihydrogen Phosphate in Aqueous Solutions at 25 °C and in Aqueous Mixtures of Urea and this Electrolyte in the Temperature Range 20–35 °C. Z. Phys. Chem., 217, 723.

8. Wang, S. L., Fu, Y. J., Zhang, W. C., Sun, X. & Gao, Z. S. 2000. In-Line Bulk Concentration Measurement by Method of Conductivity in Industrial KDP Crystal Growth from Aqueous Solution. Cryst. Res. Technol., 35, 1027.

9. Bohenek, M., Myerson, A. S. & Sun, W. 1997. Thermodynamics, cluster formation and crystal growth in highly supersaturated solutions of KDP, ADP and TGS. J. Cryst. Growth**,** 179, 213.

10. Easteal, A. J. & Woolf, L. A. 1985. Pressure and Temperature Dependence of Tracer Diffusion Coefficients of Methanol, Ethanol, Acetonitrile, and Formamide in Water. J. Phys. Chem., 89, 1066–1069.

11. Hawlicka, E. & Grabowski R. 1992. Self-Diffusion in Water-Alcohol Systems. 3. 1-Propanol-Water Solutions of NaI. J. Phys. Chem., 96, 1554–1557.

12. Wesselingh, J. A. & Krishna, R. 2000. Mass Transfer in Multicomponent Mixtures. Delft University Press, Delft.

13. Onuma, K., Tsukamoto, K. & Sunadawa, I. 1989. Measurements of surface supersaturations around a growing K-alum crystal in aqueous solution. J. Cryst. Growth, 98, 377.

14. Hatakka, H., Shipilova, O., Haario, H. & Kallas, J. 2005. Using a Mashless Transport Method in Modelling of Reactive Crystallization of Barium Sulphate. Proceedings of 12th International Workshop on Industrial Crystallization (BIWIC 2005), September 7–9, 2005, Halle, Germany (eds. Jones, M. & Ulrich, J.). Pp. 17–23.

15. Smolianski, A., Shipilova, O. & Haario, H. 2005. A Fast High-Resolution Algorithm for Linear Convection Problems: Particle Transport Method. Research Report 98. Lappeenranta University of Technology, Finland.

3. CFD simulation of gas-liquid processes

Marko Laakkonen[1], *Pasi Moilanen*[1], *Ville Alopaeus*[1], *Juhani Aittamaa*[1],
Arto Laari[2], *Ilkka Turunen*[2], *Zuoliang Sha*[2], *Ulla Ojaniemi*[3] *and Mikko Manninen*[3]

3.1 Introduction

In the chemical process industry, gas-liquid processes involving dispersion of small bubbles in a liquid are common. The modelling of these systems is more challenging than solid-liquid suspension for several reasons. Bubble shape is varying depending on the size and flow conditions and the bubbles may break or coalesce due to turbulence interactions. In most industrial cases, the gas-liquid mass transfer is relevant and has to be included in the modelling. Often a solid phase is also present introducing the complexities of a three phase system.

In the ModCheR-project, the research work in the field of gas-liquid systems focused on bubble columns and stirred reactors involving bubbly flows. The main interests were gas liquid mass transfer, CFD models including breakup and coalescence, and three phase modelling of flotation.

Mechanical agitation is used commonly in agitated reactors to improve the homogeneity of dispersion and to enhance the transfer of reacting compounds between gas and liquid phase. In large reactors, mass transfer and reaction conditions are, however, often strongly inhomogeneous. This makes the design and scaleup of agitated gas-liquid reactors a difficult task. Population balance has proved to be useful in the modelling of complex bubbly flows. It has already been applied for the investigation of bubble columns, but studies for the stirred tanks are scarce. This is surprising in a view of the fact that the size range of existing bubble sizes is often larger in the stirred tanks than it is in the bubble columns.

Phenomenological gas-liquid mass transfer models utilizing population balance for the description of local Bubble Size Distribution (BSD) and hence the gas-liquid mass transfer area were developed and validated against experiments. The aim was to obtain more generalized and reliable simulation tools for the design and scaleup of gas-liquid reactors.

---

[1] Helsinki University of Technology, Department of Chemical Technology, Chemical Engineering and Plant Design
[2] Lappeenranta University of Technology, Department of Chemical Technology, Product and Process Development
[3] VTT

Bubble columns are gas-liquid reactors where liquid forms a continuous phase and gas flows in the form of dispersed bubbles. CFD simulation of bubble columns is a very demanding task. There are several reasons for this. First of all, the hydrodynamics of bubble columns is very complex. The rising bubbles carry liquid with them upwards in the centre of the column. The liquid upflow then returns downwards at the column wall. This upflow at the centre and downflow at the wall periodically breaks down to form large turbulent vortices. The flow in the column is chaotic and turbulent at high gas flow rates.

Another additional complexity is the continuous bubble breakage and coalescence process, which controls the prevailing bubble size and therefore also the mass transfer in the column. A fully resolved CFD calculation of the bubble column requires the solution of mathematical population balance equations together with phenomenological models to describe bubble breakage and coalescence.

The algebraic slip mixture model is an attractive approach for bubbly flows, because it is robust and requires less computational power. A larger number of bubble populations are therefore feasible. The population models for bubble forming were coupled also to the mixture model in the project. The breakup and coalescence models were compared and validated against experimental data in a stirred tank test case with gas dispersion. Sensitivity analysis of the models was carried out.

In recent years, CFD model development for the complex three-phase flows of the mechanically stirred flotation cells has been started. The flotation process is a three-phase system used to separate particles in a mixture. In our study, several flotation models presented in literature were implemented in Fluent. The aim was to outline the method for modelling the flotation process using CFD.

3.2 Modelling gas-liquid mass transfer in agitated reactors

3.2.1 Experimental

Gas-liquid interactions and mass transfer were investigated in fully baffled, Rushton turbine agitated, 14 and 200 dm^3 laboratory vessels [1]. The experiments were carried out in wide range of agitation conditions to meet operating conditions in industrial gas-liquid reactors. Power consumption of mixing varied in the range 0.1–3 W/kg and gassing rates in the range 0.1 to 0.9 vvm (=m^3(gas)/m^3(liquid)/min).

Local BSDs were investigated near the vessel wall with the photography and inside the dispersion with a capillary suction probe. The experiments were made with air-water

and CO_2 – n-butanol dispersions. The problems associated to the automatic analysis of bubbles from the photographs were avoided by identifying the bubbles manually as ellipsoids from the photographs. Manually marked ellipsoids were transformed into size information by using the particle analysis tool of ImageJ 1.32 freeware. This eased the analysis significantly. The success of bubble identification is illustrated in Figure 3.1. Note the large amount of tiny bubbles.

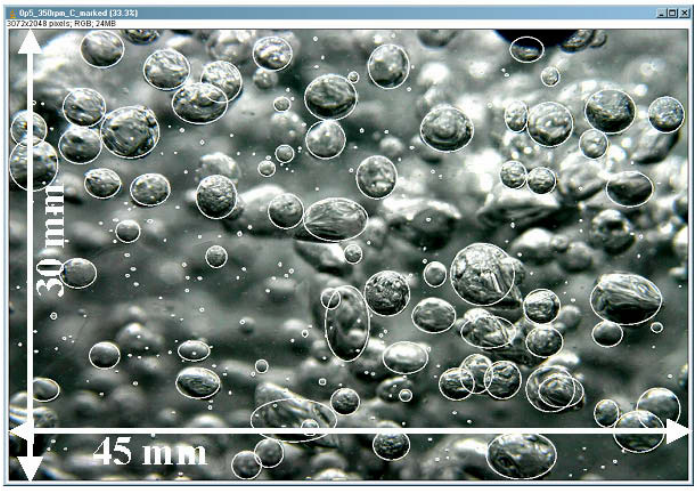

Figure 3.1. The success of automatic bubble identification.

Ungassed and gassed power consumption was measured based on torque on impeller. Accurate power consumption measurements are important, because bubble breakage and coalescence rates are determined by local dissipation rates of mixing energy. The energy dissipations due to buoyancy and the kinetic energy of gas injection become significant at high gassing rates and were considered in the modelling.

Gas-liquid mass transfer was investigated from the air-water system with dynamic gassing-in – gassing-out method by using an oxygen probe. The gas phase concentrations change during the experiment and alter the gas solubility. Gas phase dynamics was investigated by measuring off-gas concentrations with a mass spectrometer.

3.2.2 Multiblock stirred tank model

Agitation conditions are inhomogeneous even in the small laboratory stirred tanks. The non-ideal mixing must be considered in the validation of phenomenological models to avoid effects of vessel geometry on the resulting parameter values. A multiblock stirred tank model was developed for the detailed analysis of local gas-liquid hydrodynamics and mass transfer. The model consists of a limited amount of ideally mixed, connected

subregions. It is computationally efficient compared to CFD thus allowing the fitting of unknown parameters in phenomenological closure models or the investigation of long-term batch reaction dynamics. The model includes discretized population balances for bubbles, and gas and liquid mass balances for chemical compounds. Balances for scalar components in liquid are included to describe substances like biomass, which cannot be described easily as conventional chemical components.

The liquid flow rates between multiblock model subregions and local dissipation rates of mixing energy need to be given as an input data to the multiblock model, because momentum balances are not solved. Dissipations and flow rates were obtained from the CFD simulations. The dependence of predicted flow fields on the CFD simulation grid and turbulence model was minimised by scaling local dissipations with the measured power consumption and flow rates with the experimental impeller pumping numbers obtained from the literature.

The flow fields depend on the physical properties and the gassing rate. This issue was considered by simulating gas-liquid dispersions with CFD at varying operating conditions and physical properties of dispersion. Simple mathematical relations such as power law were then fitted to the CFD results to describe the change of local turbulence energy dissipation and liquid flow rate at varying hydrodynamic conditions in the multiblock model.

Multiblock stirred tank models were created for both laboratory stirred tanks and a 0.64 m^3 pilot xanthan fermenter. The vessels were divided into subregions based on the analysis of CFD simulation results based on the following criteria: 1) The subregions are arranged so that their number is minimal for accurate description of flow field. 2) The inhomogeneity of dispersion should be minimal inside a subregion. 3) The variable gradients should be nearly constant along the interface between subregions. 4) The model should be applicable for a wide liquid viscosity and gassing rate ranges. It is emphasized that processing of multiblock model flow fields from the CFD results is time-consuming and requires the matching of minor error in the mass balances. The automatic generation of subregions and internal flows would speed up this stage significantly.

3.2.3 The simulated vs. measured local bubble size distributions

Theoretical bubble breakage and coalescence models include uncertain/unknown parameters and can produce at best only order of magnitude estimates. Reasons for uncertainties are the incomplete understanding of underlying physics and the assumptions made in the model derivation. The fitting of unknown model parameters

against the experiments is necessary for the accurate prediction of local BSDs. The fitting is complicated by the fact that local BSDs, gas volume fractions, flow fields and mass transfer are related in a complicated way to each other, micro scale turbulence and physical properties of dispersion. The adjustment of unknown parameters against stirred tank experiments was however accepted, because creating similar turbulence conditions or investigating bubble slip, breakage and coalescence separately is difficult even in a simpler flow apparatus. The details of fitting procedure and the resulting models have been presented in [1].

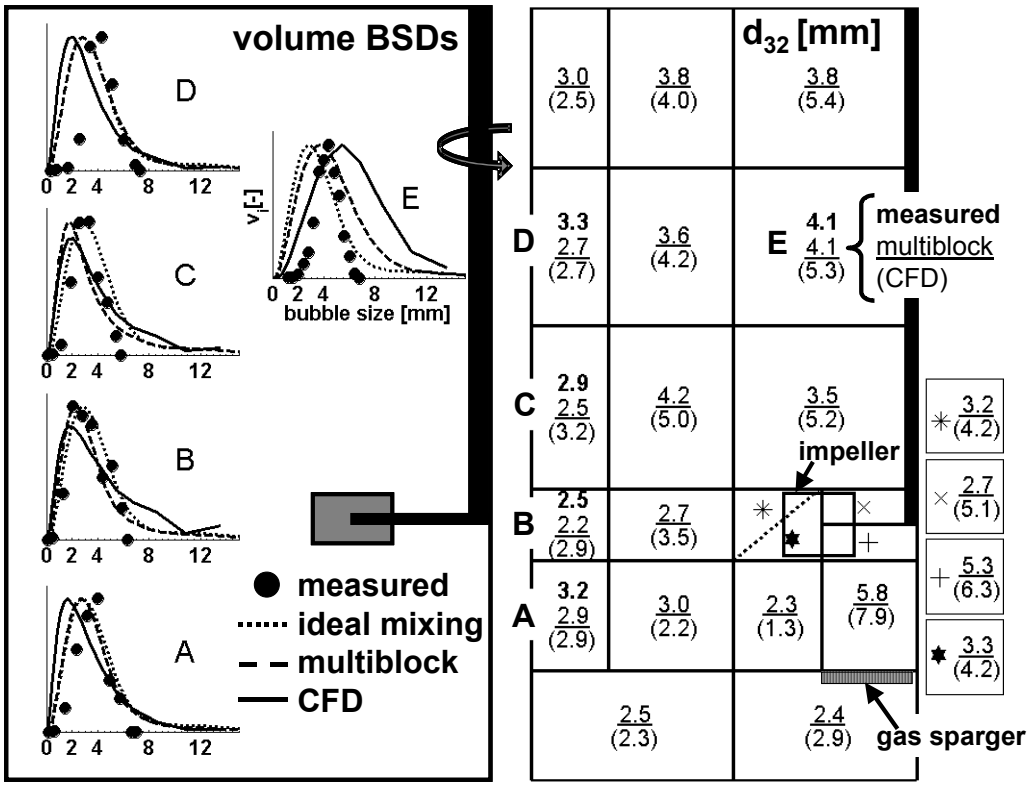

Figure 3.2. Measured vs. calculated local volume BSDs (left) and Sauter mean bubble diameters d_{32} (right), air – tap water, 200 dm^3 vessel, N = 390 rpm, Q = 0.7 vvm.

The comparison between the measured and simulated local bubble size distributions is presented in Figures 3.2 and 3.3. The CFD simulations were made by using the MUSIG model with 20 size categories (CFX-5.7) and are volume-averaged for each subregion of multiblock model. It can be seen that local BSDs are described fairly well in both air – water and CO_2 – n-butanol dispersions. The deficiencies of breakage and coalescence models or flow field modelling are possible causes for the tails in the volume BSDs but cannot be attributed to any of them alone. It is also possible that these tails exist but were not observed in the experiments. Turbulence correction of bubble slip was needed in all flow modelling approaches to ensure reasonable predictions of gas holdup thus showing the importance of this phenomenon.

An important observation was that the bubble breakage and coalescence models available for the bubble columns do not predict local BSDs very well in the stirred tanks. This shows that available models are not fully predictive at the moment. It must be emphasized that bubble breakage and coalescence have been studied in many studies under mildly turbulent conditions in the bubble columns or pipe flows even though turbulence is assumed to be the driving force for the breakage and coalescence in most available models.

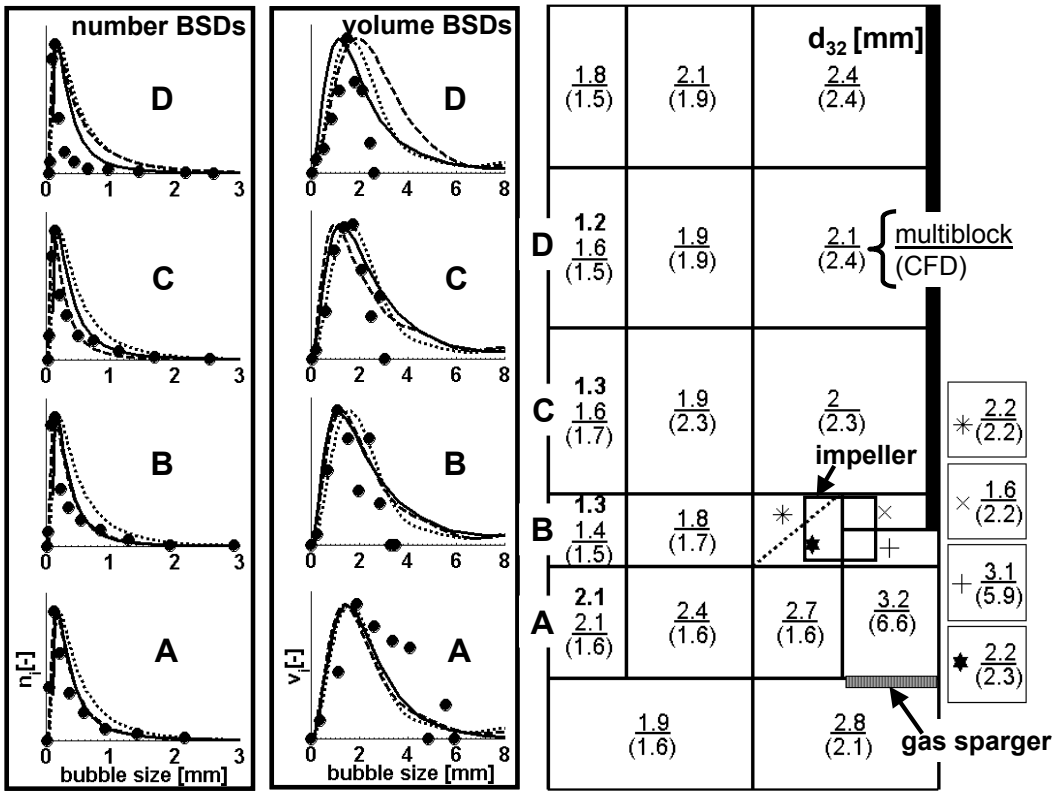

Figure 3.3. Measured vs. simulated local number (left) and volume (in the middle) BSDs (measured = markers, ideal mixing = dotted line, multiblock = dashed line, CFD = solid line) and Sauter mean bubble diameters d_{32} (right), CO_2 – n-butanol, 14 dm^3 vessel, N = 700 rpm, Q = 0.7 vvm.

3.2.4 Simulated vs. measured gas-liquid mass transfer

Gas-liquid mass transfer was investigated in the 200 dm^3 laboratory stirred tank. Mass transfer fluxes were described based on a simplified solution of Maxwell-Stefan multicomponent diffusion with resistances in both gas and liquid side. Local mass transfer areas were calculated from the validated bubble breakage, coalescence and turbulent slip models. The liquid side mass transfer correlation was adjusted to improve agreement between simulated and measured mass transfer. The details of model validation have been reported in [2].

Figure 3.4a presents the comparison of the multiblock simulations and the measured dissolved oxygen concentration profiles during absorption and desorption. The agreement is good for varying agitation conditions. This also gives further confidence to the validated PB model. The simulated times for reaching 5% of the initial oxygen concentration in the off-gas (Figure 3.4b) show generally smaller than 10% relative error compared to the experiments with mass spectrometry. This indicates that multiblock model is able to describe the gas phase dynamics realistically.

Predicted local mass transfer coefficients are presented for two simulation cases in Figures 3.5. The simulations show that mass transfer is more homogeneous in "high stirring speed/low gassing rate" -case (Q = 0.36, N = 475 rpm) than in "low stirring speed/high gassing rate" -case (Q = 0.7, N = 312 rpm) as expected. In both cases, mass transfer occurs mainly above the gas sparger and in the impeller discharge flow including the region where flow strikes to the wall. The results highlight the need to consider mixture inhomogeneities in the analysis of mass transfer experiments. In particular, non-ideal mixing of gas has a significant effect on the analysis of mass transfer results. Also, the dynamics of oxygen probe showed to be important at intense agitation conditions and was considered in the analysis of results. The multicomponent mass transfer effects, instead, showed to have minor effect on the mass transfer in the present case, but may become significant if dissimilar chemical components are present or pressure is high.

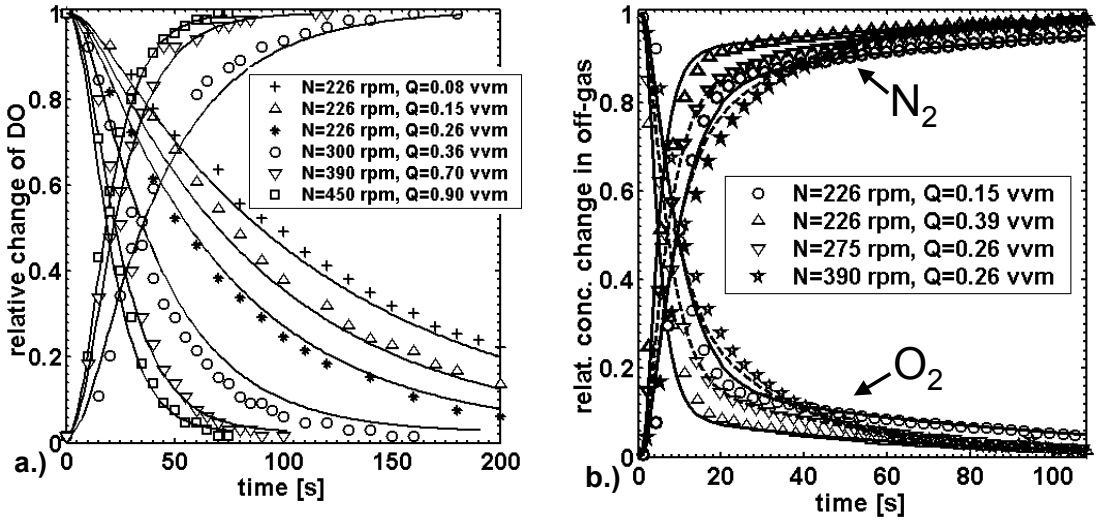

Figure 3.4. Predicted (lines) vs. measured (markers) a.) dissolved oxygen, b.) off-gas concentration profiles during desorption and absorption, air – tap water, 200 dm^3 tank.

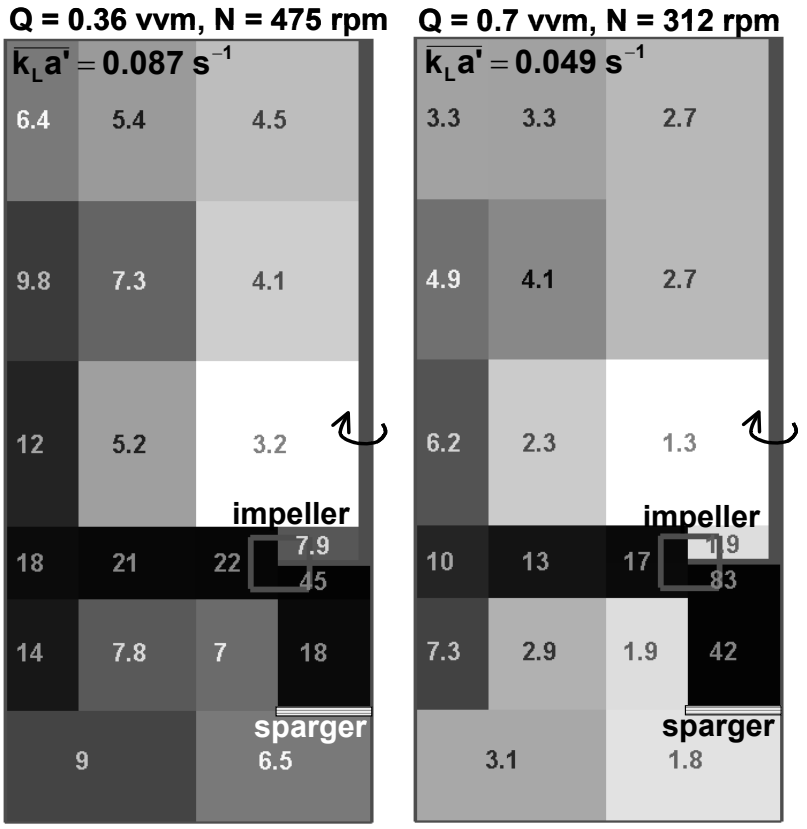

Figure 3.5. Predicted local oxygen transfer coefficients k_La [$\cdot 10^2$/s], air – tap water, 200 dm^3 tank.

3.2.5 Gas-liquid mass transfer simulations with CFD

The validated multicomponent mass transfer model and the physical property/component databases of Flowbat flowsheet simulator program were incorporated to CFX-5.7. The model was then used to investigate mass transfer in the 200 dm^3 laboratory stirred tank [2].

In the CFD implementation, chemical components and thermodynamics are obtained for the simulation from the Flowbat database. The transferring components are defined as user scalars with convection and diffusion in the CFD model. Mass transfer is defined by source and sink terms. Local turbulence conditions, pressure, temperature and concentrations are passed to the mass transfer model as parameters. The convergence of mass transfer fluxes within just few iteration steps is ensured by saving the result to the user data area (MMS) and using it as an initial guess for the next iteration. Local gas-liquid interfacial areas are calculated from the MUSIG population balance model (CFX-5.7) with the adjusted bubble breakage, coalescence and turbulent slip closures. Local turbulent energy dissipation rates predicted by the CFD are scaled with the measured power consumptions of mixing before passing them to the bubble breakage, coalescence

and mass transfer models to avoid dependences on the turbulence model and the CFD simulation grid.

CFD simulations were made with a 180° structured grid of 109 000 cells, the standard k-ε turbulence model and the MRF technique of impeller motion. The BSDs were described by 20 MUSIG size categories with geometric discretization. Three combinations of stirring speed and gassing rate were investigated: 300 rpm/0.36 vvm; 390 rpm/0.7 vvm; 450 rpm/0.9 vvm. The computation time for reaching a steady-state solution was approximately 10 days cpu-time in a linux (1.7 GHz AMD/1 Gb) workstation. The predicted distributions of $k_L a$ are presented in Figure 3.6. It is noted that they are very similar compared to the multiblock model predictions in Figure 3.5. The CPU time requirement of CFD simulation is more than 1000-fold compared to the multiblock model. In this case, the multiblock model therefore seems to be an optimal trade-off between the accuracy and CPU time.

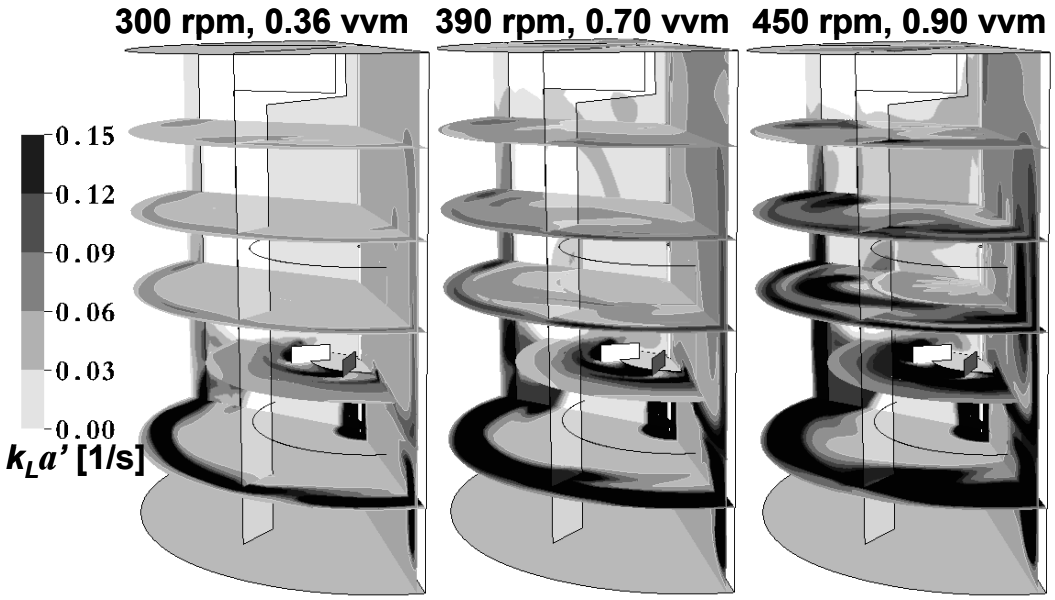

Figure 3.6. Predicted local mass transfer coefficients of oxygen in the 200 dm^3 stirred tank.

Due to difficulties in direct comparison to the measurements, CFD simulations were compared to the multiblock simulations. This should be a reasonable approximation, because multiblock simulations were validated against BSD, gas holdup and oxygen transfer experiments. The vessel-averaged mass transfer parameters are compared in Table 3.1. The CFD slightly overpredicts bubble size and underpredicts $\overline{k_L a'}$ compared to the multiblock model. This shows the sensitivity of mass transfer to the local BSDs. Overall, the results are in the same range.

Table 3.1. Vessel-averaged, mass transfer parameters, CFD (bold), #multiblock simulation.

N [rpm]	Q [vvm]	d_{32} [mm]	α [vol-%]	a_L [m^2/m^3_L]	$\overline{k_L a'}$ [s^{-1}]
300	0.36	**3.0**, #2.8	**2.8**, #2.5	**50**, #56	**0.029**, #0.033
390	0.7	**3.2**, #3.1	**5.3**, #5.4	**91**, #105	**0.061**, #0.075
450	0.9	**3.6**, #3.1	**8.2**, #7.8	**126**, #151	**0.086**, #0.124

3.2.6 Dynamic modelling of batch xanthan fermentation

Multiblock model was used to investigate the dynamics of batch xanthan fermentation. Xanthan fermentation was chosen for the study, because it is a typical example of the process that is limited heavily by the gas-liquid mass transfer and non-ideal mixing. This process is also interesting due to its significant economical value. The apparent viscosity of aqueous xanthan increases during the fermentation causing a severe oxygen transfer limitation to the microbial growth.

The bubble breakage, coalescence and mass transfer were validated for viscous xanthan dispersions in cooperation with "New Design Tool for Bioreactors" -project (NeoBio, Tekes). The details have been reported in [3]. The fermentation kinetics was found from the literature.

Xanthan fermentation was investigated in a 0.64 m^3 pilot fermenter. The multiblock model for the pilot fermenter was obtained from CFD simulations at varying xanthan concentrations (and liquid viscosities). The change of liquid flow fields during the fermentation was related to the CFD predictions in the multiblock model. Fermentation was investigated in two simulation cases: at constant (S1) and at gradually increasing stirring speed (S2). Biomass, xanthan, nitrogen and carbon source were included as reacting scalar components in the liquid phase. Water, carbon dioxide, nitrogen and oxygen were the transferring components between gas and liquid phase. The dissolved oxygen (DO) consumption and the production of carbon dioxide act as a link between bioreaction and gas-liquid mass transfer. The rediscretization of population balances for bubbles was necessary during the simulation due to significant increase of bubble size with the increasing viscosity of liquid.

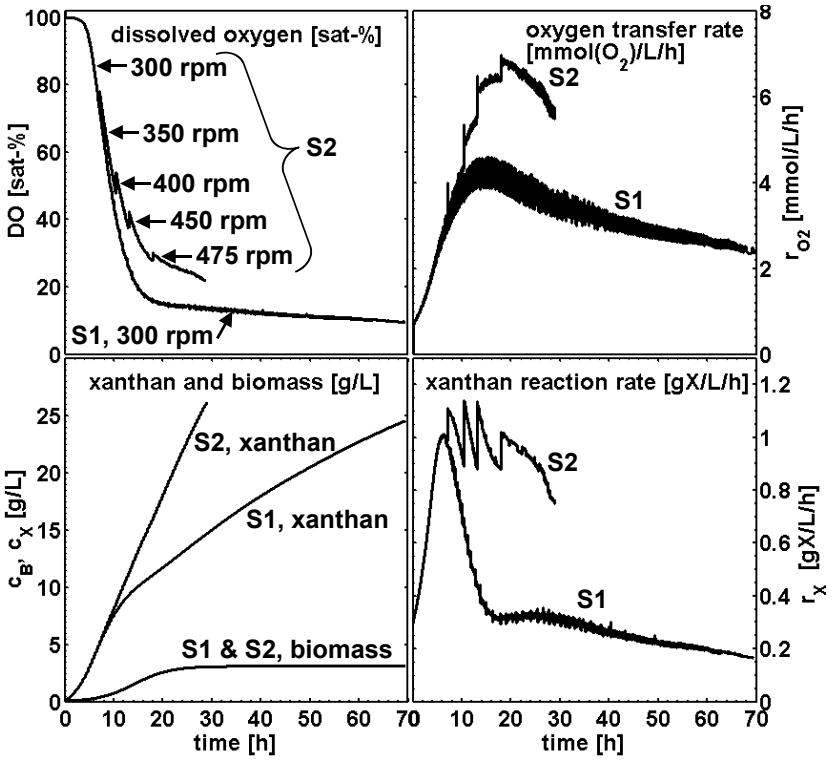

Figure 3.7. Predicted overall performance of 0.64 m^3 pilot xanthan fermenter.

The predicted overall performance of the fermenter is presented in Figure 3.7. The comparison of S1 and S2 shows the positive effect of stirring speed on the fermentation. The time needed for reaching 2.5 w-% final xanthan concentration is 70 hours for the S1 while only 29 hours are needed in the case S2. In the case S2, DO concentration decreases more slowly compared to S1, because mass transfer and mixing limitations are partly compensated by increasing the stirring speed. The main reason for the mass transfer limitation is the decrease of mass transfer area. It is caused by the increase bubble sizes that results from the increase of liquid viscosity. Oxygen transfer rates are small at the start of fermentation, because microbial concentration and xanthan production rate are small, but increase rapidly reaching a maximum. After this, mass transfer limitation causes the decrease of oxygen transfer rate and xanthan reaction rate towards the end of fermentation batch. The simulated trends agree with the experimental xanthan fermentation studies available in literature.

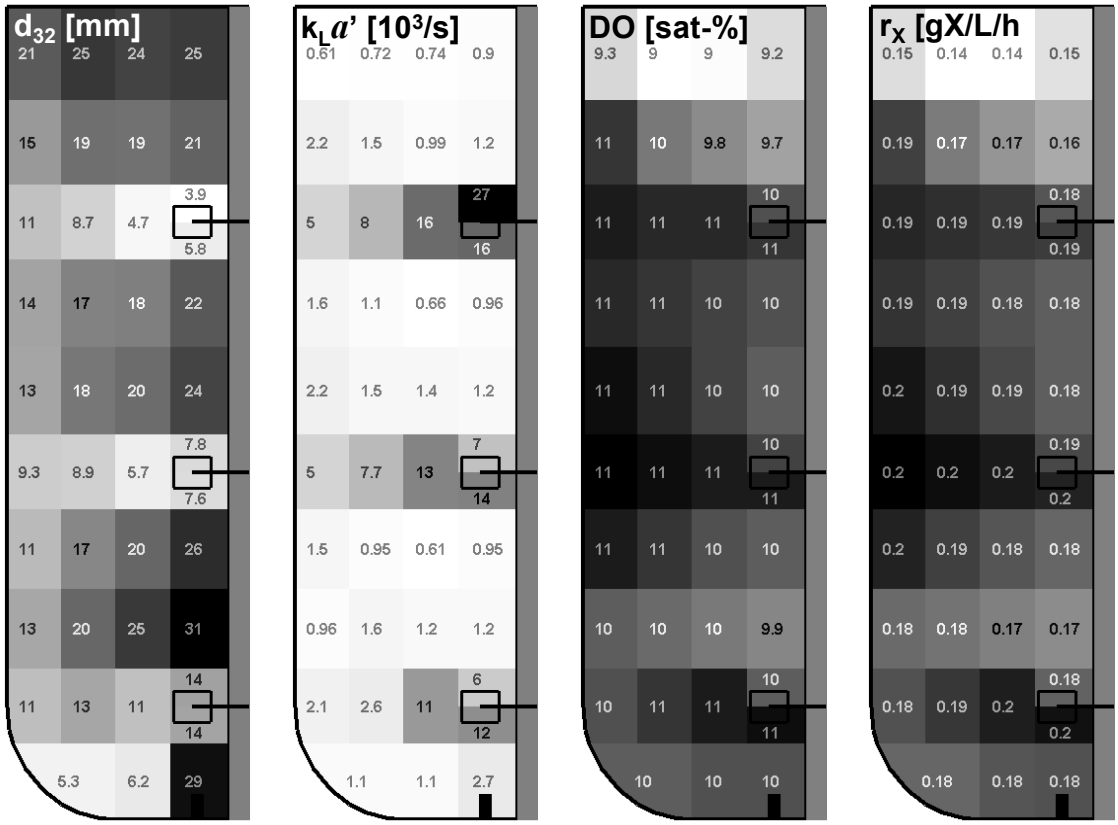

Figure 3.8. Calculated local mass transfer and reaction conditions in the xanthan pilot fermenter, N = 300 rpm, xanthan concentration 2.4 w-%, simulation time 65 h.

Figure 3.8 presents local mass transfer and reaction conditions at the end of fermentation at stirring speed 300 rpm (case S1). The results show the inhomogeneity of reaction mixture. High turbulent dissipations cause the bubble breakage in the impeller regions thus leading to larger mass transfer rates and DO concentrations. This results into inhomogeneous xanthan reaction rates.

3.2.7 Conclusions

The adjusted breakage, coalescence and turbulent slip closures predict the general trends of local gas-liquid hydrodynamics realistically. The fitting improved the accuracy of model predictions significantly, but due to complexity of turbulent gas-liquid flow and several superimposed phenomena, the fitting of unknown parameters against the local BSDs alone is not sufficient for the validation of bubble breakage and coalescence mechanisms. More detailed experiments in a simpler flow environment are needed for this.

Mass transfer simulations with the validated models were in good agreement with the oxygen transfer and off-gas experiments under varying agitation conditions. This also gives further confidence to the adjusted population balance closures. Simulations predict a strong inhomogeneity of gas-liquid mass transfer in the 200 dm^3 laboratory stirred tank. The inhomogeneities are expected to be larger in large industrial reactors so that the benefits of detailed mass transfer modelling should be even more significant for the reactor design and scaleup. The validated models should be applicable for the investigation of an arbitrary vessel size and geometry, because non-ideal mixing was considered in the validation.

The applicability of validated models for the CFD calculations was demonstrated. In the studied case multiblock model showed to be an optimal trade-off between the accuracy and CPU time. The generation of flow fields for the multiblock model is laborious at the moment but can be accelerated by developing suitable algorithms.

Long-term dynamics of batch xanthan fermentation was investigated by incorporating bioreaction kinetics and population balances for bubbles and gas-liquid mass transfer model to the multiblock fermenter model. The results demonstrate the potential of multiblock modeling for the detailed investigation of viscous, reactive gas-liquid dispersions in which mass transfer and mixing limitations are present. The results also show that population balances are necessary for the successful modelling of highly viscous gas-liquid dispersions.

3.3 Development of CFD models for bubble columns

3.3.1 Model development

Models for bubble coalescence and breakage

Accurate system and liquid composition dependent bubble coalescence and breakage rate models are essential for the CFD model to be able to describe the continuous process of breakage and coalescence in the column.

For bubble breakage some theoretical models are available in scientific literature. The validation of these models is, however, inadequate due to lack of reliable bubble size data especially at high gas volume fraction. The bubble coalescence models are even less developed. The main reason for this is the complex effect of the liquid composition on the coalescence rate. Therefore, the bubble coalescence models always require some parameters, which vary from system to system and should be determined experimentally.

The bubble coalescence models used in this work are mainly based on the work of Prince and Blanch [4]. The original bubble coalescence model of Prince & Blanch is derived for pure liquids without the effect of any surface-active compounds or contaminants. In the model the coalescence rate is calculated as a product of bubble-bubble collision frequency and coalescence efficiency. Coalescence efficiency is estimated from the film thinning time, the time required for the rupture of the film between the two colliding bubbles, and the contact time of the bubbles.

The film thinning time for film rupture, which is the same as the coalescence time, can be used as a model parameter to adjust the coalescence rate in the coalescence model to correspond experimental results. This approach has been used in the project to estimate the coalescence properties of different solutions.

For bubble breakage, three models have been used in the project. These are the model of Prince and Blanch, the bubble-wake interaction model by Colella et al. [5] and the theoretical bubble breakage model by Lehr, Millies and Mewes [6]. The Prince & Blanch model includes the critical Weber number as an adjustable parameter. The model is based on the concept of breakage by contact with turbulent eddies. The model proposed by Colella et al. is based on completely different concept, breakage by the effect of bubble wakes.

Estimation of coalescence and breakage parameters from bubble size measurements

A method to estimate the coalescence and breakage parameters for different solutions has been developed in this project. The method is based on measuring the changes of the bubble size distribution over the column height. Also, a model was developed to calculate the change of the bubble size distribution in the column using a simplified hydrodynamic model for the liquid phase and a population balance model including models for bubble coalescence and breakage. The parameters in the coalescence and breakage models can be obtained by parameter estimation comparing the measured and calculated bubble sizes. At present, the obtained results are limited to low gas volume fractions due to the limitations of the photographical method used for the measurement of bubble size distributions.

The bubble size distributions were measured in two columns. These are a cylindrical bubble column with a height of 4.6 m and a diameter of 0.078 m and a rectangular column with a height of 2.0 m, width of 0.15 m and depth of 0.03 m. The coalescence model of Prince & Blanch and the breakage models of Prince & Blanch and Colella et al. were used in the project to estimate the coalescence and breakage parameters in the cylindrical bubble column. The results are presented by Laari and Turunen [7]. Both

breakage models gave reasonable estimates for bubble breakage and it was not possible to distinguish one model from the other.

The results for the rectangular column are presented by Laari and Turunen [8]. In these experiments only the coalescence parameter was estimated. The breakage rate was calculated by the theoretical breakage rate model by Lehr, Millies and Mewes.

Estimation of coalescence properties using persistence times measurements

One drawback of the estimation of the parameters from bubble size distributions is that the method is rather tedious. It requires the measurement of the bubble size distribution from several locations in the column. Also, the measurement of bubble size distribution was not possible for high gas volume fractions due to the limitations of the photographic method used in the experiments.

A simple method was proposed by Ghosh [9–10] to characterize the liquid coalescence properties. This method was used in this project to estimate the coalescence properties of different solutions by measuring the time that a single bubble rests at free gas-liquid surface without coalescence. This time, the so-called bubble "persistence time", is related to the bubble coalescence time when two-bubbles collide in gas-liquid flow. The measured persistence times range from almost instantaneous coalescence in 10 ms to 20 seconds in solutions containing surface-active compounds. The measured persistence times were compared with the coalescence times obtained by parameter estimation from bubble size distributions (see Laari & Turunen [8]). Fort short coalescence time the measured persistence times and the coalescence time are almost identical. For longer coalescence times the measured persistence time is at least a magnitude longer than the coalescence time. This indicates that the coalescence phenomenon in the two cases is not completely identical or that the coalescence models with collision rates and coalescence efficiencies should be further studied. However, the method can be used to characterize the liquid coalescence properties and it gives some useful information how to choose a suitable parameter value for the coalescence model.

3.3.2 CFD models

Multiphase bubble column CFD models

The so called "multiphase models" are based on the idea of discretizing the dispersed phase to a number of phases, which are treated separately. The source terms for the equations of the dispersed phases are formulated by using the population balance equations. In this project the population balance solution method presented by

Hageseather et al. [11] has been used. The method is based on geometrical discretization and preserves both the number and mass balances of the dispersed phase. The bubble column CFD calculations were made by using CFX 4.4.

MUSIG model

The most often used multiphase model in bubble column applications is the MUSIG-model, which is included in CFX 4.4 and CFX 5.7. The idea of the MUSIG model is to decrease the number of the equations to be solved by solving the momentum equation only for the mean bubble size. The MUSIG model was used to characterize bubble breakage and coalescence parameters in a test case. The results are presented in Sha, Laari and Turunen [12].

Gas-liquid mass transfer was simulated using the MUSIG model approach with the solution of population balances together with bubble breakage and coalescence. Converged results were obtained when a constant value was used for the mass transfer coefficient. Interfacial mass transfer area was calculated locally from local bubble size distribution. Results are presented in Sha, Laari and Turunen [12]. However, the simulation failed when the mass transfer coefficient was calculated locally from local hydrodynamic conditions. Further studies are necessary to obtain converged results also in this case.

Multi-Phase-Multi-Size-Group model

The principle weakness of the MUSIG model is that all the bubble sizes are assumed to move in the liquid with a velocity equal to the velocity of the mean bubble size. This is clearly a severe simplification, which affects the accuracy of the calculations especially in the cases when the bubble size distribution is wide.

In this project a model called “Multi-Phase-Multi-Size-Group Model” was developed. In this model the bubble size is discretized into a number of bubble size classes. The results of these simulations are presented by Sha, Laari and Turunen [13–14]. Eleven phases were used. One phase was used for the continuous phase, and ten phases to describe the dispersed phase characterized by different bubble size. With this model, the different phases have their own velocity profiles so that the flow rate of each bubble size can be more accurately described and a more accurate volume fraction for each phase can be obtained.

The drawback of this model is the large amount of computer time required for the solution.

To lower the computer load the bubble size classes can be combined to form groups (or phases), which are used to solve the momentum equations. Thus, the number of groups (or phases) can be chosen as a compromise between the accuracy and the computational resources available.

The calculated bubble size distributions were compared to measured distributions in one test case. A reasonable agreement between the calculated and the measured distributions was found to exist (see Sha, Laari and Turunen, [13–14]).

3.3.3 Verification of the CFD calculations by PIV measurements

A Particle Image Velocimetry (PIV) measurement system provided by LaVision was received to LUT at February 2006. The equipment was used to measure liquid and gas velocity profiles in a bubble column with a diameter of 0.172 m and height 1.7 m. The obtained results can be used to verify the CFD calculations comparing the calculated and measured velocity profiles for both the liquid and the gas phase. This work is currently going on to the end of the project. Preliminary results will be published later (Laari, Turunen and Sha, [15]).

3.3.4 Computational study of bubble dynamics

The bubble dynamics, coalescence and breakage, may also be studied by direct numerical simulations. The problem for numerical simulations consists of a combination of the Navier-Stokes equations for unsteady laminar flow of two immiscible incompressible fluids together with a free boundary problem for the bubble shape. The work in this project was based on our earlier computational approach consisting of three basic components: the finite element method for spatial approximation, the operator-splitting for temporal discretization and the level-set method for interface representation. Diverse problems of bubble coalescence and breakup have been already studied with this approach. We have been able to simulate bubble dynamics, in all relevant flow and bubble shape regimes. More specifically, the following results have been achieved:

- bubble shapes in all flow regimes; rise velocities for on bubble (Smolianski, Haario, Luukka [16])
- simulations for a wobbling bubble, with vortex shedding (Haario, Smolianski, Luukka [17])
- two bubbles: coalescence, rise velocities (Haario, Laari, Luukka, Smolianski, Turunen [18])
- bubble swarm behavior: coalescence, rise velocities (Haario,Luukka, Smolianski, [19]).

The above simulations were successfully performed in all flow regimes as given, e.g., in the "bubble map" of Clift, Grace and Weber [20], including higher Reynolds number regimes with wobbling bubbles and nonsymmetric vortex shedding. To the best of our knowledge, this has not been reported earlier in the literature.

The simulations were performed in a spatially 2D domain. This naturally excludes inherently 3D phenomena, but we were positively surprised to see how many experimentally reported phenomena could be simulated with a 2D code. However, certain limitations of the approach might be observed.

Coalescence of bubbles follows a thinning of the liquid film separating them, a process that causes the rupture of the film between the two colliding bubbles. But the physical thickness of the film before coalescence (or non-coalescence) may be several orders of magnitude smaller than the grid size employed in the present algorithms. Although difficult to verify directly, it seems that the bubbles tend to "reach" each other numerically too soon and, consequently, coalescence may be overestimated. Methods to overcome these problems – multiscale modeling, meshless or particle-type numerical algorithms – are currently studied in other projects. Another natural extension is simulation 3 spatial dimensions.

3.3.5 Conclusions

A Multi-Phase-Multi-Size-Group model was developed for the CFD simulation of bubble columns. In the model the bubble size is discretized to a number of bubble classes. To reduce the calculation load these classes can be combined to form bubble size groups, for which the momentum equations are solved during the numerical solution. In this way the system can be optimized to give the most accurate result with the available computational resources.

A fully resolved CFD simulation of bubble columns requires a multiphase approach where the dispersed phase is discretized to a number of phases, which are treated separately in the calculations. The source terms for the Navier-Stokes equations are formulated through population balance equations. The population balance equations require phenomenological models to describe bubble breakage and coalescence rates.

A method to estimate the coalescence and breakage parameters from bubble size distributions was developed in the project. This method is useful and gives valuable information about the coalescence and breakage rates in bubble columns. However, because of the photographic method that was used to measure the bubble size distribution the method is still limited to low gas flow rates and holdups.

The coalescence properties of different solutions, including tap water with alcohols and antifoaming agents, were estimated by measuring the persistence time that a bubble rests at a free gas-liquid interface. The measurement of bubble persistence time gives quantitative information about the coalescence properties of different liquids. However, the correspondence to coalescence time in bubbly flow is not straightforward and should be further studied.

Theoretical models for bubble breakage are useful but they are not yet complete. Validation of the models is still not sufficient due to lack of reliable bubble size data especially at high gas flow rates. Also, the effect of gas density is still missing from the theoretical models.

One important finding in the project was the very important role of the turbulence properties in the modeling of the multiphase flow. The turbulent energy dissipation rate is a very important model parameter, which affects the bubble-bubble collision rate, bubble-bubble contact time, breakage rate and gas-liquid mass transfer coefficient. Turbulence models in the multiphase flow are not yet satisfactorily developed and turbulence should be further studied both theoretically and experimentally.

3.4 Application of algebraic slip mixture model for bubbly flows

3.4.1 Population models for bubbly flow in a stirred tank

A general population balance includes the following source terms: 1) B_B, birth due to breakup of higher particle classes, 2) D_B, death due to breakup in present particle class, 3) B_C, birth due to coalescence of lower particle classes and 4) D_C, death due to coalescence in the present particle class. In bubbly flow without chemical reactions and mass transfer, the source terms are based on the coalescence and breakup models for the bubbles.

In a CFD model, the population balance equation is formulated as follows:

$$\frac{\partial}{\partial t}\left(\rho_i \alpha_i\right) + \nabla \cdot \left(\rho_i \overline{u}_i \alpha_i\right) = \rho_i \left[B_B - D_B + B_C - D_C\right]_i \tag{3.1}$$

where α_i is the volume fraction, ρ_i density, and $\overline{u}_i$ the velocity of bubbles in class i. The algebraic slip mixture model has been used as the multiphase formulation in the simulations reported in this section [21]. In this method, each bubble class is treated as a separate phase and the phase velocity $\overline{u}_i$ is composed of the velocity of the liquid-gas mixture and the slip velocity of the bubble with respect to the mixture.

We have defined the bubble classes so that the bubble volume of each class is twice the volume of bubbles in the next smaller bubble class. Each class has an exact bubble volume. In a break-up process, the bubble of volume v_k is assumed to break in two smaller bubbles, one having the exact volume v_j of class j. The other daughter class has the volume $v_k - v_j \equiv v_c$ such that $v_{k-1} \leq v_c < v_k$. In order to ensure number conservation, the bubble v_c is divided into classes k and k-1 according to $xv_k + (1-x)v_{k+1} = v_c$.

In the coalescence process it is assumed that two bubbles, belonging to classes i and j, coalesce to form a bubble with volume $v_i + v_j \equiv v_c$. If the resulting bubble lies between size classes k and k+1, it has again to be divided to the nearest exact bubble size classes in order to ensure number conservation: $xv_k + (1-x)v_{k+1} = v_c$.

The coalescence model of Prince & Blanch [4] was applied in all our test cases. The breakup model of Luo & Svendsen [22] contains some inconsistencies [11, 23, 24, 25], which have been reported to be overcome with the model of Hagesaether et al. and the model of Lehr et al. Following the method of Luo & Svendsen, the breakup model of Lehr et al. is derived from the frequency of the arriving eddies onto the surface of the bubble and from the probability that collisions lead to breakage [6]. Here the probability that the collisions result in a breakage is determined from the balance of interfacial force of the bubble surface and the inertial force of the colliding eddy. For the breakup we have implemented the model of Luo & Svendsen [22], and the model of Lehr et al. [6]. The more complicated model of Haegesaether et al. [11, 23, 24] was not implemented, but was briefly reviewed. The models are reviewed in more details by Manninen et al. [26].

3.4.2 Results of the breakup model comparisons

The test case for the bubble population distribution studies was a laboratory size stirred reactor used in the measurements carried out in the KaNeMa-project [27]. The reactor was equipped with a standard Rushton turbine and four baffles. The water volume was 13.8 litres, with tank diameter and liquid height equal to 26 cm. The baffles were extended along the liquid surface in order to prevent formation of the central vortex. The turbine diameter was 8.6 cm, equal to the turbine disk clearance from the bottom.

Air was fed to the reactor through a pipe located 4.6 cm below the disk of the Rushton turbine. For model validations we selected a case with stirring speed 340 rpm and air feed rate 0.25 l/min. The bubble distribution was described with 16 bubble size classes such that the volume of the bubble in each class was defined as twice the volume of the next smaller class.

The mixture model [21] was used in all simulations for solving the velocities and volume fractions of the 16 bubble phases. The slightly modified correlation of Ishii & Zuber [28] was used for the bubble drag coefficient in most of the simulations [29].

The results of the calculations with the two breakup models Luo & Svendsen and Lehr et al. for the breakup kernel function are shown in Figure 3.9 for bubble sizes 0.6 mm and 1.9 mm. For coalescence, the model of Prince & Blanch was applied.

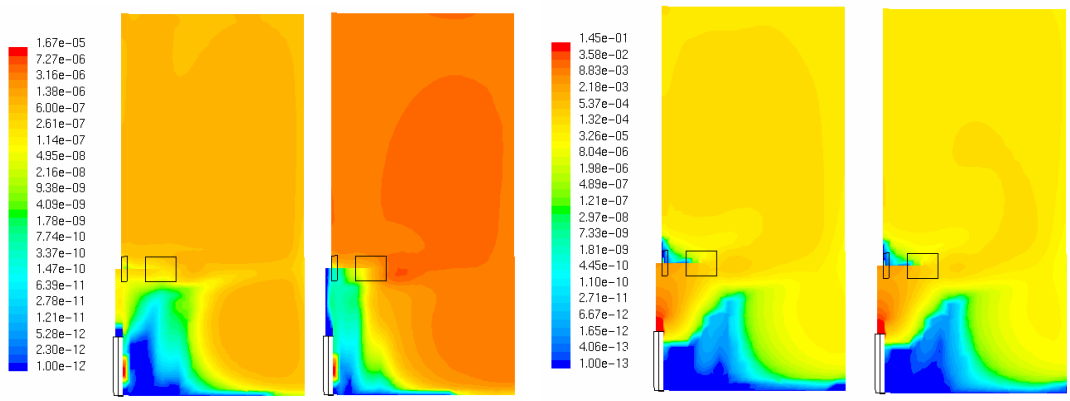

Figure 3.9. On the left: Volume fraction of bubbles in the fourth class (diameter 0.6 mm) computed with breakup model Luo & Svendsen and Lehr et al. On the right: Volume fraction of bubbles in the ninth class (diameter 1.9 mm) respectively. Note that the colour scale is logarithmic.

The results with the two breakup models were qualitatively similar. Figure 3.9 shows, however, that the model of Lehr et al. produced more small size bubbles than the model of Luo & Svendsen (on the left in Figure 3.9). The distribution of larger bubbles was quite similar with both models (on the right in Figure 3.9).

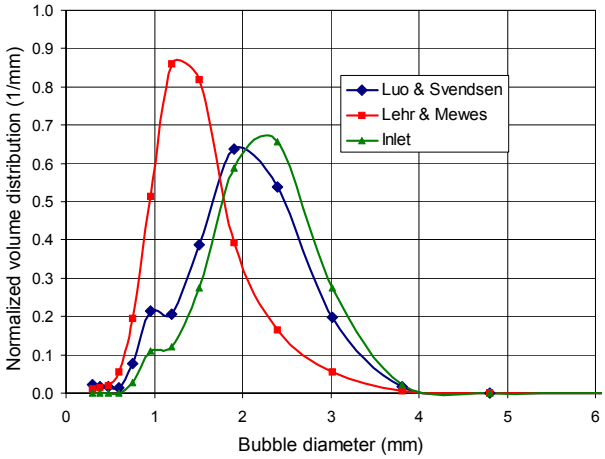

Figure 3.10. Normalized volumetric size distribution of bubbles in the reactor calculated with the models of Lehr et al. and Luo & Svendsen. In addition, the distribution of bubbles in the inlet flow is presented.

Figure 3.10 shows the volume distribution of the gas bubbles in the whole tank. The volumetric distribution is here defined as

$$v(d_i) = \frac{n_i d_i^3}{\Delta d_i \sum_i n_i d_i^3} = \frac{\alpha_i}{\Delta d_i \sum_i \alpha_i} \tag{3.2}$$

where n_i is the number density and α_i the volume fraction of bubbles in class i and Δd_i is the width of the size class i.

The curves in Figure 3.10 show the average volumetric size distribution of the bubbles in the whole volume of the stirred tank. The distribution of bubbles in the gas feed, based on the measurements, is shown for comparison. The resulting distribution obtained with the Luo & Svendsen model does not deviate much from the inlet distribution, showing that this model does not break up the bubbles appreciably. The breakup model of Lehr et al. resulted in much smaller average bubble size. The maximum of the distribution was at $d \sim 1.3$ mm in contrast to the maximum at $d \sim 2$ mm obtained with the Luo & Svendsen model.

The simulation results were compared to the measurements by Laakkonen et al. [30]. The experimental measurements have been carried out by capillary measurement and by digital imaging. The results are shown in Figure 3.11 in four measurement locations.

The calculation results were generally in poor agreement with the experimental results. At point BG which is located in the impeller stream, the capillary measurement agrees with the results obtained with the Luo & Svendsen. The model of Lehr et al. produces much smaller bubbles. The comparison to experiments is obscured by the disagreement of the two experimental results, the digital imaging technique giving a result closer to the Lehr et al. model prediction. The situation is somewhat similar at point AF, which also is in the region of the primary bubble stream from the impeller.

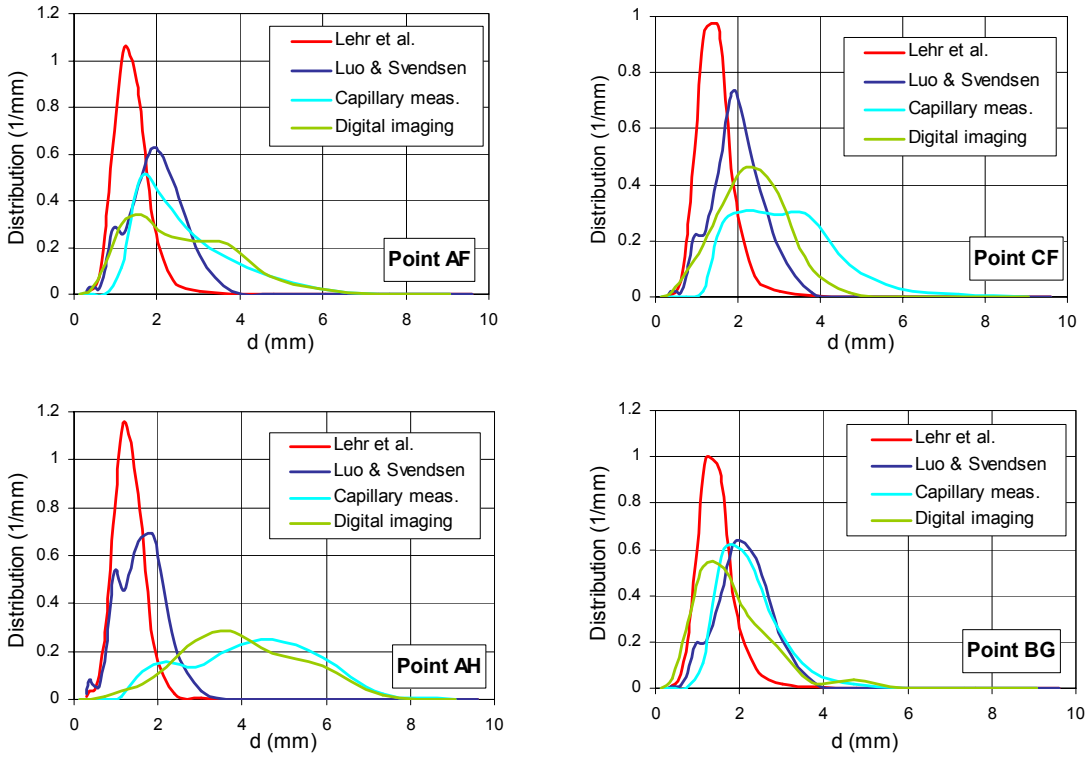

Figure 3.11. The volumetric distribution function of bubbles at four locations in the tank, cf. ref. Laakkonen et al. [30].

The results by model of Luo & Svendsen corresponded to the experimental results better than the results obtained by the model of Lehr et al. Both of the models yielded bubble size distributions which emphasize smaller bubbles more than the experimental results. In every measurement point shown in Figure 3.11, the model of Lehr et al. is found to predict even smaller bubbles than the model of Luo & Svendsen. The experimental result shows a wider bubble size distribution. In particular, the number of bubbles in the larger bubble classes was negligible in the simulation compared to the experimental results.

Compared to the experimental results, another shortage was that, the bubbles were not carried to the wall of the tank by the impeller stream, as seen in the results of the simulations in Figure 3.9. According to the experimental results, the bubbles hit the wall [30]. Several tests were carried out in order to be able to predict this behaviour: The correlation of Tomiyama for slightly contaminated liquids for calculating the terminal velocity of bubbles was tested. The simulation was carried out by Eulerian method instead of the mixture model. In addition, the realizable k-ε model of turbulence was applied. All tested model combinations yielded qualitatively the same results in this respect. The tests are reviewed in more details in the report of Manninen et al. [26].

3.4.3 Sensitivity analysis of the models

For validating breakup and coalescence models, few tests with different weighting of the source terms calculated by the models were carried out. In addition, the sensitivity of models to turbulence energy dissipation was separately analysed. For the coalescence model, the sensitivity test for volume fraction was carried out.

The behaviour of the models was tested by weighting the source terms for the bubbles calculated by the breakup and coalescence models. The effect of the weighting of the breakup source term calculated with the breakup models of Luo & Svendsen and Lehr et al. was quite different. With the model of Luo & Svendsen, the weighting of the source term with bigger coefficient seemed to shift the distribution towards the smaller bubbles. The maximum and the width of the distribution were quite similar. Respectively with the model of Lehr et al., the location of the maximum of the distribution was lowered by weighting the source term with a bigger coefficient. However, the distribution got quite narrow instead of having all sized bubbles and the maximum value of the distribution increased. The model of Lehr et al. seemed to restrict the breakage of the smaller bubbles. The small bubbles hardly broke up into smaller fragments and therefore the amount of these bubbles increased.

In calculating the source term of coalescence, the contact time for the two bubbles τ_{ij}, the initial film thickness h_0 and the critical film thickness h_f are poorly known. Thus, the coefficient was used for weighting the exponent including these terms in order to analyse the sensitivity of the model for the terms. The model did not seem to be sensitive to the terms.

The breakup model of Lehr et al. and the coalescence model of Prince & Blanch were further studied by testing the models in two cases with only one bubble size fed into the stirring tank. In the first case, the initial bubble diameter was 0.76 mm and in the second case 2.4 mm. The results showed that the coalescence model had only a slight effect on the bubble distribution: increasing the weighting coefficient by a factor of ten did not have a notable effect on the distribution. The conclusion of the analysis was that coalescence did not take place in any appreciable amount in the simulations and therefore the amount of larger bubbles was negligible.

The sensitivity of the breakup and coalescence the models for turbulent dissipation rate was studied by calculating analytically the population distribution with different energy dissipation rates. The values for turbulent energy dissipation rate were 0.25 m^2/s^3 and 10 m^2/s^3. The larger dissipation rate was met in the neighbour of the blender and the lower dissipation in some distance away from the blender. The overall dissipation rate was quite low in the stirring tank. The results are shown in Figure 3.12.

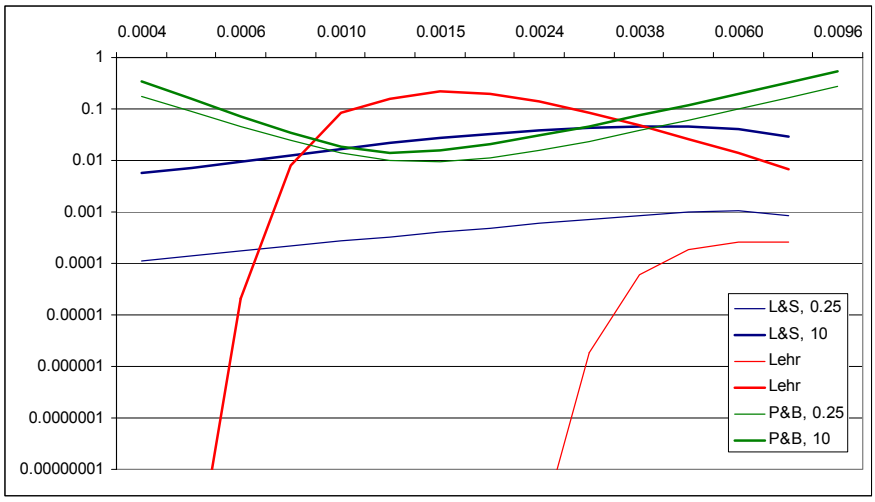

Figure 3.12. The rate of the bubbles breaking up into a fraction v_j calculated by the breakup model of Luo & Svendsen (blue lines) and by the model of Lehr et al. (red lines). Results are shown for dissipation rate 0.25 m^2/s^3 (narrow lines) and 10 m^2/s^3 (bold lines). In addition, the birth rate of the bubbles due to coalescence with dissipation rate 0.25 m^2/s^3 (narrow green line) and 10 m^2/s^3 (bold green line) are shown.

According to Figure 3.12, the model of Lehr et al. was more sensitive for the dissipation rate than the model of Luo & Svendsen. The model resulted in a greater amount of mid sized bubbles with the dissipation rate 10 m^2/s^3. While the dissipation rate decreases, the rate of breakage decreases. With the dissipation rate 0.25 m^2/s^3, the rate of breakages was significantly lower with the model of Lehr et al. The coalescence model was not as sensitive to the dissipation rate as the breakup models.

In addition, the sensitivity of the coalescence model to the amount of bubbles contained in the tank was studied. The sensitivity to the bubble volume fraction was much larger than to the dissipation rate. The magnitude of the calculated source term was increased by two orders of magnitude by tenfold increase of the volume fraction.

Therefore, the models studied for calculating the population distribution of bubbles in a stirring tank case were not applicable to the case. Sufficient dissipation rate for the breakup to take place occurred only in the neighbourhood of the agitator, according to the model of Lehr et al. In most parts of the tank, the dissipation rate was less than 0.25 m^2/s^3. Thus, the population distribution obtained by the model of Lehr et al. near the blender did not change further away from the blender. The model of Luo & Svendsen resulted in more small bubbles while the dissipation rate decreased. In addition, because the volume fraction of the bubbles in most regions inside the tank was less than 0.01%, coalescence did not occur in practice at all. Thus, the amount of large bubbles was significantly lower compared to the experimental results.

3.4.4 Conclusions

The breakup models of Luo & Svendsen, Hagesaether and Lehr et al. and the coalescence model of Prince & Blanch were studied in a case of a stirred tank. The calculated population distributions were compared to experimental results. However, the breakup model of Hagesaether was found to be computationally too intensive and was not implemented.

The breakup models of Luo & Svendsen, and Lehr et al. did not give good results when compared to the experimental results. The models produced distributions with smaller bubbles than found in the experiments. According to the location of the maximum of the size distribution, the model of Lehr et al., produced even smaller bubbles than the model of Luo & Svendsen. The shortage of the modelling was the absence of bigger bubbles, which may be a shortcoming of the coalescence model rather than the breakup models.

The sensitivity of the models to the dissipation rate was analysed in order to validate the applicability of the models to the stirring tank case. It turned out that sufficient dissipation rate for the breakup models was found only in the neighbourhood of the blender. In addition, since the volume fraction of the bubbles in most regions inside the tank was very small, the coalescence did not take place in practice at all. This explains the significantly lower amount of large bubbles when compared to the experimental results.

3.5 CFD modelling of flotation

In the flotation process, particles are attached to gas bubbles and the particle-bubble aggregates rise towards the liquid surface. The overall flotation process can be divided to a sequence of independent micro-processes. The sequence includes the approach of a particle to an air bubble, the subsequent interception of the particle by the bubble, the sliding of the particle along the surface of the thin liquid film that separates the particle from the bubble, film rupture, the subsequent formation of a three-phase contact between the bubble, particle and liquid, and the stabilization of the bubble-particle aggregate.

Based on experimental observations, the flotation separation process is considered equal to a chemical reactor and can be described by an ordinary differential equation [31]. The kinetic equation for micro-processes involved during particle-bubble collection is described by the rate of removal of the number of particles in a given volume as follows

$$\frac{dn_p^f(t)}{dt} = -k_1 n_p^f(t) + k_2 n_b^a(t), \tag{3.3}$$

where the kinetic rate constants are $k_1 = Z_{pb} P_c P_{asl} P_{stab} n_b^f(t)$ and $k_2 = Z'_{pb}(1 - P_{stab})$.

In Eq. (3.3), n_p^f and n_b^f are the number concentration of free particles and free bubbles, respectively, and n_b^a is the concentration of bubbles with attached particles. Z_{pb} is the particle-bubble collision frequency and Z'_{pb} is the detachment frequency of particles from bubbles. P_c is the probability of collision between the particle and bubble, P_a is the probability of attachment and P_{stab} is probability of stability of a bubble-particle aggregate.

3.5.1 The probability models for flotation subprosesses

The probabilities of the subprosesses of the flotation, i.e. collision, attachment and detachment can be treated independently, since the governing forces of the processes are independent having significant effect only on one of the processes. In the following, the models tested in a flotation cell are outlined. The models are presented in more detail by Ojaniemi et al. [32].

For the collision frequency, the general model of the case of negligible particle body forces used in modelling of flotation process was applied [33, 34]. In addition, the model developed further by Heindel et al. [35] was applied. In the model of Heindel et al., the particle settling velocity (v_{ps}) and the rise velocity of the bubbles (v_B) were included into the collision frequency.

The subprocess of bubble-particle collision has been studied most extensively. For the collision probability, the models of Yoon & Luttrell [36], Heindel et al. [35] and Nguyen [37] were applied.

The models of Yoon & Luttrell and Heindel et al., are based on the collision efficiency defined as a ratio of the real to ideal collision rate. Particles which approach a rising particle within a streaming tube limiting capture radius R_c can collide with a bubble. The probability P_c is computed to be the ratio of the number of particles which encounter a bubble per unit time to the number of particles which approach a bubble in a stream tube.

The model of Yoon & Luttrell is widely applied in flotation modeling. The model ignores the particle inertial forces and assumes a uniform distribution of collision over the entire upper half surface of the bubble. The model of Heindel et al. for P_c involves

effects of the particle settling velocity and the bubble rising velocity, but it is derived for the same case of the aft-and-fore symmetric intermediate flow delineated by Yoon & Luttrell. Therefore, both models assume the colliding area of particle to be the entire front hemisphere of the bubble. However, since the flow field around a bubble is established to be aft-and-fore asymmetric as the Reynolds number increases from zero, the colliding area of particle is smaller than that [38].

Nguyen has investigated the measure of the particle – bubble collision probability in a region of intermediate Reynolds number. The limitation of aft-and-fore asymmetric flow field in modelling the collision probability can be eliminated by determining the probability by the particle flux in the near proximity of the bubble surface instead of the collision rate. Thus, the collision probability according to Nguyen is determined by the particle and liquid velocity in the close proximity to the bubble surface.

The traditional models of collision efficiency, e.g. the model of Yoon & Luttrell, neglect the inertial effects of the particle and bubble collisions. The case is valid only for very small particles compared to the bubbles, i.e. the Stokes number approach zero. In addition, the bubble surface is assumed to be immobile in traditional models. However, in addition to the free and mobile bubbles, the front surface of the aged bubbles may be mobile. Therefore, the mobility of the bubble should be considered. In the model of Nguyen, the mobility of bubble surface is considered. For bubbles with an immobile surface, the asymmetry of the flow field around the bubble is stronger than with the mobile bubble.

For the attachment probability, the model of Nguyen [37] was applied. For defining the attachment efficiency, the critical angle of attachment θ_a has to be known. The angle θ_a can be determined by induction time t_i, which is the time required for the elementary steps involved in bubble-particle sliding interaction, e.g. thinning and rupture of the intervening liquid film, and the expansion of a three phase contact (solid-air-liquid). The attachment can occur, if the sliding time equals or exceeds induction time. Therefore, the critical attachment angle θ_a corresponds to a critical case of $t_s = t_i$.

In addition to the single bubble models, the models of Nguyen for the collision and attachment probabilities including the effect of gas holdup were tested.

The stability probability was delineated by the forces acting on the attached particle [39]. The attachment tenacity can be derived from the force balance. For stability of the aggregate, the tenacity has to be stronger than the detaching forces. The maximum floatable particle size can be determined by assuming the main mechanism of detachment of the particle in mechanical flotation cells to be turbulence.

The detachment of particles during the journey of the bubbles to the surface of the flotation cell was not included in the model. In an ideal system, the flotation is successful and the detachment of the particles does not occur.

3.5.2 Results of flotation simulation

The flotation process was simulated using the mixture model of Fluent 6.2.16. For the drag coefficient between water and particles, the model of Shiller & Naumann was used. The Ishii & Zuber [28] drag coefficient with slight modifications was used for the bubble and bubble-particle phases.

The simulation of flotation was calculated in a flotation cell having inner diameter 0.42 m and height 0.43 m. The rotor height was 0.108 m. The computational grid of a 60^{o} sector of the tank consisted about 94 000 cells. The speed of rotation used in modelling was 650 rpm. The gas inlet is located at the bottom of the shaft. The air bubble feed into the sector was 0.0004 kg/s, which corresponds to the air feed of 0.0024 kg/s into the whole tank. The diameter of the air bubbles was assumed to be 1 mm and the air density was 1.225 kg/m^3. The water density was 998.2 kg/m^3 and viscosity 0.001 Pa·s. The particle diameter was assumed to be 50 μm and the density of the particles was 2480 kg/m^3. At the beginning of the simulation, a 1% homogenous volume fraction of particles in water was set in tank.

The simulation of flotation was carried out using the population balance approach. The bubble-particle phases were classified into ten phases based on geometrical distribution. In each population class the number of particles attached on the bubble was two powered to the number of class, i.e. $N(bub_n) = 2^n$. For the bubble-particle phases, density was calculated by adding together the mass of the particles attached on the bubble and the mass of the air bubble, and dividing the sum by the combined volume of the bubble with particles. The viscosity of the mixture was assumed to be identical to the water viscosity.

A bubble-particle aggregate in phase n was shifted to phase n+1 after 2^n collisions, which is the difference in the number of the particles attached on the bubbles in the two phases. The implementation of the flotation models into Fluent is described in more detail in the report of Ojaniemi et al. [32].

In simulation of flotation, several model combinations from the probability models presented above were tested. With the model of Yoon & Luttrell for collision probability, the general collision frequency Z_{pb} was applied. With the collision models including the gravitational effects, the model of Heindel et al. for Z_{pb} was used. While comparing the collision probability models P_c, the probabilities for attachment P_a and

aggregate stability P_{stab} were assumed to equal one. From the calculation results, the amounts of free particles, removed particles and the total amount of particles in the tank were observed.

Both standard and realizable k-ε turbulence models were tested. The effect of the turbulence model was negligible to the flotation process. Therefore, the simulations were carried out mostly with the standard k-ε model.

Figure 3.13 shows the results for flotation with different probability models P_c as a function of time. The amount of free particles and the total amount of particles including free and attached particles are shown as percentages from the initial amount of particles. The amount of removed particles is obtained by subtracting the total amount of particles in the tank from the initial value. As seen in Figure 3.13 the removal of particles from the flotation cell is weakest with the model of Yoon & Luttrell. Thus, the gravitational effects included into the model of Heindel et al. seem to have significant influence on the flotation efficiency. In addition to the gravitational effects, the model of Nguyen included the mobility of the bubble surface. The results for flotation efficiency obtained by the model of Nguyen are close to the results obtained by the model of Heindel et al. Removal of half of the particles from the flotation cell took about 6.3 seconds with the model of Yoon & Luttrell. The respective time with the model of Heindel et al. was 3.8 seconds and with the model of Nguyen et al. 3.3 seconds.

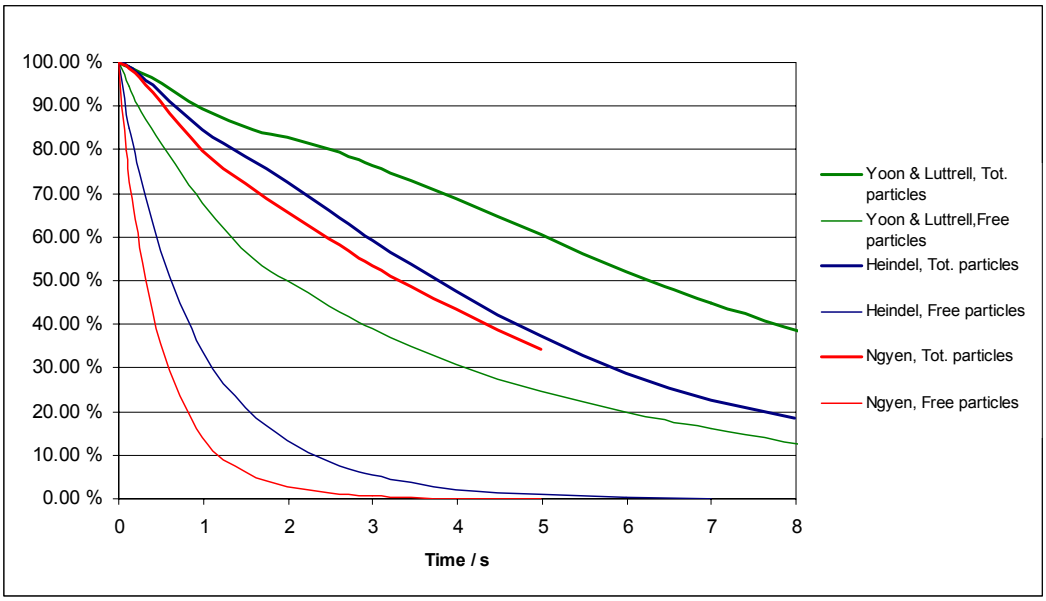

Figure 3.13. Amount of free particles (narrow lines) and total amount of particles (both fixed and free, bold lines), inside the flotation cell as a function of time, simulated by collision probability models of Yoon & Luttrell (green), Heindel et al. (blue) and Nguyen (red). The amount of particles is shown as percentages from the initial value of particles inside the tank.

The difference in flotation efficiency between the models is described by the rate of particle adherence on the bubbles. According to Figure 3.13, the model of Yoon & Luttrell predicts that after about 2 seconds 50% of the particles were adhered on the bubbles or removed from the suspension. With the model of Heindel et al., the time needed was about 0.64 seconds and with the model of Nguyen, only 0.34 seconds was needed.

In Figure 3.14, the distribution of free particles in the flotation cell are shown at time 2s for the results with collision probability models Yoon & Luttrell, Heindel et al. and Nguyen. At this time, the percentage of the particles left in the flotation cell was 50% for the Yoon & Luttrell model, 13% for the Heindel et al. model, and only 2.8% for the Nguyen model.

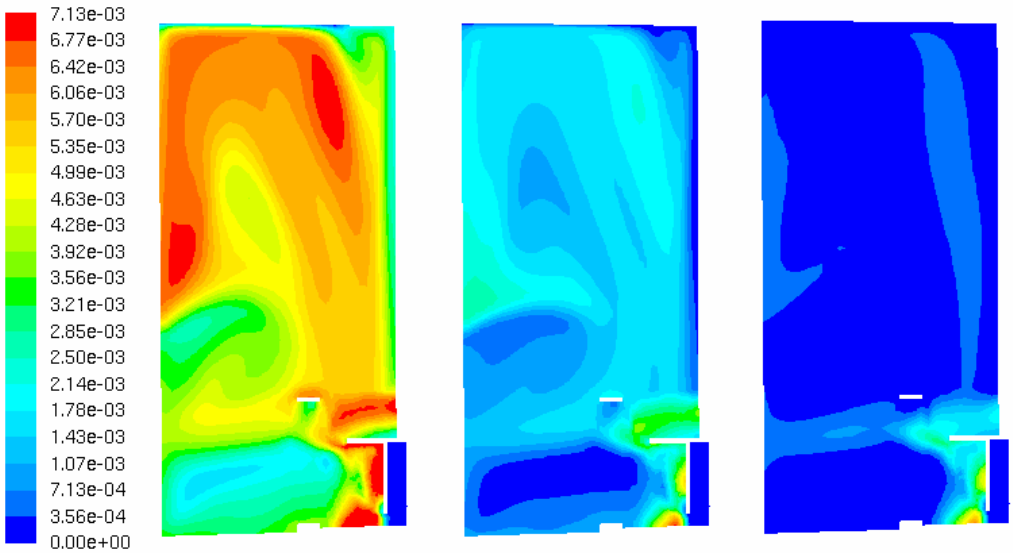

Figure 3.14. The instant particle distribution at time 2 s. Left: the collision model of Yoon & Luttrell; middle: model of Heindel et al.; right: model of Nguyen.

The flotation simulation with the models of Nguyen was further tested by including the probability models for aggregate stability and attachment. In addition, the effect of the bubble swarm (the gas hold up) on the flotation efficiency was tested. Figure 3.15 shows the results for the total amount of particles and the amount of free particles in the flotation cell as a function of time.

In Figure 3.15, the results are shown for the case of single bubble with (green lines) and without (red lines) applying the stability probability model. In addition, the results are shown for the case of stability and bubble swarm effect included (yellow lines) and for the case of stability and attachment probability included (blue lines). Figure 3.15 shows that the difference in the total amount of particles inside the tank between the models is

negligible. However, the models had some differences in the rate of particle adherence on the bubbles.

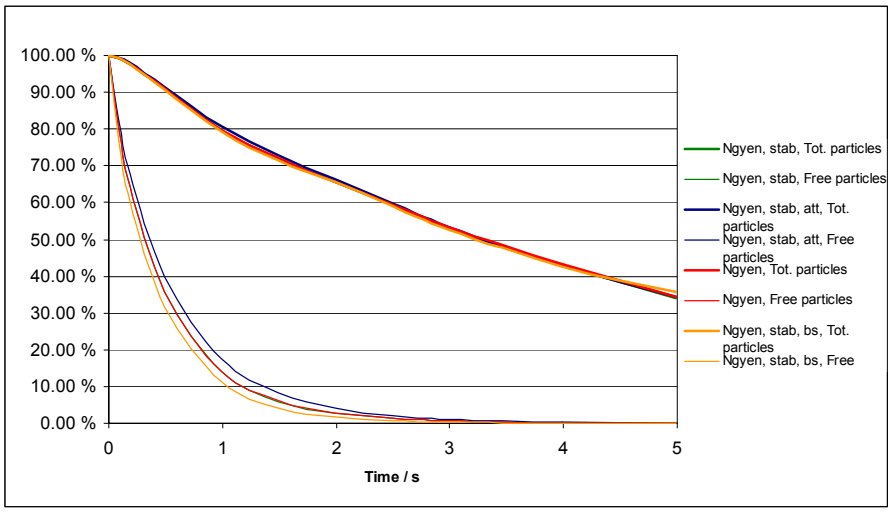

Figure 3.15. Amount of free particles (narrow lines) and total amount of particles (both fixed and free, bold lines), inside the flotation cell as a function of time simulated by several model combinations. The amount of particles is shown as percentages from the initial value of particles inside the tank.

Including the probability model for aggregate stability did not affect the flotation efficiency. In Figure 3.15, the lines describing the results for including the stability model (green lines) and neglecting the model (red lines) were overlapping. In these cases, the attachment probability was set equal to one and the results were compared to the results obtained with the attachment probability model. The time needed for encountering or removing a half of the particles from the solution was 0.38 seconds with the attachment probability model, which was 12.5% more than with the assumption of attachment probability equal to one. Thus, the effect of the attachment probability model on the flotation efficiency was insignificant in the studied case. The induction time for attachment was set to be 0.002 s in the model. A longer induction time would increase the significance of the attachment probability model and cause a stronger decrease in the flotation efficiency.

With the model of bubble swarm effect, the time needed for encountering or removing 50% of the particles from the solution was 0.30 seconds. The time was 12.6% less than the respective time with the single bubble model.

The instant distribution of particles at time 0.5 s obtained with the Nguyen models is shown in Figure 3.16. The amount of free particles was somewhat greater with the attachment probability model and a little lower with the bubble swarm effect included

when the results are compared to the case of single bubble with the assumption of attachment probability equal to one.

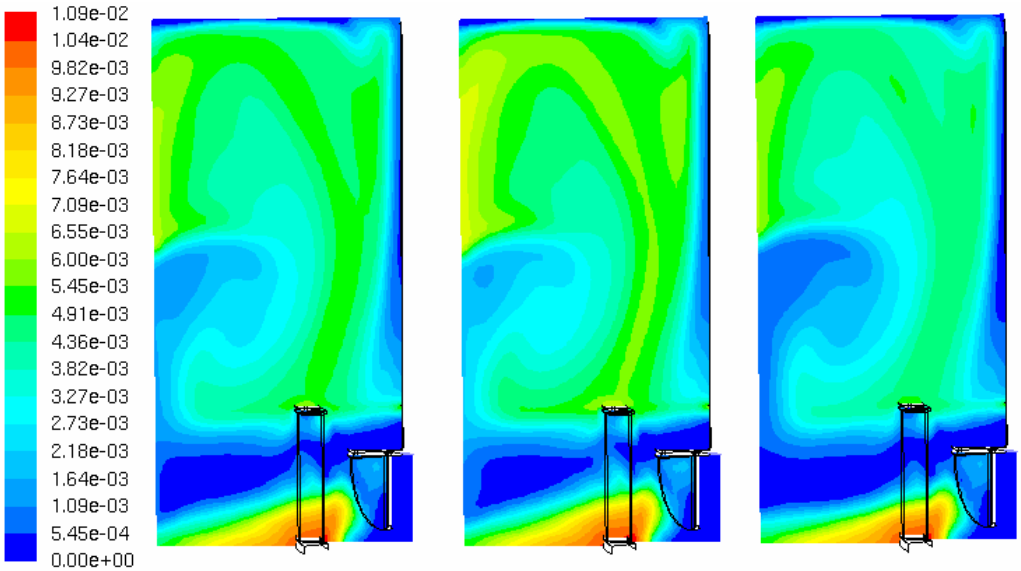

Figure 3.16. The instant particle distribution at time 0.5s. Left: the collision probability model of Nguyen for single bubble; middle: model of attachment probability included; right: the collision probability model of Nguyen for bubble swarm. The probability model for aggregate stability is included.

3.5.3 Conclusions

The flotation process in modelling has been generally assumed to consist of sequence of subprocesses, i.e. collision, attachment and particle-bubble aggregate stability, with associated probability measures. In this study, we applied the models presented in a literature for the probabilities of the subprocesses. Several model combinations were tested in order to compare the effect of the probability model on the flotation efficiency. In addition, the models of standard and realizable k-ε models were tested for modelling the turbulence. The applied turbulence model did not have significant effect on the flotation efficiency. The adherence of the particles on the bubbles and removal from the suspension was obtained as a function of time.

The models of Yoon & Luttrell, Heindel et al. and Nguyen were applied for the collision probability. The model of Yoon & Luttrell is a widely applied model. The model of Heindel et al. is based on the same assumptions as the model of Yoon & Luttrell, but includes the gravitational effects. Both of these simple models have some shortcomings. The model of Nguyen is more general, but at the same time more complex.

At first, the collision probability models were studied assuming the attachment and stability probabilities equal to one. The flotation efficiency with the model of Yoon & Luttrel was worse than with the other models, which included the gravitational effects. The difference between the models of Heindel et al. and Nguyen with mobile bubble surface was not large.

For the attachment probability, the model of Nguyen was applied, and the bubble swarm effect was included. The results were compared to the results calculated by single bubble and the attachment probability set to equal to one. The effects were not significant on the total flotation efficiency, but some differences were found in the particle adherence on the bubble. Including the attachment model decreased the adhering efficiency by 12.5%, if the induction time was set to 0.002 s. Including the bubble swarm effect increased the adherence efficiency by 12.6%. In addition, the model of aggregate stability probability delineated by the method of Nguyen was applied. In the test case with 50 μm particles, the model seemed not to have effect on the flotation efficiency.

References

1. Laakkonen, M., Moilanen, P., Alopaeus, V. & Aittamaa, J. Modelling local bubble size distributions in agitated vessels. Manuscript submitted to Chemical Engineering Science.

2. Laakkonen, M., Moilanen, P., Alopaeus, V. & Aittamaa, J. Modelling local gas-liquid mass transfer in agitated vessels. Manuscript submitted to 12th European Conference on Mixing.

3. Laakkonen, M., Moilanen, P., Alopaeus, V. & Aittamaa J. Dynamic modeling of local reaction conditions in an agitated aerobic fermenter. Manuscript accepted to AIChE Journal.

4. Prince, M. J. & Blanch, H. W. 1990. Bubble Coalescence and Breakup in Air-Sparged Bubble Columns. AIChE J., Vol. 36, No. 10, 1485–1499.

5. Colella, D., Vinci, D., Bagatin, R., Masi, M. & Abu Bakr, E. 1999. A Study on Coalescence and Breakage Mechanisms in Three Different Bubble Columns. Chem. Eng. Sci., 54, 4767–4777.

6. Lehr, F., Millies, M. & Mewes, D. 2002. Bubble-size distributions and flow fields in bubble columns. A.I.Ch.E. J., 48, 2426–2443.

7. Laari, A. & Turunen, I. 2003. Experimental Determination of Bubble Break-up and Coalescence Rates in a Bubble Column Reactor. The Canadian Journal of Chemical Engineering, 84 (3–4), 395–401.

8. Laari, A. & Turunen, I. 2005. Prediction of coalescence properties of gas bubbles in a gas-liquid reactor using persistence time measurements. Chem. Eng. Res. Des., 83, 881–886.

9. Ghosh, P. 2002. Analysis of the drop rest phenomenon. Chem. Eng. Res. Des., 80, 715–728.

10. Ghosh, P. 2004. Coalescence of air bubbles at air-water interface. Chem. Eng. Res. Des., 82(A7), 849–854.

11. Hagesaether, L., Jakobsen, H. A. & Svendsen, H. F. 2002. A Model for Turbulent Binary Breakup of Dispersed Fluid Particles. Chem. Eng. Sci., 57, 3251–3267.

12. Sha, Z., Laari, A. & Turunen, I. 2003. Identification of the Coalescence and Breakage Parameters of The MUSIG model in CFD Simulation with Experimental Data. 4th European Congress of Chemical Engineering, Granada, 21–25 September, 2003.

13. Sha, Z., Laari, A. & Turunen, I. 2004. Implementation of Population Balance in a Multiphase Model in the CFD Simulation of a Bubble Column. CHISA 2004, 16th international congress of Chemical and Process engineering, 22–26 August 2004, Praha, Czech Republic, E3.2.

14. Sha, Z., Zhou, H., Laari, A. & Turunen, I. 2006. CFD study on the influence of bubble size distribution on the flow hydrodynamics in bubble column. Submitted to CHISA 2006, 17th international congress of Chemical and Process engineering, 27–31 August 2006, Praha, Czech Republic.

15. Laari, A., Turunen, I. & Sha, Z. 2006. A study of flow hydrodynamics in bubble column using Particle Image Velocimetry (PIV). Submitted to CHISA 2006, 17th international congress of Chemical and Process engineering, 27–31 August 2006, Praha, Czech Republic.

16. Smolianski, A., Haario, H. & Luukka, P. 2003. Numerical Bubble Dynamics. Proceedings of the European Symposium on Computer Aided Process Engineering – 13, Elsevier, 2003, pp. 941–946.

17. Haario, H., Smolianski, A. & Luukka, P. 2005. Vortex shedding behind a rising bubble and two-bubble coalescence: a numerical approach. Appl.Math.Modelling, Vol. 29, Issue 7, 615–632.

18. Haario, H., Laari, A., Luukka, P., Smolianski, A. & Turunen, I. 2004. Computational modelling of complex bubble interaction. Research Report 85. ISBN 951-764-886-3. Lappeenranta University of Technology, Finland.

19. Haario, H. Smolianski, A. & Luukka, P. Numerical study of dynamics of single bubbles and bubble swarms. In press.

20. Clift, R., Grace, J. R. & Weber, M. E. 1978. Bubbles, Drops, and Particles. Academic Press, London.

21. Manninen, M., Taivassalo, V. & Kallio, S. 1996. On the mixture model for multiphase flow. VTT Publications 288. VTT, Espoo.

22. Luo, H. & Svendsen, H. F. 1996. Theoretical model for drop and bubble breakup in turbulent dispersions. AIChE J., Vol. 42, No. 5, 1225–1233.

23. Hagesaether, L. 2002. Coalescence and Breakup of Drops and Bubbles. Ph. D. Thesis, Norwegian University of Sience and Technology, Trondheim.

24. Hagesaether, L., Jakobsen, H. A. & Svendsen, H. F. 2002. Modeling of Dispersed Phase Size Distribution in Bubble Columns. Ind. Eng. Chem. Res., Vol. 41, 2560–2570.

25. Wang, T., Wang, J. & Yong, J. 2003. A novel theoretical breakup kernel function for bubbles/droplets in a turbulent flow. Chem. Eng. Sci., Vol. 58, 4629–4637.

26. Manninen, M. & Ojaniemi, U. 2006. Population models for bubbly flow in a stirred reactor. Report VTT-R-02997-06. VTT, Espoo.

27. Aittamaa, J., Laakkonen, M. & Moilanen, P. 2005. Modelling and measurement of gas-liquid mass transfer. In: Multiphase flows and industry (MANDI). Final report. Ed. Manninen, M. Project report PRO5/P5006/05. VTT, Espoo.

28. Ishii, M. & Zuber, N. 1979. Drag Coefficient and Relative Velocity in Bubbly. Droplet of Particulate Flows. AIChE J., Vol. 25, No. 5, 843–855.

29. Manninen, M., Ojaniemi, U., Taivassalo, V. & Liiri, M. 2005. Multiphase models in process simulation. In Multiphase flows and industry (MANDI). Final report. Ed. Manninen, M. Project report PRO5/P5006/05. VTT, Espoo.

30. Laakkonen, M., Moilanen, P. & Aittamaa, J. 2005. Local bubble size distributions in agitated vessels. Chem. Eng. J., Vol. 106, 133–143.

31. Bloom, F. & Heindel, T. J. 2003. Modeling Flotation Separation in a Semi-batch Process. Chem. Eng. Sci., 58, 353–365.

32. Ojaniemi, U. & Manninen, M. 2006. Three phase CFD modelling of flotation. Report VTT-R-02999-06. VTT, Espoo.

33. Bloom, F. & Heindel, T. J. 2002. On the Structure of Collision and Detachment Frequencies in Flotation Models. Chem. Eng. Sci., 57, 2467–2473.

34. Koh, P. T. L. & Schwartz, M. P. 2003. CFD Modeling of Bubble-Particle Collision Rates and Efficiencies in a Flotation Cell. Minerals Engineering, 16, 1055–1059.

35. Heindel, T. J. & Bloom, F. 1999. Exact and Approximate Expressions for Bubble-Particle Collision. Journal of Colloid and Interface Science, 213, 101–111.

36. Yoon, R. H. & Luttrell, G. H. 1998. The Effect of the Bubble Size on Fine Particle Flotation. Min. Process. Extractive Metall. Rev. 5, 101–122.

37. Nguyen, A. V. 1999. Hydrodynamics of Liquid Flows around Air Bubbles in Flotation: A Review. Int. J. Mineral Processing, 56, 165–205.

38. Phan, C. M., Nguyen, A. V., Miller, J. D., Evans, G. M. & Jaemeson, G. J. 2003. Investigations of Bubble-Particle Interactions. Int. J. Mineral Processing, 72, 239–254.

39. Nguyen, A. V. 2003. New Method and Equations for Determining Attachment Tenacity and particle Size Limit in Flotation. Int. J. Mineral Processing, 68, 167–182.

4. CFD model development in trickling and pulsing flow in solid/liquid/gas systems

Katja Hynynen[1], Ville Alopaeus[1], Juhani Aittamaa[1] and Mikko Manninen[2]

4.1 Introduction

The scope of the project was to develop an efficient CFD model for trickling and pulsing flow through a trickle-bed reactor. Models should properly take into account phase interactions between the three phases present: gas, liquid and solid of which the last one is stationary. The aim was to produce efficient tools for design and optimization of trickle-bed reactors as well as to understand the local phenomena taking place in the reactor, based on which the models were developed. In practice this was done by performing experiments consistent with simulations which were then used to verify the models. For this, an experimental setup, which would yield proper information, was designed and built in the first half of the project. Development of the experimental setup was continued throughout the project and its utilization will continue in the follow-up project. To gain information about the existing models in the literature a comprehensive literature study was performed, whilst designing and building the experimental setup. This provided the grounds for the model development and simulations in general.

4.2 Experimental setup

Even though there exists a relatively wide database of experiments conducted in a laboratory scale trickle-bed reactors, data concerning liquid distribution in two-phase flow is not very common. Also, at the early stage, most of the experiments were done in columns with such a small diameter that the wall effect has been quite significant. In the studies, which have combined CFD simulations and experiments, a large enough column diameter has normally been used to justify the ignoring of this phenomenon. However, when using a column barely exceeding the large enough D/d_p ratio, the arguable insignificant effect of the wall is still transferred to the model. When this model is then used to model reactors that are 10 to 20 times larger than laboratory scale reactors, the error might not be so insignificant after all.

[1] Helsinki University of Technology, Chemical Engineering and Plant Design
[2] VTT

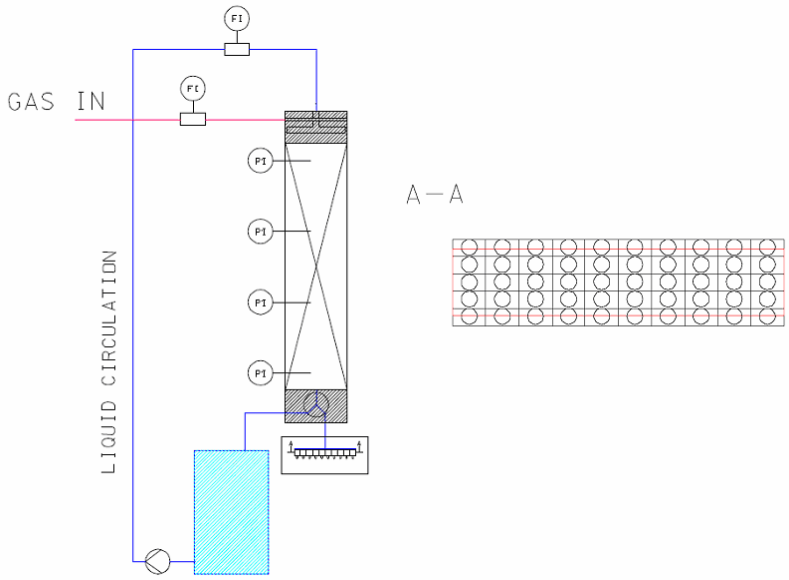

Figure 4.1. General description of the experimental setup and the liquid collector design: Gas and liquid are fed to the top of the catalyst bed through separate distributors of which the liquid distributor is changeable. Gas exits the setup along with the liquid phase. Liquid flow can be led either to the circulation tank or to flow through the liquid collector device. The height of the bed is alterable from (0.25 to 2.0) m. The bed height of 1.0 m, containing four pressure sensors along the bed height, was used throughout the current project.

The key characteristics of the experimental setup are described below and the general description of the setup is presented in Figure 4.1. Photographs of the experimental setup are shown in Figure 4.2.

- Instead of using a circular column the experimental column was designed to have a rectangular cross sectional area (25 cm x 5 cm). This would allow conjoining of two significant dimensions in one setup: wide and narrow dimension of which in the first one the wall effect is insignificant and in the last one it is not.
- Besides the pressure gradient and liquid holdup measurements the experimental setup was equipped with a specific liquid collector, which allows the measuring of the liquid distribution at the end of the reactor. This yields information of the wall flow at the narrow dimension and of the liquid horizontal distribution at the wide dimension. An advantage of the use of a liquid collector instead of a tracer experiments is that it gives information purely on the mechanical dispersion of liquid without the disturbance of the molecular diffusion.
- Related to the liquid horizontal distribution in the wide dimension of the bed, the liquid distributor was designed to be changeable. During the project, two different distributors were used: uniform and central (Figure 4.3)

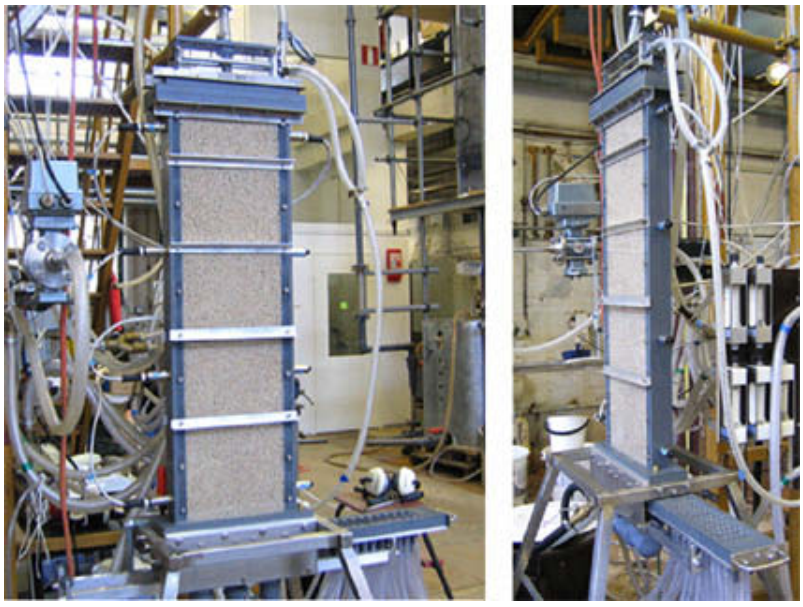

Figure 4.2. Experimental setup that was designed and built during the project.

The experimental setup was primarily designed for two phase flow, but it is also suitable for one phase pressure drop measurements. This is important as the Ergun parameters (E_μ, E_ρ), which are central in one and two phase flow modelling, are bed specific. Even though, especially for spherical particles, there are a lot of reported measurements, the unconventional shape of our experimental setup encouraged to determine the values of the parameters for the experimental setup. Also the shape of the particles varied somewhat.

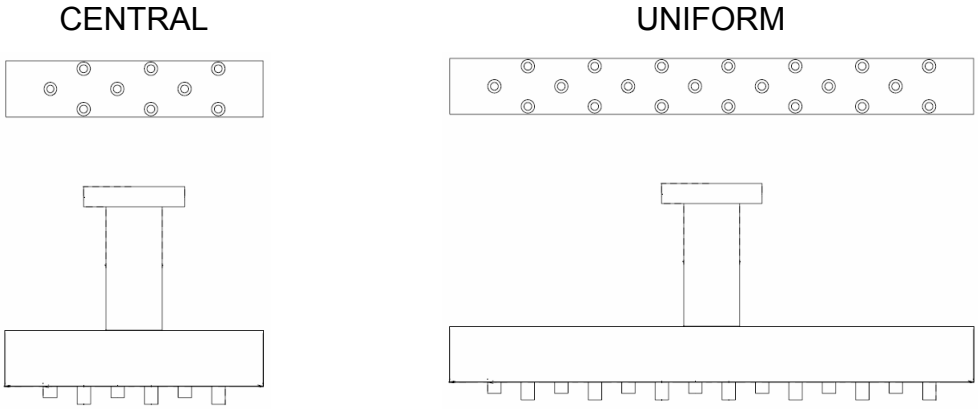

Figure 4.3. Liquid distributor designs. The uniform distributor distributes liquid evenly along the whole cross-sectional area of the bed, and the central distributor covers 1/3 of the central section of the wide dimension.

The summary of the variables in the experiments, which are also the starting values in the simulations:

- mass flow for gas and liquid feed flows
- bed length (0.25–1.0) m, packing material and porosity
    - glass spheres (d_p ~ 4 mm) [particles A]
    - glass spheres (d_p ~ 2 mm) [particles B]
    - alumosilicate spheres (d_p ~ 5 mm) [particles C]
- liquid distribution: uniform/central (Figure 4.3).

Summary of the measurements, which are used to validate the simulation models:

- pressure sensors
    - determination of the pressure gradient at the catalyst bed
- liquid collector
    - information about the wall flow and horizontal distribution of the liquid flow
    - liquid dynamic holdup measurements[3]

4.3 Experiments

4.3.1 One phase experiments

Ergun parameters are somewhat dependent of particle characteristics (such as size and shape) as well as their orientation in the catalyst bed. This makes them bed specific and they are quite often determined for each packed bed in question. The determination of the parameters can be done from measurements of one phase pressure drop. This is easiest done with gas as a flowing fluid. The experimental results are presented in Table 4.1 and Figure 4.4. For comparison Figure 4.4 also presents the pressure drop calculated using the original Ergun parameters (E_μ = 150, E_ρ = 1.75), which have been determined also with spherical particles. They clearly over estimate the pressure drop for all three particles. Reasons can be sought from the irregular shape of the particles used in the experiments as well as from the unconventional shape of the experimental setup – the rectangular cross sectional area allows more even settling of the particles than they would in a small diameter round column, in which the original Ergun experiments were conducted. The more even organization of the particles was also seen in notably small

[3] During the current project a correlation was used to estimate the static holdup which is needed to determine the total holdup of the liquid phase (= dynamic holdup + static holdup). However, at the end of the project measurements of the static holdup was performed for particles A and they will be continued to cover also the rest of the particles.

values of bed porosity. The determined Ergun parameters were used later on as empty bed Ergun values for two phase flow simulation with CFD.

Table 4.1. The fitted Ergun parameters for particles A, B and C.

	E_μ	E_ρ
Particles A (glass spheres, $d_p \sim 4$ mm)	167	1.02
Particles B (glass spheres, $d_p \sim 2$ mm)	116	0.90
Particles C (alumosilicate spheres, $d_p \sim 5$ mm)	167	0.86

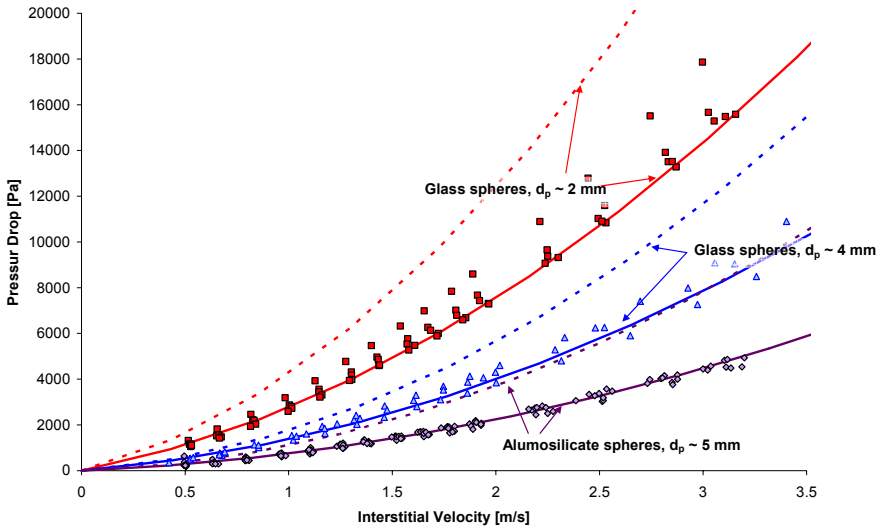

Figure 4.4. Measured one phase pressure drop for particles A (glass spheres; dp ~ 4 mm), particles B (glass spheres; dp ~ 2 mm), and particles C (alumosilicate spheres; dp ~ 4 mm). The solid line illustrates the pressure drop calculated with the bed and particle specific Ergun parameters from Table 4.1 and the dotted lines illustrates the pressure drop calculated with the original Ergun parameters (Eμ = 150, Eρ = 1.75).

4.3.2 Two phase experiments

Prewetting of the catalyst bed is an important factor when performing experiments. Three methods were examined, which all resulted in quite different flow textures. The three methods were the following:

- No prewetting.
- **Levec**-prewetting
  Prewetting is done by simply flooding and entraining the bed before the beginning of the experiment.
- **Kan**-prewetting
  Prewetting is done by first operating the experimental setup in the high interaction, pulsing regime after which the flow rates are decreased to the wanted values.

In the two first ones flow is closer to channel flow than to film flow. Even though the wall phenomenon is present with all methods, the flow texture is clearly more uniform in nature with Kan-prewetting method (Figure 4.5).

It is quite interesting to notice that from the two actual prewetting methods it appears that prewetting of the bed by merely flooding enhances the wall flow.

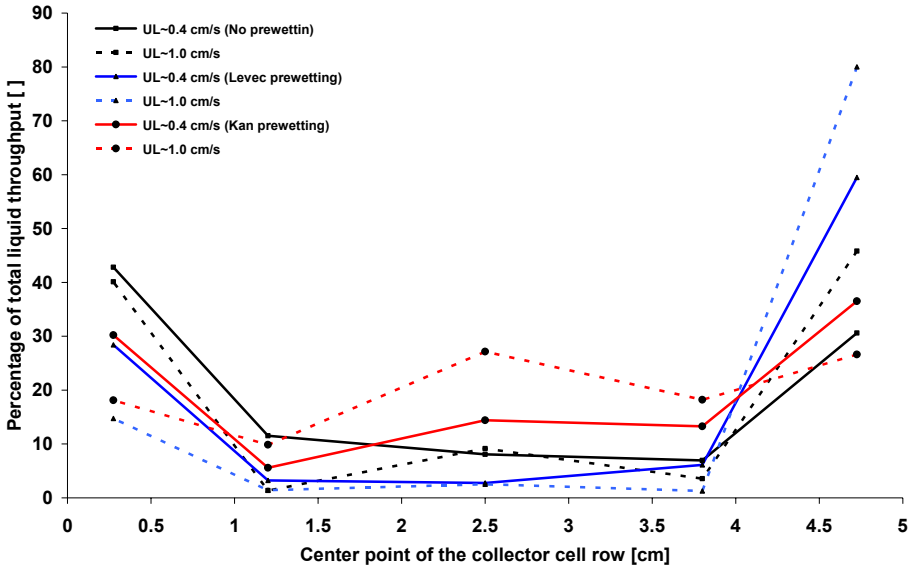

Figure 4.5. Comparison of the wall flow with different prewetting methods using a gas flow rate of: u_G ~ 0.36 m/s and two liquid flow rates: u_L ~ [0.4, 0.1] cm/s.

During the project two phase experiments were performed using the Levec prewetting method and experiments with the Kan prewetting method were started, but not yet completed. While developing the equipment and the experimental setup, measurements were performed mainly with glass spheres (d_p ~ 4 mm) as they were easiest to handle and thus most experiments were done with them. All two phase measurements available are presented in Table 4.2.

Table 4.2. Two phase data measured during the project.

	Gas flow rate [m/s]	Liquid flow rates [cm/s]	Liquid distributor	Pressure data	Prewetting methods
Particles A	0	0.4, 0.7, 1.0	Uniform	No	No prewetting
	0.08	0.4, 0.7, 1.0	Uniform, Central	Yes	Levec
	0.13	0.4, 0.7, 1.0	Uniform, Central	No	No prewetting, Levec
	0.21	0.4, 0.7, 1.0	Uniform, Central	Yes	No prewetting, Levec
	0.36	0.4, 0.7, 1.0	Uniform, Central	No	No prewetting, Levec, Kan
Particles B	0.08	0.4, 0.7, 1.0	Uniform,	Yes	Levec
	0.21	0.4, 0.7, 1.0	Uniform,	Yes	Levec
Particles C	0.08	0.4, 0.7, 1.0	Uniform, Central	Yes	Levec
	0.21	0.4, 0.7, 1.0	Uniform, Central	Yes	Levec

For each experiment performed with a certain gas and liquid flow rate, packing and liquid distributor the liquid distribution and holdup were determined using the liquid collector setup. Pressure was recorded in four positions of the bed. For particles A and C experiments were performed with both distributors, but for particles B, due to insufficient time, only uniform distributor was used.

Experiments with central distributor yielded information about horizontal dispersion of the liquid phase. Figure 4.6 demonstrates horizontal distribution using particles A and C with all data available. Levec prewetting was used in all the experiments. It can be noted that the horizontal dispersion is more pronounced with porous, alumosilicate spheres. Particles are of the same shape and thus the possible contributing factors are the size and material. Since horizontal dispersion due to the size of the particle should be stronger with smaller particles, the packing material (porosity, roughness, liquid-solid contact angle) has to have a significant influence on the liquid dispersion.

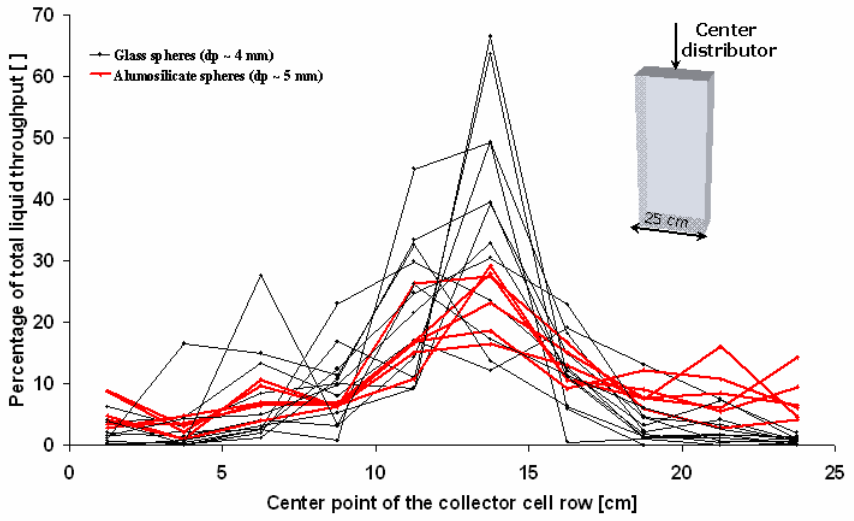

Figure 4.6. Horizontal distribution of the liquid at the bed outlet using the center distributor with particles A and C. Varying gas and liquid flow rates were used.

Same effect of particle material can also be seen in Figure 4.7, which demonstrates the wall effect in the experimental column. In the narrow dimension of the bed the column width to particle diameter ratio is smaller with alumosilicate spheres in comparison with either of the glass spheres and thus the wall flow should also be most severe accordingly. For both particles A and C the ratio is small enough to implicate significant wall flow in the narrow dimension of the bed. With alumosilicate spheres (particles C) the flow texture is, however, more uniform also in the narrow dimension of the bed. It can also be noted for glass spheres (particles A) that as the liquid flow increases the flow texture doesn't become more uniform, but instead more channels are form. In this case the liquid forms another channel to the center of the bed. This is in accordance with the prewetting method used as increased liquid flow in non-prewetted bed should result in spreading of the existing channels, but in case of Levec-prewetting it should result in formation of new channels.

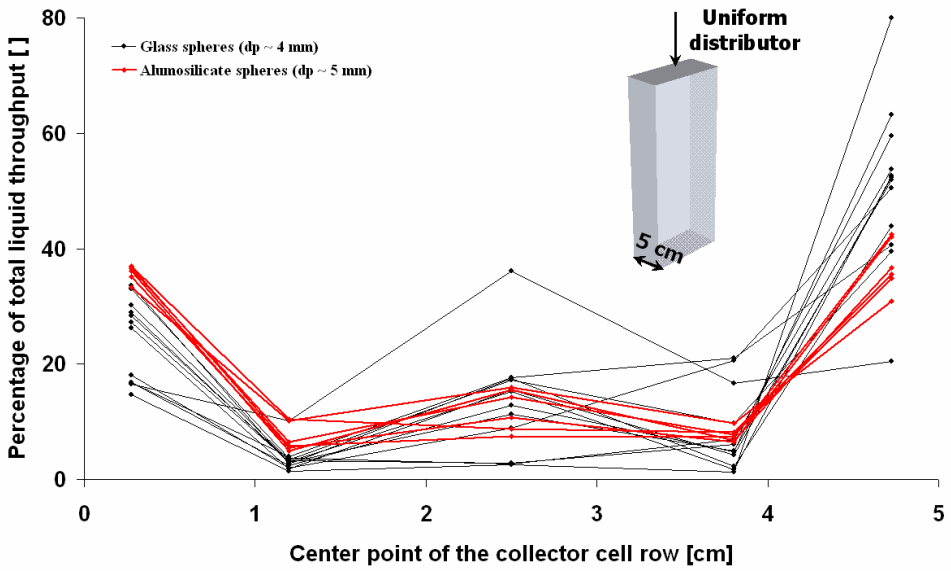

Figure 4.7. Investigation of the wall effect using the uniform distributor with particles A and C. Varying gas and liquid flow rates were used.

4.4 Modeling

Modelling activities within the current project can be roughly categorized as follows:

- Computational fluid dynamics approach (CFD) embedded with necessary effective interaction models and solving the Navier-Stokes equations numerically.
- Analytical solution of simplified form of momentum balance equations and above mentioned interaction models.
- Cellular interaction models, which has been developed in the scope of this project, that are structurally comparable but simple than Lattice-Boltzmann model.

4.4.1 CFD modelling

Various closure models, developed to close the conservation equations for two phase flow through packed bed, can be found from the literature. They are all conceptually quite close to one another. All are based on the one phase Ergun equation which is then modified to account for the presence of the second phase. During the current project these models and their basis were evaluated after which some of them were implemented in to the CFD program and tested and evaluated more thoroughly.

Validation of the CFD models has been traditionally based on comparison of global hydrodynamic parameters such as the pressure gradient and the liquid holdup to

experimental data. In addition, basically all modelling in the field has been two dimensional. In the current project, however, a three dimensional grid was used to take into consideration both key dimensions of our experimental setup; the wide dimension (25 cm) in which the wall effect is not significant and the narrow dimension (5 cm) in which the wall effect plays an important role. Also the liquid distribution at the end of the packed bed was used to estimate the validity of the models. Another specialty was that, instead of modelling the feed as a uniform mixture of gas and liquid corresponding to the actual feed flow rates, the feed was modelled as point inlets to correspond the actual design of the distributor. Based on these comparisons the current models proved to be insufficient in many aspects and further development of these models was found to be essential.

In the experiments the wall effect played quite significant part in the narrow dimension of the bed. This naturally affects the resistance caused by the bed as the porosity at the wall region is notably higher and hence it affects the pressure drop. The CFD model failed to bring out this effect in the narrow dimension even though a porosity distribution was used to account for the more porous region of the bed near the wall. The CFD was also unable to disclose the channelled nature of the flow, which was not even anticipated as the model currently lacks the surface forces causing the phenomena. As a result, however, the pressure drop was severely underestimated with uniform liquid distributor. The situation was somewhat better for central distributor, in which the liquid load is greater in central region when compared to the uniform feed causing more evenly wetted region between the walls (Figure 4.8). This emphasizes the importance of obtaining an even flow field when the experimental results are used to validate CFD models. The parity plot for measured and modelled pressure drops is presented in Figure 4.9.

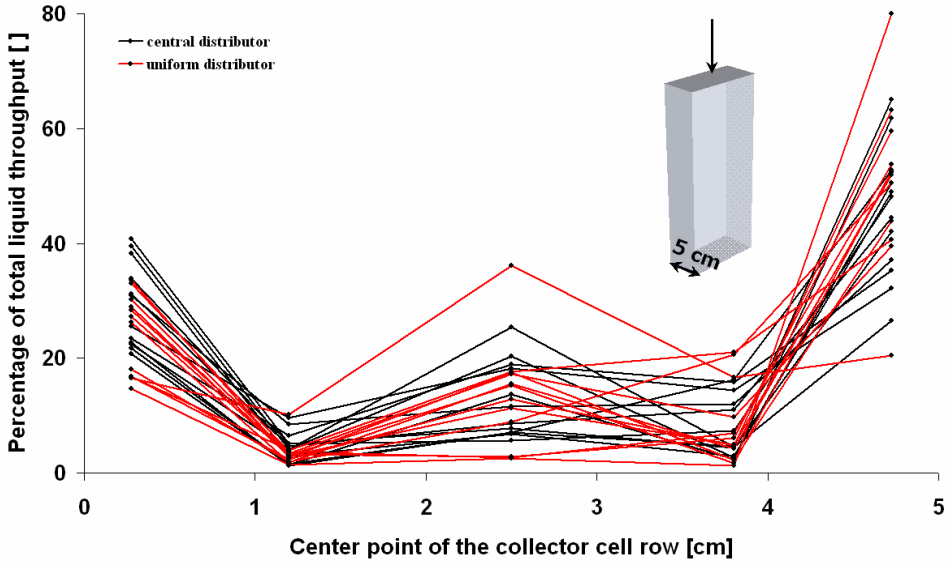

Figure 4.8. Comparison of the wall effect with central and uniform distributor.

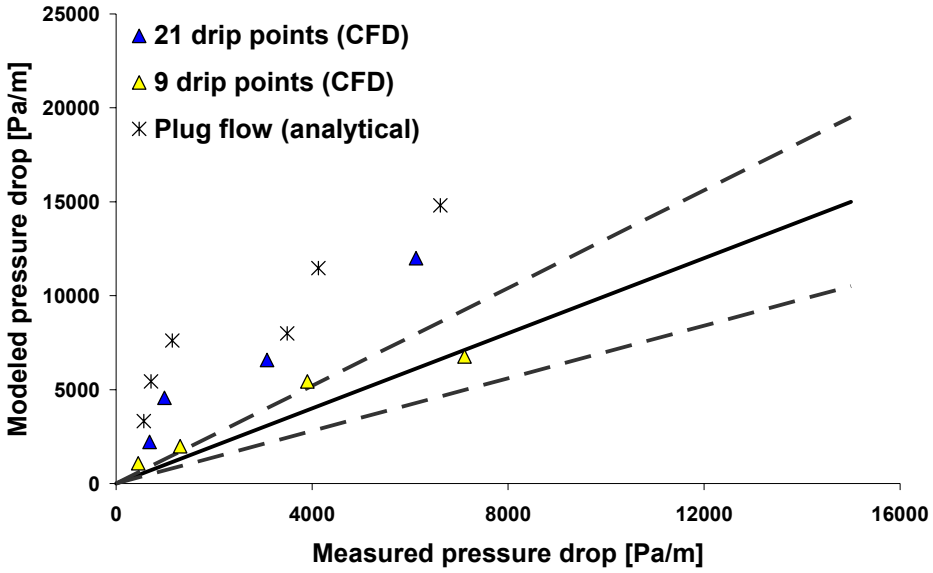

Figure 4.9. Parity plot of measured and simulated pressure drop.

The parity plot of the measured and modelled total liquid holdups is presented in Figure 4.10. Here a better fit is obtained with uniform distributor. This is caused by the flaws in the model used, which caused static liquid appear in areas of the grid were liquid shouldn't practically appear at all. This will naturally become more apparent when simulating the central distributor as the extent of the liquid free area is greater. Thus the discrepancy between the simulations and the experiments, caused by the deficiencies of

the model, becomes quantitatively more significant. Modifications to the CFD model (explained in more detail in the following section) improved this flaw notably.

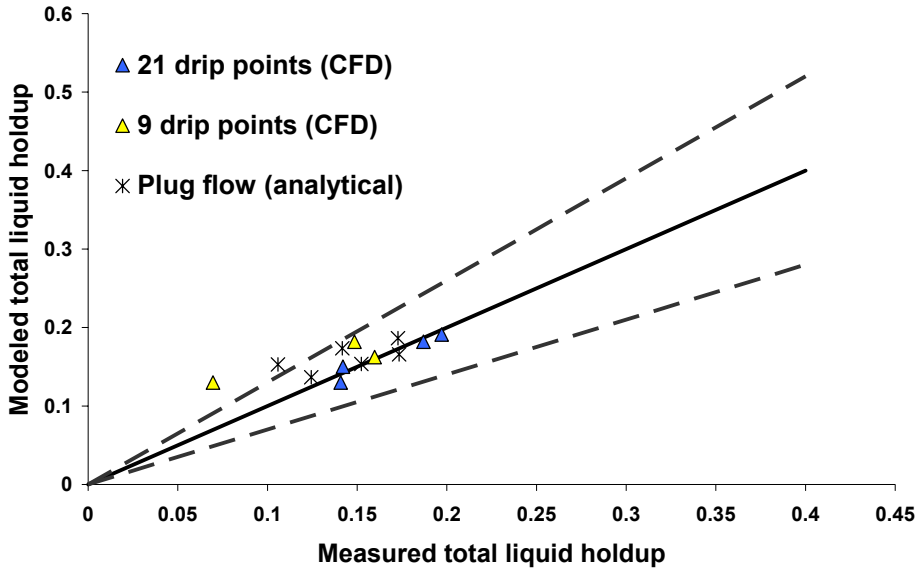

Figure 4.10. Parity plot of measured and simulated total liquid holdup.

Investigation of the liquid distribution in the wide dimension of the bed yielded interesting information about the material effect as already explained in the experimental section of the report. Comparison of the modelled distribution to measured ones is presented in Figure 4.11. Here the capillary pressure refers to the capillary pressure model of Attou & Ferschneider [1].

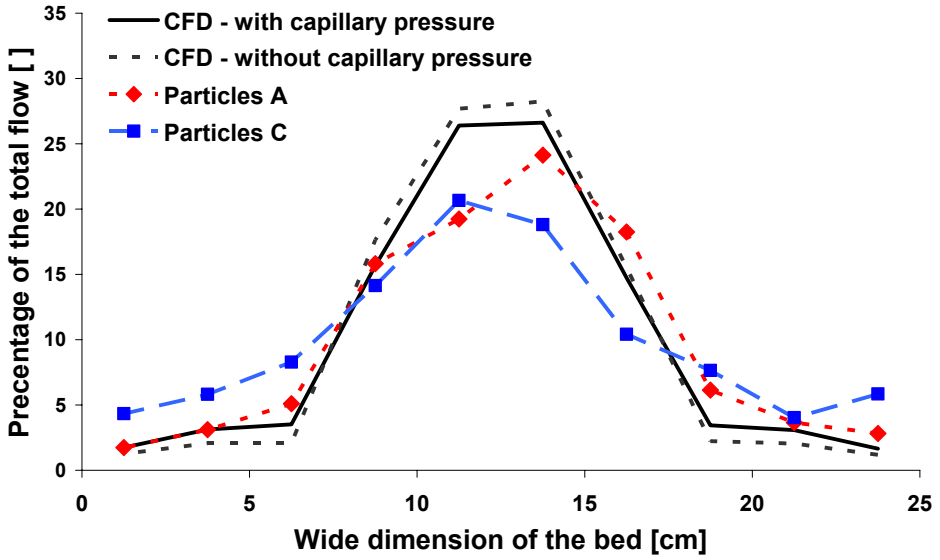

Figure 4.11. Horizontal liquid distribution at the end of the bed with gas superficial velocity of u_g ~ 0.25 m/s and liquid superficial velocity of u_l ~ 1.0 cm/s.

The fit between glass particles and the model is quite good regardless of whether the capillary pressure term is used or not, leading to the conclusion that the capillary pressure term, at least presented in the way Attou & Ferschneider have done it, is not sufficient to account for the liquid horizontal dispersion. Considering the capillary pressure phenomenon, the model lacks the key surface characteristics of the packing material. The capillary pressure term will be overviewed in more detail later on the text. It is, however, obvious that the characteristics of the packing material should be taken into consideration in the model.

4.4.2 Model improvement

The evaluation of the terms in current interaction models lead to some improvements to describe the phenomena more realistically. Also the necessity of including additional parameters into the model was noticed based on the experiments. The modifications to the current models and additional terms under development are reviewed in the following paragraphs.

Interaction terms

Gas-solid interaction term

Earlier when modelling two phase flow most authors omitted gas-liquid interaction from their models based on argumentation that it was not significant. This idea is based on the fact that due to laboratory scale restrictions most experimental equipment operates in atmospheric pressure with only moderate gas flow rate with air as a gas phase. In these circumstances the gas phase density is quite small and it might appear that changes in gas velocities have only little or no impact on the pressure drop. Later on it was discovered that gas-liquid interaction is in fact significant and it was included to the models. Now the interactions considered were liquid-solid, gas-liquid and gas-solid of which the last two are in the matter of fact exclusive in case of completely wetted catalyst resulting in double effect on the gas phase. This was long over looked because when performing an order of magnitude analysis, in ordinary flow conditions, the impact of liquid-solid interaction term is dominant and the double effect is compensated with only small changes in volume fractions. It does, however cause problems in situation of partially dry catalyst (Figure 4.12). More orthodox way would be to take either gas-liquid or gas-solid interaction into account based on the bed status – wetted or dry. In this case an ordinary one phase Ergun equation can be used to model gas-solid interaction in case of dry bed instead of the modified one, which has been a somewhat used approach in the literature, and the two terms can be taken into account based on e.g. the external wetting efficiency of the bed. An example of such an approach and its effect to the obtained solution is presented in Figure 4.13.

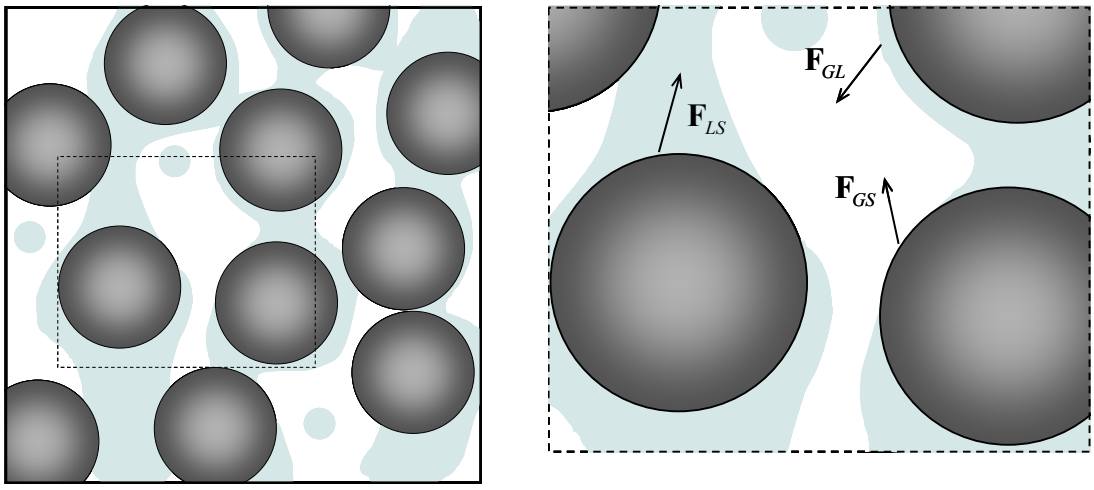

Figure 4.12. Effect of the uneven liquid distribution caused for example by channeling to the forces affecting the flow.

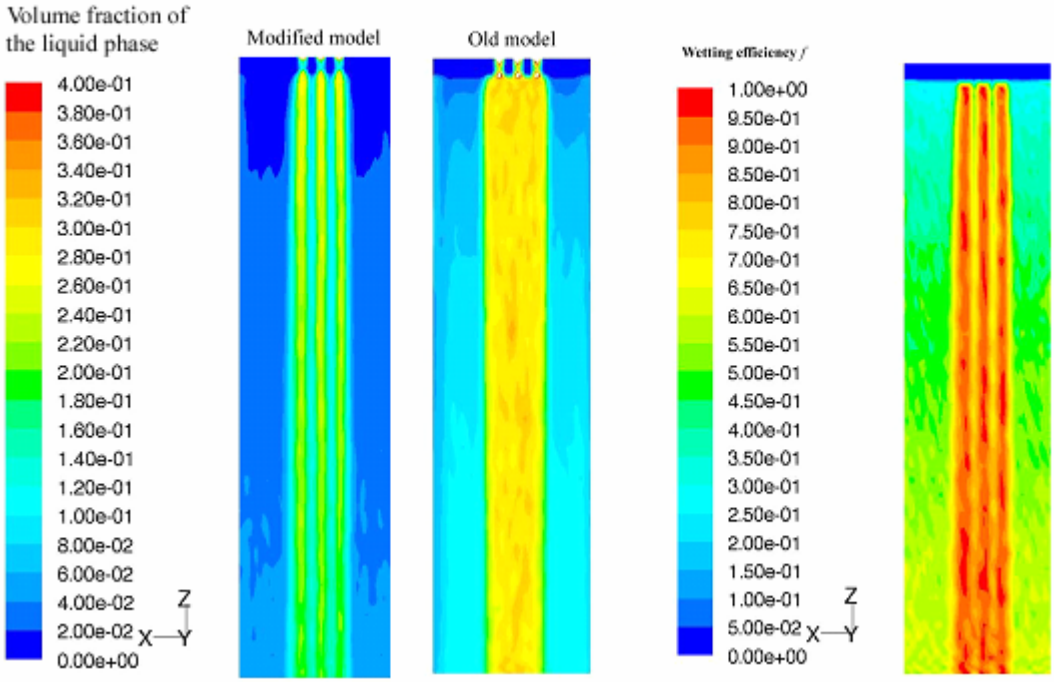

Figure 4.13. Resulting liquid phase distribution with central liquid distribution using one of the old models from the literature (Tung and Dhir, 1988) and with modified model. The wetting efficiency f has been estimated with the correlation of Pironti et al. (1999). It can be seen that the predicted liquid holdup is unrealistically large with the old model in places were practically no liquid is fed.

Gas-liquid interaction term

When considering the gas-liquid interaction term the liquid and solid are considered to form a porous medium with an effective porosity equal to the gas volume fraction in the bed, α_G. In addition an effective catalyst diameter has traditionally been considered to account for the liquid film over the catalyst. It is, however, quite idealistic approach to consider the liquid as an uniform film over the catalyst. An alternative way has been developed during this project which is based on the assumption the liquid is firstly placed in the contact points between the particles (Figure 4.14) and spreads out more with increasing liquid volume fraction. This implies that with smaller gas volume fractions the gas is able to flow in straighter flow patterns e.g. the flow rate of the gas phase is less tortuous than when compared with the empty bed value. In the developed model the tortuousity experience by the gas phase is dependent of the liquid-solid contact angle θ, which is expressed as a function of gas volume fraction and used to correct the Ergun constants [2]:

$$E_{\rho,q} = 6 f_\tau T_q^{\,3} \tag{4.1}$$

$$E_{\mu,q} = 72 T_q^{\,2} \tag{4.2}$$

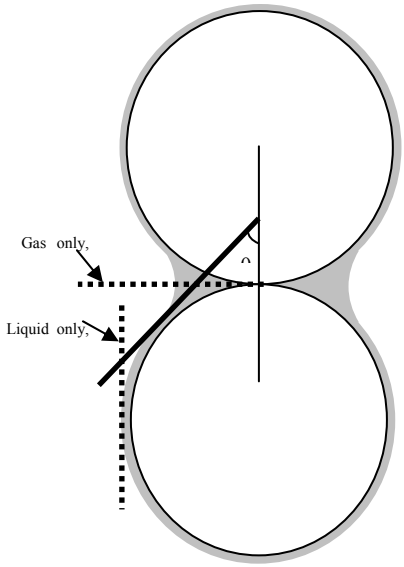

Figure 4.14. Schematic picture of liquid saturation effect on tortuousity.

Liquid solid interaction term

In the literature the derivation of the liquid-solid interaction and the basic assumptions behind it is often quite poorly documented. Thus the derivation was redone using annular flow approach (Figure 4.15). This results in an interaction term consistent with

the one derived by Attou et al. [3]. The idealization of the flow path is often compensated by using bed-specific Ergun constants. However, when considering once again Figure 4.14, it can be concluded that with increasing gas volume fraction the liquid experiences a more and more tortuous flow pattern. Thus the tortuousity experience by liquid phase is always greater than the empty bed value, and further modifications to the current models are in place. This is another advantage of using dynamics Ergun constants over effective catalyst diameter in gas-liquid interaction term. It also acknowledges the changes in liquid flow pattern in varying circumstances which has up till now left unconsidered.

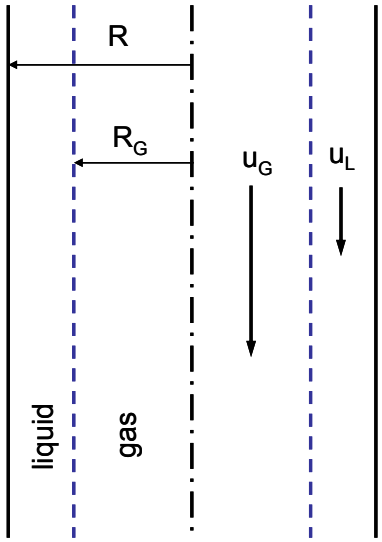

Figure 4.15. Schematic presentation of the annular flow approach.

The improved closure terms developed in the scope of the project are as follows. Some of the terms, such as the dynamic tortuousity, are still under development.

Liquid-solid interaction term:

$$F_{LS} = \left\{ \frac{E_\mu(T_L)(1-\varepsilon)^2 \mu_L}{\alpha_L^2 d_{eff}^2} + \frac{E_\rho(T_L)(1-\varepsilon)\rho_L|\overline{u}_L|}{\alpha_L d_{eff}} \right\} \alpha_L \overline{u}_L \tag{4.3}$$

Gas-liquid interaction term:

$$F_{GL} = \left\{ \frac{E_\mu(T_G)(1-\alpha_G)^2 \mu}{\alpha_G^2 d_{eff}^2} + \frac{E_\rho(T_G)(1-\alpha_G)\rho|\overline{u}_G - \overline{u}_L|}{\alpha_G d_{eff}} \right\} \alpha_G (\overline{u}_G - \overline{u}_L) \tag{4.4}$$

Gas-solid interaction term:

$$F_{GS} = \left\{ \frac{E_\mu(T_0)(1-\varepsilon)^2 \mu}{\varepsilon^2 d_{eff}^2} + \frac{E_\rho(T_0)(1-\varepsilon)\rho|\overline{u}_G|}{\varepsilon d_{eff}} \right\} \varepsilon \overline{u}_G \tag{4.5}$$

Equations for liquid and gas phase tortuousity (T_0 is the empty bed tortuousity):

$$T_L = \frac{T_0}{\cos\left(\frac{\pi}{2}\alpha\right)} \tag{4.6}$$

$$T_G = \frac{T_0 + 1}{2} + \alpha\left(\frac{T_0 + 1}{2} - 1\right) \tag{4.7}$$

Capillary pressure

Capillary effects play a role in trickle bed reactors, because two immiscible fluids are in contact in the pores. The capillary pressure is defined as the pressure difference between the nonwetting and wetting phases (gas and liquid in the trickle bed reactor) and is determined by the local curvature of the interface [4]:

$$p_c = p_G - p_L = \sigma\left(\frac{1}{R_1} + \frac{1}{R_2}\right) = \frac{2\sigma}{R^*}, \tag{4.8}$$

where σ is the interfacial tension between gas and liquid phases, and R_1 and R_2 are the principal radii of curvature. The mean radius of curvature R^* is of the order of particle size. The capillary pressure depends on the material properties (the liquid-solid contact angle), on the geometry of the pores and on the liquid saturation. In trickle beds, the capillary pressure is important, because it is responsible for capillary dispersion tending to spread the wetting fluid [5].

Several correlations can be found in the literature for the capillary pressure. In CFD simulations, the expression of Attou et al. [1] is commonly used [6, 7]. The formulation of Attou et al. is based on geometrical considerations and has the form

$$p_c = 2\sigma\left(\frac{1-\varepsilon}{1-\alpha_G}\right)^{1/3}\left(\frac{5.42}{d}\right)F\left(\frac{\rho_G}{\rho_L}\right), \tag{4.9}$$

where the function F takes into account the high pressure effects. Eq. (4.9) is, however, inadequate, because it does not take correctly into account the shape of the liquid-gas interface in the pendular liquid rings at he contact points of the particles (cf. Figure 4.16). In addition, the model of Attou et al. does not include the dependence on the contact angle.

The other semiempirical formulation frequently used is based on the dimensionless Leverett J-function which is an attempt to reduce the dependence of the capillary pressure on liquid phase saturation to a common function [4]. The original expression is

$$J(S_L)=\frac{p_c}{\sigma}\sqrt{\frac{k}{\varepsilon}}, \tag{4.10}$$

where k is the medium's permeability. In reality, different correlations of the J-function are needed for different situations. An example is the fit of Grosser et al. to Leverett's original data [8]:

$$J(S_L)=0.48+0.036\ln\left(\frac{1-S_L}{S_L}\right). \tag{4.11}$$

An analytical treatment of the capillary pressure can be carried out assuming the liquid is confined in the pendular rings of Figure 4.16. We make use of the toroidal approximation that the liquid bridge has the form of a surface of revolution of a circular arc. Then the two radii of curvature are given by

$$R_1 = R\frac{1-\cos\varphi}{\cos(\varphi+\theta)} \tag{4.12}$$

$$R_2 = R_1 - R\left[\sin\varphi+(1-\cos\varphi)\tan(\varphi+\theta)\right] \tag{4.13}$$

where R is the diameter of the particle, θ is the contact angle and φ is defined in Figure 4.16. R_2 is always negative and R_1 is positive, if the liquid bridge is concave as in Figure 4.16. The liquid volume in the ring can also be expressed analytically as a function of the angles φ and θ.

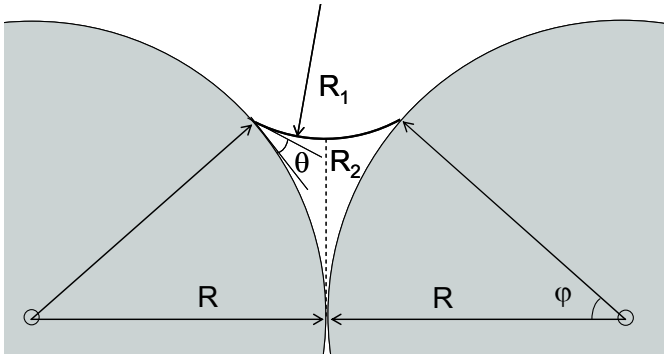

Figure 4.16. Notation used in derivation of the principal radii of curvature of the pendular liquid ring in a contact point of two spherical particles.

Using Eq. (4.8) the capillary pressure can be expressed as a function of φ and relating the volume of the ring to the liquid saturation, S_L can also be expressed as a function of φ. In the final step, iterative solution is required to obtain the capillary pressure (or *J*) as a function of S_L. A practical approach is to fit a suitable correlation for the *J* vs. S_L curve for a given contact angle. This approach offers a rational way to model the capillary effect and it contains all relevant parameters. The hysteresis effect caused primarily by the different values of the contact angle in the imbibition and drainage processes can also be modelled.

Horizontal dispersion, surface effect

It has been acknowledged in the previous sections considering the experimental results, that the material properties are an essential factor affecting liquid horizontal distribution. Therefore a development and implementation of a horizontal dispersion term was started, but not yet finished during the project.

The most reasonable way to carry out the modelling of radial dispersion considered to be through modelling the dispersion with a diffusion type term. For example Gunn [9] performed experiments concerning radial dispersion and he separated the molecular diffusion and the convective dispersion as two different contributing factors:

$$\frac{1}{Pe} = \frac{1}{Pe_f} + \frac{\varepsilon}{\tau \,\mathrm{Re}\, Sc} \tag{4.14}$$

where Pe_f is the fluid-mechanical Péclet number. Gunn presents few correlations for Pe_f for various particles, which is a good starting point for the term development. In addition a measurement to determine the coefficient of radial dispersion using the existing experimental setup has been considered. The development of the term is continued in the follow-up project.

4.4.3 Simplified, analytically solvable models

The design procedure for processes including trickle bed reactors (as well as any other industrial processes) is usually iterative, including an initial screening phase, preliminary process design for cost estimates, refined information related to the feed composition and flow rates as well as product specifications, and so forth until a detailed design for each equipment is provided along with a precise heat and material balances. During this process, various levels of process models are needed. The most often used are those implemented in flowsheet simulators, along with correlations that can be either included in the simulators or used separately to analyze various factors of the process. For trickle beds, the most important hydrodynamic parameters are pressure drop over the catalyst bed, phase holdups, and catalyst wetting. In the commercial flowsheet simulators, the available models for trickle bed reactors are very limited. In best cases so far, a plug flow model can be used with chemical kinetics and gas-liquid equilibrium, along with a separate correlation for pressure drop.

Since current CFD models are still too heavy to be used to simulate a full-sized trickle bed reactor, during the project an analytically solvable model was developed to facilitate the design process. An order of magnitude analysis was performed to simplify the momentum equations to obtain analytically solvable equations. Since main use of the simplified analytical model is meant to be as a tool for sizing and designing industrial reactors, the model has been tested in different circumstances: Newtonian liquids, non-Newtonian liquids, trickling flow regime and pulsing flow regimes. Model predicted the pressure drop and liquid saturation in a satisfactory manner for several various circumstances as shown Figure 4.17 and Figure 4.18.

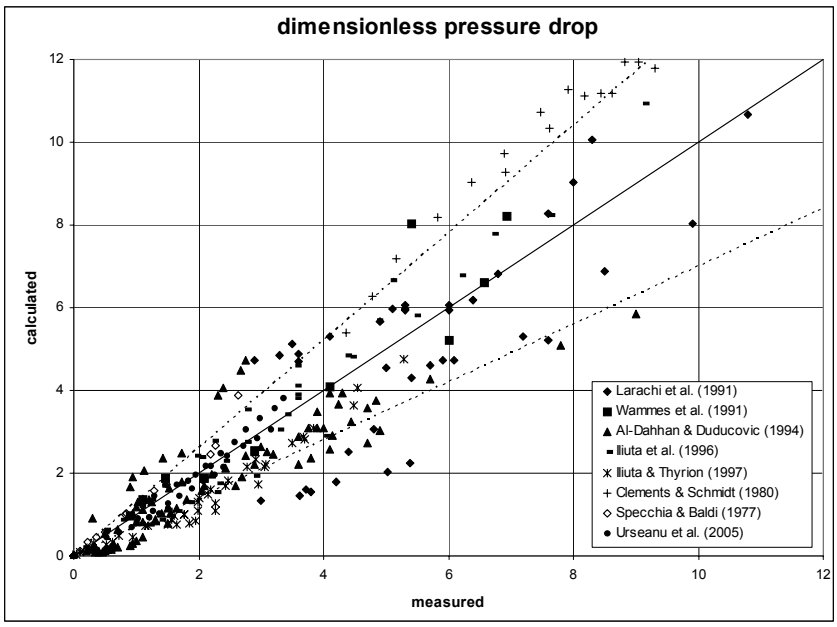

Figure 4.17. Parity plot of calculated and measured dimensionless pressure drops $\frac{dp}{dz\rho_L g}$*. Dashed lines correspond to ±30% relative errors.*

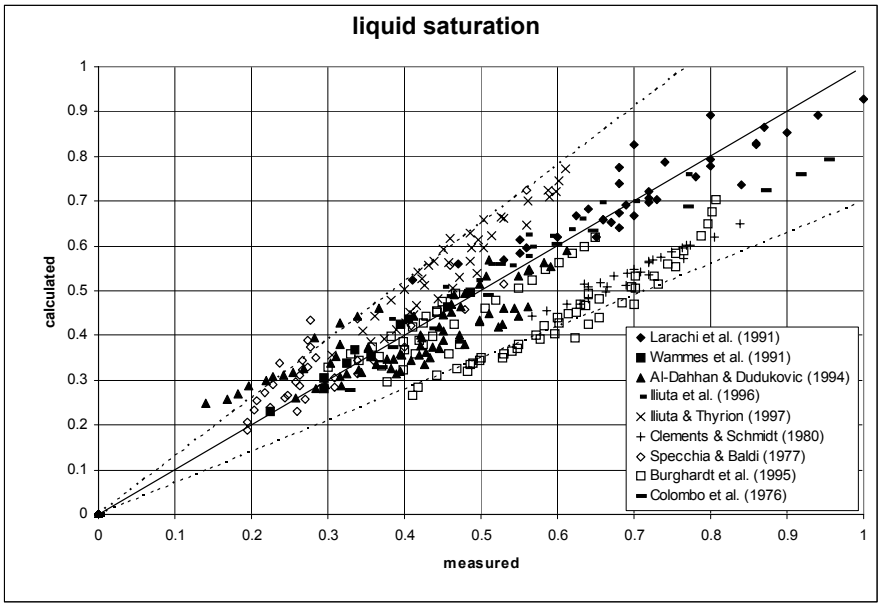

Figure 4.18. Parity plot of calculated and measured liquid saturations. Dashed lines correspond to ±30% relative errors.

4.4.4 Cell interaction models

In the project, also a simplified flow distribution model was developed [10]. It is based on random flow of liquid elements in the inter-particle voids. At the present moment, the model is two-dimensional, but can be extended into three dimensions in a straightforward manner. In Figure 4.19, possible random events in the model are shown.

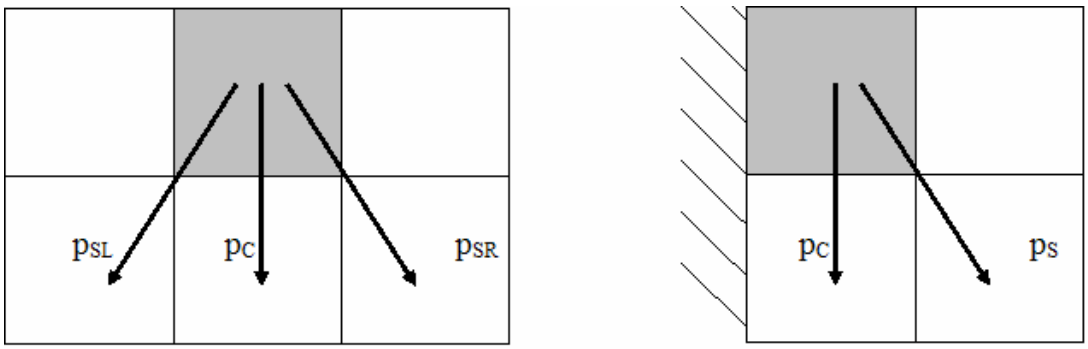

Figure 4.19. Possible random events for a liquid element.

The model parameter consists of probabilities for movements to various directions. Liquid distribution evolution is solved by sequential solution of the liquid hold-up field. Overall parameters for movement at each time step is a product of individual probabilities as

$$p_{side} = p_{\Sigma} p_S F_{\varepsilon} F_W \tag{4.15}$$

$$p_{center} = p_{\Sigma} p_C F_{\varepsilon} F_W \tag{4.16}$$

where subscript Σ refers to probability of movement in general, s and c refer to the direction, ε refers to porosity variation effects and W refers to the wetting effects. Further factors can be included in the model as well.

The model also consists of a field describing wetting of the catalyst. It is assumed that if a cell is full of liquid, it becomes also wetted, and if it is not full, there is a probability according to which the wetting disappears. For wetted particles, the liquid element movement probability is higher than for dry particles. This actually predicts pulsing, which is also a characteristic feature of real trickle beds.

The basic parameters describing radial and axial movement probabilities can be deduced directly from point feed or step impulse experiments. For example radial dispersion coefficient and corresponding probability are related as

$$p_{S0} = \frac{1}{Pe_r}, \text{ where } Pe_r = \frac{d_P}{D_r}\frac{u_L}{\varepsilon}. \tag{4.17}$$

In *Figure 4.20*, a typical point feed simulation with time-averaged (left) and instantaneous (right) liquid distribution is shown.

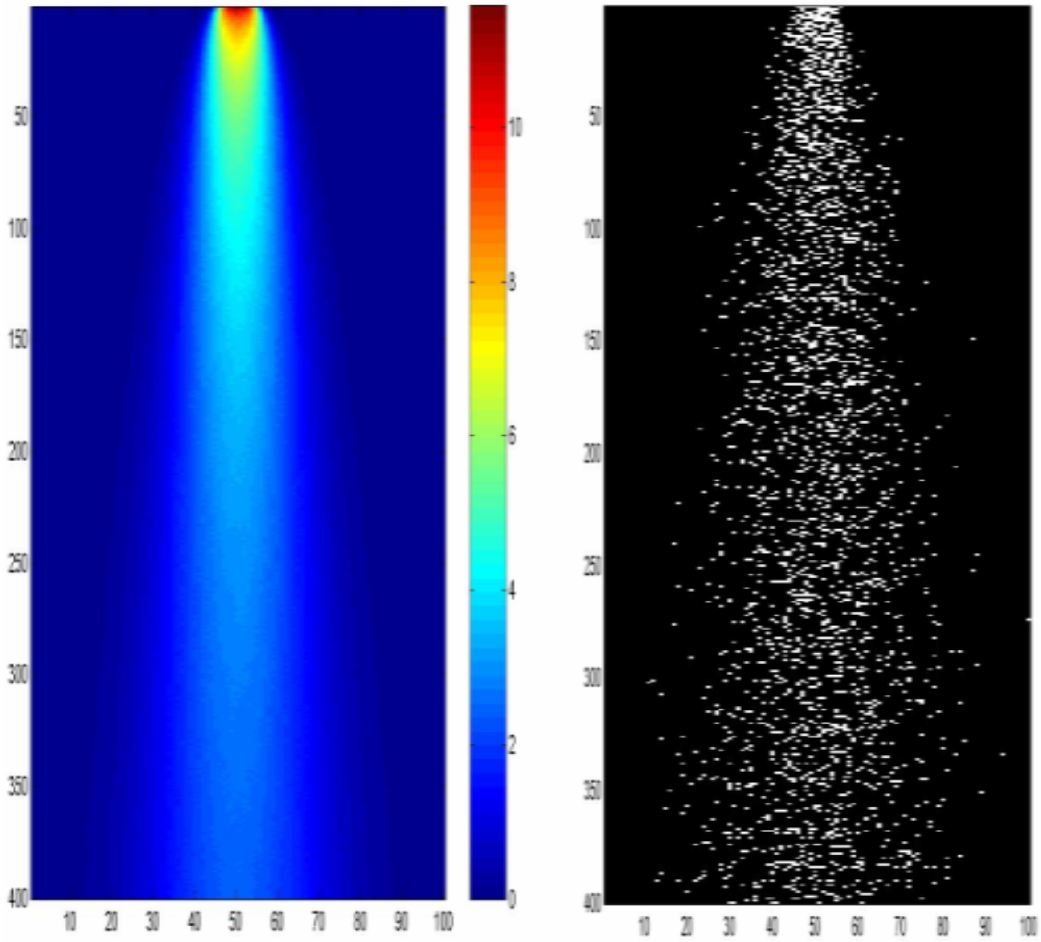

Figure 4.20. Time-averaged (left) and instantaneous (right) liquid distribution from a point source.

References

1. Attou, A. & Ferschneider, G. 2000. A two-fluid hydrodynamic model for the transition between trickle and pulse flow in a cocurrent gas-liquid packed-bed reactor. Chem. Eng. Sci., 55, 491.

2. Holub, R. A. 1990. Hydrodynamics of trickle bed reactors. D.Sc. thesis, Washington University, St. Louis, MO.

3. Attou, A., Boyer, C. & Ferschneider, G. 1999. Modelling of the hydrodynamics of the cocurrent gas-liquid trickle flow through a trickle-bed reactor. Chem. Eng. Sci., 54, 785–802.

4. Bear, J. 1972. Dynamics of fluids in porous media. Dover Publications, Inc., New York.

5. Novy, R. A., Toledo, P. G., Davis, H. T. & Scriven, L. E. 1989. Capillary dispersion in porous media at low wetting phase saturations. Chem. Eng. Sci., 44, 1785–1797.

6. Jiang, Y., Khadilkar, M. R., Al-Dahhan, M. H. & Dudukovic, M. P. 2002. CFD of Multiphase Flow in Packed-Bed Reactors: I. k-Fluid Modeling Issues. AIChe Journal, 48, 701–715.

7. Gunjal, P. R., Kashid, M. N., Ranade, V. V. & Chaudhari, R. V. 2005. Hydrodynamics of trickle-bed reactors: Experiments and CFD modeling. Ind. Eng. Chem. Res., 44, 6278–6294.

8. Grosser, K., Carbonell, R. G. & Sundaresan, S. 1988. Onset of pulsing in two-phase cocurrent downflow through a packed bed. AIChE Journal, 34, 1850–1860.

9. Gunn, D. J. 1987. Axial and radial dispersion in fixed beds. Chem. Eng. Sci., 42, 363–373.

10. Alopaeus, V., Hynynen, K. & Aittamaa, J. 2006. A cellular automata model for liquid distribution in trickle bed reactors. Accepted to Chem. Eng. Sci.

5. Drag reduction effects

Marko Laakkonen[1], Suvi Jussila[1], Asta Nurmela[1], Iiro Pulkkinen[1], Juhani Aittamaa[1], Pentti Saarenrinne[2], Hannu Eloranta[2], Taija Saikkonen[2], Markus Honkanen[2], Markus Olin[3], Timo Pättikangas[3] and Mikko Manninen[3]

5.1 Introduction

Drag Reducing Agents (DRA) have potential applications in the control of turbulence and other transport phenomena. An important application of DRA is to improve the capacity and to reduce the costs of oil pumping in pipelines. DRA effects have been investigated mostly from pipe flows. In this work, DRA effects were measured from agitated vessels and pipes. The aim was to get information for the validation of phenomenological DRA-models.

Among the many strategies employed for drag reduction in wall-bounded flows, polymer additives are the most efficient, yet the most intricate. The complexity of the phenomenon stems from the small amount of microscopic polymer molecules needed to achieve significant drag reduction: drag reduction up to 80% have been achieved with only a few ppm concentrations. However, despite extensive experimental and theoretical efforts, the drag reduction mechanism is still under debate (see Dubief et al. [1]). The exact details as to how minute concentrations of polymer molecules can create large reductions in turbulent drag are still unknown.

Drag reduction (DR) caused by the presence of small amounts of high molecular weight polymer in a turbulently flowing liquid is a well-known and much studied phenomenon. However, it continues to be incompletely understood from a mechanical point of view.

Drag reduction in turbulent flows by polymer additives has been known for last 50 years and the phenomenon has been applied to many industrial applications, but modelling has not been quite as successful as utilisation (e.g., Gyr & Bewersdorff [2]). Theories for the polymeric drag reduction are available and for example direct simulations at high enough Reynolds numbers have been carried out, but only in very simple flow geometry (e.g., Benzi et al. [3], Yu & Kawaguchi [4], Dubief et al. [5], Min et al. [6], Ptasinski et al. [7], Dimitropoulos et al. [8], Sureshkumar et al. [9]).

---

[1] Helsinki University of Technology, Department of Chemical Technology, Chemical Engineering and Plant Design
[2] Tampere University of Technology, Institute of Energy and Process Engineering
[3] VTT

5.2 Effects of DRA on power number, bubble size distribution and mass transfer in agitated vessels

5.2.1 Experimental setup

Experiments were carried out in geometrically similar 14 and 200 dm^3 laboratory tanks. The vessels are fully baffled including also surface baffles to avoid surface aeration at high agitation speeds. The investigated impellers were Rushton turbine and 45° pitched blade turbine. The pumping direction of pitched blade impeller was downwards. The power consumption of mixing was measured with a strain gauge at one second intervals. Torque was measured five minutes and averaged. Other investigated quantities were bubble size distribution (with photography) and oxygen mass transfer (with dynamic absorption – desorption method). The measurements from aerated dispersion were motivated by the fact that bubble size and mass transfer depend on microscale turbulence, which is altered by the addition of DRA. The gas was injected to the bottom of vessel through a ring sparger.

The experiments were carried out with water-soluble polyacrylamide (PAA) (SNF, Floerger FA920) at varying concentrations (2, 16, 32, 100 wppm) and stirring speeds (Re = 40 000 – 120 000 in 14 dm^3 vessel; Re = 114 000 – 368 000 in 200 dm^3 vessel). The effects of molar mass were investigated by using 3, 10 or 20 M PAA (M = $1 \cdot 10^6$ g/mol). For reference, some experiments were also carried out with the 20 M PAA that was available as an aqueous solution.

5.2.2 Results

Power consumption

Figure 5.1 shows measured power numbers ($= P / \rho D^5 N^3$) at varying Reynolds numbers for Rushton turbine in the 200 dm^3 vessel. The intervals of variation are also presented for each measurement point. It can be seen that DRA has no detectable effect on the power. The smaller power numbers of 20 M/100 wppm solution at high Reynolds numbers seem to result from a more significant surface aeration compared to other investigated solutions. It is noted that this PAA had different origin than other investigated PAA samples.

The measured power numbers of mixing for the pitched blade turbine from the 200 dm^3 vessel are presented in Figure 5.2. Power number increases with Reynolds number. This slightly contradicts with a general observation that power number should be constant in the turbulent flow regime. It should be noted that due to smaller power number, the measurement accuracy is not as good as with Rushton turbine at low stirring speeds.

The measurements indicate that PAA has no significant effect on the mixing power. In the pitched blade turbine experiments, surface aeration was less significant than in the experiments with Rushton turbine.

The gradual degradation of 20 M PAA was investigated at constant stirring speed 220 rpm in the 200 dm^3 vessel. No change of power number was observed during 180 minutes.

Similarly, the measurements from the 14 dm^3 vessel with both Rushton and pitched blade turbines indicate that PAA has no influence on the power consumption. The degradation of PAA was investigated also in the 14 dm^3 vessel. The power number increased slightly but this trend is within the limits of measurement accuracy.

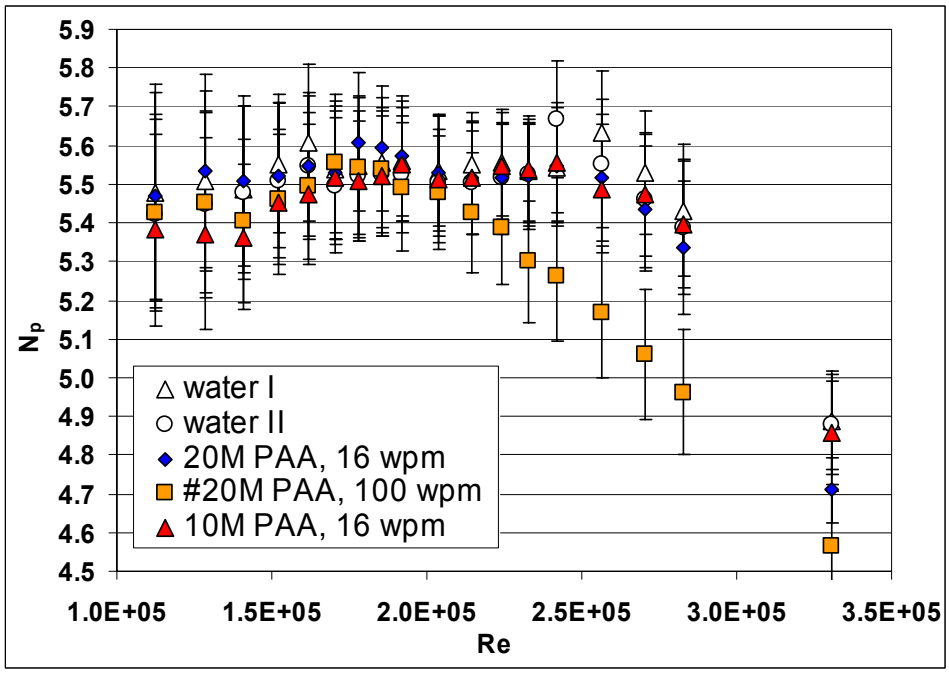

Figure 5.1. Power number vs. impeller Reynolds number, Rushton turbine, 200 dm^3 vessel. #PAA supplied as an aqueous solution.

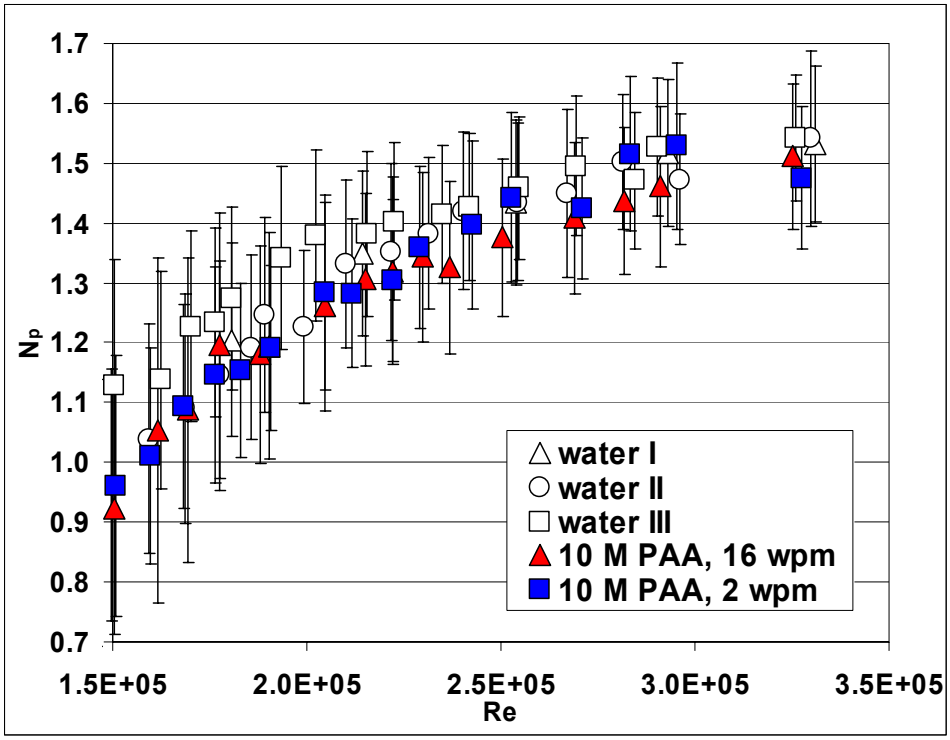

Figure 5.2. Power number vs. impeller Reynolds number, pitched blade turbine, 200 dm^3 vessel.

Bubble size distributions

Photographs from gassed aqueous PAA solutions in 200 dm^3 vessel are presented in Figure 5.3. The photographs were taken through transparent vessel wall just above the impeller plane in the mid-plane between baffles. It can be seen that bubbles are notably smaller in the 20 M/32 wppm PAA solution than in other solutions. This further indicates that physical properties of this PAA grade deviate from other tested PAA grades (SNF, Floerger FA920). It is possible that 20 M PAA itself or some of its additives acted as surface-active agents, which stabilize bubble surface and inhibit the tendency of coalescence.

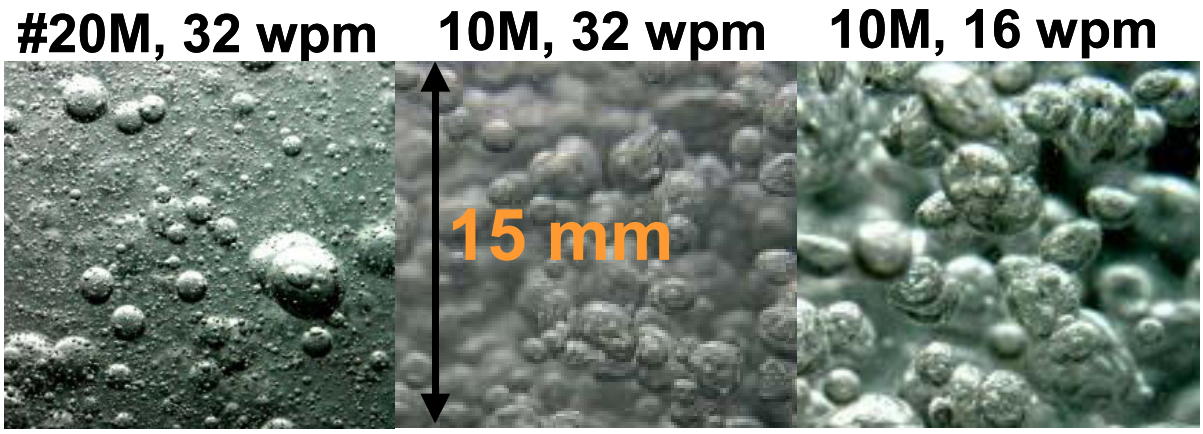

Figure 5.3. Photographs from gassed aqueous PAA-solution, stirring speed 390 rpm, gassing 0.7 vvm, Rushton, 200 dm^3 vessel. #PAA supplied as aqueous solution.

The analysed bubble size distributions, arithmetic and Sauter mean bubble diameters are presented in Figure 5.4. The comparison shows the deviation of 20 M PAA solution. In the 10 M PAA solutions bubbles are slightly smaller than in tap water. Bubble sizes also decrease with increasing PAA concentration. The changes in surface-active properties of liquid are a possible explanation.

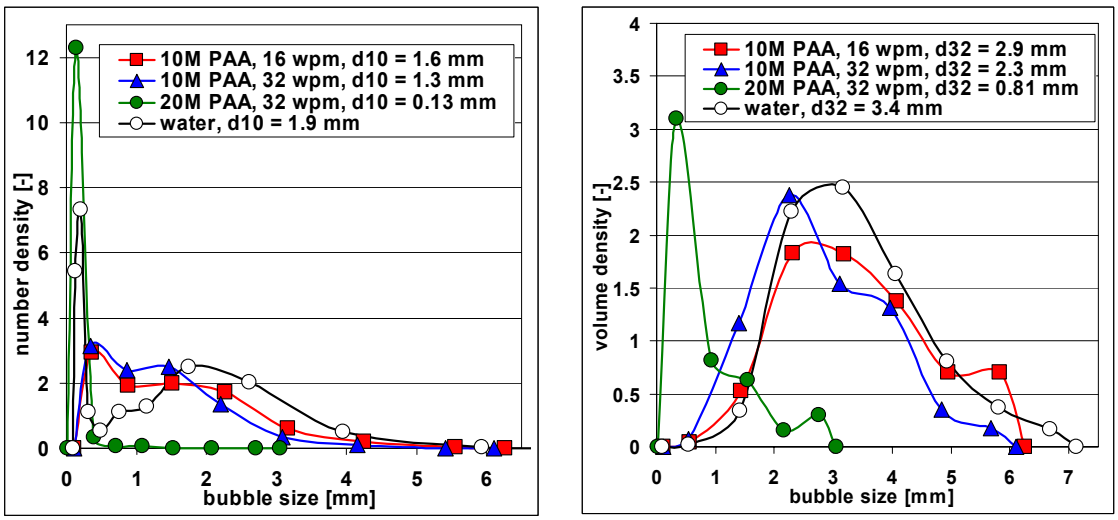

Figure 5.4. Bubble number (left) and volume (right) size distributions, stirring speed, 390 rpm, gassing 0.7 vvm, Rushton, 200 dm^3 vessel, #PAA supplied as aqueous solution.

Mass transfer measurements

Measured oxygen transfer coefficients are presented in Table 5.1. The values are obtained as an average from several measurements. The mass transfer coefficients from water, and 10 M PAA are equal within the limits of measurement accuracy while 20 M

solution shows deviation also in this respect. A possible cause for the low oxygen transfer coefficient in 20 M solution could be that small bubbles have a stabile surface, which causes the decrease of mass transfer rates. On the other hand, small bubbles have a larger interfacial area/volume ratio. It is emphasized that mass transfer rates are related complicatedly to several phenomena in the stirred tanks.

Table 5.1. Measured oxygen transfer coefficients from 200 dm^3 vessel, stirring speed 390 rpm, gassing 0.7 vvm.

System	PAA (wpm)	k_La (20 °C) (1/s)
Water	0	0.054
PAA, 10 M	16	0.049
PAA, 10 M	32	0.051
PAA, 20 M$^{\#}$	32	0.024

5.2.3 Conclusions

The effects of PAA on the power consumption of mixing, bubble size distribution and gas-liquid mass transfer were investigated in the agitated 14 and 200 dm^3 vessels. The PAA was observed to have no effect on the investigated quantities, although it may still alter microscale turbulence. The results also indicate that some PAA grades or their ingredients may act as surface-active agents, which affect on surface aeration, bubble size distribution and gas-liquid mass transfer.

5.3 Effects of DRA on flow and turbulence in stirred tank reactors

5.3.1 Background

A large number of journal articles have been published over the past 50 years. Only few recently published papers are reviewed here. A more comprehensive review of literature can be found for example in Gyr and Bewersdorff [2].

Most of the literature considers turbulent channel flow especially in pipes. Two principal theoretical concepts have been put forward to explain the phenomenon of drag reduction by polymers. The first can be attributed to Lumley [10], who proposed a

mechanism based on the extension of the polymers. He postulated that stretching of randomly coiled polymers, primarily in regions with strong deformations such as the buffer layer, increases the effective (extensional) viscosity. The result is damping of small eddies, a thickening of the viscous sublayer and consequently drag reduction. Lumley also mentions that the influence of the polymers on the turbulence only becomes important when the time scale of the polymers (e.g. the relaxation time) becomes larger than the time scale of the flow, which is known as the onset of drag reduction. The second theory, attributed to de Gennes [11], is that drag reduction is caused by the elastic rather than the viscous properties of polymers. This idea is supported by experiments showing that drag reduction also occurs when the polymers have been injected in the centre of the pipe.

As concluding remarks on the influence of high polymer additions to the channel or wall bounded flow field according to the cited literature can be stated:

1. The high polymer drag reduction mechanism is proposed to be based on stretching of randomly coiled polymers primarily in regions of strong deformations in which the effective viscosity is increased. This can only happen if the time scale of the polymers (relaxation time) is larger than the time scale of the flow. This is called the onset of drag reduction.
2. The stretching process is assumed to restructure the turbulence at small scales by forcing it to satisfy local axi-symmetry with invariance under rotation about the axis aligned with main flow which emphasizes the anisotropy of turbulence. This tendency increases when the polymer concentration is increased until maximum drag reduction (MDR) limit is achieved.
3. The reduction of the Reynolds shear stresses is considered to be caused by the disturbed turbulence production mechanism. The wall vortices that sustain turbulence in a Newtonian fluid are destroyed. The interaction of the polymer additives with fluctuating flow field is taking place.
4. The effectiveness of the polymer depends on the presence of aggregates. The large polymer filaments break up to smaller aggregates and they are more effective in destroying turbulent flow structures.
5. Polymers change the energy flux from large to small scales. A strong modification of the nature of the Richardson cascade is observed, which leads to a substantial depletion of the energy content of the small scales. It is argued that the viscoelastic forces at small scales obstruct the cascade. This eventually decreases the value of dissipation rate and terminates the cascade at larger scale than Kolmogorov length. It is also argued that the extensional motions in the flow could not only potentially stretch the polymers, but also elastically force

the polymer structures, contributing to a more significant damping of the normal velocity fluctuations.

6. The Reynolds stress is strongly decreased. The resulting Reynolds stress deficit is compensated by a polymer shear stress which for the highest drag-reduction cases is 40–50% of the total stress. It implies that there must be a contribution of the polymers to the stress.
7. The pressure-strain term, which is responsible for energy transfer from the streamwise direction to the other directions, is the most reduced term in the kinetic energy budget and this explains the enhanced anisotropy of the flow. The polymer dissipation of the mean flow and the turbulent kinetic energy are transferred into elastic energy of the polymers which in its turn is then dissipated by polymer relaxation.

These remarks are then applied to a stirring tank flow field. This highly three dimensional turbulent flow field is far different from the channel flows with well defined main flow direction and implicit boundary layer. The wall boundary layer in mixing tank is difficult to describe. It depends on existence of baffles and turbine type. Typically the boundary layer is in its developing state. The bulk area of the flow field can be divided to the impeller zone and upper and lower zones. The impeller zone is highly turbulent and three dimensional flow field. There are typically strong vortical (coherent) flow structures at the scale of the impeller vanes. In upper and lower zones there is typically more or less decaying turbulence with low turbulence production by boundary layers and baffles. In addition to the turbulence created velocity fluctuation there are two other fluctuation sources. The periodic fluctuation caused by the rotating impeller blades and by vibrations of the shaft and other structures like baffles. The periodic fluctuation caused by the rotation of the impeller can be removed by synchronizing measurements to the angle position of the blade. The vibration caused velocity fluctuation can not be removed.

5.3.2 Mixing tank with a Rushton turbine and water soluble high polymer

Preliminary tests

Preliminary measurements were made in a cylindrical vessel with inner diameter of 260 mm. The liquid height was 260 mm and volume 14 dm^3. Rushton turbine had six blades (height 30 mm) and diameter of 140 mm. The vertical image area covered the space between blade tip and vessel wall. Measurements study a 40 x 50 mm^2 area in the cross-section in the turbine discharge zone. The measurements were synchronized to start at same shaft and blade angle position. From this position onwards was taken 1428 double

frames. The measurements were made with a High Speed PIV-system at three different impeller rotation speeds 2, 4 and 6 Hz. The frame rate was selected so that 25 frames were taken between two blades (angle 60°). The frame rates were 100, 200 and 300 Hz. Measurements were made with pure water and 15 ppm polymer water solution. The boundary layers at the vessel wall were not studied.

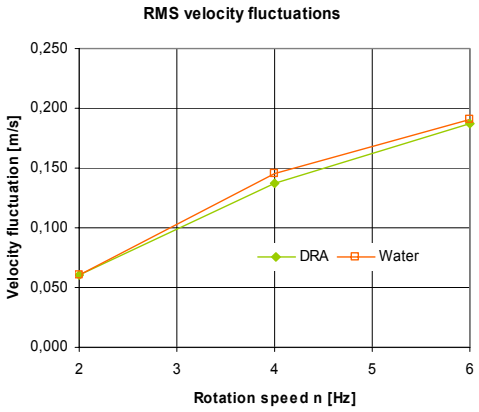

Figure 5.5. RMS velocity fluctuations at different rotation speeds for water and DRA cases.

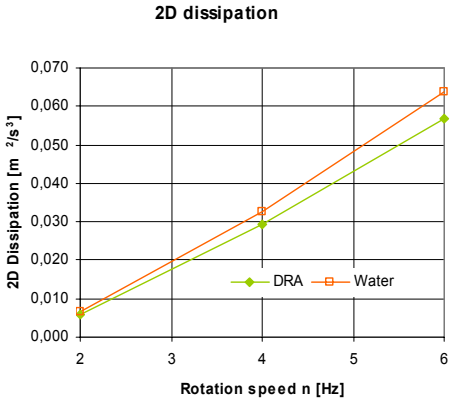

Figure 5.6. Average 2D dissipation values at different rotation speeds for water and DRA.

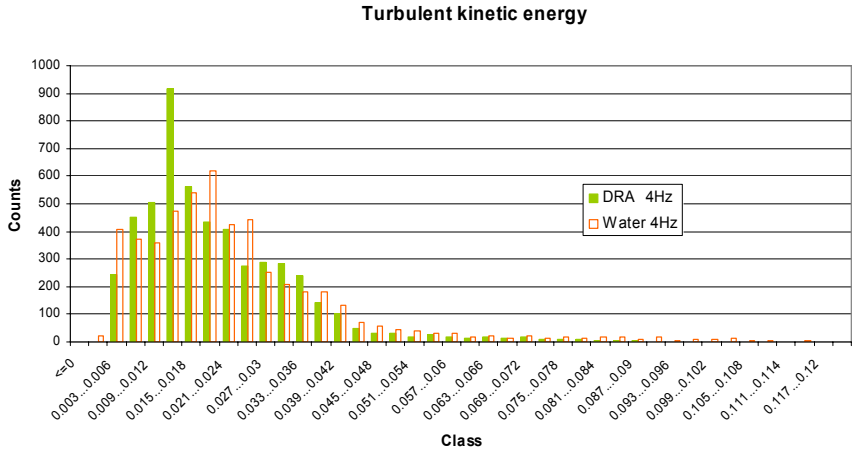

Figure 5.7. Number density histograms for turbulent kinetic energy at 4 Hz rotation speed.

Some results are shown in Figures 5.5–5.7. There is no significant difference (less than 6%) between root mean square (rms) velocity fluctuation values for water and DRA cases at different rotation speeds (Figure 5.5).

Instead of that, the difference for 2D dissipation is more than 10% lower for DRA case for all rotation speeds. The number density distributions of turbulent kinetic energy doesn't differ much at 4 Hz rotation speed for water and DRA cases as shown in Figure 5.7. The same apply also for rotation speeds 2 and 6 Hz. The other measurement results (not shown here) reveal that the turbulent kinetic energy and the 2D dissipation have same values for the water and DRA cases as function of rotation angle at 2 Hz, but there is a remarkable difference at angle positions 10°…35° at 4 Hz (Saikkonen et al. [12]). At 6 Hz the turbulent kinetic energy values collapse together but the 2D dissipation shows a remarkable difference.

From these results can be concluded that in a mixing tank flow field the DRA effects can be seen best as a function of position angle between two blades. At low rotation speeds there is no difference between the water and DRA cases. When the speed is increased the difference is remarkable. The onset of DRA effect requires a minimum rotation speed and then the maximum values of the turbulent kinetic energy are increased. The 2D dissipation rate shows overall lower values when the DRA is working. These findings are in line with the remarks made in previous chapter.

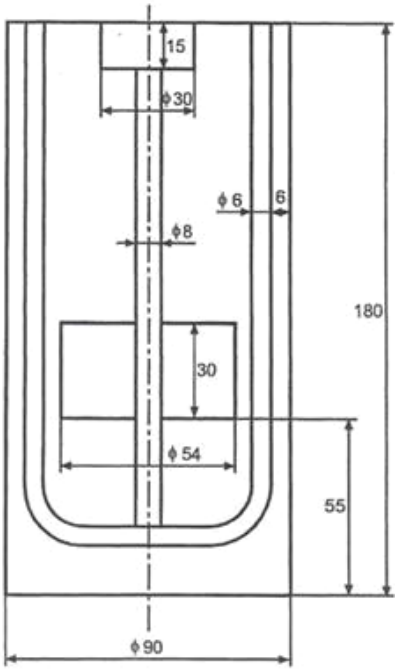

Figure 5.8. Mixing vessel and its dimensions. The mixer has two blades.

DRA effects in a small mixing tank

The inside dimensions of the vessel are given in Figure 5.8. The volume is 1 liter. The used rotation speeds were 120 and 300 rpm. The measurements were made with a Stereo-PIV setup. Two CCD cameras were set in 90° angles and the light sheet was

brought in to the middle plane of the cameras through the bottom of the vessel. The image effective size was 29.5 x 17.2 mm^2. All three instantaneous velocity components were measured in plane which was perpendicular to the plane of support rods (perpendicular to the paper plane in Figure 5.8). The position of the blade was measured at angles 120° …+20° …220°. At angle 90° the blade was in measurement plane (in light sheet plane).The instantaneous velocity field was calculated from images by using adaptive multi-pass algorithm starting from 128x128 pixels interrogation area size to the 16x16 pixels area from measured double frames. The vector spacing was 0.185 mm with 50% overlap. Seeding particles were hollow glass spheres with a diameter 10 μm. The turbulence measurements were made with pure water and with 30 ppm polymer water solution.

The instantaneous velocity field results were calculated from the measured 300 to 500 double frames. These vector images were then locally averaged for each vector to get local time mean quantities and to estimate local maximum values at certain blade angle.

First is explained results for the 300 rpm case with and without DRA. Local maximum values as function of blade angle for the following quantities are presented: Absolute and turbulent kinetic energy, time mean velocity, rms velocities, turbulent Reynolds stresses and 2D dissipation estimate (Figures 5.9–5.14).

Absolute and turbulent kinetic energy as a function of blade angle is presented in Figure 5.9 for water and DRA solution. There is small difference in absolute and turbulent kinetic energy values near the blade at angles 120° and 140°. Same applies also for average maximum velocities in Figure 5.10. Only small differences can be detected. The rms velocities differ more for blade angles 120°, 140° and 160° (Figure 5.11). The largest difference is to the radial direction which is also the main flow direction. In all cases the values for pure water are higher. In Figures 5.12 and 5.13 is shown the maximum turbulent Reynolds normal and shear stresses. In both case the radial direction stresses differ remarkably each other for water and DRA cases at blade angles 120°, 140° and 160°. The flow seems to be more anisotropic in this area. The local maximum dissipation in Figure 5.14 shows different behavior. At angle 120° the difference is smallest and increases for larges angles. This can be explained by the attenuation of the turbulence because of the polymer stresses. At small angles the measurement resolution is inadequate for correct dissipation measurement.

These measurements together with measurement made for 120 rpm case show that values of all the turbulence quantities are reduced in DRA case. Powerfully turbulence increases the effect of DRA, which means that the effect is highest in the trailing vortices behind and near the blades. DRA reduces the maximum values and at the same time the average values are remaining almost unchanged. Also the movement of the trailing vortices is more unstable.

In Figures 5.15 to 5.18 is shown turbulent kinetic energy for water and DRA and turbulent 2D dissipation for both cases. The stronger attenuation for the DRA case can be seen from Figures.

Second measurement set was made through the bottom of the vessel at the middle height of the blades in the cases pure water and 30 ppm polymer at two rotation speeds 120 and 300 rpm. Measurements were synchronized to blade angles 90° and 170° . The image area was 41 x 51 mm^2, which is almost half of the vessel cross-section. The velocity vector spacing was 0.638 mm, which means that the spatial resolution is too low for accurate dissipation measurements. Anyway the results are comparable to some extent. The results are presented for 120 rpm case for following quantities: average velocity field, turbulent kinetic energy and estimates for dissipation (Figure 5.19).

The average velocities are at blade middle level in top figures of Figure 5.19 slightly different. The size of the trailing vortices is larger for the water case, but the maximum values of velocities are at the same level. The size of high values area of turbulent kinetic energy is in the middle pictures of Figure 5.19 quite similar, but the zone of high values is bigger for the DRA case. The 2D dissipation rate is strongly reduced for DRA case as can be seen from the bottom figures. These findings suggest that the magnitude of the average velocities and dissipation are reduced and that the maximum values of the turbulent kinetic energy are increased. This is in line with DRA effects which suggest that the polymers added damping reduces the velocities and dissipation but because the onset behavior the maximum values of kinetic energy are increased.

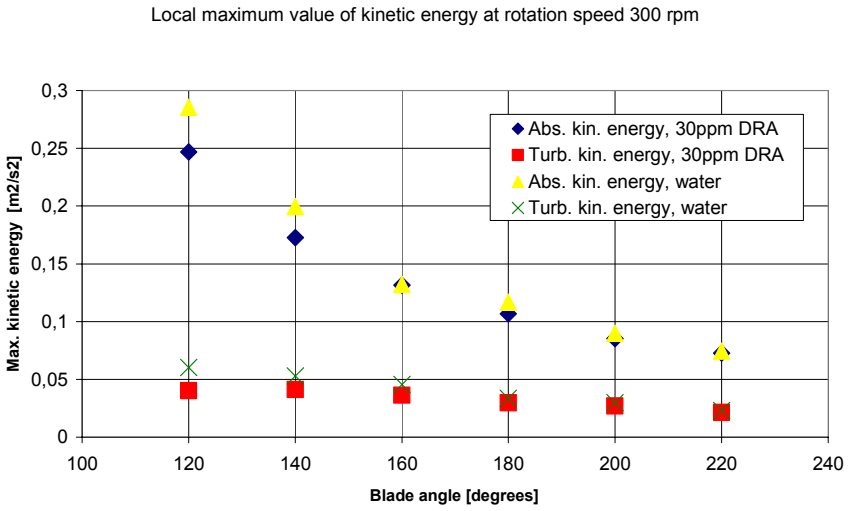

Figure 5.9. Local maximum of average turbulent kinetic energy as a function blade angle.

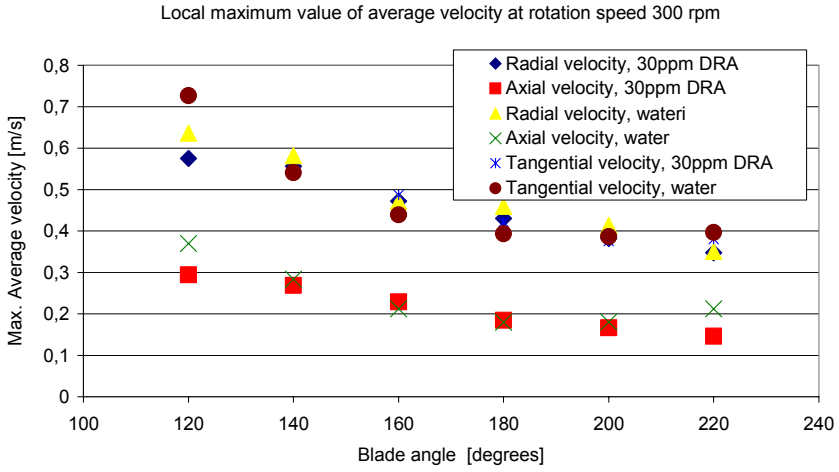

Figure 5.10. Local maximum average velocity as a function blade angle.

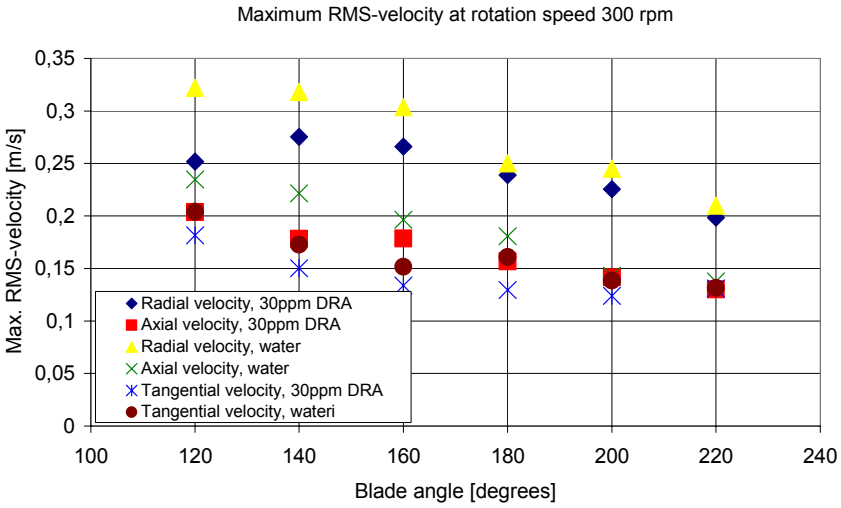

Figure 5.11. Local maximum rms velocity as a function blade angle.

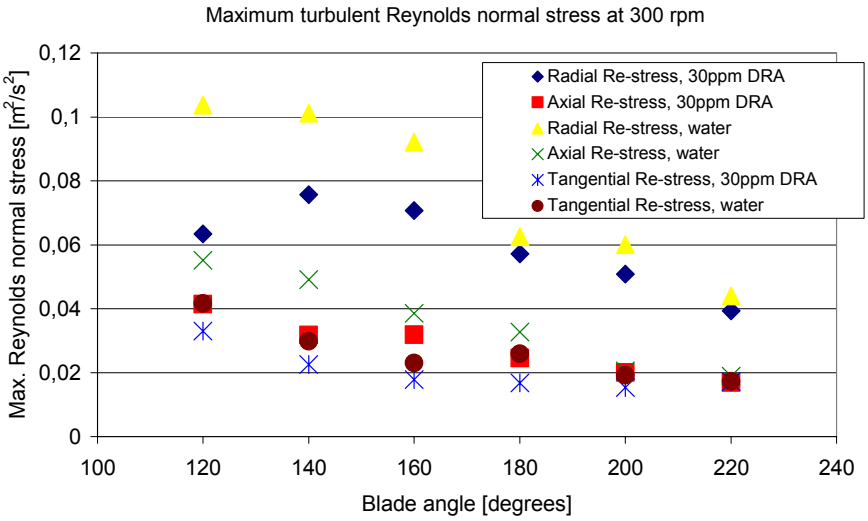

Figure 5.12. Local maximum average Reynolds normal stress as a function blade angle.

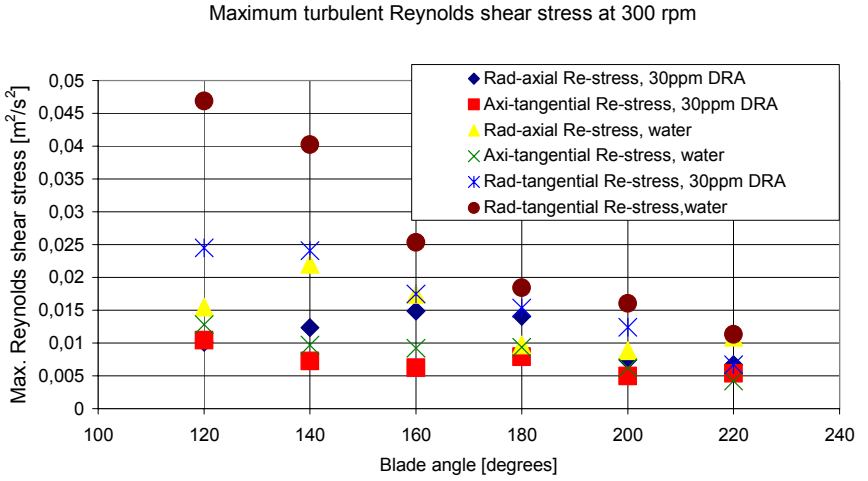

Figure 5.13. Local maximum average Reynolds shear stress as a function blade angle.

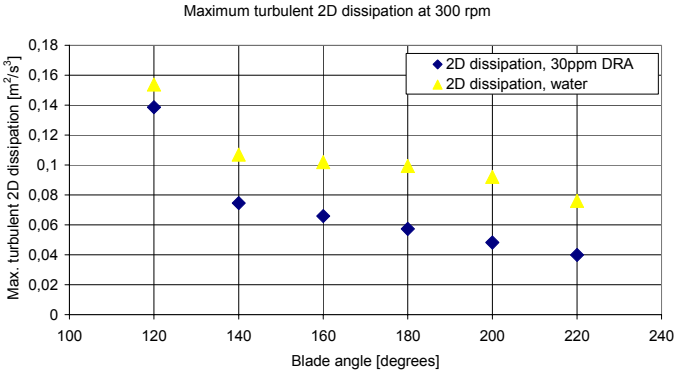

Figure 5.14. Local maximum average dissipation rate as a function blade angle.

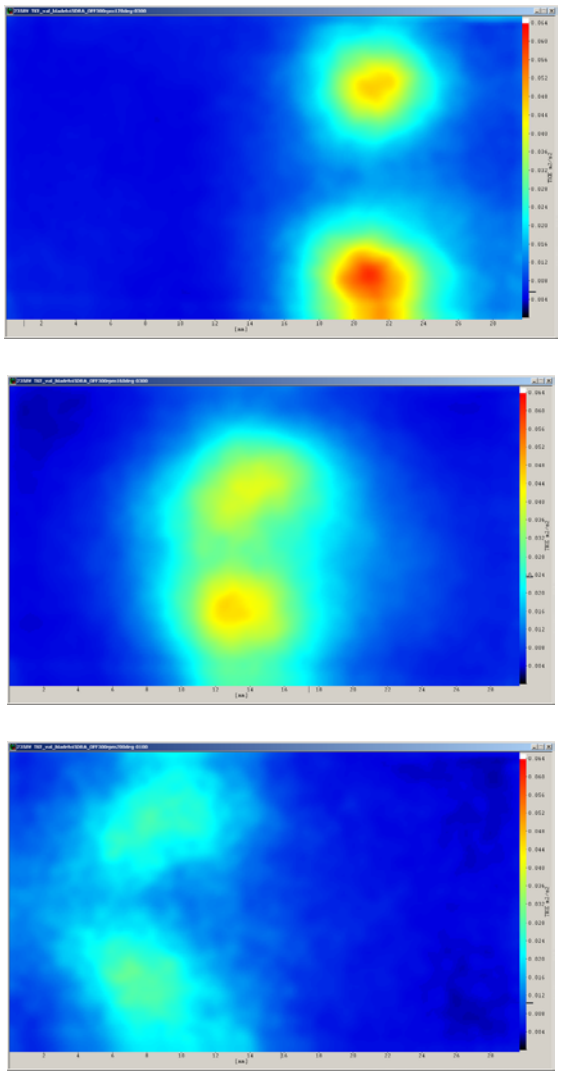

Figure 5.15. Turbulent kinetic energy at angle positions 120°, 160° and 200°. Water, 300 rpm.

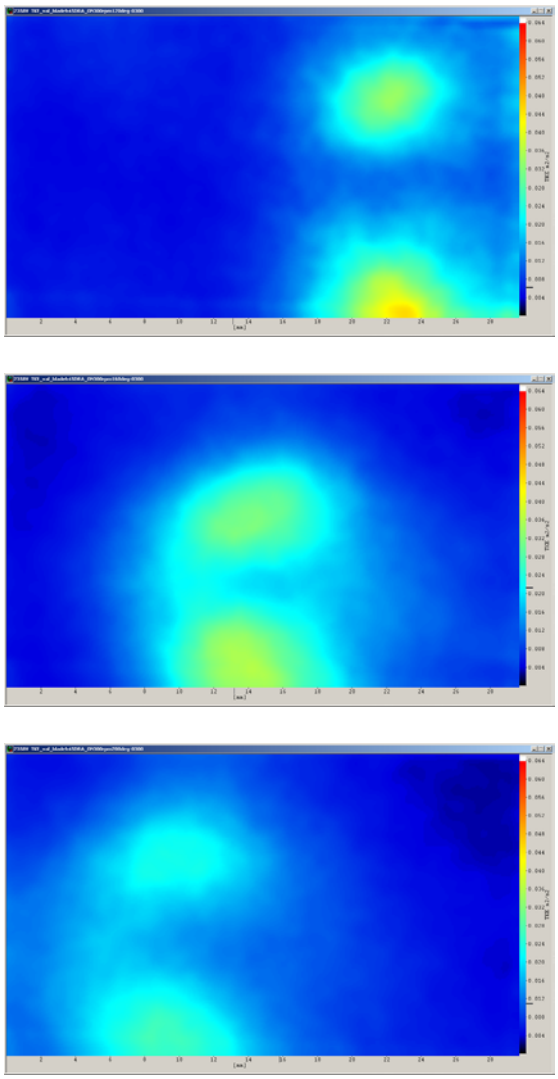

Figure 5.16. Turbulent kinetic energy at angle positions 120°, 160° and 200°. DRA, 300 rpm.

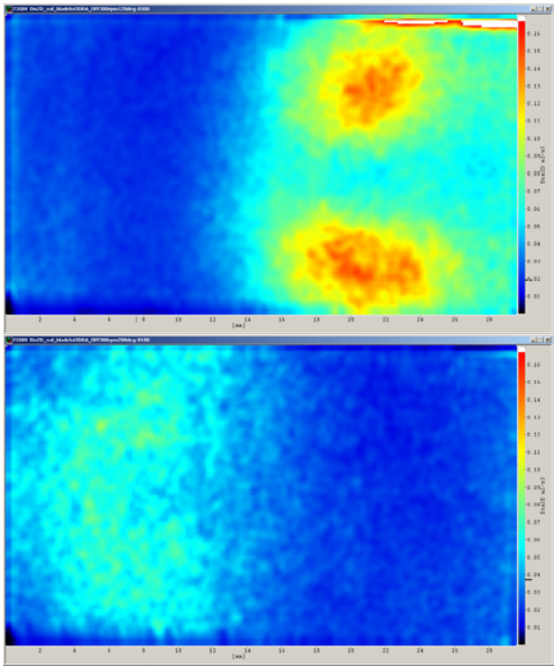

Figure 5.17. Turbulent 2D-dissipation rate at angle positions 120° and 200°. Water, 300 rpm.

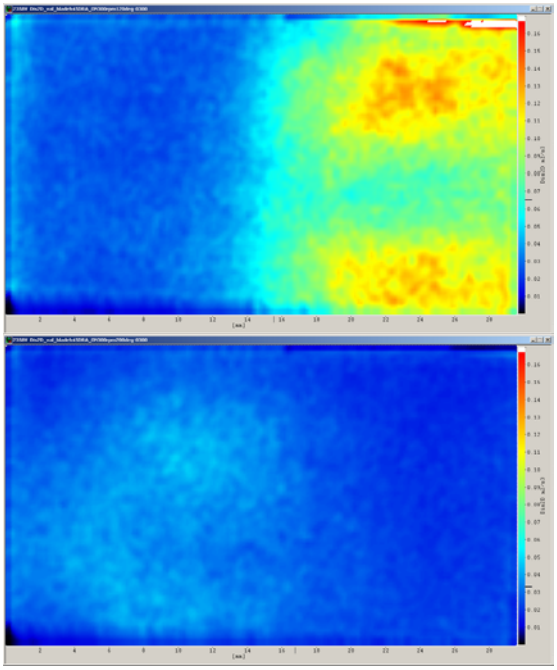

Figure 5.18. Turbulent 2D-dissipation rate at angle positions 120° and 200°. DRA, 300 rpm.

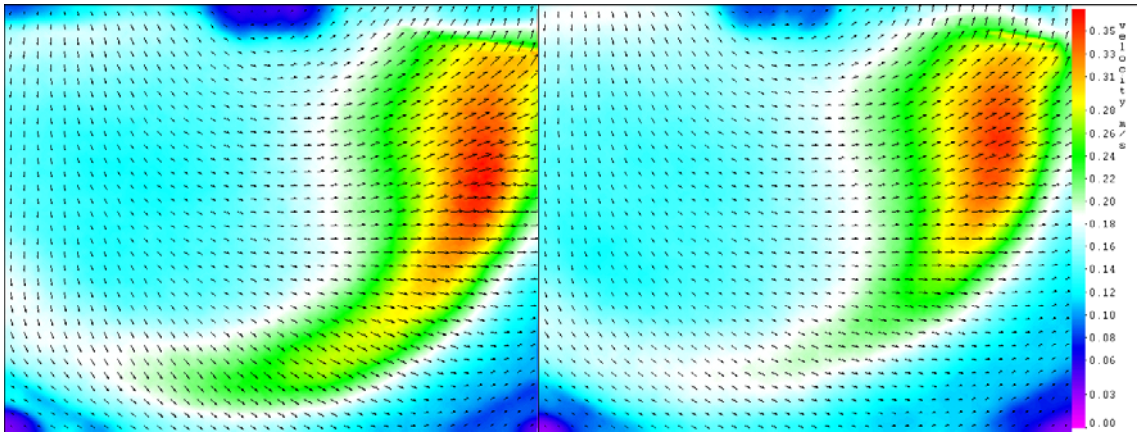

Average velocity, water
Max. velocity: 0.370 m/s
Average velocity: 0.183 m/s

Average velocity, water-DRA-solution
Max. velocity: 0.359 m/s (–3%)
Average velocity: 0.175 m/s (–4%)

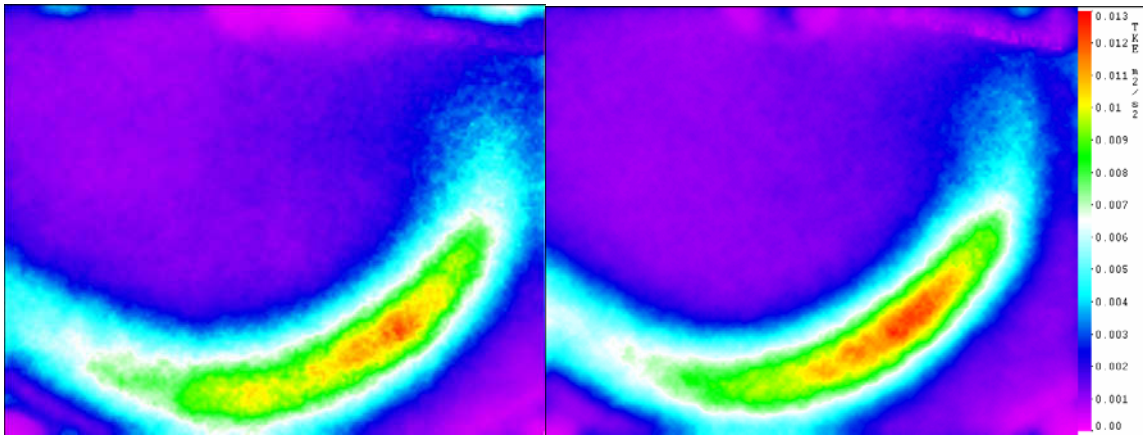

Turbulent kinetic energy, water
Max.value: 0.0126 m^2/s^2
Average value: 0.0031 m^2/s^2

Turbulent kinetic energy water-DRA-solution
Max.value: 0.0129 m^2/s^2 (+2%)
Average value: 0.0029 m^2/s^2 (–6%)

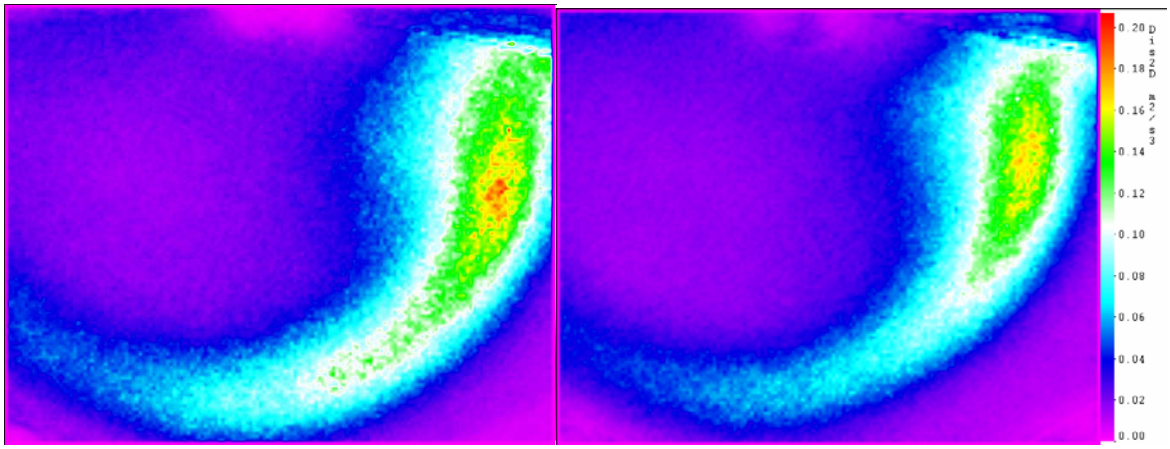

Dissipation, water
Max.value: 0.207 m^2/s^3
Average value: 0.046 m^2/s^3

Dissipation water-DRA-solution
Max.value: 0.181 m^2/s^3 (–13%)
Average value: 0.040 m^2/s^3 (–13%)

Figure 5.19. Average turbulence quantities.

5.3.3 Mixing tank with pitched blade turbine and hydrocarbon soluble high polymer

Tank without baffles

This section explains the measurements made in a mixing tank with non aromatic hydrocarbon (LIAV 230) with DRA and without it. The drag reducing agent was either NECADD 447 or 547 and toluene solution. Measurements were made with two rotation speeds 250 and 120 rpm, with two high polymers and with and without baffles.

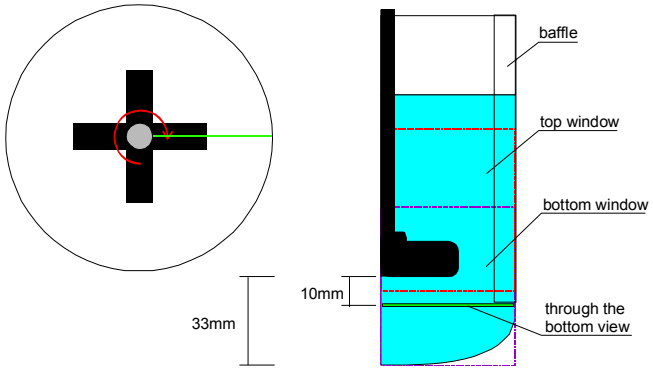

Figure 5.20. Glass tank and measurement areas.

The dimensions of the glass tank are given in Figure 5.20. The rotor was pitched blade type. All the results presented in the following are obtained using a rotor speed of 250 rpm. The vessel was filled with 700 ml of liav230 and the rotor was aligned in the middle of the vessel, so that the rotor was 33 mm above the bottom. For the 10 ppm case, 3.8 ml of DRA-toluene -mixture wais added to liav230. A PIV-system, which was synchronized to the rotor position, was used for the measurements. A set of 100/500 images were acquired for each angular position.

In the axial-radial -plane two windows were measured. The first one covers the upper part of the vessel (referred as “top-window”). The lower window covers bottom of the vessel (referred as “bottom-window”). Both windows are 50 x 65mm^2 in size. When baffles were installed in the vessel, the measurement region was limited to the area between rotor axis and baffle edge, resulting a window size of 40 x 65mm^2. The PIV-system was synchronized to the rotor angle and a set of 500 (or 100 for the baffles case) velocity fields were measured for the rotor angles of 0°, 15°, 30°, 45°, 60° and 75°. Thus rotor angle averaged results can be presented.

For the experiments in the tangential-radial -plane, the laser sheet was leveled 10 mm below the rotor and camera was looking through the bottom of the vessel (thus this

plane was referred as “through the bottom -window”). The measurement area in this plane covered ¼ of the vessel, which means dimensions of 50 x 50mm^2. In this plane, the synchronization to the rotor angle was not used. Despite the strong curvature of the bottom of the vessel, rather good velocity fields were obtained in this plane. Basically there was no problem to perform experiments above the rotor level, but then synchronization was needed and the field of view was limited.

The mean flow pattern in terms of velocity vectors is presented first (Figure 5.21). These fields are obtained by first computing mean velocity fields for each rotor angle and then averaging these fields. This is also the procedure in the following, when averaged quantities (e.g. turbulence kinetic energy) are presented without a note on any specific rotor angle.

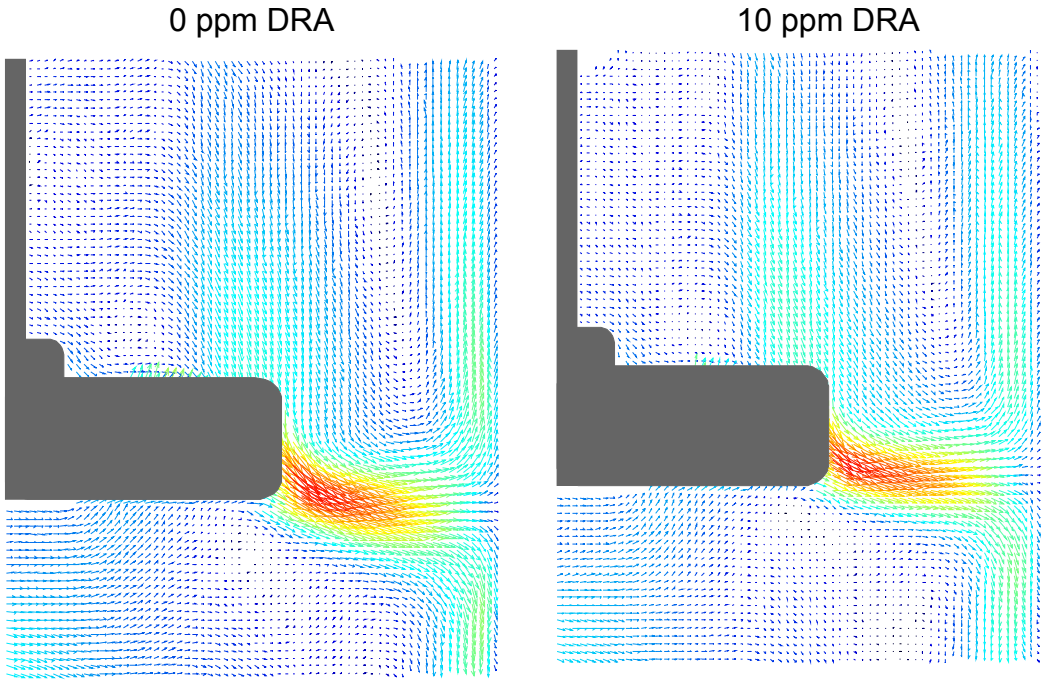

Figure 5.21. Mean velocity vector fields (230 rpm, 0 ppm and 10 ppm high polymer).

Mean flow fields in the bottom of the vessel are not presented here. The mean flow pattern for the 10 ppm case shows that strong secondary motions cannot be found below the rotor.

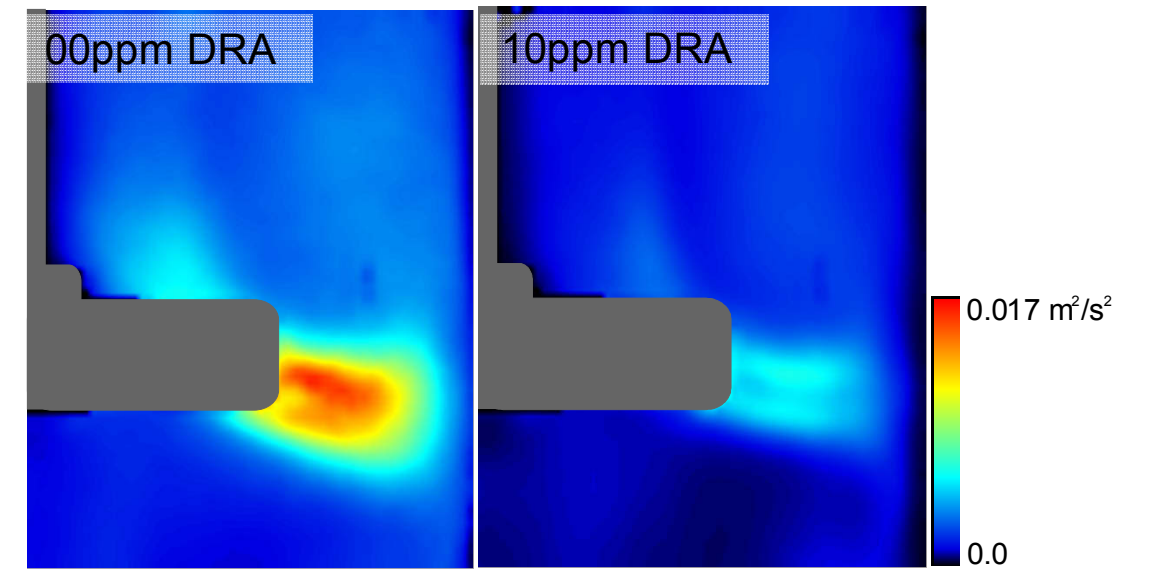

Figure 5.22. Turbulent kinetic energy fields.

More dramatic difference between 00 ppm and 10 ppm cases can be observed for the averaged turbulence kinetic energy (Figure 5.22). Without DRA the turbulence kinetic energy level is three times higher than with DRA. In both cases turbulence energy is restricted to the vicinity of the rotor.

The degradation of DRA was tested by repeating same experiment after 8 hours of mixing, which was the time needed to measure two window positions and six rotor angles for each. Turbulence kinetic energy for the 0deg rotor angle was compared for cases 00 ppm, 10 ppm (immediately after the addition of DRA) and 10 ppm + 8 hrs of mixing. The turbulence level after 8 hrs of mixing starts to rise again, but does not reach the level of 00 ppm case. The degradation was observed also in the PIV-images (not shown here), where tracer particle size grows due to agglomeration of particles. This was not observed in pure liav230 (or any application in water), which indicates the DRA molecules interact with tracer particles. Therefore any measurements with DRA should be conducted within few hours after the addition of DRA.

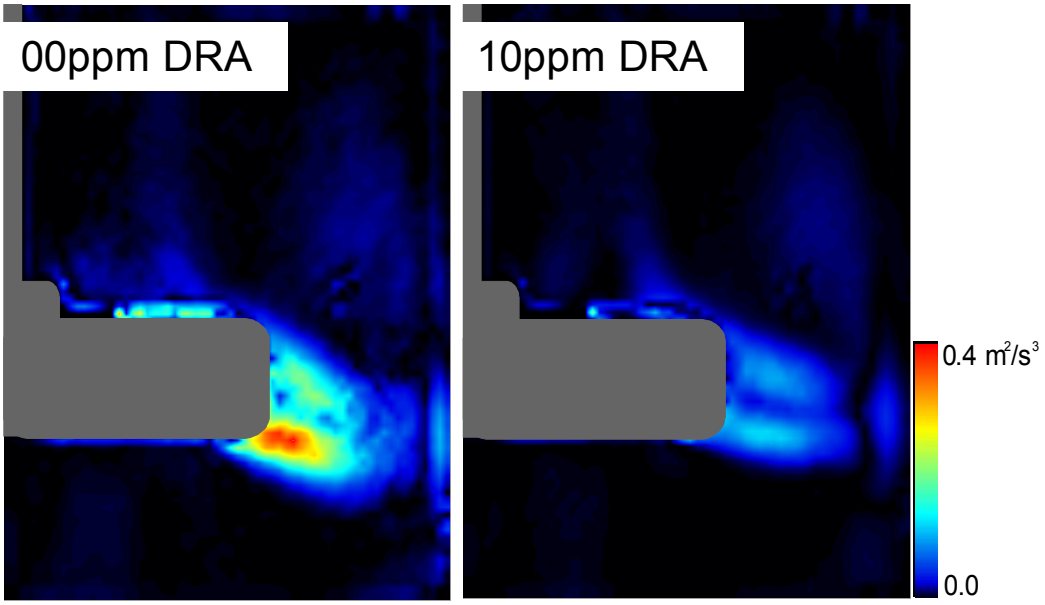

Figure 5.23. Turbulence production term from turbulent kinetic energy equation.

Turbulence production terms from turbulent kinetic energy equation (squared terms) are the following:

$$-\overline{u_i u_j}\frac{\partial \overline{U}_j}{\partial x_i} = \left\{ -\overline{u_1 u_1}\frac{\partial \overline{U}_1}{\partial x_1} - \overline{u_1 u_2}\frac{\partial \overline{U}_2}{\partial x_1} - \overline{u_1 u_3}\frac{\partial \overline{U}_3}{\partial x_1} \right.$$

$$- \overline{u_2 u_1}\frac{\partial \overline{U}_1}{\partial x_2} - \overline{u_2 u_2}\frac{\partial \overline{U}_2}{\partial x_2} - \overline{u_2 u_3}\frac{\partial \overline{U}_3}{\partial x_2}$$

$$\left. - \overline{u_3 u_1}\frac{\partial \overline{U}_1}{\partial x_3} - \overline{u_3 u_2}\frac{\partial \overline{U}_2}{\partial x_3} - \overline{u_3 u_1}\frac{\partial \overline{U}_3}{\partial x_3} \right\}$$

Turbulence production is computed using those terms available from PIV-data (no tangential velocities or tangential gradients). Production follows the trends explained for turbulence kinetic energy. Addition of DRA severely reduces turbulence production (Figure 5.23).

Turbulence dissipation term from turbulent kinetic energy equation is the following:

$$\nu\overline{\left(\frac{\partial u_i}{\partial x_j}+\frac{\partial u_j}{\partial x_i}\right)\frac{\partial u_j}{\partial x_i}} = \nu\Bigg\{ \boxed{2\overline{\left(\frac{\partial u_1}{\partial x_2}\frac{\partial u_2}{\partial x_1}\right)}} + 2\overline{\left(\frac{\partial u_1}{\partial x_3}\frac{\partial u_3}{\partial x_1}\right)} + 2\overline{\left(\frac{\partial u_2}{\partial x_3}\frac{\partial u_3}{\partial x_2}\right)}$$

$$+ \boxed{\overline{\left(\frac{\partial u_1}{\partial x_2}\right)^2}} + \boxed{\overline{\left(\frac{\partial u_2}{\partial x_1}\right)^2}} + \overline{\left(\frac{\partial u_1}{\partial x_3}\right)^2} + \overline{\left(\frac{\partial u_3}{\partial x_1}\right)^2} + \overline{\left(\frac{\partial u_2}{\partial x_3}\right)^2} + \overline{\left(\frac{\partial u_3}{\partial x_2}\right)^2}$$

$$+ \boxed{2\overline{\left(\frac{\partial u_1}{\partial x_1}\right)^2}} + \boxed{2\overline{\left(\frac{\partial u_2}{\partial x_2}\right)^2}} + 2\overline{\left(\frac{\partial u_3}{\partial x_3}\right)^2} \Bigg\}$$

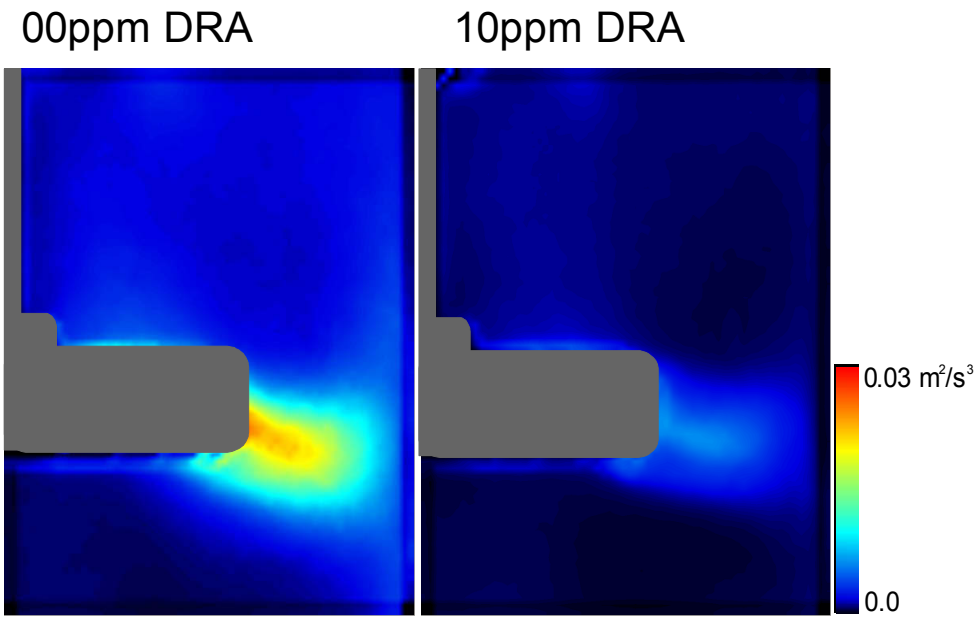

Figure 5.24. Turbulence dissipation term from turbulent kinetic energy equation.

Only terms in red squares are estimated from measurements. Higher production means also higher dissipation. Almost all the dissipation takes place close to the rotor, where gradients are strong and length scales small (Figure 5.24).

The change in the average length scale is studied by computing spatial auto-correlation functions in the region between the rotor and free surface. The homogeneity assumption is not strictly valid in the vessel making the interpretation of correlations questionable. Anyway, this technique does not show clear difference in the turbulence length scales. With DRA the spatial correlation is slightly better in the near range (0…5 mm lags), which is a sign of smoother field (larger length scale). In contrast, for larger length scales the results computed for 10 ppm case show less correlation.

Mean velocity fields in the radial-tangential -plane show remarkable difference between 00 ppm and 10 ppm cases. Without DRA there is a distinct boundary layer on the wall, whereas in the 10 ppm case the velocity remains constant right to the wall. Another difference is the mean velocity, which is higher in the 10 ppm case. This is supported by the flow visualization, which showed that fluid rises higher on the rim of the vessel.

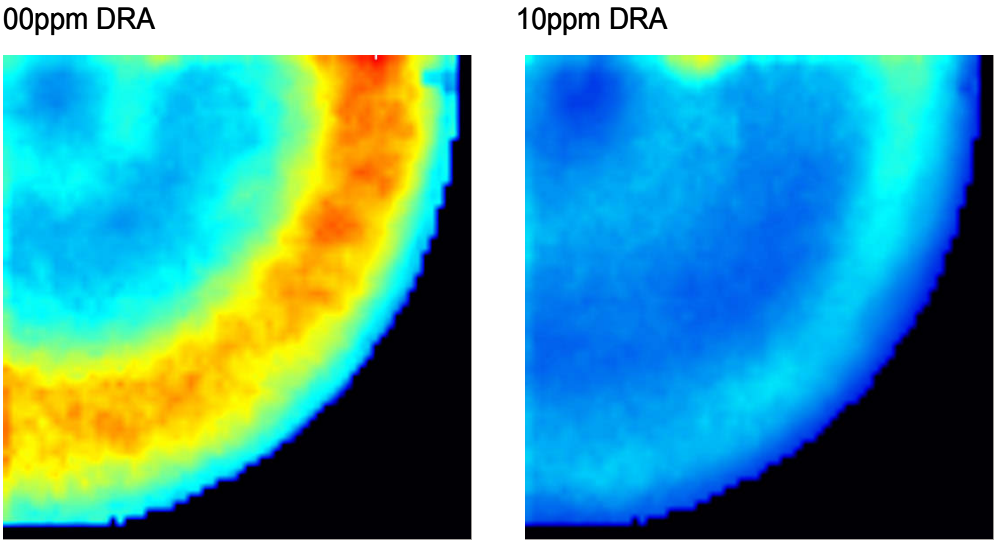

Figure 5.25. Turbulent kinetic energy fields.

Turbulence kinetic energy shows the same trend as observed in the axial-radial -plane (Figure 5.25). With DRA the turbulence energy is roughly 30% of the level measured without DRA. Thus, one conclusion is that the rotor energy in the 10ppm case is converted into solid body rotation of the fluid, because the friction at the wall is smaller and the turbulence near the wall is damped by the polymer, whereas without DRA much of the energy is converted into turbulent fluctuations.

Tank with baffles

Same results as for the no-baffles case were measured for the case, where baffles were inserted to the vessel. Since most observations are similar to the corresponding results presented above, only the most important issues are considered here. Further details can be found from Eloranta et al. [13].

In the 00 ppm case the average flow field from the rotor is directed more downwards as in the 10 ppm case. Streamlines reveal different flow patterns close to the free-surface. In the 00 ppm case, the large vortical motion starting from the rotor tip vortex extends near the free-surface. Also on the bottom half of the vessel difference between 00 ppm and 10 ppm cases is clear. In the 10 ppm case lower vortex forms closer to the rotor tip

and without DRA downward directed flow from the rotor keeps the separation of the vortices larger.

With baffles the level of turbulence kinetic energy is remarkably higher (maximum values 20 times larger) and more evenly distributed than in the previous case. The dissipation has same kind flow pattern, but the maximum values are doubled.

Baffles effectively kill the tangential motion, which is evident from the average velocity fields measured from the radial-tangential -plane. Velocities are only half of that seen in the no-baffles case. With baffles the 00ppm case shows higher mean velocity, but this is probably a result of the fact that the influence of the rotor penetrates deeper towards the bottom. Recirculation regions behind the baffles are evident and highest velocities are naturally located around the baffles.

Difference in turbulence kinetic energy with or without DRA is not as big as in the no-baffles case, but DRA clearly reduces turbulent fluctuations.

5.3.4 Further studies with two high polymers

Same results as for the previous cases were measured for the case, where two different high polymers were used at higher concentration with and without baffles at rotation speed 250 rpm. Since most observations are similar to the corresponding results presented above, only the most important issues are considered here. Further details can be found from Eloranta et al. [14].

The three tested fluids were

- case 00 ppm: 700 ml liav230 + 10 mm seeding particles
- case 30 ppm: 700 ml liav230 + 11.4 ml Necadd 447 or 547 + 10 mm seeding particles.

PIV-system was synchronized to the rotor position. A set of 100/500 images acquired for each angular position.

Dispersive mixing efficiency of the flow field can be evaluated in terms of its elongational flow components. These elongational flow components causes also polymer stretching. So it can be assumed that same parameter apply also for polymer efficiency studies. An extension parameter was used to better evaluate the differences between 00 ppm and 30 ppm cases. Definition of the extension parameter λ is

$$\lambda = \frac{S}{S + \Omega} \tag{5.1}$$

where the vorticity Ω tensor and rate of deformation tensors S are

$$\Omega = \frac{1}{2}\left(\frac{\partial U_i}{\partial x_j} - \frac{\partial U_j}{\partial x_i} \right) \qquad S = \frac{1}{2}\left(\frac{\partial U_i}{\partial x_j} + \frac{\partial U_j}{\partial x_i} \right). \tag{5.2}$$

Thus, λ obtains the value of 0.0 for pure rotation, 0.5 for pure shear (for example in a pipe flow) and 1.0 for pure deformation. It is then a dimensionless quantity which describes what the ratio of different stretching processes is. When evaluating the efficiency of the different flow fields for polymer influence not only the value of extension parameter is important but also the magnitude of (shear) stresses generated in the flow field.

Examples of instantaneous mixing parameter contours for upper half of the vessel at 250 RPM and 30 deg blade angle are given in Figure 5.26. For 00 ppm case the field seems to have smaller scales. The 30 ppm case has larger structures in the wall neighbourhood. The average values of the extension parameter show that shearing is stronger nearby the wall and that the 30 ppm case has slightly higher values towards deformation at vicinity of the propeller The probability density function of the instantaneous extension parameter at 30° blade angle in Figure 5.27 shows a bit different trend. The 30 ppm case peaks at 0.52 and has smaller values than 00 ppm case towards higher extension parameter values.

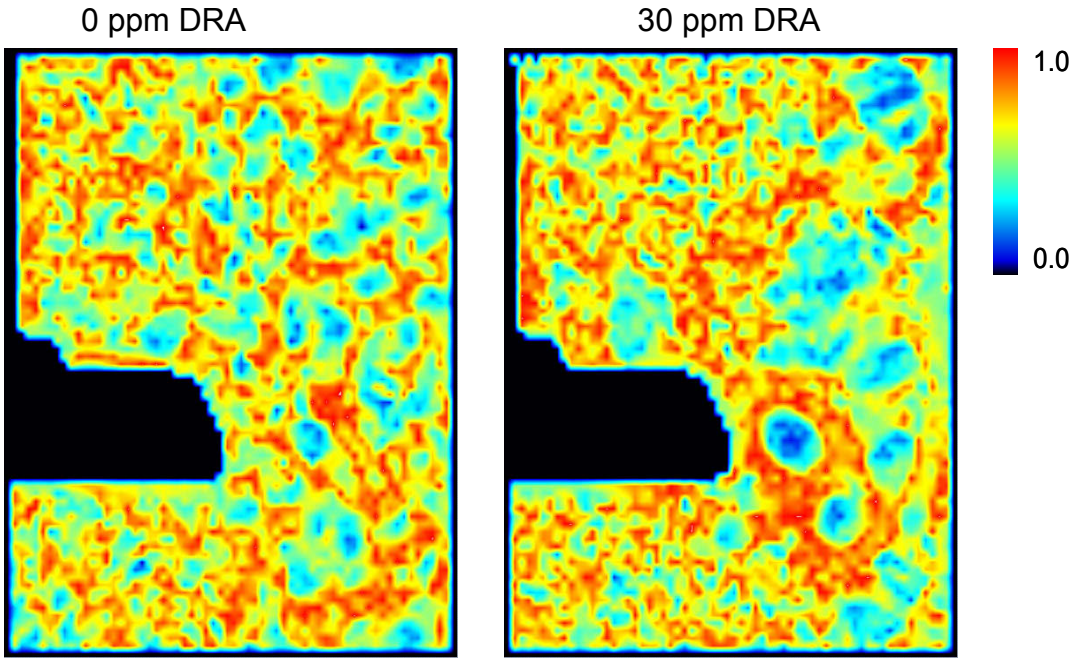

Figure 5.26. Examples of instantaneous mixing parameter contours for upper half of the vessel at 250 rpm and 30° blade angle.

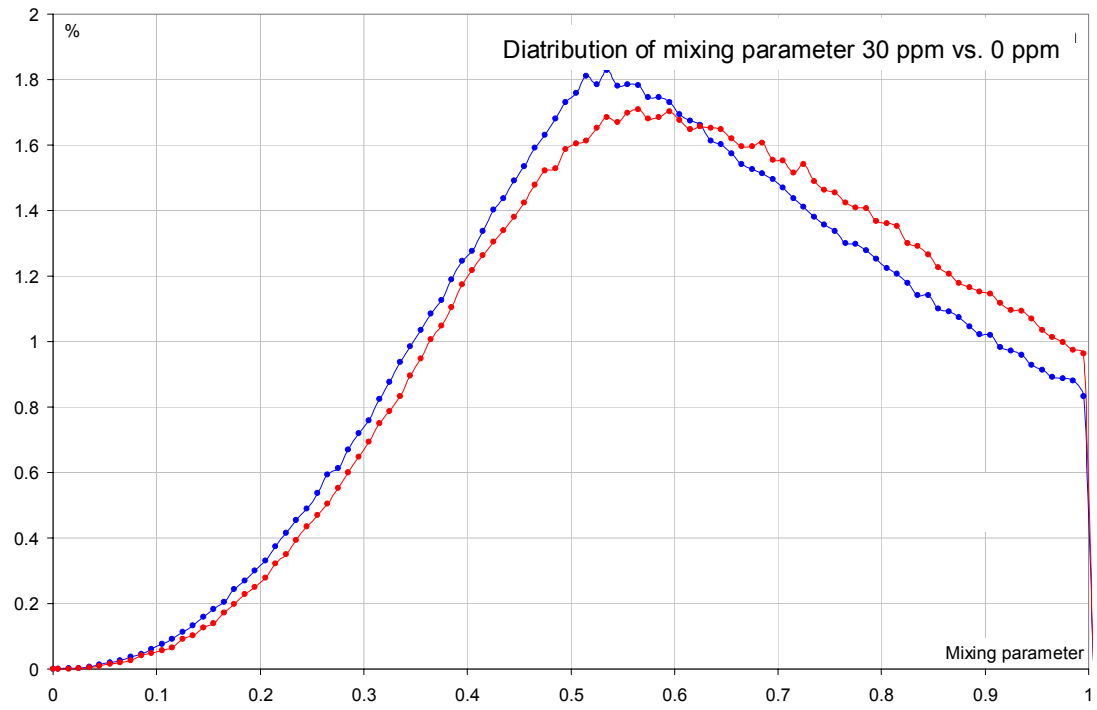

Figure 5.27. Probability density function of instantaneous mixing parameter values with and without DRA in the upper half of the vessel at 250 rpm and 30° blade angle. Blue curve: 30 ppm; red curve: 0 ppm.

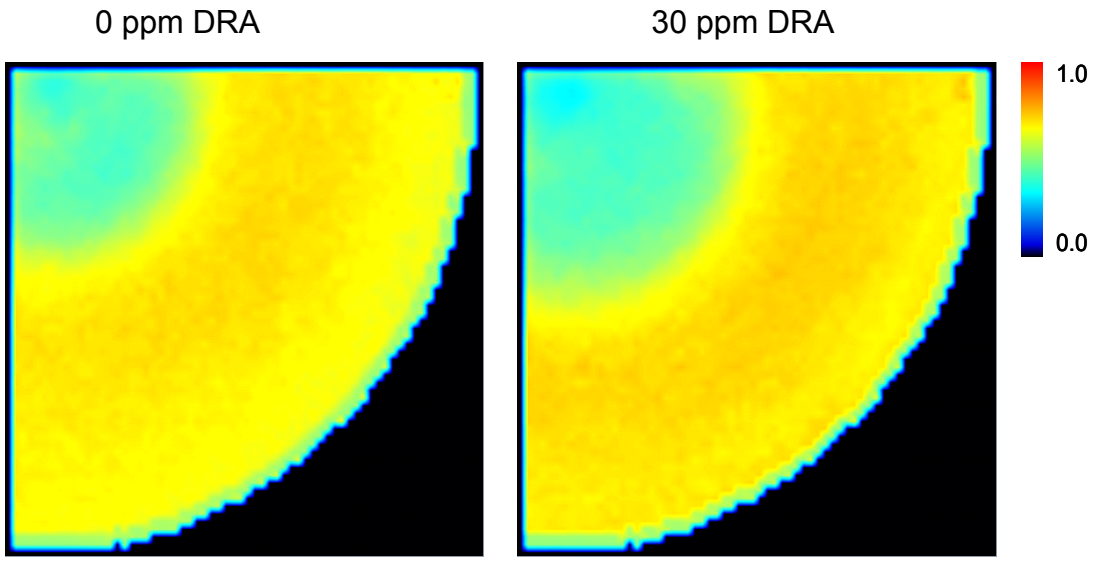

Figure 5.28. Mean contours of the mixing parameter 10 mm below the rotor at 250 rpm (no rotor synchronization).

The difference is partly explained by the fact that the flow goes more rapidly downwards at the 00 ppm case, so the contours are nearer the symmetry axis (Figure 5.28).

As a summary of these measurements can be stated that the differences in flow field properties between the two drag reduction agent is relative small. The results for the cases with and without baffles are similar as previous chapter and are reported in Eloranta et al. [14].

5.3.5 Conclusions

The effect of drag reducing agent to the flow field properties in a stirred tank reactor is difficult to evaluate, because the flow field itself is highly turbulent, three dimensional and without constant main flow direction. If there are baffles then the flow field is again more complex than without them. The effects observed in channel flows can not directly be found in a mixing tank flow field.

Section 5.3.1 lists seven remarks whose validity is now considered according to the measurements explained above. The polymer stretching caused by the flow field elongation was observed as the onset of DRA effect in measured cases. The onset requires a minimum turbulence level as noted in measurements. At low rotation speed there was not observed any effect. The effect was also not observed from spatially averaged results. Instead in blade angle resolved measurements the DRA effect was observed when the maximum values of turbulence quantities were studied. Also the effect is strongest at high turbulence positions like in trailing vortices of the blades. The tendency towards more inhomogeneous flow field could not be observed from the results. Only weak observation of this effect was that the extension parameter probability density was moved towards shear stress domination. The reduction of Reynolds stresses and root mean square velocity fluctuations was clearly observed when the maximum values of these quantities were studied. The difference in the Reynolds stresses depends on blade angle, far away from the blade the difference vanishes. This is an indication of the polymeric stress which is reduced when the turbulence intensity is lowering. The large scale turbulent structures were measured to decrease in size and number. The presence, number and size of polymer aggregates were not studied. The change in energy cascade was observed to some extent from dissipation rate measurements. All the values were higher for water case. This result is based on spatially weakly resolved measurements which results in the smaller difference in maximum dissipation values DRA vs. water at high turbulence area (near the blade). Another supporting observation for the change in energy cascade is that the spatial autocorrelation function has at low separation distances higher values. The spectrum is moved to the left. The turbulence production and dissipation terms of the kinetic energy equation were noted to be strongly reduced in DRA cases of oil solution.

The detection of the drag reduction effect in stirred tank with and without baffles is a demanding task. Not only the flow field is difficult to measure but also the phenomena are tricky. The onset and existence of maximum DRA effect make the detection even more cumbersome. The measurement at smallest scales of turbulence is required to get direct information of the effect. This is not applicable and in this work an indirect relative information is used where the quantities are compared in pure liquid and added drag reduction agent cases. Anyway the majority of the phenomena in remarks (Section 5.3.1) were observed from the measurement results. The achieved results show that the drag reduction in stirred vessel is analogous to the channel flow case; it is only more difficult to observe.

5.4 The effect of drag reducing polymers in pipe flow

5.4.1 Background

The purpose of this present work has been to provide a comparison of the drag reducing characteristics to molecular weight and polymer concentration. Solutions of polyacrylamide (PAM) as a drag reducing agent were used ranging from $3 \cdot 10^6$–$20 \cdot 10^6$ g/mol in molar mass and 4–64 wppm in concentration. Measurements of pressure drop and Reynolds number were made.

5.4.2 Equipment

The measurements of pressure drop were made according to Figure 5.29, when changes to turbulent flow caused by baffles were registered. The apparatus (Figure 5.31) consisted of two baffles, a static mixer (X101, Figure 5.32) and two flow elbows (Figure 5.33). Pressure was measured with sensors Pt102–Pt110. The average DR effect was determined between consecutive pressure sensors. DR effect was calculated as follows:

$$DR(\%) = \frac{(\Delta P_0 - \Delta P_P)}{\Delta P_0} \tag{5.3}$$

where ΔP_0 and ΔP_P are the pressure differences between sensors for water and for water-polyacrylamide solution, respectively. Measurement data was saved as Excel files, and the results for DR effect were calculated with the help of formula (5.3).

The measuring accuracy for the pressure sensors (two decimals) was not accurate enough when flow velocity was below 1 m/s. When Reynolds number was > 20000, the pressure difference was sufficient enough in order to carry out the experiments.

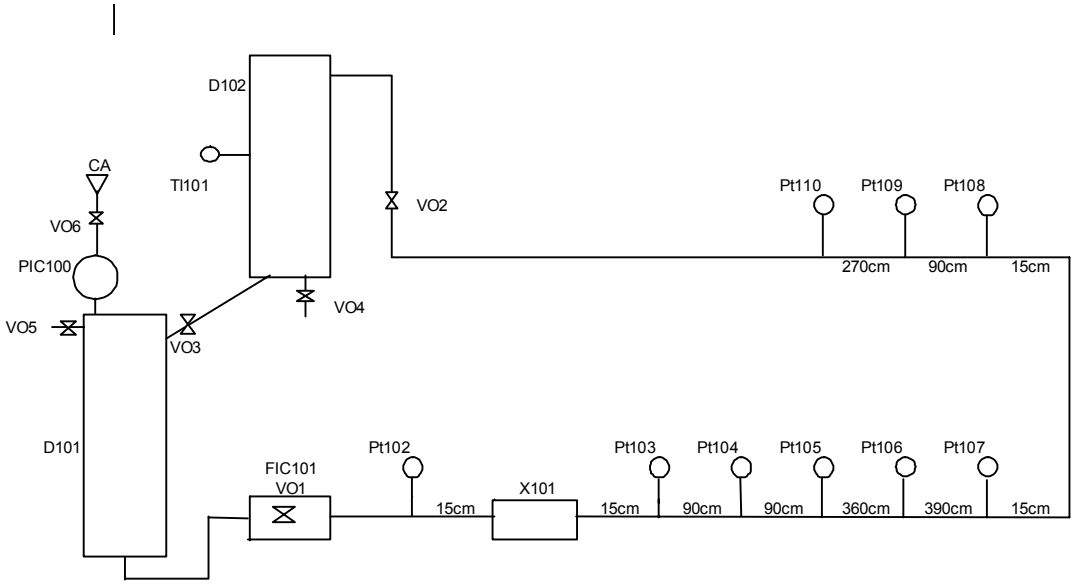

Figure 5.29. The measuring equipment.

The inner diameter of the pipe was 20 mm and combined length of the pipelines was approximately 25 meters.

5.4.3 Measurements

The water/polyacrylamide solution was made in a mixing tank D102. To achieve homogeneity of the solution and to even out the temperature the mixing was carried out over night. The measurements were made on a temperature scale of 14–18 °C. First the pressurized tank D101 was filled to a certain volume by opening the valve VO3 and the aeration valve VO5. After the tank was filled the valves were closed and the tank was pressurized with pressurized air (VO6). The driving force of liquid flow was therefore pressurized air, thus no pump was needed. The intention was to keep the polymer from degrading. The flow was adjusted with a ball valve VO1 (FIC101) to match Reynolds numbers 25000 and 40000. All the measurements were carried out twice. The data was collected with Chemwell Windowviewer InTouch 7.1.

The measurements made are collected in Table 5.2.

Table 5.2. The measurements.

Molar mass (10^6 g/mol)	Concentration (wppm)				
20	64	32	16	8	4
10	64	32	16	8	4
5	64	32	16	8	4
3	64	32	16	8	4

5.4.4 Results

The results for four different polyacrylamide solutions (molar masses 20, 10, 5 and 3 (10^6) g/mol) after the static mixer for Reynolds number 25000 are presented in Figure 5.30.

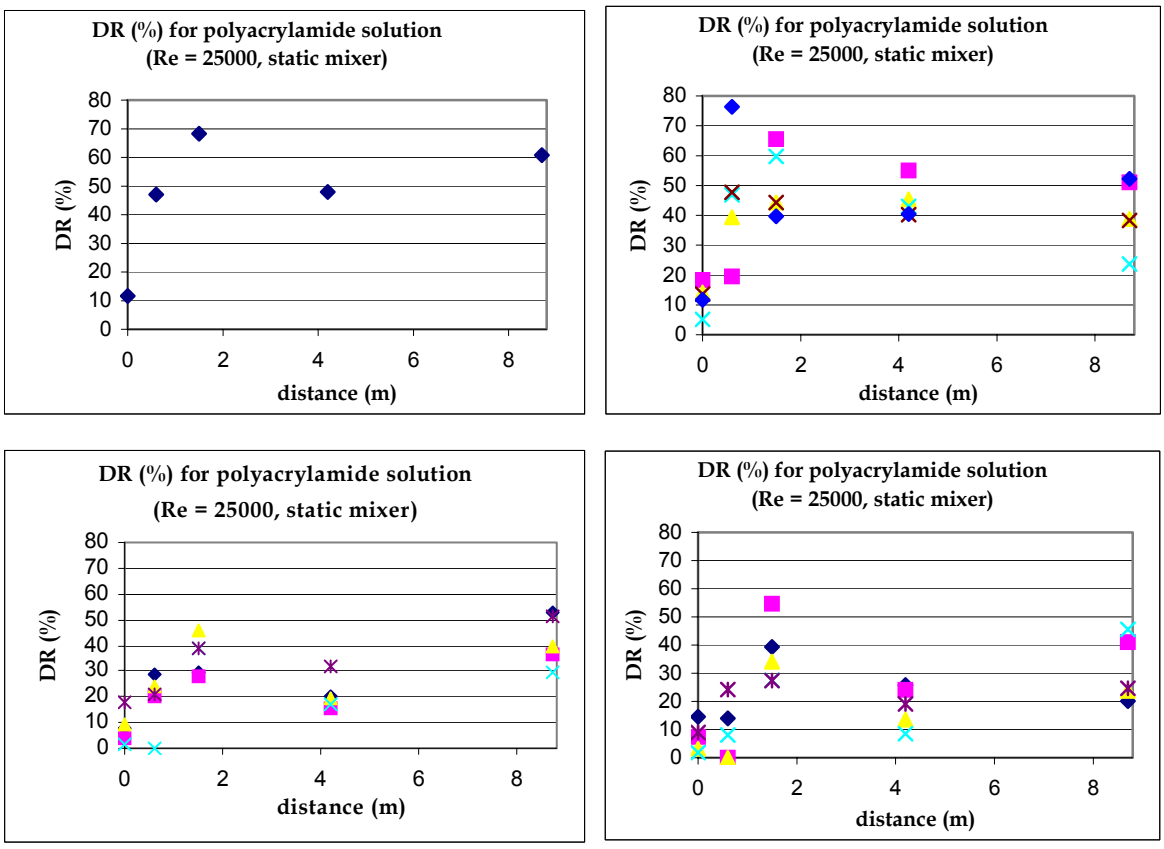

Figure 5.30. The DR effect (%) as a function of pipe length after the static mixer (20 M left upper corner, 10 M right upper corner, 5 M left down corner and 3 M right down corner). The concentrations were 64 wppm (blue), 32 wppm (pink), 16 wppm (yellow), 8 wppm (turquoise) and 4 wppm (brown).

Figure 5.31. The pressurized feed tank on the left (D101) with a tube coming from the bottom of the tank leading to ball valve (VO1). On the left upper corner is the mixing tank (D102).

Figure 5.32. Static mixer (X101) and pressure sensors Pt102 and Pt103.

Figure 5.33. Flow elbows and pressure sensors Pt107 and Pt108.

5.5 Turbulence model for polymeric drag reduction

5.5.1 Background

The possibilities and difficulties to extend the well known and much applied k-□ model [15] to suit for drag reduction calculations are studied. The goal of this work was to develop a CFD model based on well known k-□ model for polymeric drag reduction. Main actions in this work were

1. form the governing equations: momentum and simple linear dumbbell polymer stress model
2. Reynolds average the governing equations
3. apply k-□ model for velocity-, k- and□-equations without elastic stress
4. form one new equation for elastic energy, K_e and identify the new terms in the governing equations
5. write the new terms by k, □ and K_e
6. implement the model in the Fluent CFD code
7. fit the model parameters.

All these actions were successfully carried out, and the developed model is able to reduce drag correctly, if the Reynolds number is not too high. The model was tested by spatially constant coupling parameter (between k and elastic energy), but more work is needed to develop a functional dependence on turbulent parameters for this coupling parameter. Also, more work is needed to study the new term in the □-equation.

5.5.2 Governing equations for viscoelastic flow

Viscoelastic fluids and their flow properties are discussed in detail by Bird et al. [16–17], and in the following some of this work is briefly reviewed in order to further develop those models for the present purposes. The governing equations, a modified Navier-Stokes for momentum and standard continuity equation, for incompressible viscoelastic flow are [16]

$$\frac{\partial U_i}{\partial t} + U_j \frac{\partial U_i}{\partial x_j} = -\frac{1}{\rho}\frac{\partial P}{\partial x_i} + \nu_s \frac{\partial^2 U_i}{\partial x_j \partial x_j} + \frac{1}{\rho}\frac{\partial \mathrm{T}_{ij}}{\partial x_j} \tag{5.4}$$

where summation over repeated indices is assumed, and

$$\frac{\partial U_i}{\partial x_i} = 0 \tag{5.5}$$

where ν_s is the solution kinematic viscosity, ρ is the solution density and T_{ij} are the components of viscoelastic stress tensor. The viscoelastic contribution for the stress tensor satisfies the following equation for ideal Hookean dumbbell model of polymer [17]:

$$\lambda\left[\frac{\partial \mathrm{T}_{ij}}{\partial t}+U_k\frac{\partial \mathrm{T}_{ij}}{\partial x_k}-\frac{\partial U_i}{\partial x_l}\mathrm{T}_{lj}-\frac{\partial U_j}{\partial x_l}\mathrm{T}_{li}\right]+\mathrm{T}_{ij}=k_BNT\lambda\left[\frac{\partial U_i}{\partial x_j}+\frac{\partial U_j}{\partial x_i}\right], \tag{5.6}$$

where $\lambda=\zeta/4H$ is the time constant of the dumbbell, ζ is the friction coefficient (friction force $\mathbf{f}=-\zeta\mathbf{v}$) and H is the spring constant.

5.5.3 Viscoelastic energy balance

The energy budget for viscoelastic fluid flow is given by

$$\frac{d}{dt}\int\frac{1}{2}U_i^2dv=\int\Delta dv-\int\mathrm{X}dv\,, \tag{5.7}$$

where the first term on the right is the dissipation of fluid kinetic energy to heat

$$\Delta=\frac{1}{2}\nu_s\left(\frac{\partial U_i}{\partial x_j}+\frac{\partial U_j}{\partial x_i}\right)\left(\frac{\partial U_i}{\partial x_j}+\frac{\partial U_j}{\partial x_i}\right), \tag{5.8}$$

and the second term corresponds to the exchange between kinetic and elastic energy

$$\mathrm{X}=\frac{1}{\rho}\mathrm{T}_{ij}\frac{\partial U_i}{\partial x_j}. \tag{5.9}$$

The evolution of elastic energy per unit mass $K_e=\frac{1}{2}\mathrm{T}_{ii}/\rho$ is governed by

$$\frac{d}{dt}\int K_e dv=-\int\frac{K_e}{\lambda}dv+\int\mathrm{X}dv \tag{5.10}$$

where the first term on the right is the dissipation of elastic energy to heat and the second term is the same exchange term as in previous equation for fluid kinetic energy.

5.5.4 1- and 2-dimensional studies

It is straightforward to show that in 1-dimensional shear flow the elastic and viscous dissipation rates are, related as

$$\frac{K_e}{\lambda} = \frac{\mathrm{T}_{11}}{2\lambda\rho} = \mathrm{Bd}\Delta\,, \tag{5.11}$$

where a new dimensionless number Bd is defined as

$$\mathrm{Bd} = \frac{Nk_BT\lambda}{\mu_s} = \frac{\text{elastic dissipation rate}}{\text{viscous dissipation rate}}\,. \tag{5.12}$$

The diffusivity coefficient or elastic viscosity is defined as

$$\nu_E = \frac{Nk_BT\lambda}{\rho}\,. \tag{5.13}$$

Thus, the dimensionless number Bd may also be expressed as a ratio of elastic and kinematic viscosity

$$\mathrm{Bd} = \frac{\nu_E}{\nu_s} = \frac{Nk_BT\lambda}{\mu_s}\,. \tag{5.14}$$

A bit more complicated calculations show that for 2-dimensional shear flow the elastic energy K_e may be written as

$$\frac{K_e}{\lambda} = \frac{\mathrm{Bd}\Delta}{1-\lambda^2\left(\frac{\Delta}{\nu_s}-\Omega^2\right)} \tag{5.15}$$

where Ω is the 2-dimensional vorticity.

The elastic energy will approach infinity when the denominator goes to zero, which occurs when

$$\lambda \cong \frac{1}{\sqrt{\frac{\Delta}{\nu_s}-\Omega^2}}\,. \tag{5.16}$$

Eq. (5.15) will also give negative, unphysical, elastic energy values, if the product of velocity gradients and polymer timescales is high enough. The assumption of constant values of velocity and elastic tensor gradients starts also to fail, when gradients start to get these higher values, and Eq. (5.15) should therefore considered only as an indication of possible resonance points or domains.

5.5.5 Reynolds averaged models

First, the energy balance for coupled momentum and elastic stress tensor equations are studied to find the energy dissipation processes of the elasticity. Second, the coupled system is Reynolds averaged. Third, for the Reynolds averaged system evolution equations for turbulent energy, dissipation of turbulent energy and elastic energy are developed. Fourth, an equation for elastic energy in the k-ε model is added and the relevant additional terms in k - and ε -equation are studied by dimensional analysis and analysing the set of equations in log-layer. All Reynolds averaged equations are collected in Table 5.3.

Table 5.3. Reynolds averaged equations.

$$\frac{\partial \overline{U_i}}{\partial t} + \overline{U_j}\frac{\partial \overline{U_i}}{\partial x_j} = -\frac{\partial}{\partial x_j}\left(\overline{u_i u_j}\right) - \frac{1}{\rho}\frac{\partial \overline{P}}{\partial x_i} + \nu\frac{\partial^2 \overline{U}_i}{\partial x_j \partial x_j} + \frac{1}{\rho}\frac{\partial \overline{\mathrm{T}_{ij}}}{\partial x_j}$$

$$\frac{\partial \overline{U_i}}{\partial x_i} = 0 \quad \text{and} \quad \frac{\partial u_i}{\partial x_i} = 0$$

$$\frac{\partial k}{\partial t} + \overline{U_k}\frac{\partial k}{\partial x_k} = -\overline{u_i u_k}\frac{\partial \overline{U_i}}{\partial x_k} - \frac{1}{\rho}\overline{u_i}\frac{\partial \overline{p}}{\partial x_i} + \frac{\partial}{\partial x_k}\left\{-\overline{\tfrac{1}{2}u_i u_i u_k} + \overline{\nu_s u_i\left[\frac{\partial u_i}{\partial x_k} + \frac{\partial u_k}{\partial x_i}\right]} + \overline{\frac{u_i \tau_{ik}}{\rho}}\right\} - \overline{\varepsilon} - \overline{\chi}$$

$$\frac{\partial K_e}{\partial t} + \overline{U}_k\frac{\partial K_e}{\partial x_k} + \frac{1}{\rho}\overline{u_k\frac{\partial \frac{1}{2}\tau_{ii}}{\partial x_k}} = \frac{1}{\rho}\overline{\mathrm{T}}_{ik}\frac{\partial \overline{U}_i}{\partial x_k} + \frac{1}{\rho}\overline{\tau_{ik}\frac{\partial u_i}{\partial x_k}} - \frac{K_e}{\lambda}$$

$$\frac{\partial \varepsilon}{\partial t} = \left[\text{viscous part}\right] + \frac{2\nu_s}{\rho}\left[\overline{\left(\frac{\partial u_i}{\partial x_j} + \frac{\partial u_j}{\partial x_i}\right)\frac{\partial^2 \tau_{ik}}{\partial x_j \partial x_k}} + \overline{u_i\frac{\partial^3 \tau_{jk}}{\partial x_i \partial x_j \partial x_k}}\right]$$

Log surface layer in the extended k-ε model

In this section extended model is studied in log surface layer – and the approach follows the previous section. The easiest way to arrive at the log-layer equations is to start by sub layer equations and then to determine the form of the equations as the dimensionless distance, $y^+ = u_\tau y/\nu_s$ approaches infinity (e.g. Wilcox [18]). The friction velocity is given by

$$u_\tau = \sqrt{\frac{\tau_w}{\rho}} \tag{5.17}$$

where τ_w is the shear stress at the wall.

In the log-layer, the mean velocity U is in the x-direction, but the gradients in y-direction dominate

$$U_1 = U(y). \tag{5.18}$$

It is possible to simplify complete set of equations to a one-dimensional form

$$\left.\begin{aligned}
0 &= \frac{u_\tau}{\nu_s}\frac{\partial}{\partial y^+}\left[\nu_T^+ u_\tau^2 \frac{\partial U^+}{\partial y^+}\right] \Rightarrow \frac{\partial U^+}{\partial y^+} = \frac{1}{\kappa y^+} \\
0 &= \nu_T^+\left(\frac{\partial U^+}{\partial y^+}\right)^2 - \varepsilon^+ - \gamma_k \mathrm{Bd}\varepsilon^+ + \frac{\partial}{\partial y^+}\left[\frac{\nu_T^+}{\sigma_k}\frac{\partial k^+}{\partial y^+}\right] \\
0 &= C_{\varepsilon 1} C_\mu k^+ \left(\frac{\partial U^+}{\partial y^+}\right)^2 - C_{\varepsilon 2}\frac{\left(\varepsilon^+\right)^2}{k^+} - \frac{\nu_T^+ \gamma_\varepsilon}{K_e^+/\lambda^+}\left[\frac{\partial\left(K_e^+/\lambda^+\right)}{\partial y^+}\right]^2 + \frac{\partial}{\partial y^+}\left[\frac{\nu_T^+}{\sigma_\varepsilon}\frac{\partial \varepsilon^+}{\partial y^+}\right] \\
0 &= \gamma_5 \gamma_k \mathrm{Bd}\varepsilon^+ - \frac{K_e^+}{\lambda^+} + \frac{\partial}{\partial y^+}\left(\frac{\nu_T^+}{\sigma_{K_e}}\frac{\partial K_e^+}{\partial y^+}\right) \\
\nu_T^+ &= \kappa y^+
\end{aligned}\right\} \tag{5.19}$$

where

$$\begin{aligned}
y^+ &\equiv \frac{u_\tau}{\nu_s} y \\
U^+ &\equiv \frac{U}{u_\tau} \\
\nu_T^+ &\equiv \frac{\nu_T}{\nu_s} \\
k^+ &\equiv \frac{k}{u_\tau^2} \\
\varepsilon^+ &= \frac{\nu_s}{u_\tau^4}\varepsilon \\
K_e^+ &\equiv \frac{K_e}{u_\tau^2} \\
\lambda^+ &\equiv \frac{u_\tau^2}{\nu_s}\lambda
\end{aligned} \quad . \tag{5.20}$$

The velocity gradient is the same as in standard model – only the values of coefficient κ and parameter u_τ may change. If the coefficient γ_k is assumed to be a constant, it is possible to assume that k is constant like in the standard model. ε is solved from the k-equation

$$\varepsilon^+ = \frac{1}{\kappa y^+ \left(1+\gamma_k \mathrm{Bd}\right)}, \tag{5.21}$$

and substitution to the equation for turbulent viscosity gives

$$k^+ = \frac{1}{\sqrt{C_\mu \left(1+\gamma_k \mathrm{Bd}\right)}} = \frac{k_0}{\sqrt{1+\gamma_k \mathrm{Bd}}}. \tag{5.22}$$

Now, there is one free parameter κ and one free function K_e, for which there are two equations left:

$$\left.\begin{aligned} &\kappa^2 - \frac{\left(\kappa y^+\right)^3 \sigma_\varepsilon \gamma_\varepsilon}{\lambda^+ K_e^+}\left[\frac{\partial K_e^+}{\partial y^+}\right]^2 = \sigma_\varepsilon \sqrt{C_\mu}\left[C_{\varepsilon 1}\sqrt{1+\gamma_k \mathrm{Bd}} - \frac{C_{\varepsilon 2}}{\sqrt{1+\gamma_k \mathrm{Bd}}}\right] \\ &\frac{\partial}{\partial y^+}\left(\frac{\kappa y^+}{\sigma_{K_e}}\frac{\partial K_e^+}{\partial y^+}\right) - \frac{K_e^+}{\lambda^+} = -\frac{\gamma_5 \gamma_k \mathrm{Bd}}{\left(1+\gamma_k \mathrm{Bd}\right)\kappa y^+} \end{aligned}\right\}. \tag{5.23}$$

The equation set is rather complex to be solved analytically and it has been planned to find some iterative solutions. In the next section a solution assuming the first term of the second equation to be negligible is applied.

Conceptual description of the extended k-ε model

Long polymer chains in solutions are curling up big (at least compared to molecular mass) porous spherical systems, if the velocity gradients over the single polymer volume are small enough. Typical number of monomers is of the order of 10^5, which means that molecular mass is of the order of 1000–10000 kg/mol. The diameter of polymer tangles (of the discussed size class) is of the order of 100–400 nm, which means that per one monomer there can be about 10000 water molecules inside the tangle [2].

If a polymer on the other hand is in solution where velocity gradients are high enough, the polymer starts to stretch. In very high velocity gradients a polymer can open totally; further increase of at the gradient may break the polymer chain. In model calculations a polymer is typically described as an elastic dumbbell – all forces affecting only on the end "beads" of the polymer chain. A set of models have been developed to describe the force between beads.

Some conceptual reasoning is possible to obtain from the extended k-ε model without any CFD-implementations and calculations. In Figure 5.34 the energy balance of the model is sketched at low and high elasticity (viscous vs. viscoelastic flow) and degree of turbulence (laminar vs. turbulent flow). In the extended k-ε model, both the mean and turbulent flow energy might be converted to elastic energy, which can dissipate itself (possibly in some other location due to turbulent diffusion).

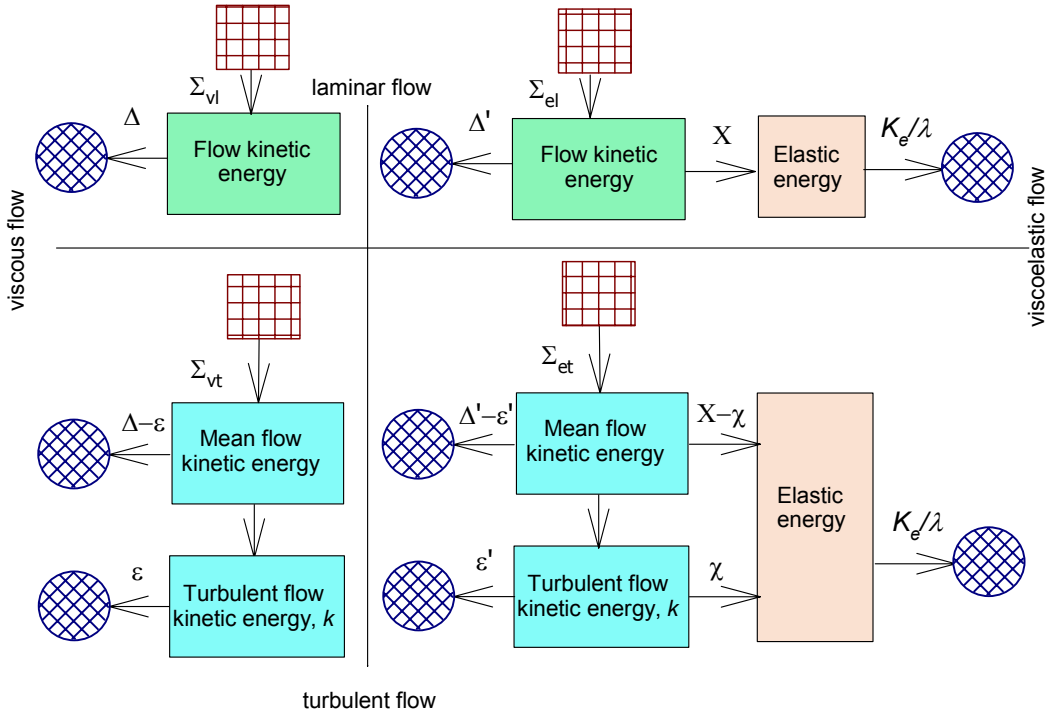

Figure 5.34. On the left hand side are viscous models while on the right hand side are viscoelastic models. The upper part is for laminar and lower part for turbulent flows. The squares denote energy source, while circles denote energy sinks or transform of mechanic energy to thermal.

It is also possible to study the energy balance in the log-layer, by comparing viscoelastic case to reference case of no elasticity (denoted by zero below, and α is the ratio of friction velocities):

$$
\begin{aligned}
&u_\tau = \alpha u_{\tau 0} \Rightarrow \\
&k = \frac{\alpha^2}{\sqrt{1+\gamma_k \mathrm{Bd}}} k_0 \\
&\varepsilon = \frac{\kappa_0}{\kappa} \frac{\alpha^3}{1+\gamma_k \mathrm{Bd}} \varepsilon_0 \\
&\frac{K_e}{\lambda} = \alpha^3 \frac{\kappa_0}{\kappa} \frac{\gamma_k \mathrm{Bd}}{1+\gamma_k \mathrm{Bd}} \varepsilon_0 \\
&\kappa^2 = \frac{\sigma_\varepsilon \sqrt{C_\mu}}{1-\gamma_\varepsilon \gamma_k \mathrm{Bd} \sigma_\varepsilon} \left(\frac{C_{\varepsilon 2}}{\sqrt{1+\gamma_k \mathrm{Bd}}} - C_{\varepsilon 1} \sqrt{1+\gamma_k \mathrm{Bd}} \right)
\end{aligned}
\quad . \tag{5.24}
$$

It is instructive to write the sum of turbulent and elastic energy and dissipation:

$$
\begin{aligned}
&k + K_e = \frac{\alpha^2}{\sqrt{1+\gamma_k \mathrm{Bd}}} k_0 + \lambda \frac{\kappa_0}{\kappa} \frac{\gamma_k \mathrm{Bd} \alpha^3}{1+\gamma_k \mathrm{Bd}} \varepsilon_0 \\
&\varepsilon + \frac{K_e}{\lambda} = \frac{\kappa_0}{\kappa} \alpha^3 \varepsilon_0 < \varepsilon_0
\end{aligned}
\quad . \tag{5.25}
$$

At maximum drag reduction by applying Virk's profile the ratio of slopes is

$$
\frac{\kappa_0}{\kappa_{Virk}} \cong \frac{11.7}{2.5} \cong 4.7 \, . \tag{5.26}
$$

On the other hand the coefficient α may be approximated by

$$
\alpha = \frac{u_\tau}{u_{\tau 0}} = \sqrt{\frac{\tau_w}{\tau_{w0}}} \approx \sqrt{1 - DR} \approx \sqrt{0.36} = 0.6 \, , \tag{5.27}
$$

where DR is the drag reduction. Therefore,

$$
\begin{aligned}
&k + K_e = \frac{\alpha^2}{\sqrt{1+\gamma_k \mathrm{Bd}}} k_0 + \lambda \frac{\kappa_0}{\kappa} \frac{\gamma_k \mathrm{Bd} \alpha^3}{1+\gamma_k \mathrm{Bd}} \varepsilon_0 \\
&\varepsilon + \frac{K_e}{\lambda} = \frac{\kappa_0}{\kappa} \alpha^3 \varepsilon_0 = 4.7 \times 0.6^3 \varepsilon_0 \cong \varepsilon_0
\end{aligned}
\quad . \tag{5.28}
$$

If $\gamma_k \mathrm{Bd}$ is high

$$
\frac{K_e}{\lambda} \cong \varepsilon_0 \, . \tag{5.29}
$$

Therefore, the energy balance changes from turbulent energy and dissipation to elastic energy and its dissipation – the flow should anyway still be characterized as turbulent.

5.5.6 Summary and conclusions

It is a difficult task to modify the viscoelastic governing equations to an extension of k-ε model. There are many reasons for that: there exists several polymer models and the tensor character of elastic term must be governed by a scalar equation, not to mention generally poor knowledge about turbulence.

Anyway, it was possible to develop an extended k-ε model, but many approximations, which may be plausible or not, were done. These approximations should be tested both in simple pipe flows and also in more complicated flows. A comparison with present and future direct numerical simulations (DNS) will help in the formation of better terms to various correlations, but in this work results from DNS were applied only in very limited fashion.

Model fitting and testing against experiments was made only in the sense that model was implemented in Fluent 6.1 and fitting was made to observe the formation of Virk's profile, which was successful. The plausibility of fitted parameters is left open, as is the link of parameter values to real polymeric properties. The developed extended model includes a prediction of the dependence on these polymeric and system properties, but it was not yet tested.

In future the extended k-ε model may be improved by wider application of both results from direct numerical simulations and experimental data (both in simple and more complicated geometry). The model implementation is directly extendable to complicated geometry. The energy flux from mean flow to elastic energy should be, though, considered, and its implementation may demand some more programming work for a suitable UDF (User Defined Function) in Fluent. And, the possibility of dynamic exchange coefficient between turbulent kinetic energy and elastic energy may be worth of more studies, because it may make the model more realistic and extend the applicability, which was observed to be limited – at least at higher values of Reynolds number.

References

1. Dubief, Y., Terrapon, V. E., White, C. M., Shaqfeh, E. S. G., Moin, P. & Lele, S. K. 2005. New Answers on the Interaction Between Polymers and Vortices in Turbulent Flows. Flow, Turbulence and Combustion, 74, 311–329.

2. Gyr, A. & Bewersdorff, H.-W. 1995. Drag reduction of turbulent flows by additives. Kluwer Academic Publishers, Dordrecht, the Netherlands. ISBN 0-7923-3485-X.

3. Benzi, R., De Angelis, E., L'vov, V. S., Procaccia, I. & Tiberkevich, V. 2005. Maximum Drag Reduction Asymptotes and the Cross-Over to the Newtonian Plug. Under consideration for publication in J.Fluid.Mech.

4. Yu, B. & Kawaguchi, Y. 2004. Direct numerical simulation of viscoelastic drag-reducing flow: a faithful finite difference method. J. Non-Newtonian Fluid Mech., 116, 431–466.

5. Dubief, Y., Iaccarino, G. & Lele, S. K. 2004. A turbulence model for polymer flows. Center for Turbulence Research, NASA Ames/Stanford Univ., pp. 63–73.

6. Min, T., Yoo, J. Y., Choi, H. & Joseph, D. D. 2003. Drag reduction by polymer additives in a turbulent channel flow. J. Fluid. Mech., Vol. 486, 213–23.

7. Ptasinski, P., Boersma, B., Nieuwstadt, F., Hulsen, M., Van Den Brule, B. & Hunt, J. 2003. Turbulent channel flow near maximum drag reduction: simulations, experiments and mechanisms. J. Fluid Mech., Vol. 490, 251–291.

8. Dimitropoulos, C. D., Sureshkumar, R. & Beris, A. N. 1998. Direct Numerical Simulation of Viscoelastic Turbulent Channel Flow Exhibiting Drag Reduction: Effect of the Variation of Rheological Parameters. J. Non-Newtonian Fluid Mech., 79, 433–468.

9. Sureshkumar, R., Beris, A. N. & Handler, R. A. 1997. Direct numerical simulations of turbulent channel flow of a polymer solution. Phys. Fluids, 9 (3), 743–755.

10. Lumley, J. L. 1969. Drag reduction by additives. Annu. Rev. Fluid Mech., 1, 367–384.

11. de Gennes, P. G. 1990. Introduction to Polymer Dynamics. Cambridge University Press.

12. Saikkonen, T., Eloranta, H. & Saarenrinne, P. 2005. DRA-vesiliukoksen käyttäytyminen sekoitinsäiliössä. TTY, energia- ja prosessitekniikka, tutkimusraportti.

13. Eloranta, H., Pärssinen, T. & Saarenrinne, P. 2003. Results from DRA measurements in a mixing vessel. TUT, Energy and Process Engineering, Research report.

14. Eloranta, H., Pärssinen, T. & Saarenrinne, P. 2004. DRA effect measurements in a mixing vessel. TUT, Energy and Process Engineering, Research report.

15. Jones, W. P. & Lauder, B. E. 1972. The prediction of laminarization with a two-equation model of turbulence. International Journal of Heat and Mass Transfer, Vol. 15, 301–314.

16. Bird, R. B., Hassager, O. & Armstrong, R. C. 1977. *Dynamics of polymeric fluids*, Vol. 1, Fluid mechanics. John Wiley & Sons, New York. 470 p.

17. Bird, R. B., Hassager, O., Armstrong, R. C. & Curtiss, C. F. 1977. *Dynamics of polymeric fluids,* Vol. 2, Kinetic theory. John Wiley & Sons, New York. 357 p.

18. Wilcox, D. C. 1993. *Turbulence modelling for CFD.* DCW Industries, La Cañada, California. 460 p.

6. Modelling of fluidised beds

Sirpa Kallio[1], *Alf Hermanson*[1], *Ulla Ojaniemi*[2], *Mikko Manninen*[2]
Veikko Taivassalo[2] *and Maiju Seppälä*[2]

6.1 Background

Fluidised beds are used e.g. in chemical and metallurgical industries and in energy production. In all these processes, mixing of solids and gas-solid interaction are of utmost importance. The flow patterns in fluidised beds are characterized by large fluctuations in velocities and solids concentration. Several length scales are simultaneously important, ranging from the particle length scale to clusters of particles and voids of different sizes and to the scale of the process itself. Due to the complexity of fluidization processes, they constitute a challenge for both measurement techniques and computational fluid dynamics (CFD) modelling. Better possibilities to simulate mixing of gas and solids in fluidised beds are of interest for further process improvement. Both experimental studies and development of CFD models are required.

CFD modelling of fluidised beds is today most often done using the kinetic theory model of granular flow and a transient description. Problems in the modelling still exist. The large size of industrial processes makes it impossible to resolve the finest structures of the flow by using fine computational meshes. Kallio [1] showed that simulation results can be significantly improved especially in case of processes with high fluidization velocities by modifying the drag laws of the commercial computer codes. A new drag model, developed using the macroscopic drag model of Poikolainen [2] as a starting point, was implemented in Fluent and used for simulation of fluidised beds. In this model, for very dense suspensions close to minimum fluidization conditions the drag force is calculated from Ergun [3] equation. In more dilute conditions, the same models as used in Poikolainen [2] are utilized in slightly modified forms. The gas-solid exchange coefficient is given in the form

$$K_{sg} = \frac{3}{4} C_D \frac{\varepsilon_s \varepsilon_g \rho_g \left|\vec{v}_s - \vec{v}_g\right|}{d_s} \frac{1}{(\chi)^2} \tag{6.1}$$

where χ is the ratio of slip velocity to the terminal velocity of a particle. For dense suspensions the two-phase theory of bubbling beds yields [4]:

---

[1] Åbo Akademi University, Heat Engineering Laboratory
[2] VTT

$$\chi = v_{sl} / v_t = \frac{v_{b\infty}}{v_t} \frac{1}{\varepsilon_s} \frac{\varepsilon_{s,mf} - \varepsilon_s}{1 - \varepsilon_s} + \frac{U_{mf}}{v_t} \frac{1}{1 - \varepsilon_s}. \tag{6.2}$$

For more dilute suspensions the slip velocity is obtained from an empirical correlation of exponential form [4]:

$$v_{sl} / v_t = A \varepsilon_g^B. \tag{6.3}$$

The drag law for a single particle is used in extremely dilute gas-solid suspensions. Thus gas-solids drag force is calculated from a piecemeal function. Several alternative ways to interpolate between the above equations in the intermediate suspension density ranges were tested in Kallio [1] and on basis of the tests the best alternative was selected. In the model, calculation of C_D is done such that in the more dilute conditions (solids volume fraction up to 20%) the voidage function is independent of the actual slip velocity. Empirical correlations were also developed in Kallio [1] to account for the effects of particle and gas properties on the clustering tendency of a suspension and on the parameters A, B and $v_{b\infty}$ above. These equations were based on a limited amount of data from measurements of three different suspensions. Thus they are not necessarily very reliable for other suspensions and fluidization conditions and should be modified in the future when more data is available. The voidage function, by which the single particle drag force is multiplied in the drag model, is illustrated in Figure 6.1.

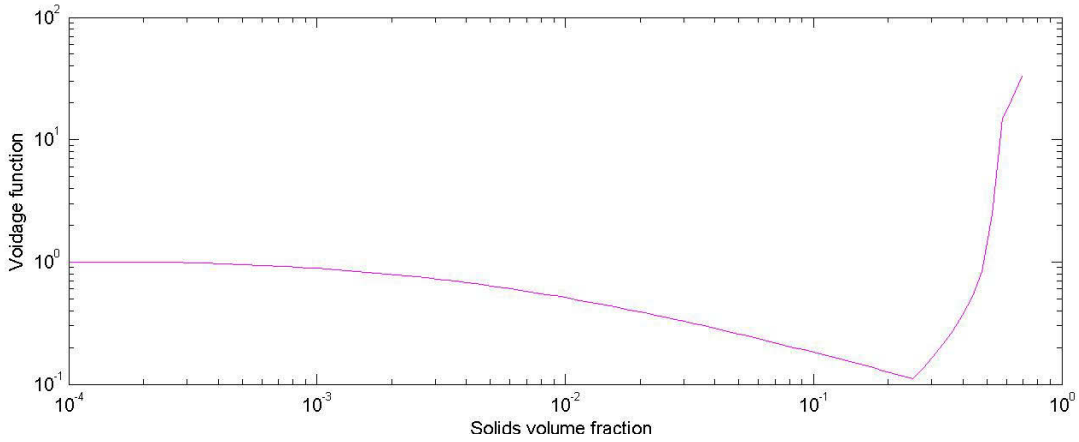

Figure 6.1. The voidage function used for particle diameter 230 µm, solid density 1800 kg/m^3, and slip velocity 1 m/s.

Since the equations above are based on time-averaged description of fluidization states, they yield in principle the maximum clustering correction necessary in a CFD simulation. The finer the mesh, the smaller should the required clustering correction be. Thus in practical calculations, the parameter values suggested in Kallio [1] can be taken

as a starting point and modified when necessary e.g. due to changes in mesh size or particle properties.

In case of bubbling beds, simulation results are fairly good without corrections to the drag force [5], whereas at higher velocities, modified drag laws seem necessary at least when the computational mesh is not extremely fine. The model described above gives reasonably good results for small and even fairly large circulating fluidised bed (CFB) risers as long as the mesh spacing is below 10 cm. Unfortunately, the model with its present parameters doesn't yield good results in simulations of large industrial processes in 3D. Up to 10 million elements of 10^3 cm^3 would be required for largest risers, which is not possible in practice due to the long computation times. Thus for the large risers, other methods need to be developed. Smaller fluidised beds and details of larger furnaces can still be studied. Even in these cases, further validation studies are necessary, since only one experimental study was used for model validation in Kallio [1] and no comparisons with measured gas and solids mixing have been done. Validation of CFD models with and without modifications to the drag law has been one of the main objectives of the present work.

6.2 Measurements of flow patterns and mixing in a turbulent fluidised bed

In the earlier validation studies at Åbo Akademi University and at Technical Research Centre of Finland (VTT) experimental results from bubbling and circulating beds have been used to improve and to validate CFD models [5], [6]. Data on gas and solids mixing in the lower dense part of a CFB have so far been lacking and further measurements and validation simulations were thus required. Similar conditions prevail in a turbulent bed and at the bottom of a CFB. In this work, fluidization characteristics and gas and solids mixing in dense suspension conditions was studied in a 2D turbulent bed cold model.

The transparent walls of the turbulent bed cold model are 0.9 m wide and 1.25 m high. The distance between the walls is 15 mm. Air distributor at the bottom consists of 9 rectangular orifices with side length 12.1 mm. Three orifices of the same type are placed at the right wall at 35 cm, 50 cm and 70 cm heights, respectively. Two fixed bed heights were used in the experiments, 20 cm and 30 cm. Air flow rates in the experiments were 1250 l/min, 1000 l/min, 750 l/min, 500 l/min, and 350 l/min, corresponding to superficial velocities 1.54 m/s, 1.23 m/s, 0.93 m/s, 0.62 m/s and, 0.43 m/s, respectively.

At the lowest velocity tested, bubbles were observed. The bed behaved like a typical bubbling bed with a distinct bed surface. At all the higher velocities, no clear bubbles

were observed. Instead, a complicated pattern of dense suspension mixed with voids of varying shapes was seen. As the fluidization velocity was increased, the bed expanded and splashes of solids rose higher up. At the walls, a region of down-flowing solids was formed. When the gas velocity was further increased, more and more fine structures were observed and the bed expanded. In all the tests, a dense bottom bed with high average solids concentration could be observed. Narrow strands of dense suspension exist at all heights. The fraction of particles contained in these strands increases as a function of height and thus they are relatively more important in the upper parts of the bed. Figure 6.2 shows typical flow patterns at the highest fluidization velocity tested, 1.54 m/s.

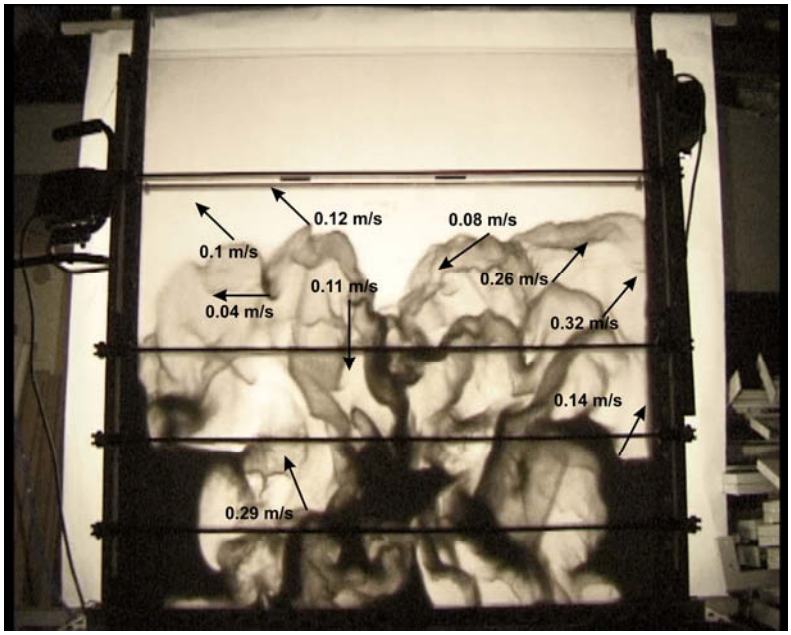

Figure 6.2. Flow structure and velocities of interfaces between dense and dilute suspension at air flow rate 1250 l/min (U = 1.54 m/s).

The experiments were recorded on video with Sony DCR-VX1000E video camera at 25 Hz and the video images were analyzed by an in-house Visual Basic code. Totally 750 video images, corresponding to 30 s, were analyzed from each experiment. The image analysis of the turbulent bed consisted of the analysis of the solids concentration profiles, of the analysis of the voids and of the analysis of the dense suspension regions. For each of the bubbles/voids, the image processing code calculated the location, nominal diameter, and the velocity of the upper edge. Axial profiles of average solids concentration at the different fluidization conditions are shown in Figure 6.3. A dense bottom region is seen in all cases. Increase in fluidization velocity leads to a decrease in solids concentration at bed bottom.

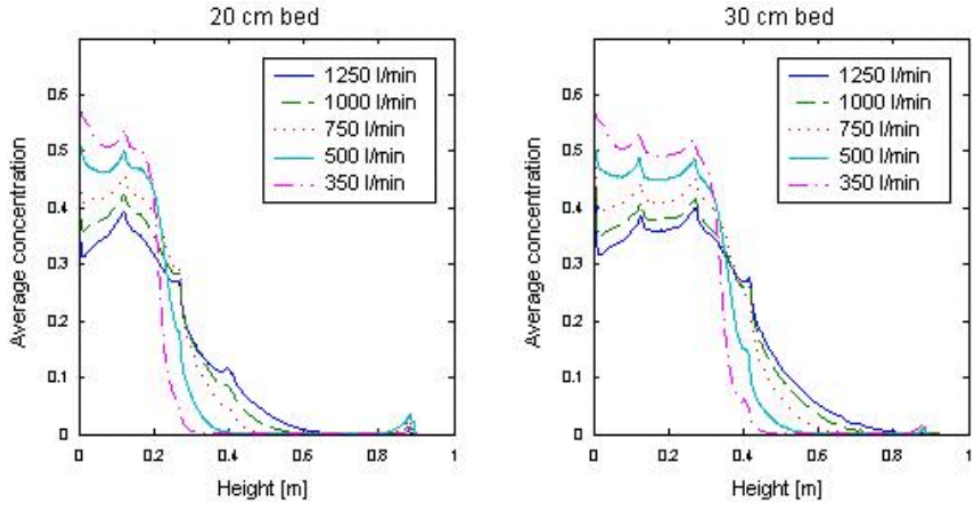

Figure 6.3. Average solids concentration (volume fraction) profiles at the different gas velocities in the 20 cm and the 30 cm high bed, respectively. The sudden peaks in the curves are caused by errors in the interpolation of pixel colors in the areas covered by support beams.

In addition to fluidization tests, gas mixing studies with CO_2 as tracer were conducted to evaluate the penetration depth of gas jets. These experiments were done using a bed with fixed bed height of 20 cm. A small amount of CO_2 was mixed in air and the produced mixture was blown into the bed at 35 cm, 50 cm and 70 cm heights, respectively, either horizontally or downwards at 45 degrees angle. The amount of gas blown through an orifice was in most experiments 250 l/min. In some tests the gas flow rate was reduced to 125 l/min. In addition, the effect of the velocity at the orifice outlet was studied by reducing the orifice outlet area in some tests from the original 12.1 mm x 12.1 mm to 10.5 mm x 10.5 mm. Fluidization velocities 1.54 m/s, 1.23 m/s and 0.93 m/s (flow rates 1250 l/min, 1000 l/min and 750 l/min) were used in the tests. The concentration of CO_2 was measured at 118 cm height above the bottom plate at 5 cm intervals for 10 s at each measurement location. In addition to measurements at the top of the equipment some measurements were done at lower elevations through small holes drilled through the walls.

It was observed that the spread of gas downwards was poor and took place quite suddenly on rare occasions. A probable explanation for this spreading downwards could be the fall of a dense cluster close to the orifice outlet, which could push the jet downwards. Lateral mixing mainly took place at the elevation just above (10–20 cm above) the jet entrance level. Gas velocity at orifice outlet had only a minor effect on mixing. The main parameter affecting penetration length of a gas jet was found to be the height at which the jet enters the bed, which is correlated with the local wall layer thickness as well as the suspension density in the vicinity of the orifice outlet. Also the fluidization velocity and the gas flow rate through the orifice affect lateral mixing of

gas. These effects are illustrated in Figure 6.4. The experiments on turbulent fluidization and gas mixing are described in full details in Kallio and Hermanson [6].

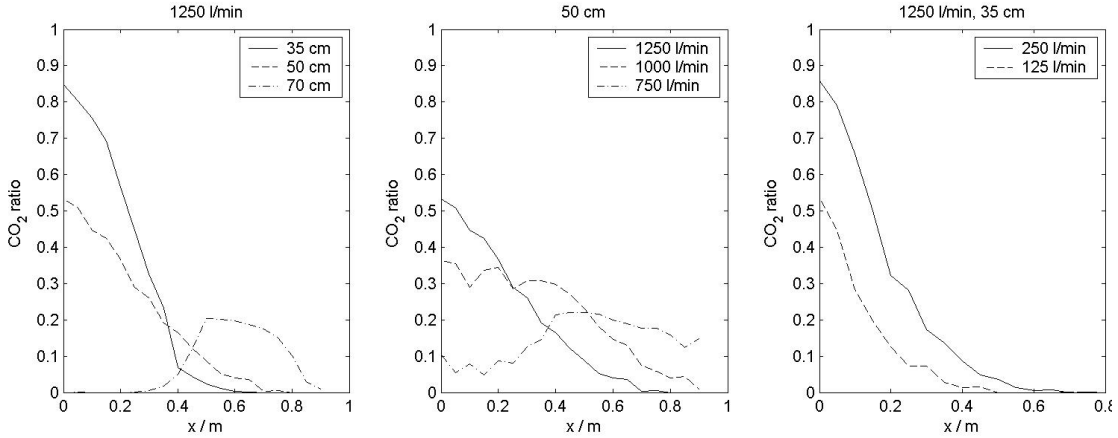

Figure 6.4. Effects of process parameters on spreading of a gas jet blown through an orifice at a side wall: the effect of the height at which the jet enters the bed (left), the effect of fluidization velocity (middle) and the effect of the gas flow rate through the orifice (right). CO_2 ratio is the ratio of the measured average concentration at 118 cm height to the concentration at orifice outlet. x is the lateral distance to the side wall.

A couple of experiments were also conducted to gain information on solids mixing. Tracer particles were fed through the orifice at 0.7 m height on the right wall. The size of the red tracer particles ranged between 0.84 mm and 1.19 mm and the material density was 1050 kg/m^3. The number of particles observed in the left low corner was counted from video recordings. The effect of fluidization velocity on solids mixing was clearly visible in the results. At fluidization velocity 1.54 m/s the particles were fairly uniformly distributed after 20s whereas at fluidization velocity 0.93 m/s mixing was slower and particles moved in loose groups even 2 minutes after feeding.

6.3 Simulations of turbulent fluidization

Some of the experiments described above were simulated by means of the Eulerian multiphase models of CFD software. The simulated cases corresponded to the experimental arrangement, where the packed bed height was 0.20 m and the volume flow of air fed into the bed was 1250 l/min. The air was fed to a space below the grate, from where the air spread into the bed through the nine openings of the grate with a given pressure drop, as in the earlier study of bubbling bed simulations [5]. At first, the base turbulent bed was simulated. In addition, the case with the secondary air introduced into the bed was simulated. In the simulations with secondary air inlet, the side opening at the height of 0.35 m was applied. The amount of the secondary air

through the side opening was about 250 l/min. The air was first fed horizontally into the bed and in the second case it was directed 45 degrees downwards.

Two different sized grids were used in the simulations. The basic grid consisted of about 12000 cells and the denser grid of about 16000 cells. The grid was made denser in the area of the turbulent bed in order to facilitate smaller grate openings in the model. The main motivation for this was to be able to study the effect of the velocity of the air fed through the grate openings while the volumetric flow was constant. Changing the size of the side opening increased the air velocity at the secondary opening from 35 m/s to 46 m/s. The simulations were carried out using the version Fluent 6.1.18 [7].

Most simulations of turbulent bed were performed with the hydrodynamic models that gave the most realistic results for the bubbling fluidised bed [5]. For the momentum exchange coefficient K_{sl} the model of Gidaspow was used and for the kinetic viscosity of the solid phase $\mu_{s,kin}$ the model of Gidaspow et al. was applied. The simulation was carried out as turbulent flow using both grid sizes. Turbulence was modelled using the dispersed k-ε model of Fluent for multiphase flows.

Figure 6.5 shows typical images of the results for the turbulent bed in tested cases. Qualitatively the results obtained with the two grid sizes are quite similar. In the studied base turbulent bed cases (bed without side opening), the dense areas of bed particles were found close to the edges of the bed. Inside the bed, the particles formed narrow strings and clusters. In the center region of the bed, the clusters were present all the time. The size, location and number of the clusters varied continuously with time due to coalescence and break-up. The strings of the particles splashed into the free region above the bed. With qualitative inspection, the differences between the two simulations illustrated in Figure 6.5 were small.

The secondary air feed seemed to have only slight effect on the bed behaviour despite the used air velocity or direction. This is in accordance with the measurement results. In Figure 6.5, the instant distributions of particles inside the bed are shown for the results with horizontal secondary air feed. In studied cases, the gas penetration distance showed to be quite short and the added air seemed to restrict to the neighbouring region of the side opening, which agrees well with the experimental observations in the same flow conditions (see Figure 6.4). The clusters and strings were formed in a same manner as without the secondary air feed.

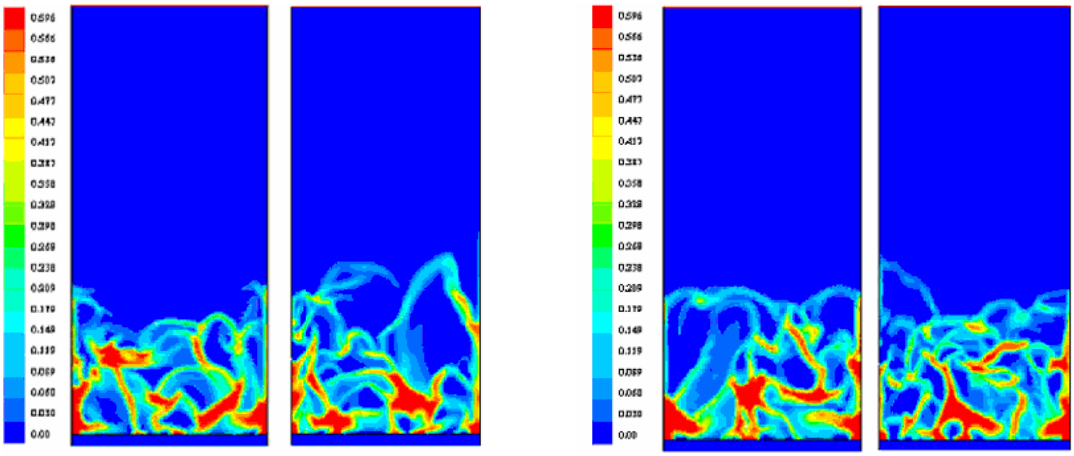

Figure 6.5. On the left: typical images of turbulent bed behavior computed with base grid and horizontal secondary air feed (air velocity of 35 m/s). On the right: turbulent bed behavior computed with dense grid and horizontal secondary air feed (air velocity of 46 m/s).

The simulation results were analysed statistically in order to find out more quantitatively the differences between the tested models and grid densities. The analyses were performed by calculating the time averages of the particle densities of the simulation period. The simulations of turbulent bed were carried out about five seconds with both grids with and without the side opening, and the data for analyses was collected every 25 ms. The analyses were performed using the MatLab software. In addition, the spatial variability of the particle concentrations was analysed. The results are described in full details in Ojaniemi, Manninen and Taivassalo [8].

6.3.1 Validation of turbulent bed simulation results

The time averages calculated for the simulation results were compared to time averages calculated for the experimental results. The averages were compared as a function of bed height and as lateral profiles at the bed heights 0.20 m, 0.40 m, 0.60 m and 0.80 m. The results for the base turbulent bed are shown in Figures 6.6 and 6.7. As shown in Figures 6.6 and 6.7, the experimental and simulated results differ qualitatively. According to the experimental results in Figure 6.6, the bottom bed is much denser than the simulations predict. In contrast, the CFD prediction higher up in the bed shows a smaller particle volume fraction than found in the measurements.

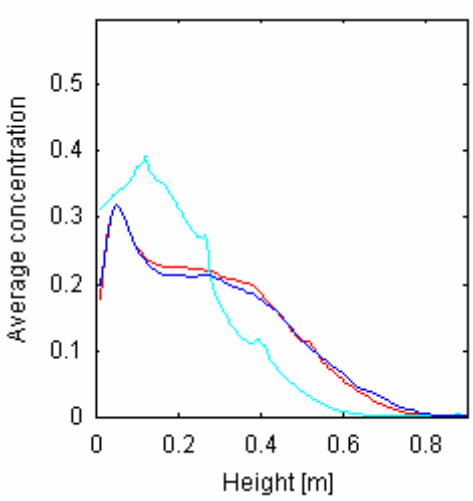

Figure 6.6. Time averaged volume fractions of particles as a function of bed height. The studied simulation cases are colored as follows: red – base grid, blue –dense grid. The experimental average of particle densities is shown by the light blue line.

In Figure 6.7, compared to the simulated results the experimental results show the overall average bed density to be higher at the bottom of the bed. However, the shape of the lateral average profile was similar in the experimental and simulated results. In the upper parts of the bed, the averaged concentration of particles was higher in the simulated results, as seen in Figure 6.7. In addition, the particles of the simulated bed splashed higher. A clear difference between the experimental and simulated results at the higher parts of the bed was that the particle concentration at the edges of the bed was clearly greater in the simulation results.

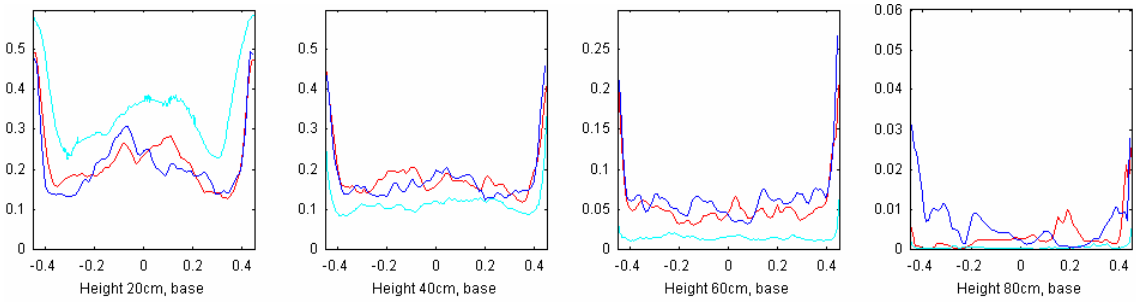

Figure 6.7. Lateral profiles of time averaged particle volume fractions at bed heights 0.20 m, 0.40 m, 0.60 m and 0.80 m. The studied simulation cases are colored as follows: red – base grid, blue – dense grid. The experimental averaged results are presented by the light blue line.

The averaged particle volume fractions obtained with the two grid sizes did not differ significantly, as shown in Figures 6.6 and 6.7. Thus, the velocity of the air fed through the grate openings at the bottom of the bed had only negligible effect on the bed behaviour.

By the qualitative analysis of the simulation results, the time averaged simulation results were consistent with the general understanding of turbulent bed behaviour. In the tested cases, the particle volume fraction was near the packed bed density at the edges of the bed. Inside the bed, the density of the bed varied with time from dilute to dense, yielding a quite small time average of particle volume fraction. Next to the dense regions of particles at the edges of the bed, the averaged particle volume fraction was lower than elsewhere inside the bed, e.g. in Figure 6.7 at the height of 0.20 m.

6.3.2 Simulation of mixing in a turbulent fluidized bed

The cases with secondary air feed were analysed similarly to the base turbulent bed analysis. In Figure 6.8, the results for time averaged volume fractions of particles are shown for the base turbulent bed and extra air feed cases with the air velocity of 35 m/s at side opening and for corresponding experimental cases.

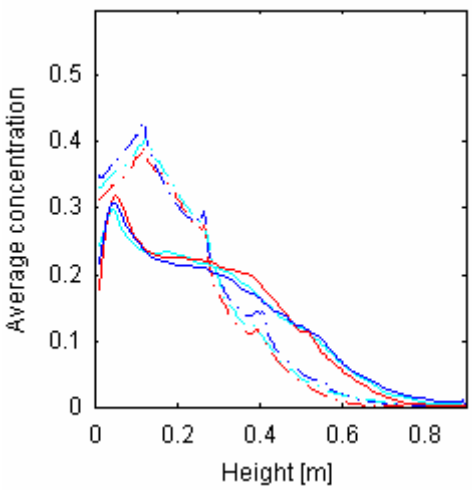

Figure 6.8. Time averaged volume fractions of particles vs. bed height. The studied simulation cases are coloured as follows: red – basic bed, blue –bed with horizontal secondary air feed, light blue – bed with directed secondary air feed. The experimental average of particle densities are shown by dash-dotted line (– · –). The simulation results with the base grid are shown by solid lines.

Figure 6.8 show that the secondary air feed does not have a significant effect on the overall bed density. Close to the bottom of the bed, the effect of the secondary air was different in the experiments and simulations. In the simulations, the extra air seems to decrease the averaged bed density, whereas the experimental results show an increased density in the bottom region. The difference in the measurement results was, however, very small, roughly of the order of measurement accuracy.

On the level of the secondary air inlet, the behaviour predicted by the simulation again differs from the measured result. In the simulation, the average bed density with the horizontal and directed air feeds are quite similar, both being smaller than the basic turbulent bed density on that level. The measured results show that the bed density with the directed air feed is close to the basic bed result, whereas the horizontal feed produced a higher particle concentration. Again, the differences were quite small and could be caused by inaccuracies in the measurements. Higher up in the bed, the experimental and simulated cases were consistent. The extra air feed increased the concentration of particles independent of the direction of air feed. In general, the effect of the secondary air on the bed behaviour in simulation results was quite negligible, which is in agreement with measurements. Only above the side opening was the bed density clearly decreased. More analysis from the secondary air feed effect on the particle distribution is shown in the report of Ojaniemi, Manninen and Taivassalo [8].

The distribution of the secondary air was studied by adding a scalar variable to mark the air introduced through the side opening. At the secondary air inlet, the value for the scalar was set equal to one. The mixing of the added air was studied by calculating the time average of the scalar variable associated to the primary (gas) phase. The results are shown in Figure 6.9 for simulated and experimental cases.

On the left in Figure 6.9, the averaged value of the scalar describing the concentration of air, are shown at the height 1.18 m for the simulated cases with horizontal and directed air feed. The distribution of the scalar did not depend appreciably on the grid density, and therefore not on the velocity of the fed air. The spreading of the air into the free space above the bed seemed to be greater with horizontal air feed. On right in Figure 6.9, the results for corresponding experimental case with fluidization air flow rate 1250 l/min are shown.

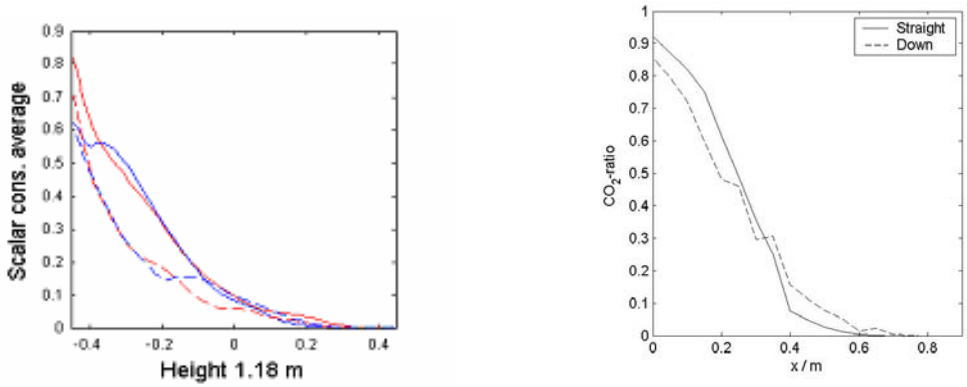

Figure 6.9. On the left: Time averaged lateral concentration of scalar value used for marking the secondary air shown at height 1.18 m. The simulation cases are coloured as follows: red – base grid, blue – dense grid. The results are shown with a straight line for horizontal air feed and with a dashed line (– –) for downwards directed air feed. On the right: Experimental results of the time averaged CO_2 -ratio (ratio of measured concentration at the height of 1.18 m to the concentration at orifice outlet). Solid line – straight (horizontal) air feed into the bed, dashed line – directed air feed.

Comparing the results in Figure 6.9 shows that the simulation results agree with the measurements qualitatively. The added air found its way mainly along the edge of side opening. The migration distance of the added air was about as long in both the experimental and simulated results. The simulation predicted slightly different behaviour for the down directed air feed than the experiment showed. The result for the horizontal secondary air feed was, however, in good agreement with the experimental result.

Particle mixing inside the bed was simulated with Fluent 6.2.16. Mixing of the particles was studied by injecting 4.3 g of additional glass beads to a flow domain of a mixed bed in 3 second's time through an additional side opening at the height of 70 cm. The size of the added particles was an averaged from the range of the particle sizes used in the experiment. The density of the particles both in simulation and experiment was 1050 kg/m^3.

Similar with the experimental results, the mixing of particles was monitored by calculating the number of particles in the region of 17 cm x 12 cm at the bottom corner opposite to the side opening. The number of mixing particles on the monitoring area is represented in Figure 6.10 as a function of time for both simulation and experimental results. As seen in Figure 6.10, compared to the experimental results of Kallio and

Hermanson [6] the simulated mixing particles entered the monitoring area clearly earlier and the mixing was slightly faster.

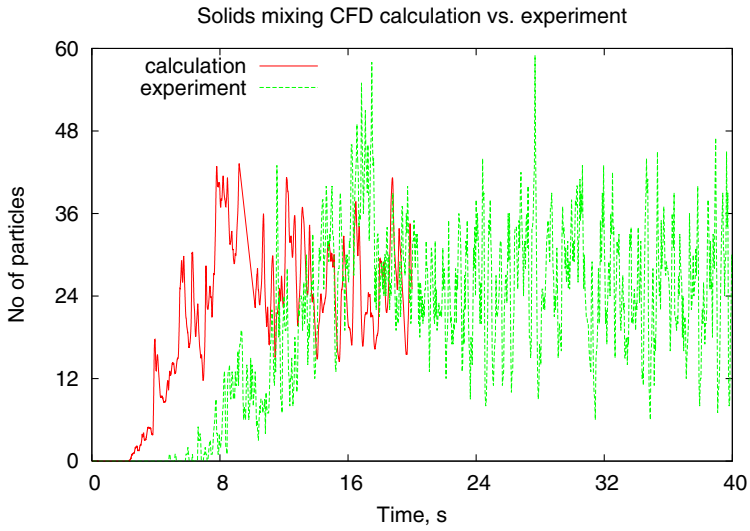

Figure 6.10. Number of additional particles in a monitoring area. Red line – results of simulation with additional particles sized 1.015 mm; green line – experimental results with particle size ranging between 0.84 mm and 1.19 mm.

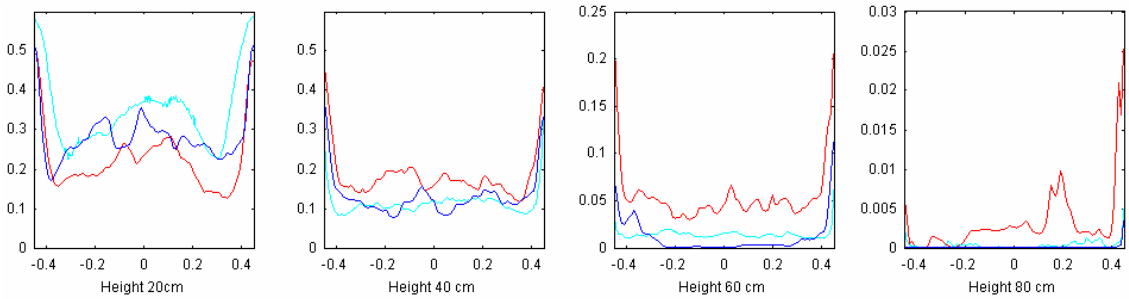

Figure 6.11. Lateral profiles of time averaged particle volume fractions at bed heights 0.20 m, 0.40 m, 0.60 m and 0.80 m with base grid. The studied simulation cases are colored as follows: red – Gidaspow model, blue – Modified model. The experimental averaged results are presented by the light blue line.

6.3.3 Turbulent bed simulation with modified drag

Because the standard drag models did not produce a sufficiently dense bottom bed, the drag force was modified according to Kallio [1] for studying the effect of correction of the term on the particle distribution inside the bed. The correction to the coefficient was made in order to decrease the drag in the dense regions of the bed.

The turbulent base bed was simulated by applying the modified model of momentum exchange coefficient K_{sl} over a period of five seconds. The lateral profiles of time averaged solids volume fractions at the bed heights 0.20 m, 0.40 m, 0.60 m and 0.80 m are shown in Figure 6.11. In addition, the corresponding averages are shown for the simulation results obtained with the Gidaspow model and for experimental results.

The results obtained by using the modified model were significantly closer to the experimental results than the results calculated using the Gidaspow model. In the dense bed region (0.2 m) the modified model was in better agreement with the measurements in the central region. Close to the walls, however, the simulated solid concentration remains much lower than the measured one. In the upper part of the bed, the particle concentrations in the side regions calculated by modified model are closer to the experimental results. The bed particles did not drift to the upper part of the bed in the same proportion as with the Gidaspow model. For example, at the height of 0.60 m, the concentration of particles was clearly lower in the results obtained with the modified model than in the results of Gidaspow model. The overall average bed density was in fair agreement with the experimental results, as seen in Figure 6.12.

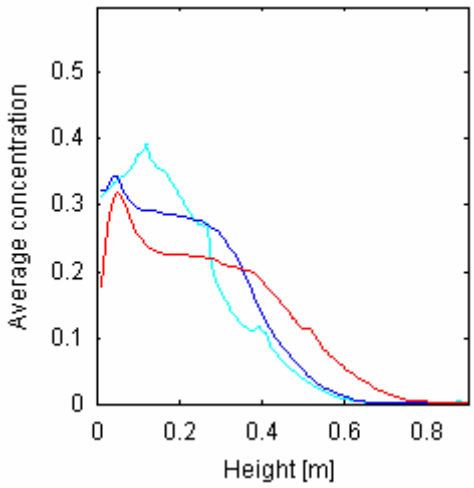

Figure 6.12. Time averaged volume fractions of particles as a function of bed height. The results of base turbulent bed with tested K_{sl} models applied are shown. The studied simulation cases are coloured as follows: red – Gidaspow model, blue – modified model. The experimental averages of particle densities are shown by the light blue line.

6.3.4 MFIX simulation

For comparison, one simulation was also conducted with the MFIX-code. To facilitate a comparison of the simulation results, the same simulation was carried out also with Fluent applying the model of Syamlal and O'Brien for the momentum exchange

coefficient K_{sl} and the model of Syamlal et al. for the kinetic viscosity of the solid phase $\mu_{s,kin}$. These simulations were carried out using the base grid and laminar flow modelling.

The computational grid used in the MFIX calculation was about the same as the base grid used in Fluent simulations. The size of the grid was about 12 000 cells. The greatest differences between the CFD simulations were numerical. MFIX uses dynamic time step and first order spatial discretization was employed [9]. Because the MFIX code does not have models for multiphase turbulence, the simulations were carried out as laminar. Otherwise, the calculation parameters were the same as in Fluent simulations.

The time average of the particle distribution was calculated for the results simulated by MFIX for the basic turbulent bed. The results were compared to the Fluent results. In Figure 6.13, the profile of the time averaged particle density is presented as a function of the bed height for the Fluent simulations with Gidaspow and Syamlal models and for the MFIX simulation (with the Syamlal models). The results obtained with MFIX were mostly in good agreement with the Fluent results. Thus, the MFIX code with faster computation is a good alternative for simulating fluidised beds.

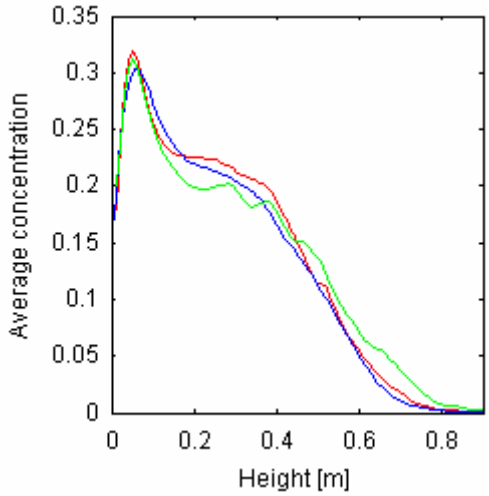

Figure 6.13. Time averaged particle distribution shown as function of bed height. The simulation cases are coloured as follows: red – Fluent simulation with the base grid and Gidaspow models; green – Fluent simulation with the base grid and Syamlal models; blue – MFIX result.

6.4 Simulations of riser flow

In Kallio [1] the new drag model implemented in Fluent 6.1.22 was tested in 2D simulations of a CFB cold model, described in Kallio [10], from which measurements of total pressure drop and local solids velocity and volume fraction are available. Particle size in the simulated case was 230 μm and the material density 1800 kg/m^3. Riser height was 7.3 m and cross-section 1 m x 0.25 m. The average superficial gas velocity above the air distributor was 4 m/s. The general fluidization characteristics shown by the simulations in Kallio [1] were qualitatively correct. Axial density profiles in CFB simulations were similar to the measured ones and fluctuations in solids velocity and concentration were at least qualitatively as expected on basis of measurements. In the present project, the simulation approach used in Kallio [1] was extended to 3D. The transient 3D simulation was conducted, as earlier in 2D, by means of the kinetic theory model of Fluent 6.1.22 CFD software [11]. Solids circulation was taken into account by adding to the riser bottom region a mass source term equal to the mass leaving the riser. Solid phase kinetic viscosity was calculated from the model by Syamlal et al. [12]. For the gas phase, k-ε model of turbulence was used.

Figure 6.14 illustrates instantaneous flow patterns in the 3D simulation. The structure of the solids distribution in the 3D simulation is similar to what was observed in 2D. A distinct dense bed is seen at riser bottom. Clusters of particles are seen at higher elevations. They look similar to the ones obtained in 2D simulations. A denser region is shown close to the roof. Solids are often collected close to the center of the back wall in the vicinity of the exit. Analysis of solids velocity distributions shows that in the dense areas close to the walls solids are falling down. The average solids downflow velocities in the wall layers are in the range 0– 5 m/s. The highest average downflow velocity 5 m/s was found in a corner.

The average pressure and solid volume fraction profiles from the 3D simulation were compared with the ones obtained from the earlier 2D simulations. The bottom bed in 3D is clearly denser than in 2D (solids volume fraction 32%; in 2D 19%) and consequently, the pressure profile shows a very steep drop in the bottom region. The increase in average suspension density at riser bottom comes most likely from the effect of the side walls: in the 3D case a dense wall layer covers all walls in the bottom region and thus the fraction of the cross-sectional area covered by dense phase is much larger in 3D than in 2D.

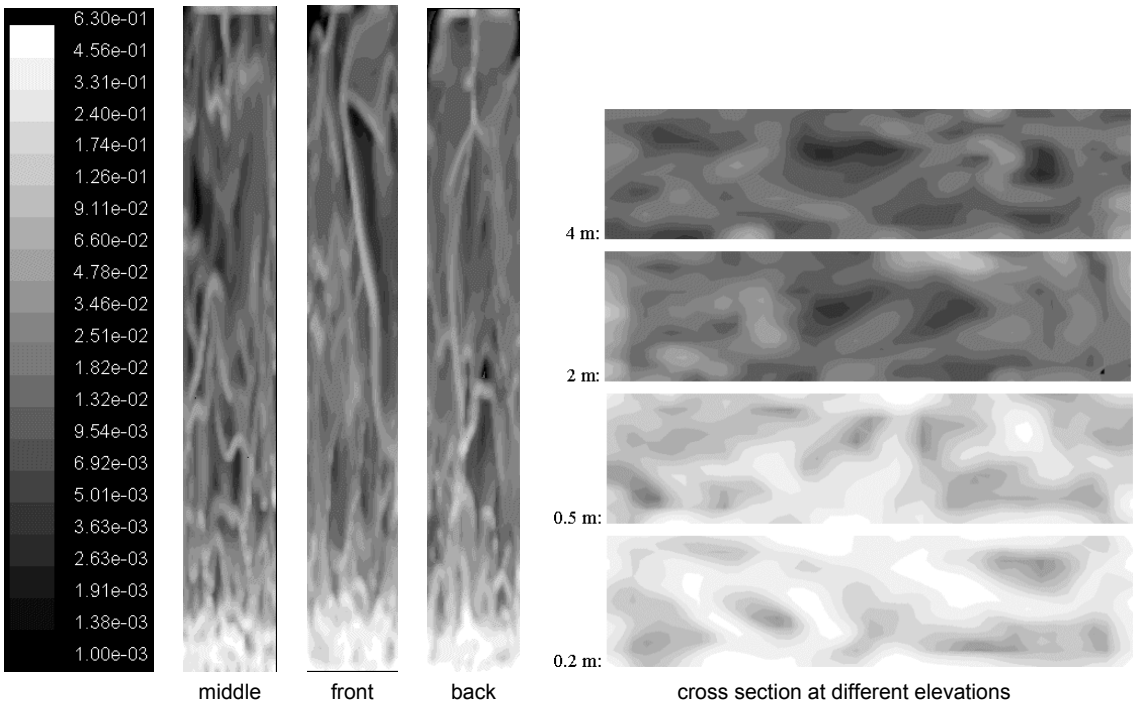

Figure 6.14. Solids volume fraction in the simulations of the CFB cold model.

As in 2D simulations, the average lateral gas and solids velocity and solids volume fraction profiles show the correct structure of the flow. At the walls, a denser region is created with solids flowing on average down along the wall. Figure 6.15 shows instantaneous values of solids volume fraction and solids velocities during 15 s simulation. For comparison, measurements of instantaneous solids velocities and volume fractions, obtained by means of an optical probe [10], are also depicted. The scatter in the measured and simulated values is quite similar. The only significant difference to measurements is seen in the corner at 2.5 m height (z = 0.04 m), where the measured volume fractions are significantly higher than the simulated ones. In general we can still say that the fluidization characteristics shown by the 3D simulation are qualitatively correct.

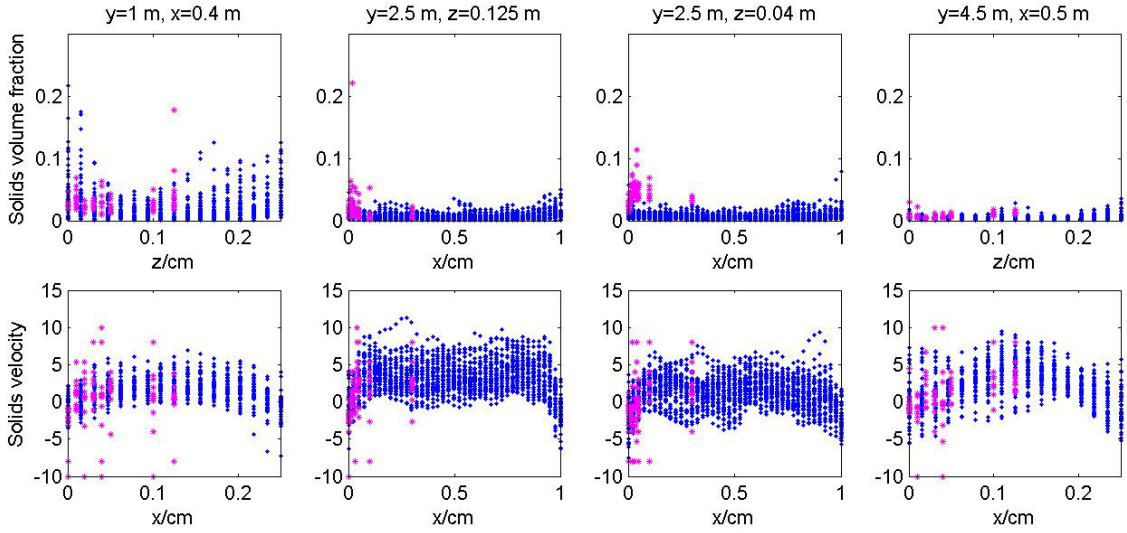

Figure 6.15. Measured (light magenta) and simulated (dark blue) values of solids volume fraction and solids velocity at 1 m (y = 1 m, x = 0.4 m), at 2.5 m (middle of the wall, y = 2.5 m & z = 0.125 m, and corner, y = 2.5 m & z = 0.04 m), and at 4.5 m height (y = 4.5 m & x = 0.5 m), respectively.

6.5 Macroscopic modelling

The kinetic theory model used above in combination with a modified drag law produces reasonably good results when the mesh spacings are between 1 cm and 10 cm (see Kallio [1]) but not when a coarser mesh is used. For large CFB risers which have to be calculated in coarser meshes one alternative would be to develop macroscopic CFD models by time averaging. Analysis of the 3D simulation results above was done in order to facilitate evaluation and formulation of macroscopic models and to give information on typical mixing characteristics of CFBs.

As a first step in the analysis we define the macroscopic average velocity as the mass weighted time average and write a time average of the convection term in the momentum equation of phase l as follows:

$$\overline{\rho_l \varepsilon_l \mathbf{v}_l \mathbf{v}_l} = \rho_l \overline{\varepsilon_l} \left(\overline{\mathbf{v}}_l \overline{\mathbf{v}}_l + \overline{\mathbf{v}_l' \mathbf{v}_l'} \right) \tag{6.4}$$

The analysis of the 3D simulation results showed that in gas phase momentum equation the macroscopic convection term expressed by means of the average velocity is larger than the corresponding fluctuation term. Both the vertical and the lateral fluctuation terms are smaller than the vertical (yy-component) transport term expressed with the average velocity. Still, the “average” lateral convection terms are an order of magnitude

smaller than corresponding fluctuations and thus a turbulence model would be required for description of e.g. lateral spreading of gas components.

For solids, fluctuations dominate over the "average" term in the lateral direction and also in the vertical direction in the splash zone. Lateral mixing is drastically reduced as a function of height whereas mixing in the vertical direction seems to improve slightly. The analysis also shows a strong similarity between the fluctuations in the gas and the solid phase indicating a strong coupling of the phases. Modelling gas phase turbulence without taking this interaction into account can thus be considered questionable.

Figure 6.16 shows a comparison of the fluctuations in the three coordinate directions. In the solid phase equations turbulent terms locally dominate over the laminar convection terms. Fluctuations and mixing phenomena seem clearly different in the vertical and horizontal directions. Therefore it would seem reasonable to model the axial and radial Reynolds stress components separately. This is contradictory to the assumption of isotropy of velocity fluctuations assumed e.g. in the macroscopic time-averaged models of Hrenya & Sinclair [13] and Dasgupta et al. [14].

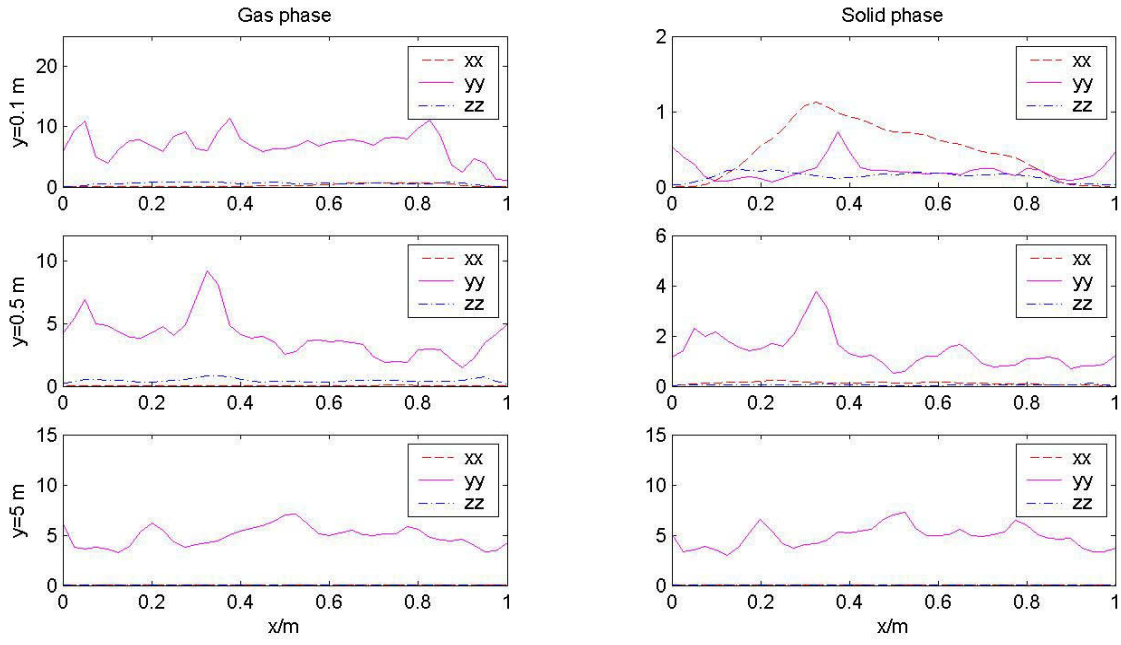

Figure 6.16. Comparison of the normal components of gas and solids velocity fluctuation tensors at three elevations (z = 0.125 m).

Macroscopic models have also been presented in Hyppänen [15], Poikolainen [2] and Kallio et al. [16]. In the present project, different averaging approaches used in the derivation of macroscopic equation systems were evaluated in the light of the conclusions drawn from the 2D and 3D simulation results. The averages considered

were mass weighted (Favre) averages, momentum weighted averages and volume averages.

The different approaches yield different fluctuation components in the continuity and momentum equations. Consequently, the required closure laws for the different sets of equations differ. Numerical treatment of the equations restricts the mathematical form of the terms that can easily be handled. In principle it would be extremely useful to include a dispersion term in the macroscopic solid phase continuity equation. It would cause solids to spread more uniformly. In addition, it would reduce the fluctuations in the concentrations during iterations and stabilize the calculations. Both momentum averaged and volume averaged velocities lead to a dispersion term in the continuity equation.

Numerical stability of the solution algorithm requires that dispersion coefficients are positive. Unfortunately, the values determined from simulations indicate that both the momentum averaged and the volume averaged velocities yield negative dispersion coefficients for solids concentration. Thus these velocities are not usable in practice. On basis of the analysis it unfortunately looks difficult to justify the inclusion of a dispersion term in the continuity equation. Thus the averaging method recommended here is mass-weighted (Favre) averaging.

6.6 Summary

In the present study, experiments were carried out for a 2D turbulent fluidised bed cold model at Åbo Akademi University. The experiments were performed using two bed heights and five fluidization velocities. The behaviour of the bed was video recorded and average lateral and vertical voidage profiles were determined. Additional experiments were conducted to study spreading of a tracer gas blown into the bed from a side wall at different heights and velocities with different fluidization conditions.

Generally accepted hydrodynamic models were tested for simulation of turbulent bed by means of the Eulerian multiphase models of CFD. The validation of the models was based on the experimental results of the 2D turbulent bed. The simulations were performed with two different grid sizes to study the effect of the velocity of the air jets on the behaviour of the bed. The simulations were carried out mostly by Fluent. In addition, the simulation of turbulent bed was performed with MFIX. For comparing the simulated and experimental results, the time averaged volume fractions of particles were calculated.

Qualitatively, the behaviour of the simulated bed corresponded to the general understanding of a turbulent bed. Between the simulated base turbulent bed cases, the differences between the results obtained by different hydrodynamic models or grid sizes were small. Comparison of the simulated and experimental results showed that the particle concentration at the bottom of the bed was significantly lower in the simulation. In addition, the particles seemed to migrate higher in the simulations. The modification of momentum exchange coefficient between the phases resulted in a better agreement with the experimental results.

Both in the simulation results and in the experimental results, the secondary air did not appreciably penetrate into the bed, but flowed upwards mainly along the edge of the bed. The effect of the secondary air on the bed behaviour in simulation results was quite negligible. Only above the side opening was the bed density clearly decreased.

In addition to the turbulent bed simulations, a 3D simulation of a circulating fluidised bed cold model was conducted using the modified model for gas-particle drag. The simulation results were compared with available measurements and the agreement was found to be good. The 3D simulation results were further analyzed and conclusions on velocity and density fluctuations in circulating fluidised bed risers were drawn.

References

1. Kallio, S. 2005. The role of the gas-solid drag force in CFB modelling of fluidization. Report 2005-3. Åbo Akademi University, Heat Engineering Laboratory.

2. Poikolainen, V. 1992. Mathematical modelling of gas-solid fluidization with a one-dimensional hydrodynamic model. Master of Science Thesis. (In Finnish.) Lappeenranta University of Technology, Finland.

3. Ergun, S. 1952. Fluid flow through packed columns. Chemical Engineering Progress, 48, 89–94.

4. Matsen, J. M. 1982. Mechanisms of choking and entrainment. Powder Tech., 32, 21–33.

5. Ojaniemi, U. & Manninen, M. 2003. Kuplivan leijupedin cfd-laskenta, Projektiraportti PRO5/P7526/03. VTT, Espoo.

6. Kallio, S. & Hermanson, A. 2005. Experimental study of flow patterns in a 2D turbulent fluidised bed cold model. Report 2005-2. Åbo Akademi University, Heat Engineering Laboratory.

7. Fluent Inc., Fluent Users' guide – Release 6.1, 2003.

8. Ojaniemi, U., Manninen, M. & Taivassalo, V. 2005. CFD Modelling of Turbulent Fluidised Bed. Report PRO5/P5025/05. VTT, Espoo.

9. MFIX Documentation, Theory Guide, Technical Note, U.S. Department of Energy, 2003, www.mfix.org.

10. Kallio, S. 1995. An experimental and numerical study of the velocity and voidage distribution in a circulating fluidised bed cold model. Report 95-7. Åbo Akademi University, Heat Engineering Laboratory.

11. Fluent Inc., Fluent Users' guide – Release 6.0, 2001.

12. Syamlal, M., Rogers, W. & O'Brien, T. J. 1993. MFIX Documentation, Volume 1, Theory Guide. National Technical Information Service. Springfield, VA, DOE/METC-9411004, NTIS/DE9400087.

13. Hrenya, C. M. & Sinclair, J. L. 1997. Effects of particle-phase turbulence in gas-solid flows. AiChE Journal, 43, 853–869.

14. Dasgupta, S., Jackson, R. & Sundaresan, S. 1998. Gas-particle flow in vertical pipes with high mass loading of particles. Powder Technology, 99, 6–23.

15. Hyppänen, T. 1989. An experimental and theoretical study of multiphase flow in a circulating fluidised bed. Dissertation. Lappeenranta University of Technology, Department of Energy Technology.

16. Kallio, S., Poikolainen, V. & Hyppänen, T. 1996. Mathematical modelling of multiphase flow in a circulating fluidised bed. Technical report. Report 96-4. Åbo Akademi University, Heat Engineering Laboratory.

7. Summary and applications of the results

7.1 CFD modelling of crystallization and crystallization design

A new method to model crystal growth was developed. It is based on calculation of the flow field and concentration distribution around single crystal. This predicts accurately mass transfer rate from bulk liquid to crystal surface where the crystal growth takes place. Model parameters were obtained from single crystal growth measurements by utilization of the flow field and mass transfer calculations. The method was also applied for crystallization processes where an admixture is present in mother liquor. Separation of the mass transfer and crystal growth by surface reaction allows the growth model to be used in varying flow and mixing surroundings i.e. through out the conditions in real crystallizer. This new model for crystal growth was used for modelling crystal growth in suspension crystallizer.

Modelling of suspension crystallizer requires modelling flow fields of particles and fluid, heat and mass transfer, and also nucleation, growth, agglomeration, breakage of crystals. All these phenomena are affected by mixing. Simulation results were verified with batch experiments in 100 dm^3 crystallizer equipped with two impellers. During the experiments temperature distribution, concentration of the mother liquor, density of suspension, and particle size distribution were measured at six locations. Velocity profiles of fluid and particle phases and also slip velocities were measured using PIV. CFD simulations gave realistic results compared to experiments.

Particle Transport Method (PTM) was combined with population balance model to describe perfectly mixed crystallizer. This model can be used later in the multiblock model to simulate industrial scale crystallization processes. The multiblock model has been successfully used in other projects to model gas/liquid processes including fermentation.

7.2 CFD simulation of gas-liquid processes

A dynamic multiblock stirred tank model was developed for the agitated multiphase reactors. The model is flexible allowing consideration of any degree of complexity from ideal to non-ideal mixing and single to multiphase systems. The model is computationally efficient so that it can be applied to the parameter fitting, flowsheet simulations or investigation of long-term batch reaction dynamics. The model was used to investigate gas-liquid agitation and mass transfer but could be applied equally to the investigation of any agitated multiphase reactor.

The developed gas-liquid mass transfer models should be applicable to the reactor design and scale-up, because they are based on scale-independent phenomenological submodels and were validated against experiments. The multiblock and CFD simulations revealed a strong inhomogeneity of gas-liquid mass transfer even in the laboratory stirred tanks highlighting the need to consider local mass transfer conditions in the design of large industrial reactors. Fermenter simulations showed that multiblock model predicts complicated effects of non-newtonian mixing and mass transfer on reactor dynamics realistically and allows the simulation of a several days' fermentation batch.

A fully resolved bubble column CFD model must include population balance equations to describe the changes in bubble size and interfacial area. The population balance equations include phenomenological models for bubble coalescence and breakage rate. During the project, the understanding about bubble coalescence and breakage has improved a great deal. The obtained results show that it is difficult to estimate bubble coalescence from the known physical properties. Therefore, it seems likely that some experimental work is always required before population balance models can be used to calculate bubble size distributions in bubble columns. Some practical methods to estimate coalescence properties for different solutions have been developed during the project. These methods include parameter estimation methods based on bubble size distribution measurements and bubble persistence time measurements. The developed methods can be used to obtain information about bubble coalescence and breakage at least in some industrial cases.

In the project, a CFD model has been developed to include population balance equations to CFD code. In this model, the bubble size distribution is discretized to a number of bubble size classes. The momentum equation is solved for each bubble size class. Hence, each bubble size class has its own velocity field. This approach is shown to give the most accurate results. However, at present time the practical application of this model is limited due to very long calculation times needed. Our proposal to overcome the computational load is to combine some bubble size classes to groups for which the momentum equations are solved. Using this approach a compromise between accuracy and calculation time can be reached, which allows also the calculation of industrial cases with reasonable accuracy and computational load.

7.3 CFD model development for trickling and pulsing flow in solid/liquid/gas systems

During this project the available models for modelling trickle bed reactors were critically analyzed and improved models were developed. Also several factors

influencing the flow, but not currently implemented into the flow models, were considered and preliminary work in relation to their implementation was done. We find that development of a truly phenomenological model, rather than just lumping all contributing factors into some experimental parameters, will benefit the modelling of industrial reactors. The small scale phenomena can be excluded from the industrial scale models and more accurate results are obtained. On the whole good progress was made and this work will provide a good foundation for the further work done in this area.

7.4 Drag reduction effects

The drag reducing effect of addition of small amounts of suitable polymer in liquids is a well known phenomenon and it has been utilised for a long time, primarily in oil pipelines for lowering pumping costs. The mechanism of drag reduction is still, however, not well understood. The measurements and theoretical model development conducted in the project give new insight to the DR-phenomenon. Especially the measurements of DR-effects in stirred reactors provided experimental data not available previously. The possible use of DRA in controlling chemical processes in stirred reactors has been recently under consideration.

The model development aimed at a turbulence model, which would include the damping effect of DRA. The k-ε type model was derived from microscopic models for viscoelastic flow. The extended k-ε model can be applied in pipe flow or more complicated geometry.

7.5 Modelling of fluidized bed risers

In general we can conclude that clear progress has taken place in our capabilities of modelling fluidised beds. This will benefit the industries utilizing fluidised bed technology, including power generation and metallurgical, chemical and petrochemical industries. The simulation results on gas and solids mixing, obtained in the current project, are qualitatively correct and even quantitatively reasonable. This will improve the industries' possibilities to study chemical processes taking place in their equipments and allows them to test effects of different parameters to improve the processes. The models tested in the present work are easily applicable in simulations of small scale processes and phenomena and will predict at least qualitatively correct results. Especially for simulation of large industrial processes, the models still need to be further developed. In this development work, the present models will serve as a good starting point.

8. List of publications produced in the project

Crystallization

Hatakka, H., Shipilova, O., Haario, H. & Kallas, J. 2005. Using a Meshless Transport Method in Modelling of Reactive Crystallization of Barium Sulphate. Proceedings of 12th International Workshop on Industrial Crystallization (BIWIC 2005), September 7–9, 2005, Halle, Germany (eds. Jones, M. and Ulrich, J.), pp. 17–23.

Hatakka, H., Shipilova, O., Haario, H. & Kallas, J. 2005. Modeling of Reactive Crystallization: Using Particle Transport Method in Unsteady-State Modeling of Crystal Growth. Proceedings of 16th International Symposium on Industrial Crystallization, September 11–14, 2005, Dresden, Germany, pp. 145–150.

Liiri, M., Enqvist, Y., Kallas, J. & Aittamaa J. 2006. CFD modelling of single crystal growth of potassium dihydrogen phosphate (KDP) from binary water solution at 30 °C. J. Cryst. Growth, 286, 413–423.

Liiri, M., Kallas, J. & Aittamaa, J. 2005. CFD modelling of single crystal growth of potassium dihydrogen phosphate (KDP) in water solution including one admixture. Proceedings of the 16th International Symposium on Industrial Crystallization, September 11–14, 2005, Dresden, Germany, pp. 187–192.

Gas-liquid processes

Haario, H., Smolianski, A. & Luukka, P. 2005. Vortex shedding behind a rising bubble and two-bubble coalescence: a numerical approach. Appl.Math.Modelling, Vol. 29, Issue 7, 615–632.

Haario, H., Smolianski, A. & Luukka, P. Numerical study of dynamics of single bubbles and bubble swarms. In press.

Laari, A., Kainulainen, M. & Turunen, I. 2004. Estimation of solid-liquid mass transfer for multiphase CFD. CHISA 2004, 16th international congress of Chemical and Process engineering, 22–26 August 2004, Praha, Czech Republic, P5.209.

Sha, Z., Laari, A. & Turunen, I. 2004. Implementation of Population Balance in a Multiphase Model in the CFD Simulation of a Bubble Column. CHISA 2004, 16th international congress of Chemical and Process engineering, 22–26 August 2004, Praha, Czech Republic, E3.2.

Laari, A. & Turunen, I. 2005. Prediction of coalescence properties of gas bubbles in a gas-liquid reactor using persistence time measurements. Proceedings of the 7th World Congress of Chemical Engineering, Glasgow Scotland, 10–14 July, 2005, 10 pages.

Sha, Z., Laari, A. & Turunen, I. 2005. CFD simulation of mass transfer with MUSIG model in bubble column. Proceedings of the 7th World Congress of Chemical Engineering, Glasgow Scotland, 10–14 July, 2005, 10 pages.

Laari, A. & Turunen, I. 2005. Prediction of coalescence properties of gas bubbles in a gas-liquid reactor using persistence time measurements. Chem. Eng. Res. Des., 83, 881–886.

Laari, A. 2005. Gas-liquid mass transfer in bubbly flow: Estimation of mass transfer, bubble size and reactor performance in various applications. Ph.D. Thesis. Acta Universitatis Lappeenrantaensis. Lappeenranta University of Technology, Finland.

Sha, Z., Laari, A. & Turunen, I. Multi-Phase-Multi-Size-Group Model for the Solution of Population Balances in CFD Simulation of Gas-Liquid Bubbly Flows. Accepted for publication in Chemical Engineering & Technology.

Laari, A., Turunen, I. & Sha, Z. 2006. A study of flow hydrodynamics in bubble column using Particle Image Velocimetry (PIV). Submitted to CHISA 2006, 17th international congress of Chemical and Process engineering, 27–31 August 2006, Praha, Czech Republic.

Sha, Z., Zhou, H., Laari, A. & Turunen, I. 2006. CFD study on the influence of bubble size distribution on the flow hydrodynamics in bubble column. Submitted to CHISA 2006, 17th international congress of Chemical and Process engineering, 27–31 August 2006, Praha, Czech Republic.

Ojaniemi, U. & Manninen, M. 2006. Three phase CFD modelling of flotation. Report VTT-R-02999-06. VTT, Espoo.

Manninen, M. & Ojaniemi, U. 2006. Population models for bubbly flow in a stirred reactor. Report VTT-R-02997-06. VTT, Espoo.

Laakkonen, M., Moilanen, P. & Aittamaa, J. 2005. Local bubble size distributions in agitated vessels. Chem. Eng. J., Vol. 106, 133–143.

Laakkonen, M., Moilanen, P., Miettinen, T., Saari, K., Honkanen, M., Saarenrinne, P. & Aittamaa, J. 2005. Local bubble size distributions in agitated vessels – Comparison of three experimental techniques. Chem. Eng. Res. Des., 83A, 50–58.

Laakkonen, M., Honkanen, M., Saarenrinne, P. & Aittamaa, J. 2005. Local bubble size distributions, gas-liquid interfacial area and gas holdups in a stirred vessel with particle image velocimetry. Chem. Eng. J., 109, 37–47.

Laakkonen, M., Alopaeus, V. & Aittamaa, J. 2006. Validation of bubble breakage, coalescence and mass transfer models for gas-liquid dispersion in agitated vessel. Chem. Eng. Sci., 61, 218–228.

Laakkonen, M., Moilanen, P., Alopaeus, V. & Aittamaa, J. 2006. Dynamic modeling of local reaction conditions in an agitated aerobic fermenter. AIChE J., 52, 1673–1689.

Alopaeus, V., Laakkonen, M. & Aittamaa, J. 2006. Numerical solution of moment-transformed population balance equation with fixed quadrature points. Chem. Eng. Sci. (in press, 2006).

Trickle reactors

Alopaeus, V., Hynynen, K. & Aittamaa, J. 2006. A cellular automata model for liquid distribution in trickle bed reactors. Accepted to Chem. Eng. Sci.

Drag reduction

Olin, M., Manninen, M. & Pättikangas, T. 2005. k-ε turbulence model for polymeric drag reduction. Project report PRO5/P5020/05. VTT, Espoo.

Koskinen, J., Manninen, M., Pättikangas, T., Leinonen, T., Denifl, P., Pöhler, H., Saarenrinne, P. & Eloranta, H. 2005. Controlling turbulence with drag reducing agents in stirred tank reactors. 7th World Congress of Chemical Engineering, Glasgow, Scotland, 2005.

Fluidised beds

Ojaniemi, U., Manninen, M. & Taivassalo, V. 2005. CFD Modelling of Turbulent Fluidised Bed. Report PRO5/P5025/05. VTT, Espoo.

Ojaniemi, U., Kallio, S., Hermanson, A., Manninen, M. & Taivassalo, V. Comparison of simulated and measured flow patterns and gas mixing in a 2D turbulent fluidized bed. Abstract submitted to 12th International Conference on Fluidization.

Kallio, S. & Hermanson, A. 2005. Experimental study of flow patterns in a 2D turbulent fluidised bed cold model. Report 2005-2. Åbo Akademi University, Heat Engineering Laboratory.

Kallio, S. 2005. The role of the gas-solid drag force in CFB modelling of fluidization. Report 2005-3. Åbo Akademi University, Heat Engineering Laboratory.

Kallio, S. & Hermanson, A. 2006. Experimental study of solids mixing in a 2D fluidized bed cold model. Report 2006-2. Åbo Akademi University, Heat Engineering Laboratory.

Kallio, S. 2006. Characteristics of gas and solids mixing in a CFB determined from 3D CFD simulations. 19th International Conference on Fluidized Bed Combustion, Vienna, Austria, 2006.

Seppälä, M. 2006. Kaasu-partikkelivirtausten numeeriset laskentamenetelmät. Master's thesis. VTT, Espoo.

Published by

Series title, number and
report code of publication

VTT Research Notes 2340
VTT–TIED–2340

Author(s)
Manninen, Mikko (ed.)

Title

Modelling of multiphase chemical reactors (ModCheR)
Final report

Abstract

The project "Modelling of multiphase chemical reactors (ModCheR)" was carried out by research groups from Helsinki University of Technology, VTT, Lappeenranta University of Technology, Åbo Akademi University and Tampere University of Technology. The model development was concentrated on CFD, but population balance models, cell interaction models and simple algebraic reactor models were also included. Extensive experimental work was carried out in order to provide data for model validation. Five topics were studied in the project. In crystallization, the subjects covered single crystal growth, batch crystallization and continuous crystallization. Both experimental work and model development were carried out. As gas-liquid processes, stirred reactors, bubble columns and flotation were studied. The modelling approaches included CFD and multiblock models. Modelling of trickle bed reactors involved both CFD and simpler approaches and important part of the work consisted of developing models for the interaction and dispersion terms in the equations. Work on drag reducing agents included measurements of the DR-effect in stirred reactors and pipe flow and model development for describing the effect of DRA on turbulence. In modelling of fluidised beds, models of turbulent bed and circulating bed were developed and validated, in particular, mixing of gas and solid, drag models, and macroscopic models were investigated. This final report describes the main results of the project. More detailed information can be found in the reports and publications produced in the project and referred to in this report.

Keywords
chemical reactors, modelling, multiphase flow, crystallization, computational fluid dynamics, trickle bed reactors, fluidised beds, drag reduction, gas-liquid processes, mass transfer, population balance, flotation

ISBN
951–38–6793–5 (soft back ed.)
951–38–6794–3 (URL: http://www.vtt.fi/publications/index.jsp)

Series title and ISSN	Project number
VTT Tiedotteita – Research Notes 1235–0605 (soft back edition) 1455–0865 (URL: http://www.vtt.fi/publications/index.jsp)	342

Date	Language	Pages	Price
May 2006	English	181 p.	D

Name of project	Commissioned by
Modelling of multiphase chemical reactors (ModCheR)	Finnish Funding Agency for Technology and Innovation (Tekes), Neste Oil Oy, Outokumpu Research Oy, Kemira Oyj, Foster Wheeler Energia Oy, OMG Harjavalta Nickel Oy

Contact	Sold by
VTT Technical Research Centre of Finland P.O. Box 1000, FI-02044 VTT, Finland Phone internat. + 358 20 722 111 Fax + 358 20 722 5000	VTT P.O.Box 1000, FI-02044 VTT, Finland Phone internat. +358 20 722 4404 Fax +358 20 722 4374

The project "Modelling of multiphase chemical reactors (ModCheR)" was carried out jointly by research groups from Helsinki University of Technology, VTT, Lappeenranta University of Technology, Åbo Akademi University and Tampere University of Technology. It included extensive measurements and model development in the topics of crystallization, gas-liquid processes, trickle bed reactors, drag reduction, and fluidised beds. New data and modelling techniques were developed for single crystal growth and suspension crystallization. Studies in gas-liquid processes included measurements and model development for stirred reactors with gas dispersion, bubble columns and flotation. Both CFD and simpler approaches were considered in modelling of trickle bed reactors, with validation data from experiments. Work on drag reducing agents included measurements of the DR-effect in stirred reactors and pipe flow and model development. CFD models for turbulent and circulating fluidised bed were developed and validated. This final report summarizes the main results of experimental work, model development and validation studies carried out in the ModCheR-project.

Tätä julkaisua myy
VTT
PL 1000
02044 VTT
Puh. 020 722 4404
Faksi 020 722 4374

Denna publikation säljs av
VTT
PB 1000
02044 VTT
Tel. 020 722 4404
Fax 020 722 4374

This publication is available from
VTT
P.O. Box 1000
FI-02044 VTT, Finland
Phone internat. + 358 20 722 4404
Fax + 358 20 722 4374

ISBN 951-38-6793-5 (soft back ed.)
ISSN 1235-0605 (soft back ed.)

ISBN 951-38-6794-3 (URL: http://www.vtt.fi/publications/index.jsp)
ISSN 1455-0865 (URL: http://www.vtt.fi/publications/index.jsp)